Extending X-ray Photoelectron Spectroscopy to Atmospheric Pressures and Above



Elizabeth S. Jones

Trinity College, University of Oxford

A thesis submitted for the degree of

Doctor of Philosophy

April 2024

Declaration

This thesis is submitted to fulfil the requirements for the degree of Doctor of Philosophy in the Department of Materials at the University of Oxford. I declare that this thesis has not been submitted, in whole or in part, in any previous application for a degree. I declare that, except where specific reference is made to the work of others, or explicit acknowledgement is given, the contents of this dissertation are the results of my own work. This thesis contains fewer than 40,000 words.

Acknowledgements

There are a great number of people I want to thank for their help over the past few years.

First of all, I wish to thank my supervisor, Rob Weatherup, for this opportunity, for your continued enthusiasm you have had for this project, and for the knowledge you have passed on. I must admit I will not miss the long beamtimes too much, but thank you for all of the many hours of effort you put in during those tough times!

I would also like to thank the wonderful members of the Weatherup research group who have been a pleasure to work with, and there are a few members I wish to thank in particular. To Josh, thank you for being so enthusiastic (and stubborn!), you made the many beamtimes so much easier and fun. I will always be grateful for the time you took to help with this work and for teaching me as much as you could during that time. To Peixi, it has been a delight to work with you on beamtimes, and the later stages of this project would not have been successful without you, thank you for your constant positivity. To Leanne, thank you for all of your support and for letting me distract you from your work. I will miss having someone to show the latest videos I have found, and remember you always deserve to leave early! To Michael and Jack, a huge thank you for making a difficult start to the PhD during the pandemic so much more enjoyable, the pub trips and late nights in labs with you were a highlight! An even bigger thank you to Jack, I am so grateful for your friendship and support without which I would not have made it through this PhD.

I have thoroughly enjoyed life at Oxford, but it would have been nothing without all of the fantastic people I met at the Oxford University Korfball Club. You have been the most welcoming, friendly, and caring group of people. I will miss you all (and of course, spending all of my Sundays at Greyfriars School)! I have been incredibly lucky

to make some close friendships through the club and the experience would not have been the same without them. Thank you to Jack and Maggie for being such amazing friends, for all of the laughs, and, most importantly, for always being up for a pub trip and enabling each other's drinking habits! Thank you Flora for all of the late night, deep conversations and for being a delightful teammate and friend (I hope you can continue to score as many goals even without me as your inspiration).

Thank you to all of my friends from St Andrews University for visiting Oxford and for your love and support, it has meant so much to me.

A very special thank you to the people have influenced me the most during my PhD: to my family, to Kara, and to Tilda, I would like to dedicate this thesis to you all.

Kara, living with you for three years during this PhD was my favourite part and words cannot even begin to describe how much you have helped me throughout this project and how much I value your friendship. I will never forget the time we had together and miss having the same conversation with you every day as we brush our teeth! Thank you for everything.

Mum, Dad, and Catherine, thank you for all of your guidance and support throughout my life, I would never have had the opportunities that got me to this point without you. I will forever be grateful for your unwavering love and for always being available for a phone call. I feel like you have lived this PhD with me, so I hope you take the credit you deserve for this project (even if you can never remember my project title!).

And lastly, but never least, thank you Tilda. I have no hesitation in saying the best thing to come out of this PhD will have been meeting you. You have been there for me through all of the highs and lows, and I will endeavour to ensure that your thesis writing is as enjoyable as you have made mine. I could not have done this without your care and love.

Publications

E. S. Jones, J. E. N. Swallow, and R. S. Weatherup, Enclosed Cells for Extending Soft X-Ray Spectroscopies to Atmospheric Pressures and Above, *ACS Symp. Ser*., 2021, **1396**, 175−218

J. E. N. Swallow, E. S. Jones, A. R. Head, J. S. Gibson, R. B. David, M. W. Fraser, M. A. van Spronsen, S. Xu, G. Held, B. Eren, and R. S. Weatherup, Revealing the Role of CO during CO_2 Hydrogenation on Cu Surfaces with *In Situ* Soft X-ray Spectroscopy, *J. Am. Chem. Soc*., 2023, **145**, 6730-6740

E. S. Jones, C. Drivas, J. S. Gibson, J. E. N. Swallow, L. A. H. Jones, T. D. J. Bricknell, M. A. van Spronsen, G. Held, M. A. Isaacs, C. M. A. Parlett, and R. S. Weatherup, *In Situ* Formation of Suspended Graphene Windows for Lab-Based XPS in Liquid and Gas Environments, *ChemCatChem*, published, 2024, 202400239.

Statement of Authorship

This section outlines work which was performed in collaboration with others.

Environmental cell designs were developed with assistance from: Joshua Gibson and Peixi Cong.

Near ambient pressure X-ray Photoelectron Spectroscopy (XPS) of a Cu foil was collected on my behalf at the Center for Functional Nanomaterials, Brookhaven National Lab, USA, by: Ashley Head, Roey Ben David, and Baran Eren.

Fitting of near-ambient pressure-XPS and atmospheric pressure near-edge X-ray absorption fine-structure spectroscopy data in Chapter 4 performed alongside: Jack Swallow and Baran Eren.

2D Raman maps of graphene transferred using a gold support were collected by: Robert Weatherup.

XPS of the etching of Au using liquid etchants within a conventional lab-based system was collected at HarwellXPS, Research Complex at Harwell, UK, alongside: Charalampos Drivas, Mark Isaacs, and Christopher Parlett.

Reference X-ray spectroscopy data of Zn and brass foils was collected on my behalf by Virginia Pérez Dieste at CIRCE beamline, ALBA synchrotron, Spain.

Contents

Abstract 10
Glossary 12
Chapter 1: Introduction 16
1.1 Introduction to Catalysis 16
1.2 Importance of Studying Catalysts under Operating Conditions 17
1.3 Current In Situ/Operando *Techniques* 20
1.4 Challenges and Examples of In Situ/Operando *X-ray Spectroscopy Techniques* 22
1.5 Thesis Outline 26
Chapter 2: Characterisation Techniques 28
2.1 X-ray Spectroscopy 28
2.1.1 X-ray Photoelectron Spectroscopy 28
2.1.2 X-ray Absorption Spectroscopy 38
2.2 Microscopy 46
2.2.1 Scanning Electron Microscopy 46
2.2.2 Scanning Transmission Electron Microscopy and Electron Energy Loss Spectroscopy 47
2.3 Raman Spectroscopy 49
2.4 Mass Spectrometry 51
2.5 Deposition of Thin Films and Nanoparticles 52
2.5.1 Physical Vapour Deposition (and Plasma Cleaning) 52
2.5.2 Nanoparticle Deposition 53
Chapter 3: Environmental Cells 56
3.1: General Design 56
3.2: Window Materials 60
3.2.1 Continuous Membranes 61
3.2.2: Perforated Membranes (with Suspended 2D Materials) 64
3.3: Environmental Cells for this Thesis 66
3.3.1: NEXAFS Cell (Version 1) 67
3.3.2: NEXAFS/XPS Cell (Version 2) 71
3.3.3 Liquid Flow Cell for Lab-Based XPS 74
3.4 Outlook 76
Chapter 4: Revealing the Role of CO during CO_2 Hydrogenation on Cu Surfaces 77
4.1 Introduction 78

4.2 Brief Overview of Methods 85
4.3 NAP-XPS and AtmP-NEXAFS of Cu 87
4.4 Mass Spectrometry of Cu Powder 98
4.5 Discussion 102
4.6 Conclusion 108
Chapter 5: Graphene as a Window for Ambient Pressure X-Ray Spectroscopy 111
5.1 Introduction 111
5.2 Transfer of Graphene using a Au/PDMS Support 121
5.2.1 Method 121
5.2.2 Characterisation 124
5.3 Experimental Applications of Graphene Membranes 130
5.3.1 Solid/Gas Interface using a NAP-XPS System 131
5.3.2 Solid/Liquid Interface using a Conventional Lab-based XPS System 135
5.4 Direct Growth of Graphene onto a Perforated Silicon Nitride Membrane 141
5.5 Conclusion 144
Chapter 6: Investigating the Behaviour of Zn during CO_2 Hydrogenation on Cu/Zn Nanoparticles at Atmospheric Pressure 146
6.1 Introduction 146
6.2 Brief Overview of Methods 153
6.3 NAP-XPS vs AtmP-XPS of Brass 156
6.4 STEM-EELS of Brass Nanoparticles 166
6.5 AtmP-NEXAFS of Brass Nanoparticles 171
6.6 Discussion 180
6.7 Conclusion 188
Chapter 7: Summary and Future Work 190
7.1 Summary 190
7.2 Future Work 194
Appendix 197
Chapter 2: Characterisation Techniques 197
Origin of Signals in SEM 197
Optical Microscopy 199
Origin of Features in Raman Spectroscopy for Graphene 201
Chemical Vapour Deposition Chamber 205
Chapter 3: Environmental Cells 208
Choice of Window Material – Transparency 208
Choice of Window Material – Stability 213

Examples of Applications of Membranes – Continuous Membranes 216
Examples of Applications of Membranes – Perforated Membranes 219
Chapter 4: Revealing the Role of CO during CO_2 Hydrogenation on Cu Surfaces . 223
Microstructural Characterisation of Cu Catalysts using SEM 223
C K-edge and O K-edge from AtmP-NEXAFS 225
Ex Situ *XPS of Cu Powder for MS Measurements* 227
Chapter 5: Graphene as a Membrane for Ambient Pressure X-ray Spectroscopy . 229
Linear Dispersion Relation of Graphene 229
O 1s of Graphene Transferred using Au/PDMS 230
CVD Growth Mechanism and Parameters 231
Suspending a Ni Film over a Perforated Silicon Nitride Membrane 233
Optimisation of CVD Growth of Graphene – Ethylene Precursor 236
Optimisation of CVD Growth of Graphene – Acetylene Precursor 243
Chapter 6: Investigating the Behaviour of Zn during CO_2 Hydrogenation on Cu/Zn Nanoparticles at Atmospheric Pressure 248
Lab-based XPS: Sputtering Profiles of Zn and Brass Foils 248
Reference Data for the Cu L_3-edge and Zn L_3-edge 251
AtmP-NEXAFS of Brass Nanoparticles: $CO_2 \rightarrow H_2 \rightarrow CO_2$ 257
References 259

Abstract

Soft X-ray spectroscopies are powerful tools to study the chemical state of surfaces with nanometre-scale surface sensitivity, and thus are of significant interest in the field of heterogeneous catalysis. Understanding how catalysts operate under reaction conditions is vital to improve their performance in areas such as energy storage and conversion, but accessing both surface chemical information and realistic reaction conditions remains an outstanding challenge.

In this thesis, environmental cells are implemented to perform *operando* X-ray photoelectron (XPS) and absorption spectroscopy (XAS) over catalysts relevant for the conversion of CO_2 to methanol; a promising route for sustainable chemical production.

Initially, an environmental cell sealed with a silicon nitride (SiN_x) window (100 nm) was used to determine the role of CO over a Cu catalyst in the hydrogenation of CO_2. High pressure XAS alongside complementary near ambient pressure (NAP)-XPS and mass spectrometry measurements determined that CO acts as an oxygen scavenger to recover active metallic sites on the Cu surface following oxidation, which is not achieved with H_2 alone at these temperatures.

To extend the environmental cell approach to enable high pressure XPS, a method to transfer graphene from its growth substrate to a perforated SiN_x membrane was developed. This method involved depositing a thin Au support onto graphene with an additional polymer frame atop. The Au layer protected the graphene from contamination and the polymer frame ensured the graphene did not wrinkle or tear substantially. The reliable transfer of graphene using this method enabled measurements of 1 bar of Ar within a NAP-XPS system, and the removal of Au with a liquid etchant in lab-based XPS.

Finally, using graphene suspended over perforated SiN_x membranes, Cu/Zn nanoparticles were studied under similar conditions to those used to study pure Cu films. Both high pressure XPS and XAS (at 1 bar) were performed to determine the role of Zn in increasing catalytic activity. Complementary scanning transmission electron microscopy revealed how the distribution of chemical species in the catalyst changes with pre-treatment conditions. The order of dosing H_2 and CO_2 gas has a significant influence on whether Cu^0/Zn^0 alloy dominates or the nanoparticles exsolve into Cu^0 and ZnO_x; the addition of CO recovers some of the alloy component.

Overall, this thesis successfully demonstrates and applies new approaches to enable high pressure soft X-ray spectroscopy of industrially-relevant catalysts under more representative reaction conditions than previously possible. The developments in environmental design and manufacture of graphene windows allowed X-ray spectroscopy to be reliably performed at 1 bar within this thesis. Since the experiments shown in this thesis, X-ray spectroscopy is now being performed at 4 bar by the Weatherup research group using the same techniques, with ambition to further increase the pressures possible for X-ray spectroscopy.

Glossary

AES: Auger-Meitner electron spectra

AEY: Auger-Meitner electron yield

AtmP: atmospheric pressure

BLG: bilayer graphene

Brass: $Cu_{70}Zn_{30}$

BSE: backscattered electrons

CEY: conversion electron yield

Continuous SiN_x membrane: a SiN_x membrane with a continuous window

CPS: counts per second

Cu^0: metallic Cu

CVD: chemical vapour deposition

DFT: density functional theory

E_A: activation energy

E_B: binding energy

EBSD: electron backscatter diffraction

E-cells: environmental cells

EDS: energy dispersive X-ray spectroscopy

EELS: electron energy loss spectroscopy

E_F: Fermi energy

E_k: kinetic energy

E-TEM: environmental TEM

EY: electron yield

FLG: few-layered graphene

FWHM (Γ): full width at half maximum

FY: fluorescence yield

GO: graphene oxide

Graphene membrane: graphene suspended over the holes of a window in a perforated SiN_x membrane

HAXPES: hard X-ray photoelectron spectroscopy

h-BN: hexagonal boron nitride

IMFP: inelastic mean free path

IPA: isopropanol

IPFY: inverse partial fluorescence yield

LHS: left-hand side

MFCs: mass-flow controllers

MLG: monolayer graphene

Mr: molecular mass

MS: mass spectrometry

NAP: near ambient pressure

NEXAFS: near-edge X-ray absorption fine-structure spectroscopy

NPs: nanoparticles

PDMS: polydimethylsiloxane

PEEK: polyether ether ketone

PEEM: photoemission electron microscopy

Perforated SiN_x membrane: a silicon nitride membrane with holes in the window

PFY: partial fluorescence yield

PMMA: polymethyl methacrylate

PVA: poly vinyl (alcohol)

QMS: quadrupole mass spectrometer

RF: radio frequency

RHS: right-hand side

RSF: relative sensitivity factor

RWGS: reverse water-gas shift

SE: secondary electrons

SEIRAS: surface-enhanced infrared reflection absorption spectroscopy

SEM: scanning electron microscopy

SERS: surface-enhanced Raman spectroscopy

SFG: sum frequency generation

Si/SiO_2: Si wafer with a 300 nm thick SiO_2 layer on top

SiN_x membrane: a membrane with a silicon nitride window supported by a silicon frame

SiN_x: enriched silicon nitride

SMSI: strong metal-support interaction

STEM: scanning transmission electron microscopy

T: temperature

TEM: transmission electron microscopy

TEY: total electron yield

TFY: total fluorescence yield

TRT: thermal release tape

UHV: ultra-high vacuum

WGS: water-gas shift

XAS: X-ray absorption spectroscopy

XPS: X-ray photoelectron spectroscopy

Zn^0: metallic Zn

ZnO_x: partially reduced ZnO, containing O vacancies

ΔG: change in Gibbs free energy

ΔH: change in enthalpy

ΔS: change in entropy

Chapter 1: Introduction

Heterogeneous catalysis plays a crucial part in our everyday lives, from catalytic converters in cars, to the catalysts used across a wide range of industrial processes which provide the chemical feedstocks for plastics, detergents, and other materials in everyday use. The performance of materials used for heterogeneous catalysis is largely determined by reactions occurring at the interfaces between the material and the liquid or gas environments.[1,2] As reaction conditions change so do these interfaces, with potentially dramatic effects on their structure, chemistry, and performance. Understanding this interfacial behaviour is increasingly important to the selection and development of new materials, particularly those related to the development of a more sustainable economy.[3–6]

The optimisation of catalysts requires understanding of the changes they undergo during operation. Common techniques to study catalyst surfaces, such as soft X-ray spectroscopies, require ultra-high vacuum (UHV) conditions which are far from the operating conditions of heterogeneous catalysis. Hence, there is a pressing need for research into extending characterisation techniques towards the operating pressures of catalysts (typically atmospheric pressure and above); which is the focus of this thesis.

1.1 Introduction to Catalysis

For a reaction to proceed the reactants must have sufficient energy to overcome the activation energy (E_A) of the reaction.[5,7,8] To increase the rate of the reaction, a higher temperature can be used which increases the proportion of reactants with energy greater than E_A.[7,8] However, increasing the reaction temperature can be costly. An alternative method to increase the rate of reaction is to introduce a catalyst. A catalyst is a material/substance that is not consumed in the reaction, but which increases the rate of reaction by providing an alternative reaction pathway with a lower E_A.[5,7,8] Therefore, the

rate is increased without increasing the temperature yielding a more economical process. The study of factors affecting the rate of a reaction is referred to as: reaction kinetics.

The catalyst active sites refer to the specific positions on the catalyst surface that are responsible for lowering the E_A of the reaction by providing preferential binding of reactants.[5,9–12] These sites should be regenerated after each reaction cycle enabling their use over a long time. However, catalysts can be deactivated, for instance by blocking or restructuring of the active sites, thus requiring regeneration processes or potential replacement.[7,13–16] Improvements in catalyst performance can be achieved by better understanding the exact nature of the active sites and the reaction pathway they promote.[11]

1.2 Importance of Studying Catalysts under Operating Conditions

Thermodynamics describes whether a reaction will proceed or not and that it depends on temperature (T), change in entropy (ΔS), and change in enthalpy (ΔH) as shown in Equation 1.1.

Equation 1.1:

$$\Delta G = \Delta H - T\Delta S$$

For a reaction to proceed spontaneously the change in Gibbs free energy (ΔG) should be negative, therefore reactions that increase entropy and decrease enthalpy (are exothermic) are favoured. The introduction of a catalyst will not change ΔG for a reaction.

For reversible reactions the position of equilibrium of the reaction will be determined by the thermodynamics under specific conditions. Equation 1.2 shows an arbitrary reversible reaction where the forward reaction is exothermic and the left-hand side (LHS) of the equation contains a greater number of moles of gas.

Equation 1.2:

$$2A_{(g)} + 2B_{(g)} \rightleftharpoons C_{(g)} + D_{(g)} \qquad \Delta H < 0, \Delta S < 0$$

According to Equation 1.1, to favour the exothermic reaction towards the right-hand side (RHS) the temperature should be decreased so that ΔG <0, since ΔH <0 (exothermic) and ΔS <0 (decrease in the number of moles of gas). Therefore, the positive TΔS term should be as small as possible to ensure the negative ΔH term dominates. Whereas, the endothermic reaction (ΔH >0) towards the LHS is favoured by an increase in temperature to ensure the negative TΔS term dominates and ΔG <0. This example demonstrates the importance of studying reactions at the relevant temperature, since temperature will greatly influence the position of equilibrium.

Pressure will also affect the position of equilibrium, as described by Le Chatelier's Principle.[8,11] Le Chatelier's Principle states that the position of equilibrium will shift to counteract any changes made to the system, for example, if temperature is increased then the endothermic reaction is preferred to decrease the temperature (indicated by consideration of Equation 1.1). If pressure is increased then equilibrium will shift to the side of the reaction with fewer moles of gas (for Equation 1.2 the equilibrium shifts towards the RHS) to decrease the pressure. Since the position of equilibrium is heavily dependent on pressure, it is important to study reactions at their relevant pressures too.

Detailed studies have been performed to demonstrate the changes a surface undergoes across a wide range of pressures.[17] It is often not sufficient to perform "post-mortem" (*ex situ*) measurements, where the reaction is stopped prior to measuring the surface and the sample is inertly transferred in vacuum, as the state of that surface may not be preserved.[18–20] Functional materials research has often relied on correlating *ex situ* characterisation results with application-related performance metrics e.g. activity/selectivity, or electrochemical cycling data. Unfortunately, in many cases this proves inadequate, as little is revealed about dynamic processes or intermediate species, and the transfer process can alter the surface composition and structure.[21] For

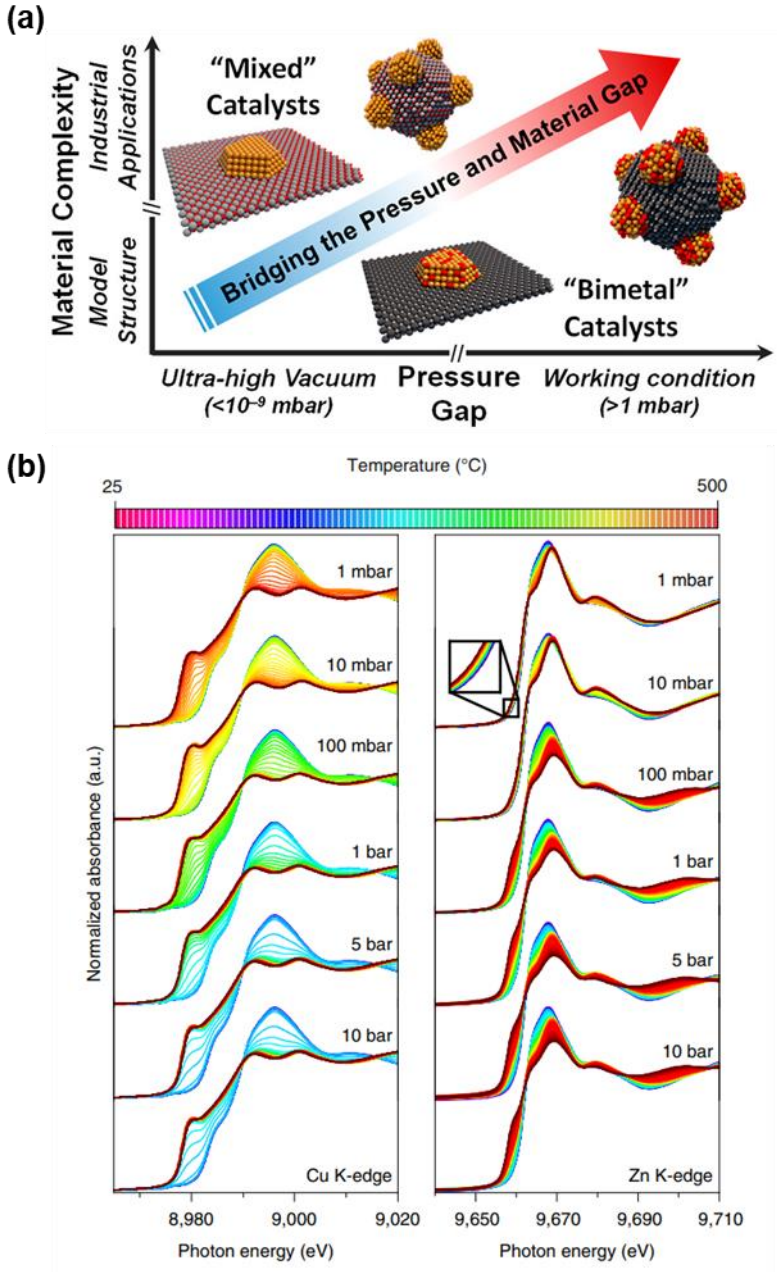


Figure 1.1: *(a) Schematic representing the required pressure and materials complexity accurately to represent industrial catalysts thus bridging the pressure and materials gap. (b) Example of the effect of the pressure gap for a Cu/ZnO/Al_2O_3 catalyst exposed to H_2 at different pressures, whilst heating from 25°C (purple) to 500°C (dark red). The Cu and Zn spectra vary with temperature where the relative variations also depend on the pressure of H_2. (a) Taken directly from J. Kim* et al.*,* ACS Catal.*, 2021,* ***11****, 8645–8677. (b) Taken directly from A. Beck* et al.*,* Nat. Catal.*, 2021,* ***4****, 488–497.*

example, the surface of Pt(557) has been observed to reconstruct when exposed to CO gas. However, upon returning to vacuum, the change is found to be reversible with the surface recovering its original state.[22] Furthermore, it is often not sufficient to study reactions at pressures much smaller than their operating conditions. The so-called "pressure gap" this introduces can alter the thermodynamics and kinetics of the reaction, as indicated in Figure 1.1 (a).[17,19–21,23,24] Bluhm *et al.* demonstrated this pressure gap for the oxidation of CO over a Ru catalyst; the difference in catalytically active sites present at different pressures was found to significantly affect the kinetics of the reaction.[20] Furthermore, relevant to the hydrogenation of CO_2 to methanol reaction which is studied in this thesis, Beck *et al.* investigated changes with pressure for a $Cu/Zn/Al_2O_3$ catalyst.[17] Figure 1.1 (b) shows that the temperature variation for Cu and Zn in hard X-ray absorption spectroscopy (XAS) is heavily dependent on pressure, and in particular the active species do not appear to form below 1 bar of H_2.[17] It is also important to consider the "materials gap" shown in Figure 1.1 (a), where a model catalyst may not provide an accurate representation of the real catalytic system.[23]

1.3 Current In Situ/Operando *Techniques*

The understanding of catalysts and surfaces under operating conditions is vital in developing solutions to issues such as: energy storage, degradation in batteries, and reducing our global CO_2 output.[5,18,25] There have thus been sustained efforts in recent decades to extend interface-sensitive spectroscopic methods to operate under more realistic reaction conditions, including higher gas pressures and liquid environments.[19,25,26] These are commonly termed *in situ* or *operando* approaches, and although these terms are not rigorously applied, *in situ* often refers to measurement in the reaction environment and *operando* measurements typically also include simultaneous measurements of reaction products.

Through the use of suitable optical windows a variety of *in situ* vibrational spectroscopic techniques have been demonstrated, including sum frequency generation (SFG), surface-enhanced Raman spectroscopy (SERS), and surface-enhanced infrared reflection absorption spectroscopy (SEIRAS), that allow the study of interfaces with atmospheric pressure gases or liquids.[2,26–28] These experiments can often be performed using lab setups providing the benefit of extended measurement time. However, the information collected is not typically element specific which can make meaningful interpretation challenging. Recent developments in windowed gas/liquid cells for environmental transmission electron microscopy (E-TEM), also present the possibility of obtaining chemical information at high spatial resolutions using electron energy loss spectroscopy (EELS).[29,30] Here, the requirement for electron transmission imposes restrictions on maximum cell thickness (tens to hundreds of nanometers), that make representative cell geometries difficult to realise, particularly for electrochemical systems.[26] Nevertheless a variety of electrochemical processes have been successfully observed.[31,32] Unfortunately, obtaining corresponding chemical information is hampered by the high electron doses required to acquire EELS of sufficient quality, as this is likely to result in excessive beam damage when applied in dense reaction environments.

X-ray spectroscopies are a common method to analyse the surface of a catalyst in a non-destructive way. X-ray photoelectron spectroscopy (XPS) is popular due to its sensitivity to chemical state via detecting emitted photoelectrons from a surface.[33] Additionally, the inelastic mean free path (IMFP) of electrons is <10 nm in a solid. Therefore, XPS is a highly surface sensitive technique.[34–36] The combination of surface sensitivity and detailed information about chemical state make it a powerful tool for studying catalysts and relevant battery materials where most of the chemistry occurs at the interface between a solid and a gas/liquid. However, the short IMFP of electrons means UHV conditions are required for detection of photoelectrons making it very difficult

to perform *in situ* measurements.[37] XAS is another powerful tool to study catalysts and provides information on local environment and bonding, as well as similar information to XPS.[38–40] There are a variety of methods to measure XAS by either detecting emitted X-rays or electrons. Therefore, depending on the chosen detection method, measurements can be performed more easily at elevated pressures compared to XPS.[37,39] Chapter 2 describes XPS and XAS in greater detail.

1.4 Challenges and Examples of In Situ/Operando *X-ray Spectroscopy Techniques*

XPS and XAS can provide powerful element-specific chemical information about interfaces; however, they typically require UHV conditions for operation.[18] The key obstacles in extending these techniques to ambient pressures are related to the short IMFP of electrons in high pressure gases and liquids.[34,36,41–44] Using high energy (hard, >5 keV) X-rays can relax these constraints and thus make *in situ/operando* measurements more straightforward through increasing the kinetic energy of electrons and, therefore, their IMFP. However, it is the short IMFP of photoelectrons in solids (<10 nm for kinetic energies <1000 eV) that is responsible for the surface sensitivity achievable with XPS.[34,41] Another consideration when using hard X-rays in XPS is the rapid decay in photoionisation cross sections as energy increases.[45] The photoionisation cross section is essentially the probability of an ionisation event taking place when a photon interacts with an atom.

Low energy (soft, <2 keV) X-rays are often preferred to provide highly surface sensitive information and detection of light elements.[19,45] The shorter attenuation length of soft X-rays restricts the possible probing depth. For example, the absorption edges of many key light elements (C, N, O, F) lie below 1000 eV, where X-ray attenuation lengths are well below 10 µm in most materials.[43]

Soft X-rays will result in a shorter IMFP of electrons meaning they do not travel far enough in liquid/gas environments to reach the detector.[2,19] Therefore, the gas environment in conventional XPS is normally restricted to pressures <10^{-5} mbar, to avoid significant inelastic scattering of photoelectrons. Early-on in the development of near ambient pressure (NAP)-XPS, differentially pumped apertures were thus introduced as a means of measuring gases at higher pressures, by reducing the distance photoelectrons have to travel through the high pressure gas.[1,24,38,46–48] Commercially-available NAP-XPS analysers use multiple differentially pumped apertures to achieve this in stages, with electrostatic lenses used to minimize signal loss by focusing photoelectrons through these apertures.[1,2,19,49] In this way, measurements can be performed at pressures of tens of mbar, allowing the study of solid, liquid and gas phases, and the interfaces between various combinations of these phases.[38,48,50] Further increases in the operating pressure of NAP-XPS are often limited by practical constraints on the path length between sample and electron analyser.

A promising approach to extend NAP-XPS to higher pressures has been the development of hard X-ray photoelectron spectroscopy (HAXPES) beamlines at synchrotrons that allow samples to be measured using hard X-rays at ambient pressures of >1 bar.[51–54] The increased IMFP of emitted photoelectrons from hard X-rays means they can travel further in dense media. Additionally, local gas injection and a grazing angle of incidence to limit the distance electrons must travel has enabled measurements up to 500 mbar in NAP-XPS using hard X-rays.[55] However, the signal was very weak which led to a low signal/noise ratio and difficulty in interpreting the data.[55]

Another appealing method to perform *in situ* measurements is by using environmental cells (E-cells) which have become more popular over recent years.[2,9,60–69,15,70,71,18,24,25,56–59] Rather than increasing the pressure of the whole vacuum system, the desired environment is contained within an enclosed volume and sealed by a

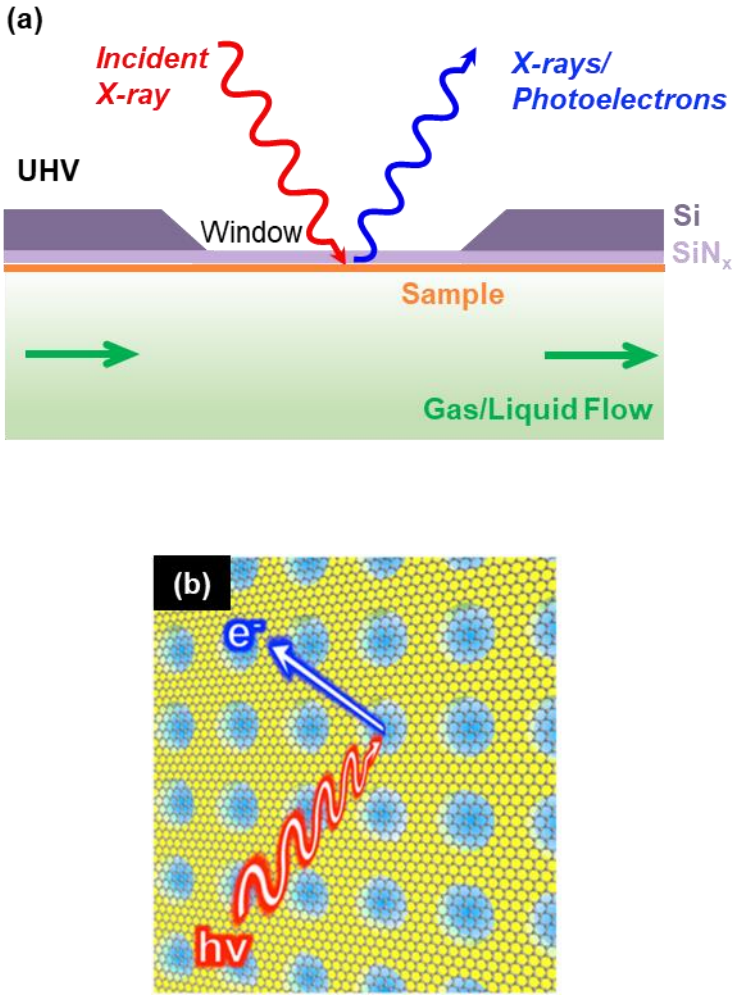


Figure 1.2: *(a) Diagram of an E-cell sealed with a silicon nitride (SiN_x) membrane sealing a flowing liquid or gas. The sample is usually deposited directly onto the window of the membrane such that it can be exposed to the environment in the E-cell (see Chapter 3 for details on other configurations). (b) Schematic showing how graphene suspends over the holes of a perforated SiN_x window to enable X-ray and electron transparency. (b) Taken directly from R. S. Weatherup* et al.*,* J. Phys. Chem. Lett.*, 2016, **7**, 1622–1627.*

membrane (Figure 1.2 (a)). The volume outside of the cell can be maintained at UHV and this places fewer constraints on the pressure of gas (or volume of liquid) compared to NAP-XPS. For this method the window of the membrane used must be able to withstand a large pressure difference across it and maintain X-ray and/or electron transparency for the relevant spectroscopy being performed. The sample is usually deposited directly onto the window of the membrane as shown in Figure 1.2 (a), with possible alternative configurations discussed in Chapter 3. A common window material is enriched silicon nitride (SiN_x). When SiN_x is 100-200 nm thick it is not suitable for measurements requiring electron transparency. Although XPS measurements have been performed using very thin SiN_x or Si windows (5-15 nm) to measure liquids in lab-based and synchrotron-based systems, they required the use of hard X-rays to provide photoelectrons with sufficient kinetic energy to escape.[52,66,72,73] Lab-based soft XPS (herein referred to as lab-based XPS) cannot be easily performed using continuous SiN_x windows as the electrons do not have sufficient kinetic energy to escape resulting in a weak signal, consequently longer measurement times would be required. Instead, a perforated SiN_x window can be used where a 2D material is suspended over the holes in the window (Figure 1.2 (b)) enabling XPS measurements over a shorter timescale. The 2D material graphene is ideal for this purpose as it is impermeable to gases, highly transparent to electrons, and highly conductive which minimises charging effects in XPS.[19,21,57–60,67,74–76] However, the reliable manufacture of graphene suspended over perforated SiN_x membranes (for convenience herein referred to as: graphene membranes) is not trivial. Graphene must usually be transferred from its growth substrate to the perforated window which often introduces tears and contamination resulting in leaks in the E-cell.[57]

1.5 Thesis Outline

This thesis will focus on the development of E-cells, graphene membrane manufacture, and the application of high pressure X-ray spectroscopy to improve understanding of heterogeneous catalyst performance. The chosen reaction is the hydrogenation of CO_2 to methanol over a Cu or Cu/Zn catalyst relevant for sustainable fuel production from CO_2. Chapter 2 outlines the basics of the characterisation techniques used, with a particular focus on X-ray spectroscopy techniques due to their relevance to the experiments performed. Chapter 3 provides more detail on the development of E-cells and their importance for *in situ/operando* X-ray spectroscopy measurements. Window materials for sealing the E-cells are compared and the specific E-cell designs used in this thesis are also presented. Chapter 4 reports a high pressure XAS study (using an E-cell) of a Cu catalyst to understand the role of CO in the hydrogenation of CO_2. It was determined that CO acts as an oxygen scavenger and effectively regenerates the catalyst should it become oxidised, where the order of dosing H_2 and CO_2 can determine whether Cu is oxidised or not. The results are complemented by NAP-XPS and mass spectrometry (MS) data. Chapter 5 details the method that was developed to transfer graphene to a perforated SiN_x support to make graphene membranes in a reliable manner; this method used a thin layer of Au and polymer frame. The manufacture of graphene membranes enabled XPS measurements of 1 bar of gas in a NAP-XPS system, and a flowing liquid in a conventional lab-based system. Chapter 6 investigates the role of Zn in promoting CO_2 hydrogenation using Cu/Zn nanoparticles (NPs) in a high pressure X-ray spectroscopy experiment. Graphene membranes and an improved E-cell design enabled sustained measurements at 1 bar with XPS and XAS. *Ex situ* scanning transmission electron microscopy- (STEM-)EELS images of Cu/Zn NPs were also collected to show the structural changes of the system. It was determined that

the order of dosing H_2 and CO_2 can irreversibly change the proportion of Cu^0/Zn^0 alloy where the addition of CO can help recover some alloy sites.

Chapter 2: Characterisation Techniques

This Chapter will outline the characterisation techniques used in this thesis. Details on specific equipment used for experiments is described in the relevant results chapter. This thesis will heavily focus on X-ray spectroscopy, hence photoelectron and absorption spectroscopy are discussed in greater detail. OriginPro software was used to present plots in this thesis.

2.1 X-ray Spectroscopy

2.1.1 X-ray Photoelectron Spectroscopy

XPS involves the excitation and subsequent emission of electrons from a material upon the absorption of discrete photon energies via the photoelectric effect, and thus probes occupied electronic states of a material.[33,37,77] XPS relies on the detection of electrons leaving the sample, hence the information depth is limited by the IMFP of electrons.[1,39] In order to collect an XPS spectrum, a discrete photon energy source is required, which is possible within a lab-based setting and does not necessarily require access to a synchrotron source.[33,37] A synchrotron source provides X-rays with a greater photon flux and variable energy, which improves the signal strength and enables depth profiling.[37,78–80]

To remove an electron from a material in XPS, the energy of the incident photon (hv) must be enough to overcome the atomic binding energy (E_B) and the sample surface work function (ϕ_s). Any leftover energy from the incident photon provides the kinetic energy (E_k') for the electron (see Equation 2.1).

Equation 2.1:

$$E_k' = h\nu - E_B - \phi_S$$

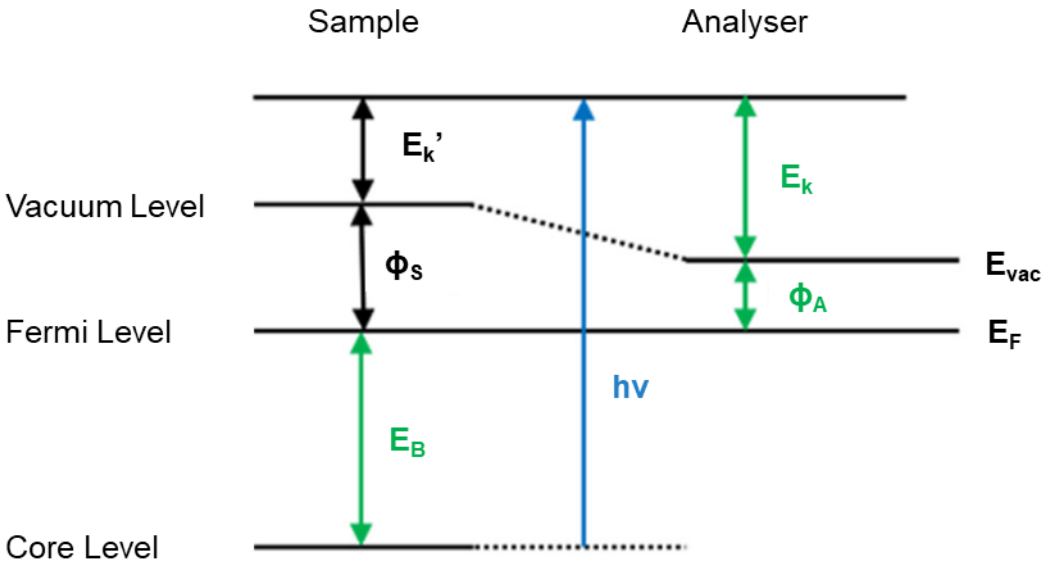


Figure 2.1: *Energy level diagram showing how the Fermi levels of the sample and analyser align. Hence, to calculate the binding energy of photoelectrons (E_B) the kinetic energy of detected photoelectrons (E_k) and the work function of the analyser (ϕ_A) should be considered. Adapted from: F. A. Stevie* et al.*,* J. Vac. Sci. Technol. A Vacuum*, Surfaces, Film., 2020,* ***38****, 063204.*

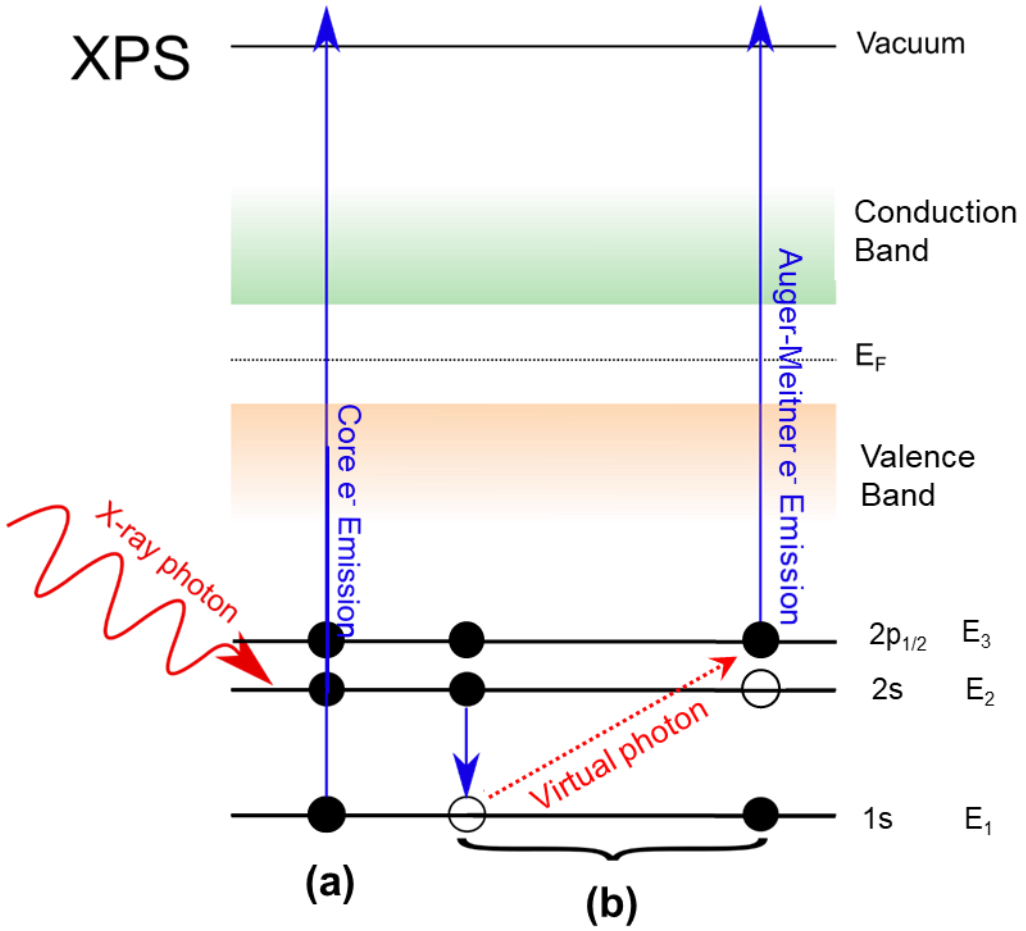


Figure 2.2: *Schematic of the physical processes occurring in XPS. (a) Core-electron emission where an incident X-ray photon directly removes a core-electron. (b) Auger-Meitner emission where another electron de-excites to fill the core-hole left by the process in (a) which releases a virtual photon to excite and remove another electron.*

Energies are referenced to the Fermi level (E_F). In XPS measurements the analyser and sample are in electrical contact so their Fermi levels align (see Figure 2.1). The work function is defined as the minimum energy to excite an electron from the Fermi level to the vacuum level and is material specific.[81] Since the analyser has its own work function (ϕ_A), a contact potential is set up between the sample surface and analyser ($\phi_A - \phi_S$). Therefore, to relate kinetic energy of photoelectrons at the analyser (E_k) to E_B, the work function of the analyser must be considered as shown in Equation 2.2 and Figure 2.1.[33]

Equation 2.2:

$$E_k = E'_k - (\phi_A - \phi_S) = h\nu - E_B - \phi_S - (\phi_A - \phi_S)$$

$$E_k = h\nu - E_B - \phi_A$$

The emitted photoelectrons detected in XPS can originate from either: a direct photoemission process (core-electron emission in Figure 2.2 (a)), or from a secondary process (Auger-Meitner emission in Figure 2.2 (b)). Core-electron emission is where the emitted electron has been removed directly by the incident X-ray photon, hence the electron's kinetic energy is directly dependent on the incident photon energy. The binding energy is characteristic of a particular energy level of a specific atom, and therefore can be used to identify elements present in a sample. The spectroscopic notation used for core-electron emission is the element symbol followed by the core-level the electron originated from, e.g. C 1s is an electron whose binding energy is associated with the 1s orbital in carbon.

Auger-Meitner emission involves an electron (from E_2) filling the core-hole left by core-electron emission (in E_1). This de-excitation releases a virtual photon which can excite another electron to leave the sample (from E_3). The kinetic energy of Auger-

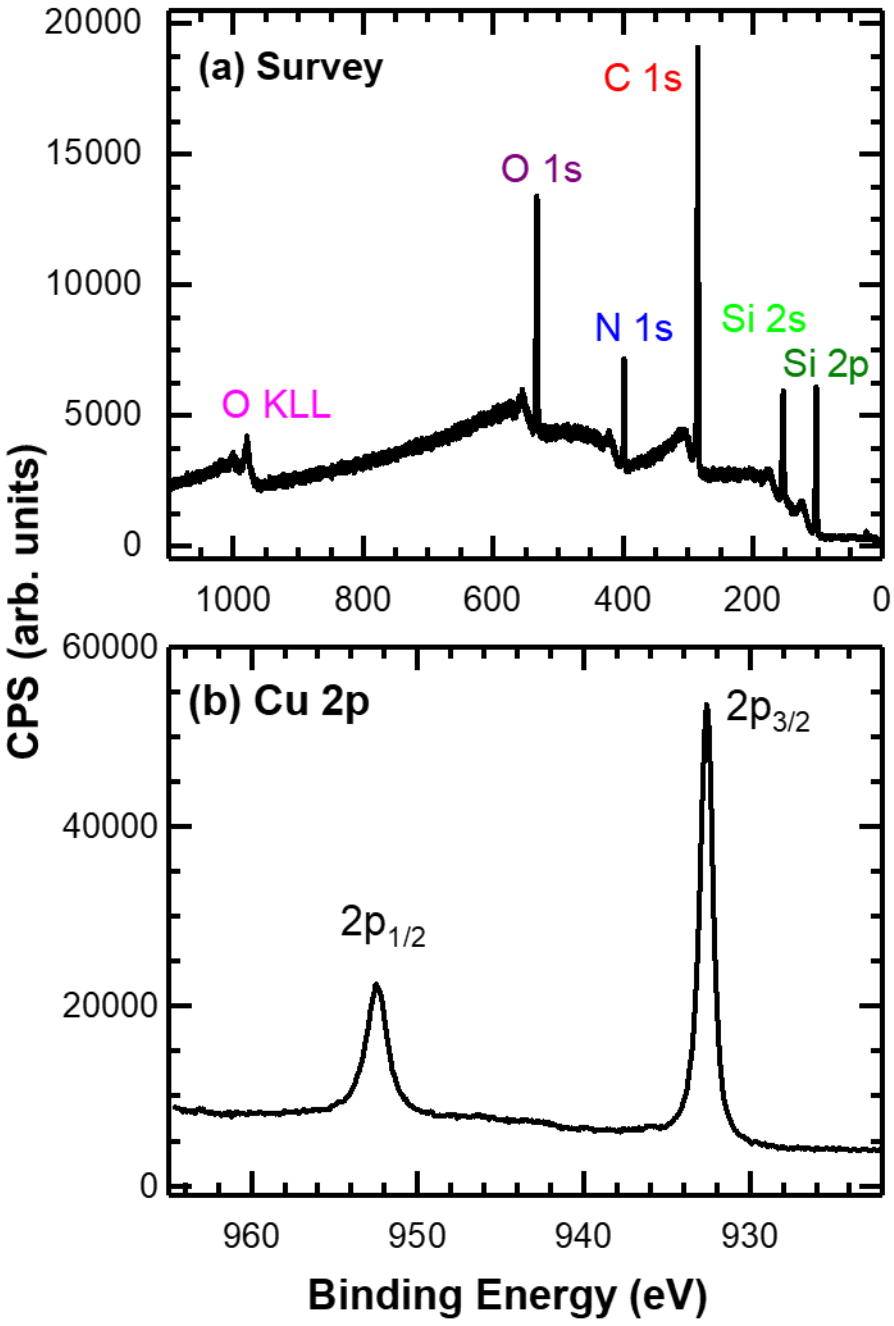


Figure 2.3: *Example XPS spectra. (a) Survey scan from graphene suspended over a perforated SiN_x membrane, from results presented in Chapter 5. (b) Cu 2p region from a sputtered piece of $Cu_{70}Zn_{30}$ foil from results presented in Chapter 6. The y-axis is plotted in counts per second (CPS). Spectra were collected using an excitation energy of 1486 eV.*

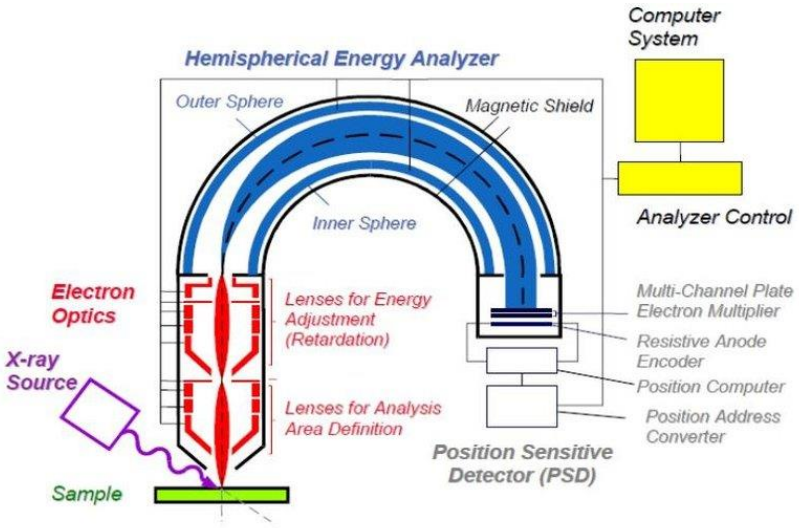


Figure 2.4: *Diagram outlining the hemispherical analyser used in XPS. Taken directly from G. R. Khan,* Appl. Phys. A Mater. Sci. Process*., 2020,* ***126****, 311.*

Meitner electrons depends on the energy difference between the energy levels involved as shown in Equation 2.3, hence is independent of the incident photon energy.

Equation 2.3:

$$E_k = E_1 - E_2 - E_3 - \phi_S$$

The X-ray notation used for Auger-Meitner electron spectra (AES) states the element followed by a list of three letters corresponding to energy levels (K for 1s, L_1 for 2s, L_2 for $2p_{1/2}$, L_3 for $2p_{3/2}$, etc.) which are ordered in the following way: the level the core-electron was removed from via the photoelectric process (E_1), the level the electron de-excited from the fill the core-hole (E_2), and the level the final electron is removed from (E_3). For example, Figure 2.2 (b) shows the process which releases a KL_1L_2 electron, note: transitions are often written without the numerical subscript.

Figure 2.3 (a) shows an example XPS survey spectrum of graphene suspended over a perforated SiN_x membrane. Spectra are collected by exposing the sample to monochromated X-rays (the monochromator prevents additional minor X-ray components from contributing to the spectrum) and excited electrons are collected at the analyser. In XPS, a hemispherical analyser (as shown in Figure 2.4) is used to filter electrons of a specific kinetic energy, controlled by electrostatic lenses, within a specified range, known as the pass energy.[82] Only electrons within that kinetic energy range will be successfully deflected by the electrostatic fields and, hence, detected. During a measurement the number of electrons detected (counts) is recorded whilst scanning over a range of kinetic energies and in the final spectrum kinetic energy is converted to binding energy using Equation 2.2. The value of ϕ_A is often unknown, therefore spectra are calibrated using a reference point. XPS spectra are often displayed using counts per second (CPS) which averages the number of counts over iterations of spectra. Figure 2.3 (a) shows an increasing background as the electron's binding energy increases

(kinetic energy decreases). This is because once electrons are emitted they undergo inelastic scattering before escaping from the sample which decreases their kinetic energy, therefore there is an increase in background signal at a binding energy above characteristic peaks. The background is subtracted using mathematical functions to represent this phenomenon; in this thesis a Shirley background is subtracted from XPS spectra.[83]

Survey spectra scan over a wide range of binding energies using a high pass energy and large step-size to maximise the signal over a short measurement period (Figure 2.3 (a)). Detailed scans of specific regions are collected over a narrower binding energy range using a lower pass energy and smaller step-size to increase the resolution of peaks (Figure 2.3 (b)). A lower pass energy means the signal strength is lower than in a survey spectrum, but repeat iterations are used to increase the signal-to-noise ratio over a relatively short measurement period. Data which was compared in this thesis were collected using the same pass energy.

Figure 2.3 (b) shows the Cu 2p region which contains two peaks: $2p_{3/2}$ and $2p_{1/2}$. For all core-level excitations, apart from 1s, there will be two peaks as a result of spin-orbit coupling (j-coupling). Equation 2.4 shows the equation for j, where s is the spin quantum number (s = ±1/2 for electrons) and l is the angular momentum quantum number (l = 0, 1, 2 for s, p, d, respectively).

Equation 2.4:

$$j = |l + s|$$

Different j states will have a different associated binding energy and a degeneracy of: 2j+1. The degeneracy of each state determines the occupancy and hence, the relative intensity between peaks. For example: Cu 2p has $2p_{1/2}$ and $2p_{3/2}$

states with a ratio of 1:2, in comparison Cu 3d has $3d_{3/2}$ and $3d_{5/2}$ states with a ratio of 2:3 for intensity.

The binding energy of electrons is not only characteristic for a given element, but is also sensitive to the chemical and bonding environment of the atom they originated from.[39] Electronic effects can result in energy shifts of peaks in XPS, referred to as its chemical shift. For example, the presence of a neighboring atom with a greater electronegativity will draw valence electrons away, consequently core electrons are drawn closer to the nucleus and their binding energy is increased. One of the main difficulties in interpreting XPS spectra comes from chemical shifts of nearby peaks resulting in significant overlap which requires careful analysis to separate a broad feature into individual peaks. Furthermore, reliable peak assignment often requires *a priori* assumptions about the chemical species present including suitable standard spectra, and can be complicated by sample specific challenges with reliable energy calibrations.[84]

To fit peaks, software, such as CasaXPS, have pre-defined functions to aid the fitting procedure. A common peak-fitting function is a convolution of a Gaussian and Lorentzian peak shape, usually called a Voigt function.[33,83,85] The Lorentzian contribution accounts for the natural broadening of spectral lines due to the core-hole lifetime from Heisenberg's uncertainty principle in quantum mechanics.[86] The Gaussian contribution is from the broadening due to sample and instrument factors such as: amorphous materials result in broader peaks compared to crystalline materials, or due to the finite widths of slits/apertures and detector elements.[86] Conducting samples, e.g. Cu, tend to have an asymmetric line shape towards high binding energies and are therefore often fitted with a Doniach-Sunjic line shape.[87] The asymmetry originates from emitted electrons interacting with free electrons in the conduction band.

The short IMFP of electrons requires UHV conditions in the analysis chamber for XPS to prevent scattering of electrons so that they can travel from the sample surface to

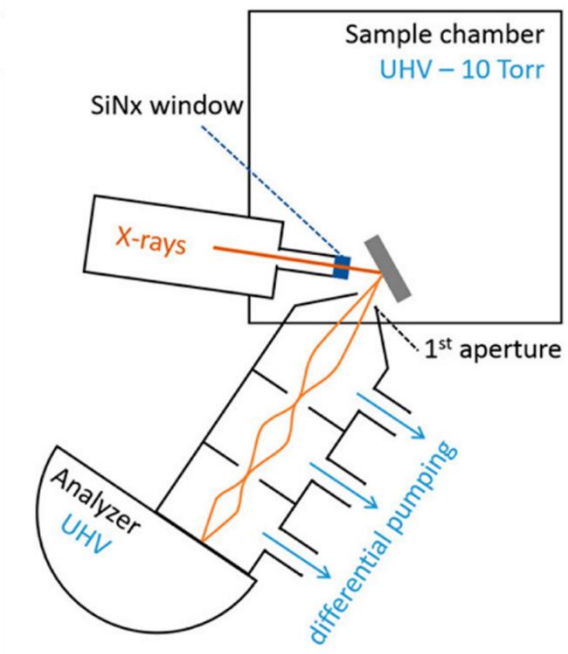


Figure 2.5: *Diagram of the differential pumping system used in NAP-XPS systems, first developed by Siegbahn* et al*. Taken directly from X. Lian* et al*.,* J. Phys. Chem. Lett.*, 2022, **13**, 8264–8277.*

the analyser. One of the primary aims of this thesis is to investigate surfaces of catalysts under as close to operating conditions as possible, therefore there is a need to extend XPS to higher pressures. Figure 2.5 shows one of the first developments for increasing the operating pressure of XPS performed by Siegbahn *et al.* in 1969, now referred to as NAP-XPS.[18,24,47] NAP-XPS systems utilise a differential pumping system so that a low gas pressure can be maintained at the sample surface and the pressure is rapidly decreased to a vacuum near the analyser, effectively increasing the IMFP of electrons through the local gas pressure at the sample.[46,47,88] The performance of NAP-XPS has been improved through the incorporation of electrostatic lenses.[49] NAP-XPS systems have been commercially available for over a decade and can routinely perform measurements at tens of mbar. However, this still falls far below the pressures of most industrial processes (>1 bar). Recently, by using tender/hard (>2 keV) X-ray sources to increase photoelectron kinetic energy, and thus IMFP, it has been possible to extend NAP-XPS to measure solid-liquid interfaces,[72,89] and surfaces in 1 bar gas environments.[51] However, photoionisation cross-sections decrease with increasing photon energy, making it challenging to measure light elements such as O and C with sufficient signal-to-noise ratios on reasonable timescales.[2,25,89–91] As discussed in Chapter 3, the use of E-cells can enable the combination of soft X-rays and pressures of 1 bar for XPS.

All XPS data presented in this thesis was analysed in CasaXPS software.

2.1.2 X-ray Absorption Spectroscopy

XAS involves the excitation of ground state electrons into excited states above E_F and thus probes information from the unoccupied electronic states (Figure 2.6 (a)). XAS measures how the degree of absorption of X-rays incident on a sample varies with energy, and hence requires a tunable X-ray source. As photon energy is varied, a sharp increase in absorption (usually called an absorption edge) occurs when electrons can

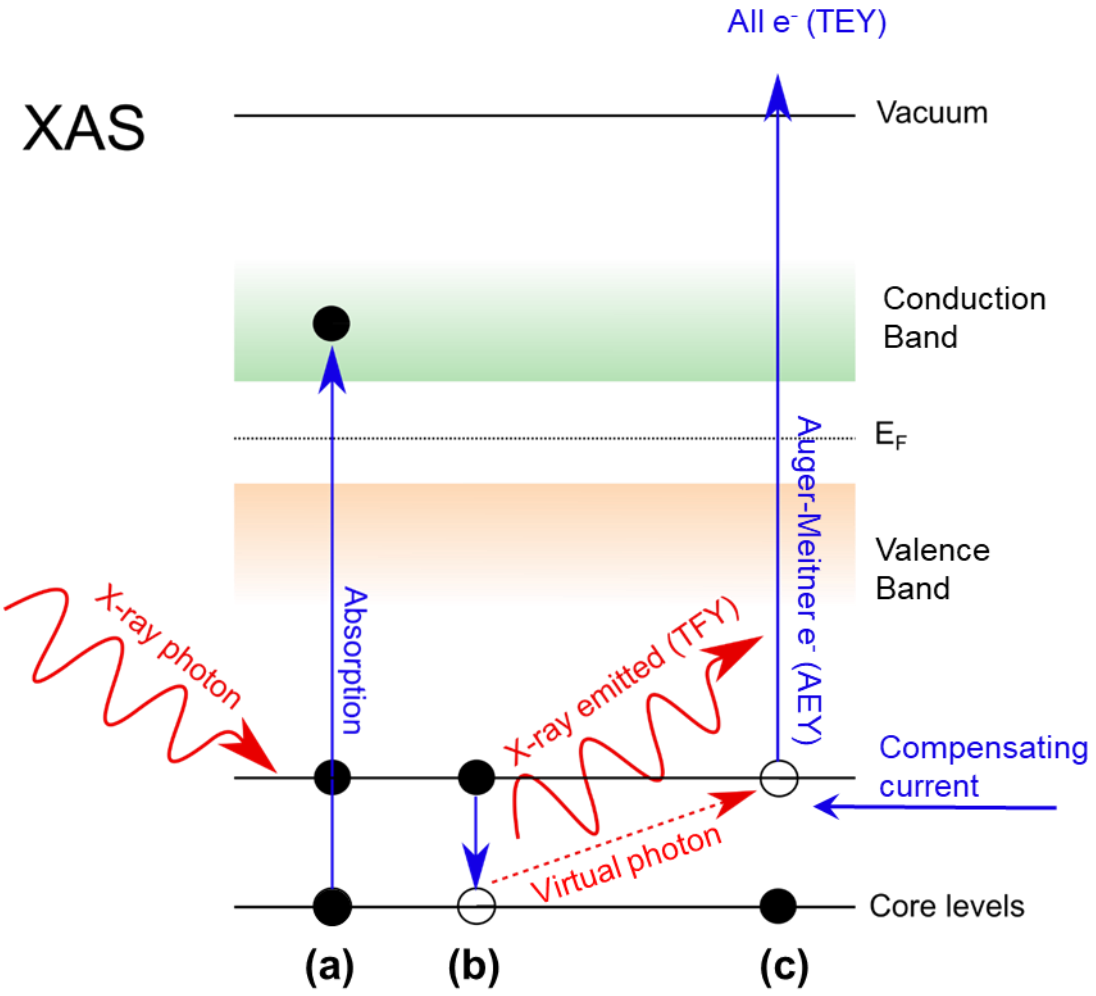


Figure 2.6: *Schematic of the physical processes occurring in XAS. (a) The energy of the incoming X-ray photon matches the transition energy, so the photon is absorbed and an electron is excited to an unoccupied state. (b) Following excitation an electron can de-excite to fill the core-hole and release a photon (TFY). (c) The de-excitation can cause the emission of secondary electrons (AEY), some of which will be scattered and lose energy (TEY). Electrons which are removed during absorption can be replaced, and hence measured by a compensating current.*

transition from their core-level to available states above E_F.[25,39] Due to the well-defined symmetry of the orbitals being excited, only certain transitions are allowed from a given orbital as defined by quantum mechanical selection rules, with the strongest spectral features occurring from the first dipole-allowed transitions ($\Delta\ell = \pm 1$).[92] The requirement for a tunable X-ray source is a major disadvantage compared to XPS, since tunable X-ray sources are expensive and mainly found at synchrotron sources, hence XPS is more widely available in lab-based systems.[18] However, more lab-based XAS systems are becoming available for the tender/hard X-ray range.[93]

The X-ray notation used to describe absorption edges states the element followed by the letter of the orbital from which the excited electron originates. For example, K-edges measure transitions from 1s and L-edges measure transitions from 2s or 2p. For L-edges a subscript is added to specify the orbital: L_1 is 2s, L_2 is $2p_{1/2}$, and L_3 is $2p_{3/2}$. The specific features for particular transitions are discussed in more detail in the relevant results chapters.

XAS is typically subdivided into near-edge X-ray absorption fine-structure (NEXAFS), and extended X-ray absorption fine-structure (EXAFS).[25] NEXAFS measurements concentrate on the energy range very close to the transition edge and this gives information on the chemical environment, oxidation state, and local charge distribution. These measurements are dominated by interactions from electronic structure.[25,39] EXAFS extends absorption measurements to energies higher than the transition edge to completely remove the electron from the atom, providing more information on coordinating atoms, crystal structures, and interatomic distances. These measurements are dominated by interactions from electron scattering.[25,94]

It is common for EXAFS to use hard X-rays to measure across wide photon ranges, whereas NEXAFS often uses soft X-rays. A typical energy range required for EXAFS to obtain information in the extended region is ~1000 eV and no absorption

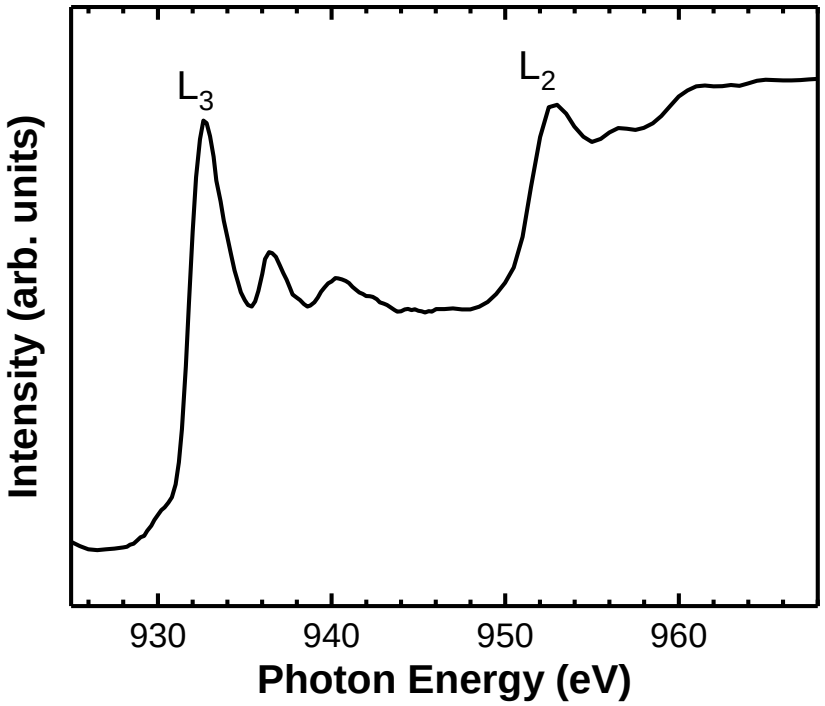


Figure 2.7: *Example NEXAFS spectrum from the Cu $L_{2,3}$-edge. Spectrum taken from Chapter 5 for Cu NPs exposed to 50 mbar of Ar at room temperature. The L_3 and L_2 edges are labelled and resonance features can be seen above the edge, in this case indicating the presence of metallic Cu.*

edges from other elements should be present in this range.[39,95] Edges probed with soft X-rays for common elements (O, C, N) and those used within this thesis (Cu and Zn) are all within the 250-1200 eV range. Therefore, extended regions of these elements all contain an edge from another element. Hence, performing EXAFS of regions in the soft X-ray regime (<2 keV) is not common and focus on the near-edge region. In comparison, edges in the hard X-ray regime tend to be separated by a greater energy range enabling EXAFS measurements. NEXAFS is used in this thesis due to its application to soft X-rays yielding high surface sensitivity and information on oxidation state and chemical environment which is beneficial for studying the state of catalysts. For example, in Figure 2.7, a Cu $L_{2,3}$-edge is shown for Cu NPs exposed to 50 mbar of Ar at room temperature. Figure 2.7 indicates the two edges seen in this range for Cu: L_3 and L_2 from transitions from $2p_{3/2}$ and $2p_{1/2}$ respectively. The high energy resonances near the edge are important for Cu as they indicate metallic Cu is present.[96] Furthermore, the Zn L_3-edge (also important in this thesis) begins at ~1010 eV, so EXAFS is not possible for the Cu $L_{2,3}$-edge in Cu/Zn samples.

To interpret XAS data, when spectra are recorded from samples of known oxidation state, then for many materials fingerprinting methods can be used as a basis for data interpretation. If this is not possible, interpretation can be more difficult and computational techniques may be needed to simulate spectra.[97] This can be a non-trivial task, but the detailed information about electronic structure that is available from XAS provides a strong motivation to pursue even challenging interpretation tasks.

XAS can be measured using a variety of modes utilising both photons and electrons to detect the extent of X-ray absorption (Figure 2.6). The probing depth of XAS can thus range from similar to XPS up to the attenuation length of X-rays (Figure 2.8). A simple way to measure X-ray absorption would be to compare the intensity of incident and transmitted X-ray beams at a range of energies (Figure 2.8). The difference between

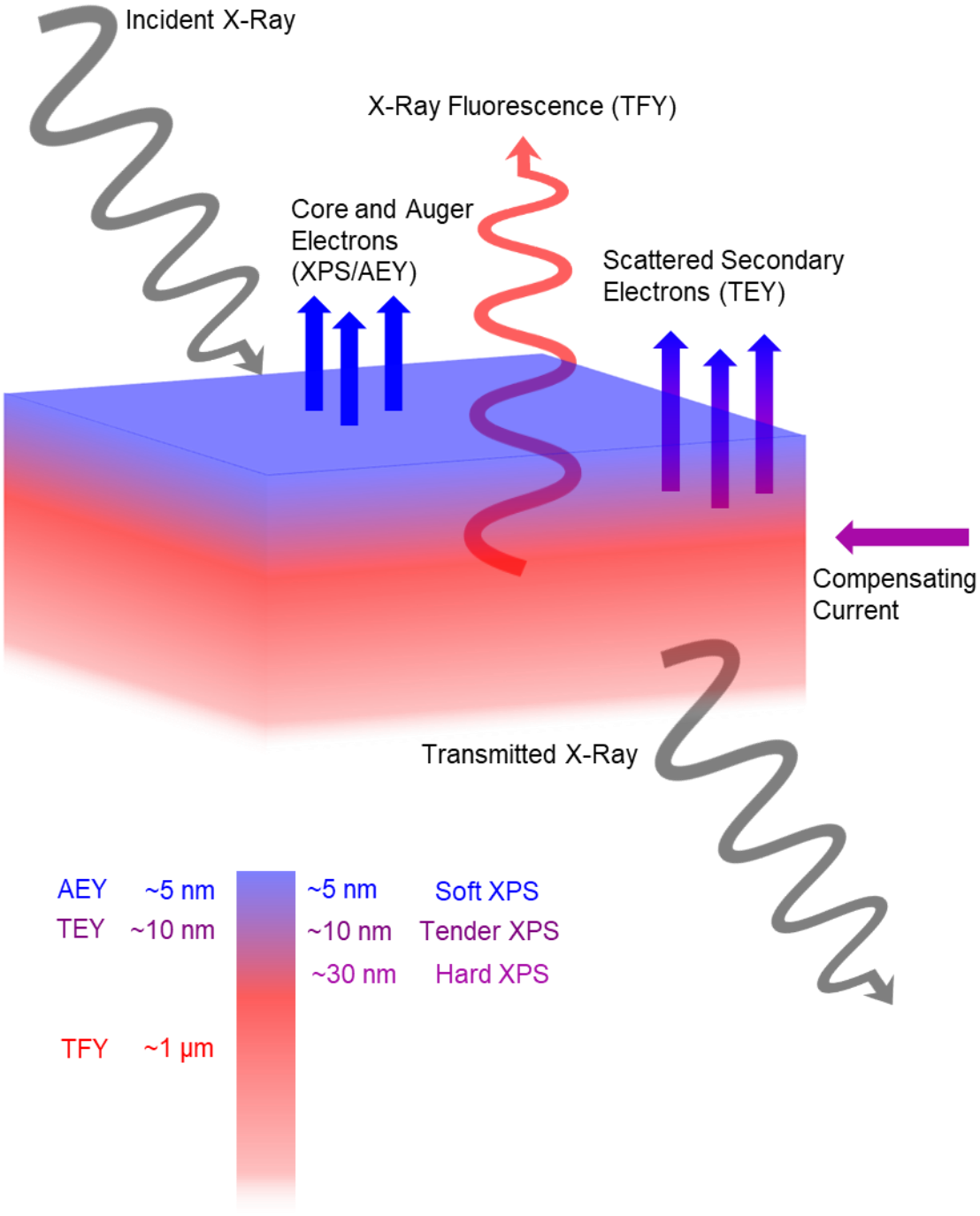


Figure 2.8: *Sketch showing how the probing depths of different detection methods compare. AEY and XPS contain more surface sensitive information (~5 nm), followed by TEY (~10 nm), and TFY is more bulk sensitive (~ 1 µm).*

these intensities would reflect the amount of absorption, where the absorption process is described by the Beer-Lambert law.[25] This, however, is often not a practical approach in the soft X-ray regime, as it requires careful preparation of a very thin sample to avoid X-rays being fully absorbed in the material.[64] Additionally, transmission XAS is a bulk sensitive technique, so is not suited to measuring surface or interfacial reactions which is important for this thesis.

Soft XAS data is more commonly collected using indirect methods to measure absorption which can be separated into fluorescence yield (FY) or electron yield (EY) methods. Following X-ray absorption, the excited electron can de-excite and release a photon with energy equal to the transition energy gap (Figure 2.6 (b)). FY involves collecting photons emitted from the sample where the degree of absorption is proportional to the number of emitted photons. If emitted photons are collected indiscriminately then this is referred to as total fluorescence yield (TFY). Emitted photons can be filtered based on their energy resulting in partial fluorescence yield (PFY); this is often utilised to avoid self-absorption effects in inverse PFY (IPFY). [98,99] The details of self-absorption are not discussed here, because FY measurements were not used in this thesis. FY measurements provide primarily bulk-sensitive measurements (several μm), as it is a photon-in photon-out method so the information depth is defined by the attenuation length of the X-rays. Hence, in this thesis EY is used to provide more surface sensitive information (Figure 2.8).[39]

Instead of releasing a photon, the de-excitation of the electron into the core-hole created can result in the excitation of another electron which is removed from the atom through the exchange of a virtual photon (Figure 2.6 (c)). Auger-Meitner electron yield (AEY) measures the production of Auger-Meitner electrons (as in XPS) where the analyser selectively measures electrons of a specific kinetic energy.[37] Additional secondary electrons are also produced by inelastic scattering of photoelectrons

produced within the sample. The number of escaping electrons correlates to the number of absorption events.[100,101] Total electron yield (TEY) measures all of the emitted electrons – regardless of energy – through either a collection electrode above the sample surface or via a compensating current to replace emitted electrons. TEY is less surface sensitive (~10 nm) compared to XPS or AEY (~5 nm). TEY signal arises from emitted electrons with a wide range of energies up to that of the X-ray energy by including all scattered electrons, rather than a well-defined narrow range of kinetic energies (Figure 2.8). Information from different depths can be measured using a combination of detection methods; for example, using TFY to collect information from a bulk solid or solution and simultaneously collecting TEY which provides more surface (or interface) sensitive information.[39,61,62]

Conversion electron yield (CEY) was initially developed to be more surface sensitive compared to TEY by measuring the drain current through a gas environment such that electrons emitted from the sample surface cause gas ionisation events; the current is measured between two electrodes either side of the gas with an applied electrical bias.[65,102] The idea was that ionisation events only occur for electrons with kinetic energy above a threshold value, however the generation of low energy secondary electrons by Auger-Meitner emission originating from near the surface resulted in CEY not being as surface sensitive as initially thought.[65,102] CEY as a detection method implicates the importance of distinguishing how the drain current is collected from the sample. In experiments shown in this thesis, the drain current for E-cells is collected between the sample and an electrically-isolated additional electrode where current flows between the two electrodes through ionisation events of the gas contained within the E-cell, herein referred to as EY-XAS (similar to CEY). In this thesis, EY-XAS is the detection of a drain current through ionisation events in the gas and TEY-XAS measures emitted electrons through an analyser cone (like in XPS).

Both X-ray spectroscopy techniques discussed in section 2.1 are non-destructive techniques. But, when utilising the high brilliance provided at synchrotrons, samples can be susceptible to beam damage via radiolysis of the gas or liquid environment.[57] A variety of facilities were used throughout this thesis to collect X-ray spectroscopy. The specific facility used for the relevant data is stated in the results chapters.

2.2 Microscopy

2.2.1 Scanning Electron Microscopy

Scanning electron microscopy (SEM) involves directing an electron beam (of a specific energy) and raster-scanning the sample surface. Incident electrons will interact with the sample and undergo elastic and inelastic scattering before exiting the sample. Further details on SEM can be found in the Appendix (Figure A2.1).

SEM is a highly useful technique as different signals from the sample provide a range of information. In this thesis, SEM was used to image graphene without needing to transfer it to another support, therefore avoiding defects or contamination introduced during the transfer process (which was done for optical microscopy in Figure A2.2).[103] To collect an image of graphene, the secondary electron (SE) signal was collected using a 2 kV incident electron beam to minimise the contribution of backscattered electrons (BSE). The presence of graphene on the catalyst appears darker compared to the catalyst below where thicker areas of graphene will appear even darker. SEM was also used to characterise Cu catalysts using a beam energy range of 2-20 kV and both SE and electron backscattered diffraction (EBSD) images were collected to confirm the morphology and polycrystalline nature of the surface.

2.2.2 Scanning Transmission Electron Microscopy and Electron Energy Loss Spectroscopy

Transmission electron microscopy (TEM) is similar to SEM in that a sample is irradiated with a high energy electron beam. However, rather than measuring the scattered electrons, the transmitted electrons are detected (Figure 2.9 (a)).[104,105] This places restrictions on the thickness of the sample (<100-200 nm) since it must be thin enough for electrons to pass through the sample. Transmitted electrons will be scattered by different amounts and are detected at a phosphorescent screen or camera (following several stages of focusing after the sample which is not detailed here).[104,105] In the bright field image, areas where electrons have been scattered or blocked by the sample will appear dark, whereas areas where electrons pass straight through the sample appear bright, and grey areas are where electrons are partially scattered/blocked usually at the edge of particles. The dark field image excludes the unscattered beam by placing detectors at an angle to the transmitted beam (Figure 2.9 (b)). In dark field images the bright areas are from electrons scattered by the sample and dark regions are where the electron beam passes straight through (which has been excluded). Figure 2.9 (b) shows the geometry of different detectors: the bright field (BF) detector is directly below the transmitted beam, the annular dark field (ADF) detector is concentric with the BF detector so that it excludes the unscattered beam, and the high-angle ADF (HAADF) detector provides a higher contrast for different atomic masses since heavier elements will increase the degree of electron scattering.[106]

TEM offers a high resolution (<1 nm) as well as information on a sample's crystal structure through diffraction of the electron beam. STEM builds an image pixel-by-pixel by scanning across the sample and collecting electrons transmitted at each point. The interaction of electrons with the sample can yield information on the chemical

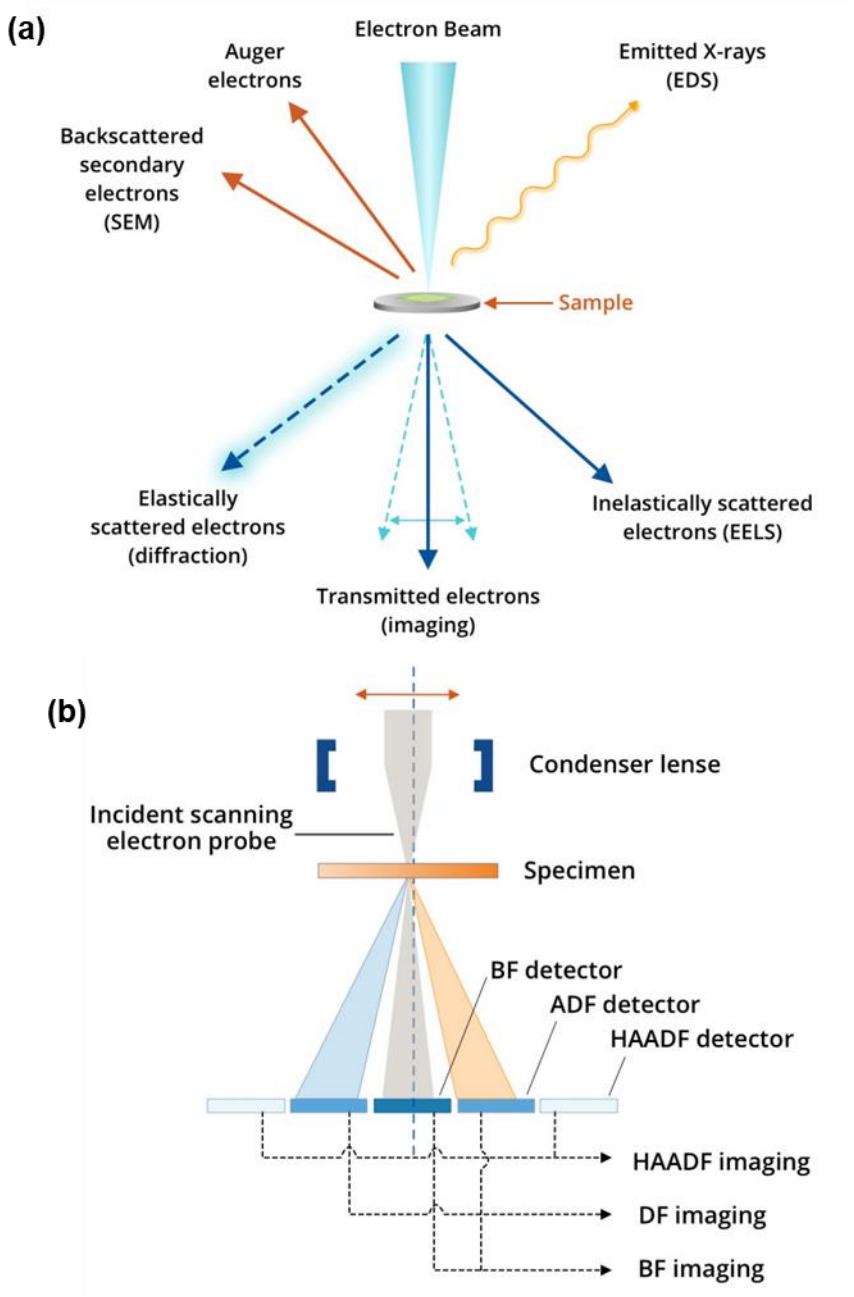


Figure 2.9: *(a) Diagram outlining the different information which can be collected in TEM. (b) Diagram showing the position of different detectors for TEM relevant for bright field or dark field images. (a) and (b) Taken directly from Introduction to TEM (MyScope), https://myscope.training/TEM_Introduction_to_TEM, (accessed 22 March 2024).*

composition through spectroscopy. STEM combined with spectroscopy measurements provides a high resolution map of elements across the sample.

EELS is used in this thesis alongside STEM to determine the distribution of Cu and Zn species across NPs and measure the oxidation state changes in Cu. In EELS, the energy of inelastically scattered electrons is measured to determine the energy lost by electrons which is used to excite other electrons in the sample. Similar to XAS, the energy lost by electrons directly corresponds to the characteristic absorption energy of that atom. EELS can hence be used to plot absorption spectra where the intensity of electrons for a specific energy loss is recorded. Excited electrons can de-excite, like in TFY, and the energy of the emitted X-rays can be detected also to determine compositional information in energy dispersive X-ray spectroscopy (EDS).

Sample preparation in this thesis involves depositing NPs onto Au coated holey carbon TEM grids. The Au coating was important to ensure the TEM grid composition did not interfere with the spectroscopy of the samples. All STEM and EELS were collected at ePSIC at Diamond Light Source, UK (MG35498) using a JEOL ARM200CF optimised for atomic resolution spectroscopy. STEM and EELS were collected with the help of staff at ePSIC: Christopher Allen, and David Hopkinson, with additional help from Longxiang Liu.

2.3 Raman Spectroscopy

Raman spectroscopy is a fast, non-destructive, and high-resolution technique commonly used to determine the quality and number of layers of graphene.[107–110] A typical Raman spectrum of monolayer graphene (MLG) is shown in Figure 2.10, the three main peaks are labelled: D (~1350 cm^{-1}), G (~1580 cm^{-1}), and 2D (~2700 cm^{-1}).[109–111] The G peak is observed for all sp^2 hybridised carbons where its position can be used to determine which sp^2 structure is present. The intensity of the D peak correlates directly

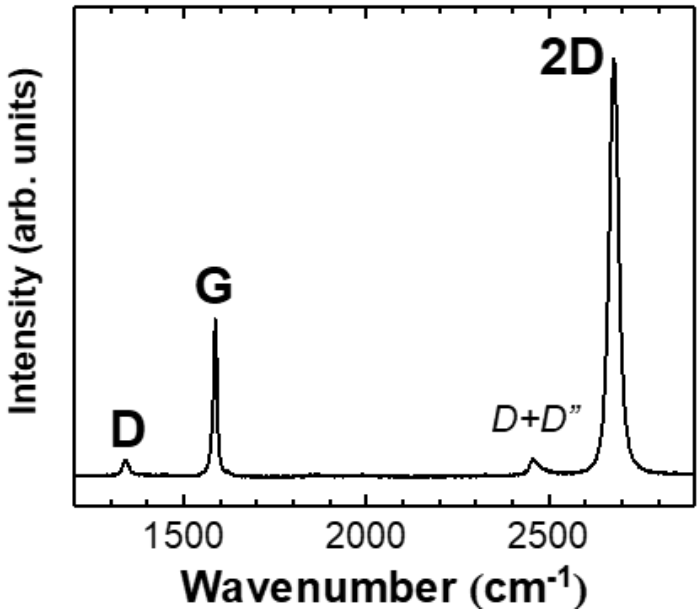


Figure 2.10: *Example Raman spectrum of MLG transferred to Si/SiO_2.*

with the presence of defects in graphene (see the Appendix for details). In highly defective samples other peaks (e.g. D+D" in Figure 2.10) can also appear.[109,110]

The common analysis of Raman spectra considers three main quantities: I_{2D}/I_G, full width at half maximum (FWHM) of 2D (Γ_{2D}), and I_D/I_G (where I is the peak height).[112] High-quality MLG should include a 2D peak fitted by a single Lorentzian function with a Γ_{2D} <40 cm^{-1} and I_{2D}/I_G ≥2.[112] The I_D/I_G ratio is proportional to the level of defects in graphene so should be as low as possible. At wrinkles or areas of few-layered graphene (FLG) the values of Γ_{2D} and I_{2D}/I_G are all expected to increase, where I_D/I_G can decrease at areas where graphene layers overlap but will increase at defective MLG sites.

All Raman data in this thesis was collected using a Renishaw InVia Microscope with a 532 nm laser using a 1800 /mm grating. Peaks were fitted with a single Lorentzian function to determine the FWHM and the peak heights. Raman spectra were performed on graphene transferred to Si/SiO_2 (300 nm) wafers (PI-KEM) from the growth substrate using the conventional polymethyl methacrylate (PMMA) support technique, unless stated otherwise (as in Chapter 5).[19] Note: Si/SiO_2 is used to abbreviate Si/SiO_2(300 nm). 300 nm thick SiO_2 enables graphene to be visible under an optical microscope (see Figure A2.2 in the Appendix). Raman spectra are plotted with intensity varying with wavenumber (cm^{-1}), where energy is inversely proportional to wavenumber.

2.4 Mass Spectrometry

MS allows the composition of a gas mixture to be determined where solid samples must be vapourised to be measured. The gas is initially ionised to form charged particles, usually by heating a metal coil to release electrons which will remove electrons in the sample, thus creating positive ions. The positive ions are then accelerated towards electromagnets which will deflect the charged particles. The degree of deflection is dependent on the mass/charge ratio of the ion, where lighter and more highly charged

ions are deflected more. Typically, most systems use a set of quadrupole magnets and vary the strength of the voltages applied to affect the trajectory of different mass/charge ratio ions. For a given strength of magnetic field, only a narrow range of mass/charge ratio ions can pass through successfully to be detected. By varying the magnetic field strength to detect a range of different masses the relative amount of molecules and elements can be determined.

In this thesis, MS was used in combination with a catalytic reactor where experiments were performed at the Research Complex at Harwell using a Hiden Analytical Catlab microreactor module. The Cu powder catalyst was dosed with gas and heated to simulate reaction conditions and the reaction products were directly flowed into a continuous sampling mass spectrometer. Quartz tubes were used throughout the system.

2.5 Deposition of Thin Films and Nanoparticles

2.5.1 Physical Vapour Deposition (and Plasma Cleaning)

The deposition of thin films used physical vapour deposition (PVD) techniques. Cu and Cr (Chapter 4), and Ni thin films (Chapter 5 and the Appendix) were deposited using radio frequency (RF) magnetron sputtering. The PVD deposition chamber was inside a glovebox (MBraun, PROvap with sputtering capabilities) and contained a rotating sample stage orientated upside-down; therefore, samples were stuck to microscope slides using Kapton tape to ensure they did not fall off during deposition. All targets had a 2" diameter and a minimum purity of 99.999%. The base pressure of the PVD reached ~$1x10^{-6}$ mbar before dosing Ar gas (20 sccm, $1x10^{-2}$ mbar) which was ionised to strike a plasma (~50 W). Once the plasma was formed it would begin sputtering the target with high energy ions. RF sputtering, as opposed to DC sputtering, prevents the build-up of positive charge on the target which can lead to film uniformity

issues. The magnet behind the target in magnetron sputtering helps to trap electrons, thus preventing them from sputtering the substrate yielding faster deposition rates. Every deposition included a pre-sputter of >20 minutes to remove any oxide layer formation on the target, during which the sample was covered with a shutter. The deposition power (50-100 W) and time were varied accordingly depending on the desired thickness, stability, and stress of the thin film.[113]

The thickness of films was determined using mechanical profilometry (Dektak) of step heights created using a mask on Si wafers during deposition. The thickness was calibrated for a given: target, deposition power, and time. During deposition the thickness was monitored using a quartz crystal microbalance and the power was maintained at a constant value to achieve reproducible film thicknesses.

Thermal evaporation of Au onto graphene was performed using a Leybold L560 evaporator at the thin film facility in the Physics Department, University of Oxford. The low energy of the impinging Au atoms is such that they do not etch graphene in comparison to the high energy particles produced in RF magnetron sputtering.[114]

Cu/MLG was plasma cleaned using a Diener electronic, Tetra-22 Bell in a glovebox. Plasma cleaning utilised an O_2 plasma, rather than the Ar plasma used for sputtering, because O_2 plasma is more effective at removing organic matter compared to an Ar plasma.[115,116]

2.5.2 Nanoparticle Deposition

NPs were deposited using a magnetron sputtering gas aggregation (MSGA) deposition system purchased from Nikalyte.[117] The system was custom made and contained a three-target sputter head for 1" diameter targets (Figure 2.11 (a)).[117] The energy of impinging NPs was low enough that it did not damage graphene, hence this deposition technique was used in Chapter 5 and 6 to deposit Cu (~10 nm) and Cu/Zn

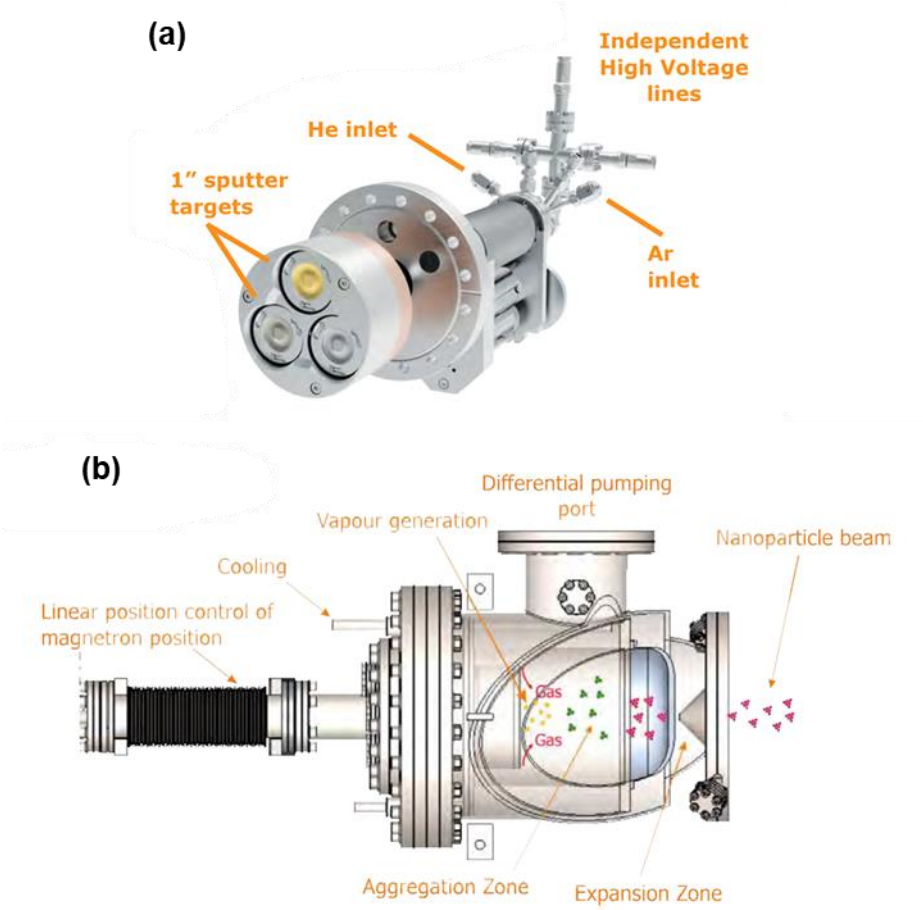


Figure 2.11: *(a) Image of the three-target sputter head for 1" diameter targets. (b) Schematic outlining how NPs are formed in the Nikalyte deposition system. (a) and (b) Taken from Nikalyte Ltd., https://www.nikalyte.com/nl-uhv/, (accessed 22 March 2024).*

(~5-20 nms, no size selection applied) NPs respectively on graphene; Cu/Zn NPs were deposited on TEM grids using the same technique.

Figure 2.11 (b) outlines the basic principles behind the Nikalyte NP deposition system. A plasma is generated in the aggregation zone (similar to RF magnetron sputtering) using Ar gas. The cooling applied to the aggregation zone results in gas phase condensation causing particles to thermalise and coalesce into NPs.[117] NPs diffuse due to the pressure gradient through the expansion zone and towards the sample. The range of NP size can be controlled by changing the length of the aggregation zone, the magetron power applied, and the gas flow and type (e.g. including helium gas). To enable size selection a quadrupole mass spectrometer (QMS) is incorporated which is able to filter the size of charged particles. It is worth noting that neutral particles are not size selected.

NP deposition was performed by Leanne Jones at Rex Richards, Oxford.

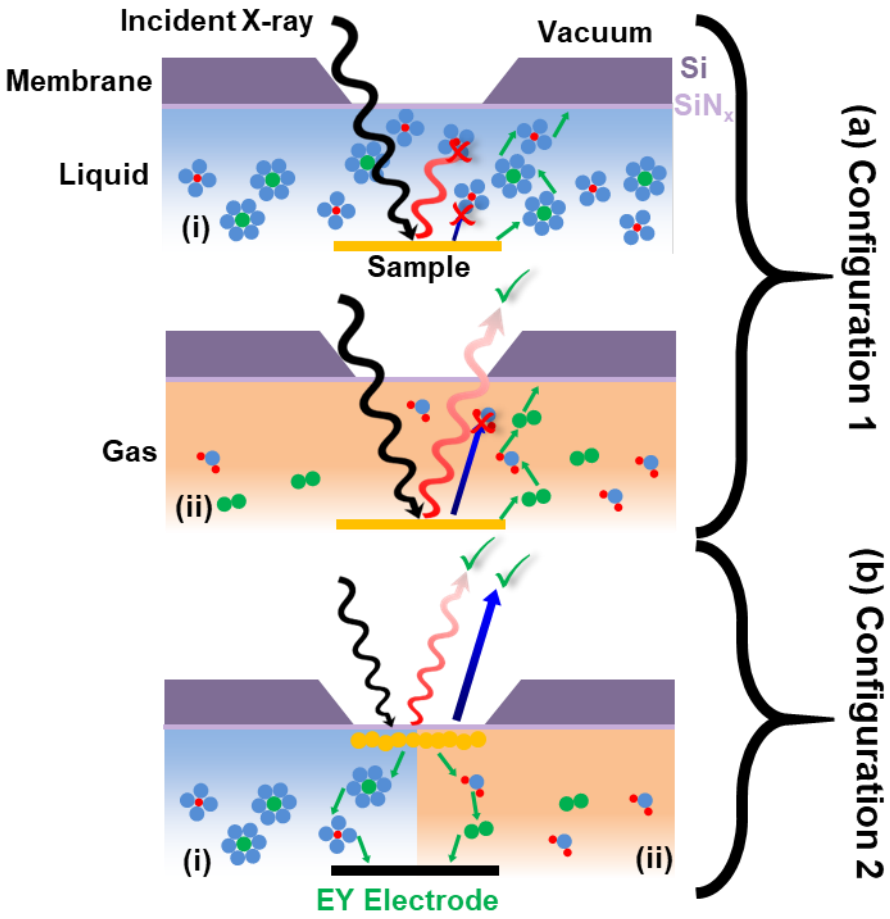
Chapter 3: Environmental Cells

In Chapter 1, the importance of applying realistic conditions in catalytic systems during their study (with X-ray spectroscopies) was discussed. The challenge of extending X-ray spectroscopies to high pressures due to the short IMFP of electrons was also discussed alongside some of the current techniques which have combated this issue. This chapter will discuss, in detail, the use of a promising alternative to perform *in situ/operando* spectroscopy: E-cells. Much of the discussion in this chapter was published in a review chapter: E. S. Jones *et al*., Enclosed Cells for Extending Soft X-ray Spectroscopies to Atmospheric Pressures and above, *ACS Symp. Ser.*, 2021, **1396**, 175–218. The specific designs of E-cells used in this thesis are also described.

The E-cell designs in Figure 3.4 and 3.6 were designed and manufactured with help from Joshua Gibson, and Peixi Cong. The E-cell in Figure 3.7 was developed by Robert Weatherup.

3.1: General Design

E-cells are a promising alternative to NAP approaches that have received increased attention recently.[6,12,63,64,66,67,95,118,37,52,57–62] E-cells involve creating a reaction environment (liquid or gas) that is sealed by a photoelectron and/or X-ray transparent window, so that there is an abrupt pressure change between the cell and the vacuum chamber to which the electron analyser and/or X-ray source are connected. This allows, predominantly, two measurement configurations as shown in Figure 3.1. Figure 3.1 (a) shows configuration 1 where the sample is placed in the cell; this is similar to the NAP approach where both X-rays and photoelectrons must pass through the reaction environment to be detected, placing few restrictions on the type of sample used.[18] However, in this configuration, unless the distance between the sample and window is kept small enough, operation remains restricted to relatively low gas pressures due to



Detection Mode		(a) Configuration 1	(b) Configuration 2
i) Liquid	FY-NEXAFS	×	✓
	EY-NEXAFS	✓	✓
	XPS	×	✓
ii) Gas	FY-NEXAFS	✓	✓
	EY-NEXAFS	✓	✓
	XPS	×	✓

Figure 3.1: *Two possible configurations for E-cell measurements. (Wavy arrows represent X-rays and straight arrows represent electrons.) (a) Configuration 1: sample behind the window meaning the interface is probed through (i) liquid or (ii) gas. (b) Configuration 2: sample on the window meaning the interface is probed through the solid sample with either a (i) liquid or (ii) gas phase environment present.*

scattering by the reaction environment. Alternatively, configuration 2 (Figure 3.1 (b)) avoids placing restraints on the environment within the cell. Configuration 2 involves either the deposition of a thin-film or NP sample onto the membrane sealing the cell thereby placing some restrictions on the material being studied.

The table in Figure 3.1 links these configurations to the detection methods which are possible. Detection methods are covered in detail in Chapter 2, but the three compared here are: NEXAFS via FY or EY, and XPS (or AEY- and TEY-NEXAFS collected by the analyser cone). The detection of X-rays in FY-NEXAFS means it is restricted by the attenuation length of X-rays which can pass relatively easily through a volume of gas (Figure 3.1 (a,ii)). X-rays would likely be attenuated by liquid in the cell (Figure 3.1 (a,i)) where the attenuation length of X-rays is ~600 nm in water (at ~600 eV), unless a high energy photon was used to penetrate the liquid allowing X-rays to illuminate the sample.[43] However, the energy of the fluorescence would still be lower than the incident photon energy and is, therefore, unlikely to escape the liquid. The short IMFP of electrons results in XPS not being possible in configuration 1 as electrons are significantly scattered by liquid and gas environments so cannot traverse through layers thicker than 100 nm. EY-NEXAFS has the flexibility to be possible across all configurations as long as there is a pathway for electrons to be collected/measured and replenished. In comparison, for configuration 2, FY-NEXAFS and XPS are both possible provided the window in the membrane is sufficiently transparent to X-rays and electrons. Since a greater number of detection methods are available in configuration 2, all experiments in this thesis use this configuration.

The membrane consists of two parts: the window and the frame (Figure 3.2 (a) and (b)). The window needs to be thin enough to be transparent to X-rays and/or electrons, while the frame should sufficiently support the window. The window must also be strong enough to maintain a large pressure difference between the reaction conditions inside

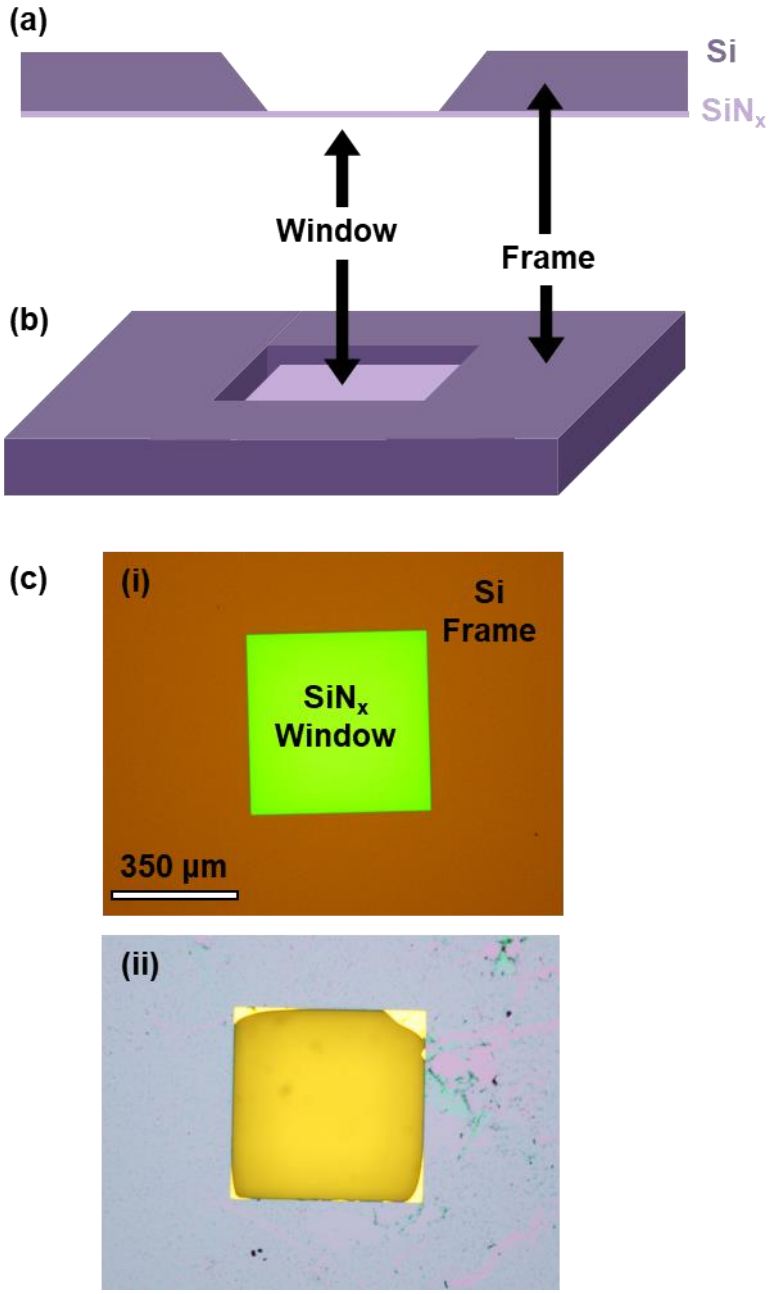


Figure 3.2: *(a) Diagram of the cross-section and (b) 3D view of a SiN_x membrane. The window must be very thin such that it is transparent to X-rays and/or electrons, whilst the frame supports the fragile window. (c) Optical microscope images of (i) a continuous SiN_x membrane and (ii) a broken SiN_x membrane where the window has burst (light blue area is residual graphene from a transfer attempt as discussed in Chapter 5).*

the cell and the vacuum conditions of the measurement chamber, as well as be impermeable to the molecules in the reaction environment.[19,119] This provides limitations on the window materials possible as well as the size, shape, and design. In Figure 3.2 (c,i), a SiN_x membrane is shown, but there are a range of materials that windows can be made from as discussed in section 3.2. (Note on terminology: for convenience a membrane with a SiN_x window and a Si frame is referred to as a SiN_x membrane.)

Whilst existing NAP approaches have proved extremely valuable in recent years with numerous synchrotron and lab-based systems now available, in a number of areas the use of E-cells may offer particular advantages.[78–80] E-cells enable a much higher attainable pressure and minimal contamination of the measurement chamber and analyser with a greater versatility in geometry of the reaction environment.[18] E-cells also allow for shorter distances for X-rays to traverse through matter for NEXAFS and shorter escape distances of photoelectrons for XPS resulting in higher signal intensity. E-cells can potentially be accommodated in a conventional UHV system, or alternatively used in combination with a NAP system to help ameliorate the risk to measurement systems associated with sudden cell rupture (Figure 3.2 (c,ii)) and reduce the requirements on the E-cell's leak-tightness.[120]

3.2: Window Materials

Having discussed the general design of E-cells and membranes, the window materials used in membranes available for sealing E-cells, their suitability for different types of measurements, stability under reaction conditions, and challenges in their fabrication/application must now be considered. Charging effects are also an important factor as irradiating a sample with X-rays will cause electrons to leave the sample resulting in an accumulation of positive charge on the sample which needs to be compensated for.[1] Such charging alters the apparent binding energies of photoelectrons in XPS and distorts peak shapes making it hard to reliably discern real chemical shifts,

although these artefacts can be avoided through the use of suitably conductive membranes.

3.2.1 Continuous Membranes

A popular choice of material for windows is SiN_x, which is used widely in the field of electron microscopy.[61,62,127,64,101,121–126] The formula for silicon nitride is Si_3N_4; however, the windows are often manufactured with a different ratio of Si:N to reduce stress across the window which facilitates greater flexibility in manufacturing. Therefore, in this thesis SiN_x notation is used.[128] Si_3N_4 has a well-defined crystal structure, the change in stoichiometry to SiN_x will change the crystal structure to being more amorphous. SiN_x membranes are readily available with different window thicknesses and sizes, and exhibit relatively high thermal and chemical stability.[128] Continuous membranes contain a complete window (Figure 3.2 (c,i)) and are differentiated from perforated membranes (see section 3.2.2). Continuous SiN_x membranes with windows of tens to hundreds of nanometers in thickness are suitable for use in NEXAFS measurements and can often sustain >1 bar pressure differences. However for soft XPS, such windows are typically too thick to be permeable to low energy photoelectrons. Endo *et al.* demonstrated the use of ultra-thin SiN_x (5 nm) or Si (15 nm) in a lab-based XPS system and mitigated the fragility of these thin windows with very small window sizes (30 x 30 µm).[66,72] This small window area, in comparison to typical lab-based X-ray spots sizes of 100 µm, potentially limits the strength of the XPS signal that can be collected. These limitations can be overcome by utilising a highly focused X-ray beam, or extended measurement time, however this increases the risk of beam induced radiolysis (beam damage). Soft X-rays lead to more beam induced effects compared to hard X-rays due to the greater photoionisation cross-section for lower energy X-rays. Using hard X-rays will also increase the IMFP of photoelectrons such that they can traverse the window.

Materials are often deposited on the window using PVD techniques. These are typically conductive layers that help avoid charging and can then themselves be used as a working electrode in electrochemical experiments.[61,62,91] The largest drawback of using SiN_x is that the signal from silicon and nitrogen will limit the regions which can be studied, for example, requiring non-nitrogen based reactions as both the N absorption edge and XPS core level signals will overlap and likely be dominated by SiN_x. Other elements (B, Al, P, S, and Cl) will be encompassed in the Si signal in XPS too placing further limitations on reactions to be studied. This is an important consideration given that one of the major advantages of using soft X-rays is their large photoionisation cross-section for elements such as C, N, and O and particularly as the use of soft X-rays is a focus of this thesis. More generally, an inherent issue with NEXAFS is for C, O, and N there is only one possible edge which can be measured (at 280, 530, and 400 eV respectively) and an overlapping signal from the window material prevents recording a signal from these elements.

Alternative window materials to SiN_x include Si and silicon carbide (SiC) where a Si frame is used in both cases.[72,124] Both have the advantage of avoiding the N edge in NEXAFS measurements. However, similarly a weakness of using SiC is the presence of C which is another important element in absorption and photoemission measurements. SiC has high photon transmission in the 60-120 eV and 410-1240 eV range and also has a higher thermal conductivity than SiN_x, which may make it preferable for measurements in these energy ranges and when uniform heating is required.[129] Neither SiC nor SiN_x are electrically conductive at room temperature. Typically, SiC membranes are double the cost of SiN_x membranes, hence SiN_x is often preferred.

In this thesis, 100 nm thick continuous SiN_x windows were used for NEXAFS measurements. SiN_x was chosen due to its low cost and stability alongside the fact that nitrogen was not an element of interest. 100 nm thick SiN_x was thin enough to be suitably

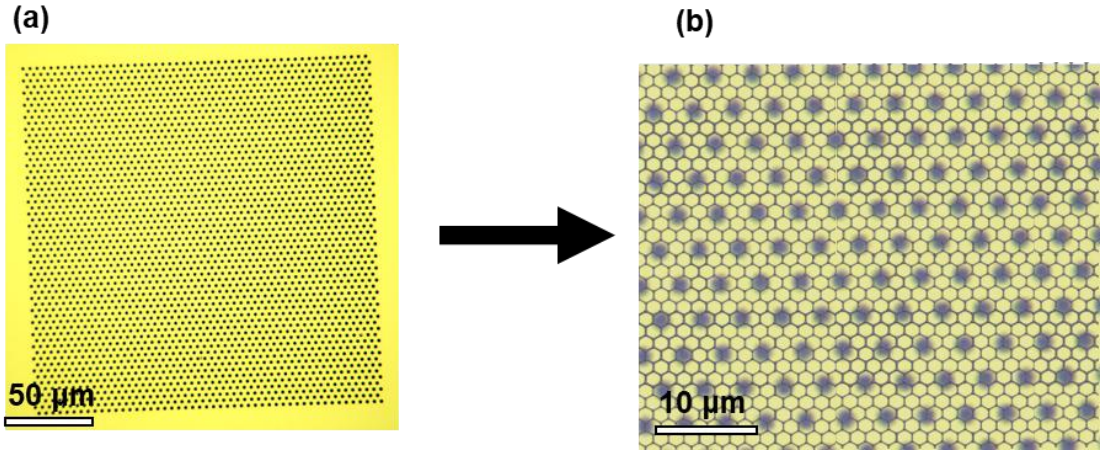


Figure 3.3: *Top view of (a) the window of a perforated SiN_x membrane and (b) how graphene suspends across the holes of the membrane ensuring it seals an environment inside the E-cell. (The size of holes relative to the structure of graphene is not to scale.)*

transparent for X-rays and was relatively strong making the membranes easier to handle than some of the very thin windows used in literature (5-15 nm).[66,72] The Appendix contains a detailed discussion on balancing transparency and stability when choosing a membrane, as well as a section outlining more examples of the application of continuous SiN_x membranes. The membranes were purchased from Silson.[128] For experiments requiring electron transparency, perforated SiN_x membranes were considered.

3.2.2: Perforated Membranes (with Suspended 2D Materials)

The continuous membranes discussed so far are mainly used for NEXAFS measurements without additional requirements beyond X-ray transparency. For XPS a number of studies have used perforated rather than continuous SiN_x membranes (see Figure 3.3).[21,57,60] Perforated membranes differ from continuous membranes as they incorporate an array of holes in the window that are hundreds of nanometers to several micrometers in diameter, rendering the window of the membrane permeable to photoelectrons. A larger hole increases the area of interest and experimental signal, however the likelihood of a leak also increases. To ensure an adequate seal against the gas or liquid inside the E-cell, an additional material is required to cover the holes, but must still maintain photoelectron transparency. Stable 2D materials, such as graphene and hexagonal boron nitride (h-BN), are strong enough to maintain large pressure differences, impermeable to gas molecules, and are also thin enough to be electron transparent; therefore, they are an ideal choice for use in conjunction with a perforated SiN_x membrane.[74,76,130] Graphene is often preferred over h-BN due to its electronic conductivity which helps reduce charging effects, but h-BN can be preferable when its high thermal and chemical stability are required (particularly in oxidising environments).[19,131,132] It has been theorised that non-wrinkled, defect-free graphene could withstand up to 100 bar of pressure when suspended over a 200 nm hole, therefore

graphene membranes are an exciting prospect in extending *operando* studies to higher pressures.[76]

The greatest difficulty with producing these types of membranes is the suspension of uniform and undamaged 2D materials. An early method used percolated graphene oxide (GO) flakes suspended over a single small hole in SiN_x, presumably as it was easier to ensure a continuous layer.[58] However, the increased thickness of GO compared to graphene attenuates the XPS signal to a greater degree relative to the interface, and may mean higher energy X-ray excitation or longer counting times are required to ensure sufficient photoelectron transmission. The most common method of manufacturing graphene membranes is to transfer continuous graphene from its growth substrate to the window of a perforated SiN_x membrane. However, the transfer process often introduces tears, defects, and impurities into the graphene which make it weaker and more likely to burst under pressure.[133,134] The transfer process means successful transfer of graphene is very difficult and requires a high level of skill. One of the topics covered in this thesis is trying to improve the reliability of the manufacture of graphene membranes for integration into E-cells. These methods are described in detail in Chapter 5.

In this thesis, 200 nm thick perforated SiN_x windows with graphene suspended (monolayer or bilayer) were used for XPS (and some NEXAFS) measurements. Graphene's electron transparency and high strength made it suitable for high pressure measurements requiring the detection of electrons.

In all experiments, soft X-rays were used to maintain surface sensitivity, hence placing limitations of the thickness of windows which could be used whilst maintaining reasonable measurement timescales. The Appendix contains a detailed analysis showing the importance of choosing an appropriate thickness window for a given X-ray energy range. Overall, soft X-rays require thinner membranes for an optimal signal

strength in XPS, but often at the expense of stability. Graphene, however, is electron-transparent whilst being very strong, but the integration of graphene membranes is far from trivial. Hence, the manufacture and application of graphene membranes has been a focus in this thesis.

Overall, there are a wide variety of options for window materials. In general, the application of continuous membranes to E-cells is simpler than perforated membranes due to the additional step required to suspend a 2D material over the window of a perforated membrane. A drawback of continuous membranes can be that the window material may interfere with the signal from the sample. Additionally, the commonly-used window thicknesses are too thick for detecting photoelectrons in XPS and are therefore limited to NEXAFS studies; unless very thin windows (e.g. 5 nm) are used.[66] Graphene membranes would offer the flexibility of both XPS and NEXAFS measurements. Once the window material has been selected, then an appropriate E-cell design is also required. A few examples of the application of E-cells are discussed in the Appendix. The ultimate aim would be to make *in situ*/*operando* experiments more accessible and, therefore, confidently use E-cells in lab-based XPS systems with minimal risk to damaging apparatus.[12,24] This requires a reproducible and relatively easy and cost-effective method of suspending graphene over perforated SiN_x membranes (see results in Chapter 5).

3.3: Environmental Cells for this Thesis

This section details the three E-cell designs used in this thesis. In designing each cell the following was considered: substance to be sealed (liquid or gas), whether heating was required, and the relevant detection methods to be used.

3.3.1: NEXAFS Cell (Version 1)

The E-cell shown in Figure 3.4 was used to collect NEXAFS at pressures of up to 1 bar whilst heating up to 300°C.[71] The main body was made from 304 stainless steel CF16 vacuum flanges and the cell was designed to be directly integrated onto the endstation at B07-C (Diamond Light Source, UK).[79,80] Steel was chosen as it is relatively durable and steel vacuum flanges were readily available. This was the first cell design so it was important that the parts were accessible to perform proof-of-concept measurements and, should they be successful, then alternative materials could be considered. Gases were introduced into the cell through 316 stainless steel tubing connected via 1/16" Swagelok fittings where inlet gas flow was controlled via mass-flow controllers (MFCs) within the beamline setup. Pressure in the cell could also be controlled using a variable pumping valve on the outlet. The cell incorporated two type K thermocouples. The first thermocouple, as shown in Figure 3.4, was fed through the body of the cell to read temperature within the cell cavity and recorded a drain current from the sample. The second thermocouple was wrapped around the outer body of the cell and enabled resistive heating of the cell (not shown in Figure 3.4). The poor thermal contact and limited resistive heating of the thermocouple resulted in 300°C being the maximum achievable temperature prior to burning out the thermocouple.

Viton O-rings can be used to seal the membrane to the rest of the cell, but these were not suitable in this case because Viton O-rings cannot typically operate above 100°C. In UHV systems Cu gaskets are used to seal vacuum flanges where a knife edge from each flange cuts into the Cu gasket when pressure is applied to create the gas-tight seal. Unlike Viton, Cu is more suitable for high temperature applications. Therefore, a Cu gasket was incorporated into the cell design between the top and bottom vacuum flanges which had knife edges to create a seal. A hole was drilled into the Cu gasket to allow gases in the cell cavity access to the sample. However, the force required to seal

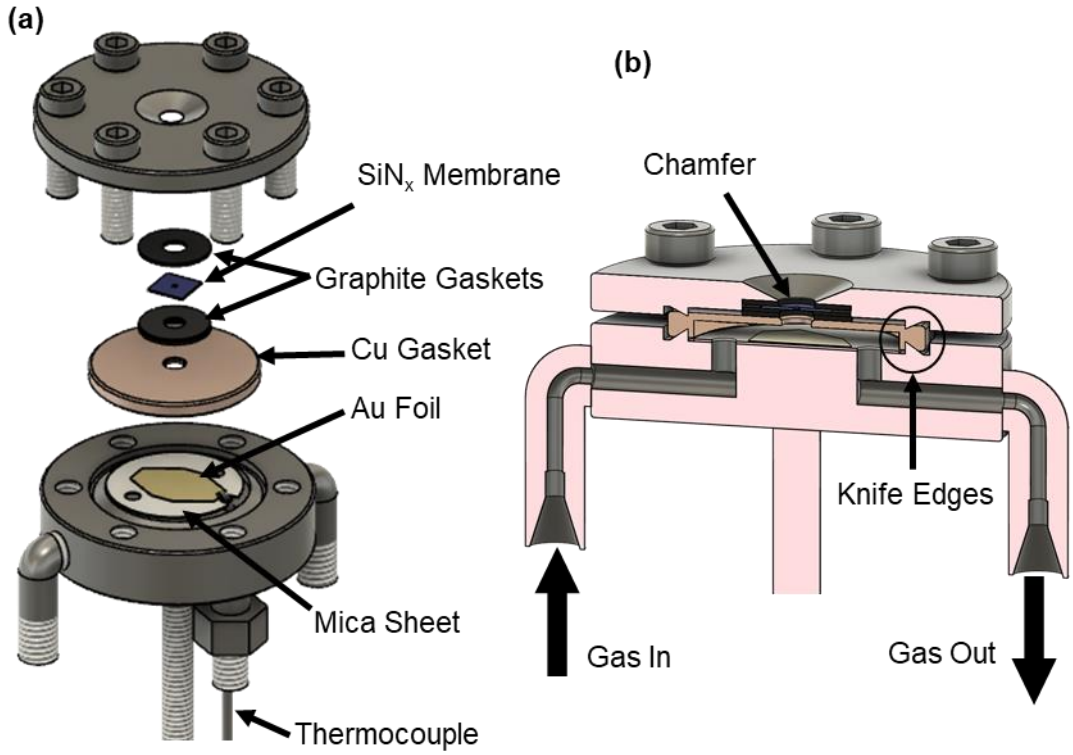


Figure 3.4: *Schematic diagram of the cell used for high pressure NEXAFS. (a) Exploded view showing the arrangement of stacked cell components. (b) Cross-section of the assembled cell.*

the two flanges together with the Cu gasket would shatter a SiN_x membrane if the same force was used to seal the SiN_x membrane. An initial solution was to try to deposit a thin metal layer (e.g. Cu or Ni) and heat the membrane to bond it to the Cu gasket via diffusion bonding.[135] This method did not yield much success as the temperature required to bond the membrane was too great and broke the membrane upon cooling; this was most likely due to the different thermal expansion coefficients between SiN_x and the metal. The solution was to incorporate graphite gaskets (Figure 3.4 (a)) either side of the membrane which protected it. Graphite (Klinger) is very soft meaning the force was reduced on the membrane and a leak-tight seal was made through indentations in the graphite. Sealing of the cell was still challenging as the bolts needed to be tightened enough to seal the cell body whilst being loose enough to avoid breaking the membrane. To prevent the top flange from shadowing the sample from incident X-rays, a chamfer was added to the lid (Figure 3.4 (b)).

For EY-NEXAFS measurements a current flow was measured between two electrically isolated points across a gas. It is worth noting that at this stage graphene membrane manufacture was not reliable enough to perform TEY-NEXAFS or XPS, therefore EY-NEXAFS was the most surface sensitive (~10 nm) detection method available.[37,136] Upon irradiating the sample, excited electrons leave the surface, which becomes positively charged and acts as one electrode. The sample deposited on the window is in electrical contact with the graphite gaskets and, therefore, the cell body, meaning another electrode is required which is electrically isolated from the cell body. In this case a piece of Au foil on top of an insulating sheet of mica was placed at the bottom of the cavity of the cell.[92] The thermocouple, which was fed through the cell to measure temperature, was placed such that it was touching the Au foil, therefore the thermocouple also measured the drain current. A disadvantage of this setup was that temperature and the drain current could not be measured simultaneously. To mitigate for this the

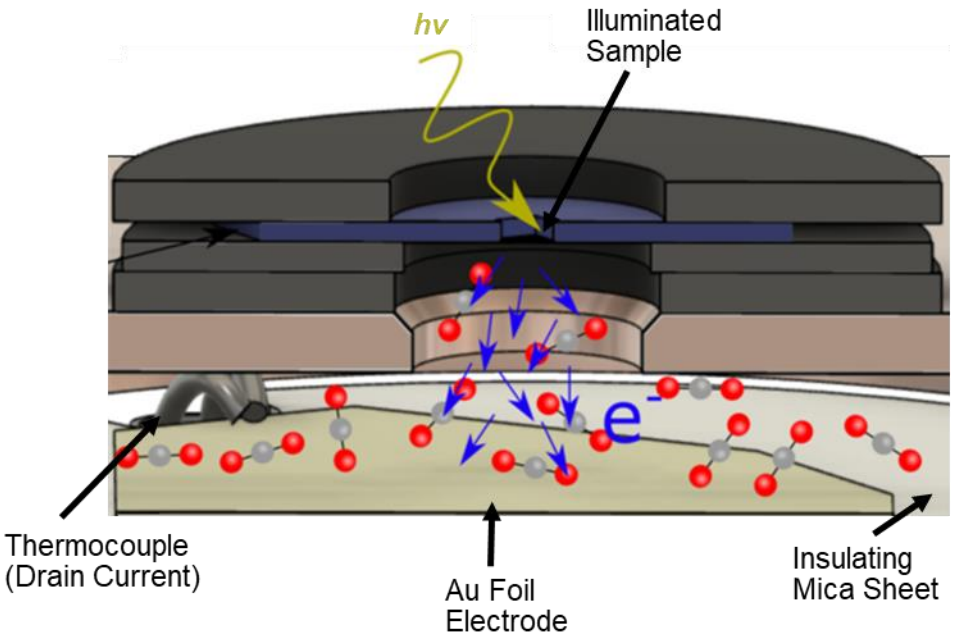


Figure 3.5: *A magnified schematic indicating the direction of incoming X-rays (hv) and generated electrons with the cell filled with CO_2 gas (relevant for Chapter 4). The EY-NEXAFS signal is obtained from the current between the Cu thin film sample and the Au collection electrode.*

temperature was allowed to stabilise upon changing conditions in the cell, prior to applying a fixed power during measurements. Figure 3.5 shows how current flows between the sample and Au electrode by ionising the gas in the cell enabling electron transfer. This means the drain current will be influenced by the gas pressure and composition in the cell which can be corrected for by applying a bias between the electrodes.[137]

The cell design in Figure 3.4 was used in experiments presented in Chapter 4 to perform high pressure gas-phase EY-NEXAFS measurements in a NAP system at a synchrotron.

3.3.2: NEXAFS/XPS Cell (Version 2)

The cell design shown in section 3.3.1 was successful in performing EY-NEXAFS measurements at high pressure. Having utilised this cell as a proof-of-concept study, a few aspects of the cell design needed improvement, in particular: separate temperature and drain current measurements, more control in sealing the membrane (this is very important for a graphene membrane which is more fragile), and a more efficient method of heating the cell.

Figure 3.6 (a) shows the improved cell design which was used to collect high pressure NEXAFS and XPS (up to 1 bar) at temperatures of 200°C at B07-C (Diamond Light Source, UK) and CIRCE (ALBA, Spain) beamlines.[78–80] The cell has been tested further following these experiments and reached pressures of 4 bar whilst measuring XPS, and can achieve temperatures of ~400°C.

The main cell body is made from custom-designed stainless steel pieces. One of the first changes to the cell was to alter its design to enable the membrane and cell to be sealed separately. Figure 3.6 (b) indicates the different set of bolts which sealed each part. The small bolts sealed the sealing cross to the lid (Figure 3.6 (a)) which applied

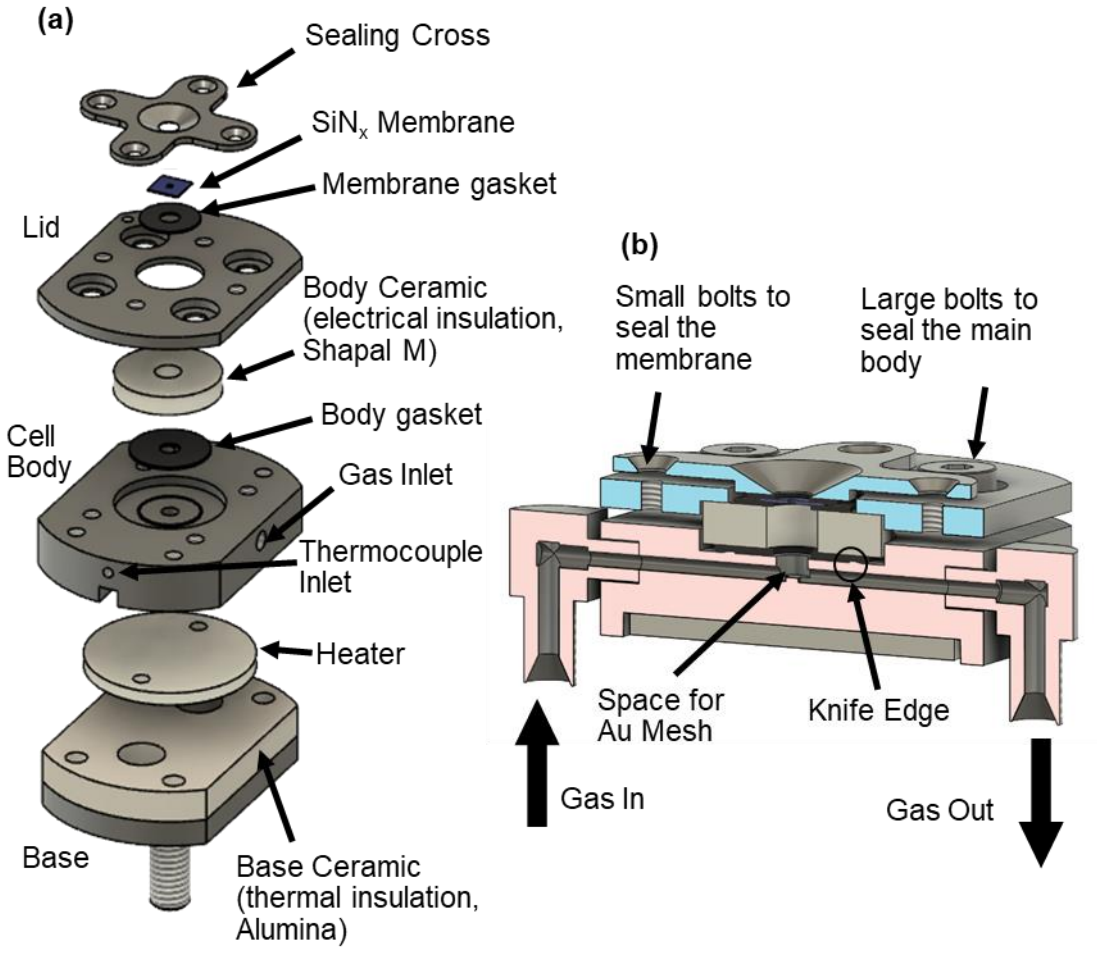


Figure 3.6: *Schematic diagram of the improved cell design used for high pressure NEXAFS and XPS. (a) Exploded view showing the arrangement of stacked cell components. (b) Cross-section of the assembled cell. The different shading colours indicate electrically isolated components.*

pressure to the SiN_x membrane only, providing more control when sealing it. The Cu gasket was removed and replaced with more graphite. From the previous design it was realised that graphite alone was sufficient to seal the cell and membrane. Therefore, the design was simplified to only contain graphite. A small knife edge was machined into the cell body to aid the graphite in sealing the cell (Figure 3.6 (b)). The large bolts compressed the body gasket between the body ceramic and the knife edge in the cell body, forming a gas tight seal. An added benefit of this design is the easy changeover of samples. The large bolts did not need to be removed when changing samples. Instead, only the sealing cross was removed. The greater control in sealing the membrane meant more fragile graphene membranes could be used. At the time of designing this cell a reliable method of transferring graphene had been developed, therefore XPS and TEY-NEXAFS measurements were now possible. Experience in sealing the membranes showed that the sealing cross should not be over-tightened, since cell expansion upon heating could break the membrane during measurements.

The cell was heated using a graphite heater (purchased from Thermic Edge Ltd., UK, part number; PCPBNC10) placed at the bottom of the cell. To ensure efficient heating of the sample a thermally insulating base ceramic piece (alumina) was attached below the heater to ensure good physical contact between the heater and the cell body, maximising the heat transfer. A small hole was drilled into the cell body such that a type K thermocouple probe could be inserted to record temperature near the sample.

The final main improvement was the incorporation of a separate drain current connection for EY-NEXAFS measurements. The cell was designed to electrically isolate the sealing cross, membrane and lid from the rest of the cell body (as indicated by the different shading colours used in Figure 3.6 (b)). To do this an electrically insulating, but thermally conductive, ceramic piece (Shapal Hi M Soft, Precision Ceramics, UK) was placed beneath the graphite gasket under the membrane. Additionally, mica washers

were used for the large bolts which sealed the lid to prevent electrical contact to the cell body. The sample acts as one electrode (and is in electrical contact with the sealing cross and the lid) whilst the cell body acts as a second electrode. To aid conduction of electrons through the gas to the cell, by shortening the path length for electrons, a small piece of Au mesh was placed in the cavity in the cell. Hence, a wire was connected to the top of the lid and measured a drain current for EY-NEXAFS.

The cell design in Figure 3.6 was used in experiments presented in Chapter 5 and 6 to perform high pressure gas-phase EY-NEXAFS, TEY-NEXAFS, and XPS measurements in a NAP system at a synchrotron.

3.3.3 Liquid Flow Cell for Lab-Based XPS

The final cell design used in this thesis did not require the ability to heat and was designed to be used in a conventional lab-based XPS system, see Figure 3.7 (i). The main body of the cell is made from polyether ether ketone (PEEK) with Swagelok-compatible PEEK tubing inserted for flow of liquid in and out of the cell. The membrane is sealed to the PEEK cell using Viton O-rings which are more leak-tight than graphite. Viton O-rings were suitable in this case as heating was not required. A leak-tight seal was essential for application of the cell within a lab-based system, where equipment could be damaged if liquid leaked out of the cell. This is in contrast to the NAP systems used for the other cells, which can maintain operation even with small gas leaks. No additional components were incorporated for EY-NEXAFS as this cell was specifically designed for XPS measurements only.

The E-cell was used at HarwellXPS, at the Research Complex, and was inserted into the main chamber via a linear manipulator, allowing for quick introduction using a separated loading chamber. Feedthroughs were mounted on the manipulator to allow flow of the etching solution, which were connected to the cell with PEEK tubes (inner diameter of 0.6 mm).

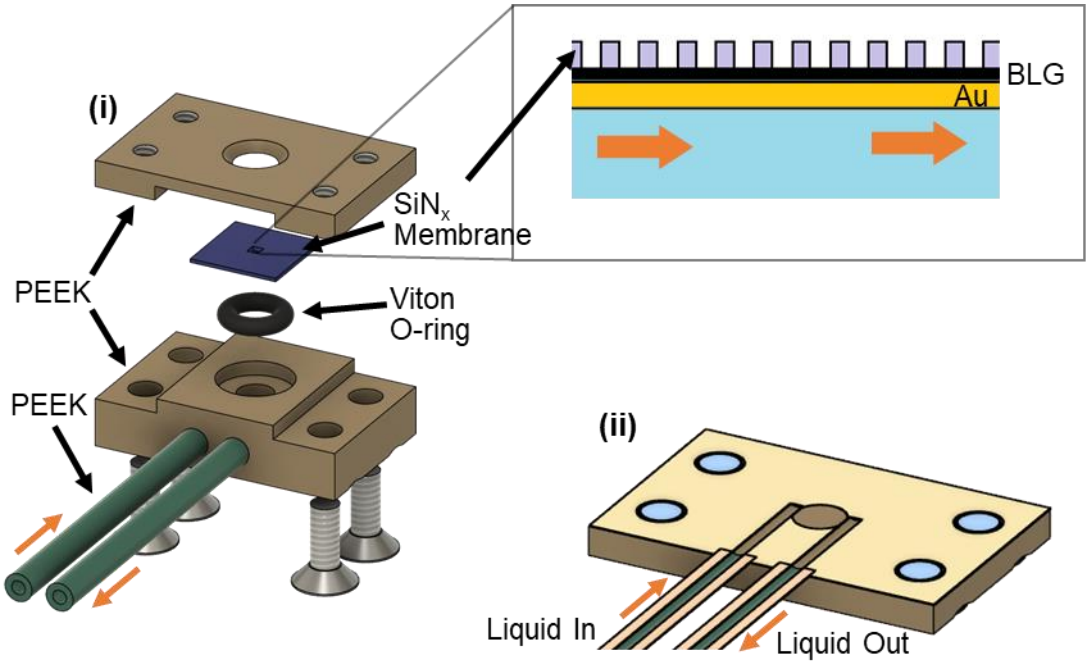


Figure 3.7: *Schematic of liquid flow cell made from PEEK used for conventional lab-based XPS. (i) Expanded view of the cell showing how the cell was sealed by a SiN_x membrane atop a Viton O-ring, the inset shows BLG and Au suspended over the holes of the perforated window relevant to experiments presented in Chapter 5, (ii) horizontal cross-section showing how liquid entered the cell through the PEEK tubes.*

Figure 3.7 shows Au coated bilayer graphene (BLG) suspended over the holes of a perforated SiN_x membrane sealing a KI/I_2 solution. This was used in the experiment presented in Chapter 5 for measurements in a conventional lab-based XPS system.

3.4 Outlook

This chapter has discussed the different designs of E-cells used for X-ray spectroscopy and the considerations for choosing an appropriate window to seal the cell depending on the desired chemical information, detection method, and environment. The final section focused on the development of different cell designs which were used in this thesis. In particular, the improvements made between designs of cells for use at synchrotron facilities have been highlighted and discussed. The next chapter will consider the first use of the initial cell design, in this thesis, alongside a continuous SiN_x membrane.

Chapter 4: Revealing the Role of CO during CO_2 Hydrogenation on Cu Surfaces

The hydrogenation of CO_2 to methanol over Cu-based catalysts has received growing attention recently due to its potential application in producing green energy alternatives. To optimise the catalyst for this reaction it is important to understand how it operates under reaction conditions, where surface-sensitive spectroscopy measurements are often limited to low pressures. E-cells, as discussed in Chapter 3, can be used to perform measurements at more realistic operating pressures, thus providing new insights into the operation of the catalyst. In the first instance, for simplicity, EY-NEXAFS measurements of a Cu film deposited on a continuous SiN_x membrane were utilised to study the effects of gas composition on the oxidation state; this did not rely on the manufacture of graphene membranes hence it was simpler to produce samples. The ability to probe this system in real time and at high pressure proved to be invaluable. To complement this data: NAP-XPS and MS measurements were also collected, as well as SEM to characterise the morphology of different Cu catalysts used (see the Appendix).

The content covered in this chapter was published: J. E. N. Swallow, E. S. Jones *et al.*, Revealing the Role of CO during CO_2 Hydrogenation on Cu Surfaces with *In Situ* Soft X-Ray Spectroscopy, *J. Am. Chem. Soc.*, 2023, **145**, 6730–6740. The initial draft of the paper was written by Jack Swallow. I performed the subsequent edits and rewrites, therefore the majority of the content shown in this chapter is my own work or is research I contributed to. Some data analysis was done by Jack Swallow and Baran Eren. NAP-XPS data was collected by: Ashley Head, Roey Ben David, and Baran Eren. Atmospheric pressure (AtmP)-NEXAFS data was collected with help from: Jack Swallow, Joshua Gibson, and Robert Weatherup.

4.1 Introduction

The decarbonisation of industrial processes is central to reducing global CO_2 emissions and current societal reliance on unevenly-distributed fossil fuel resources.[10,11,146,147,138–145] 10 years ago the reliance on fossil fuels was such that 22 million tonnes of coal, 85 million barrels of oil, and 10 billion m^3 of natural gas were consumed every day.[138] The finite nature of fossil fuels demanded a change from fossil fuels as a source of electricity and fuel.[11,138–140,144,146] Renewable resources (e.g. wind and solar) and nuclear power generation have become a greater part of the infrastructure of energy generation in recent times. However renewable resources can be unreliable in consistent production of energy as they often rely on the climate.[138,142,143] Therefore, the need to efficiently store energy has also become a prevalent issue. Alongside this, the annual global CO_2 emission from the use of fossil fuels has increased from 25.2 billion tonnes to 36.7 billion tonnes in the last two decades. Whilst there was a decrease in 2020 due to the pandemic, that number is expected to continue to rise.[11,142] The continued increase of CO_2 emission has caused global CO_2 concentration to reach ~420 ppm which is over 150% of the pre-industrial level of 270 ppm.[10,138,144] CO_2 greatly contributes to the greenhouse gas effect that causes climate change; for example, the global temperature has increased continually over recent decades with 2023 as the hottest year on record.[148] It is clear that the use of fossil fuels and CO_2 production cannot continue at this rate.

A potential solution to energy production and storage which avoids fossil fuels is the use of H_2 produced by the electrolysis of water; the so-called “Hydrogen Economy”.[138,140,142] Electricity, from renewable sources, is used to create H_2 via electrolysis and upon burning H_2 energy is released with zero CO_2 emissions, hence it is an efficient energy storage solution from a renewable resource. However, the difficulty in storing H_2 gas coupled with its high explosivity means the use of H_2 has yet to become

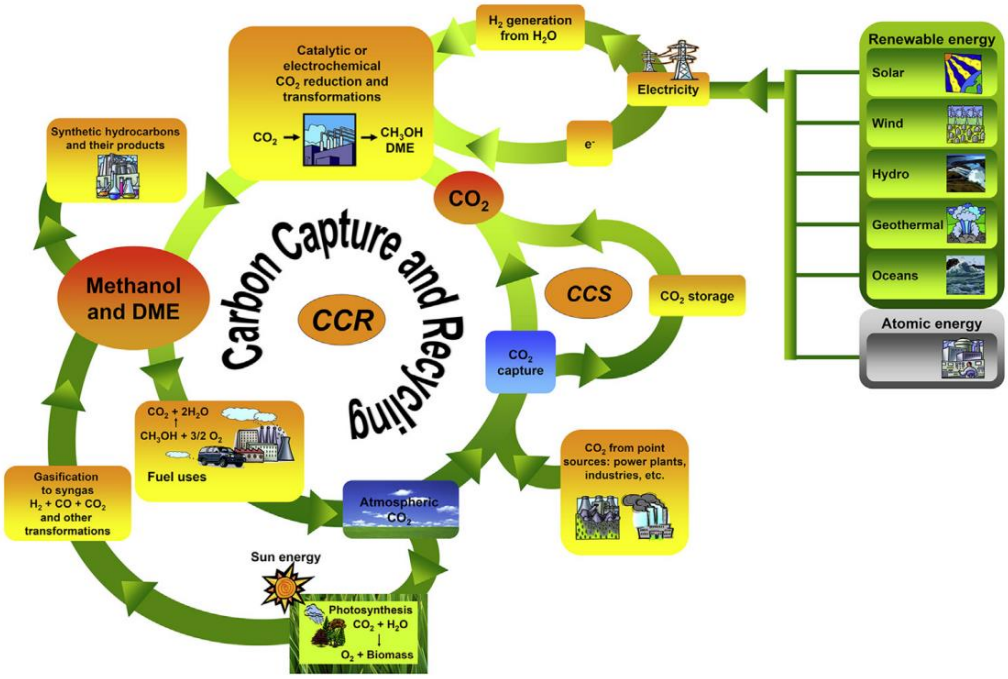


Figure 4.1: *Schematic demonstrating the carbon cycle within the Methanol Economy. Taken directly from A. Goeppert* et al.*, Toward a Sustainable Carbon Cycle: The Methanol Economy,* Elsevier Inc.*, 2018, 919-962.*

viable; additionally, the catalysts required for electrolysis of water (e.g. Pt/Ir) are very expensive.[140,147]

Methanol (CH_3OH) provides an appealing alternative to hydrogen, especially as it is far easier to store, giving rise to the so-called "Methanol Economy".[11,142–144] Methanol synthesis by hydrogenation of CO_2 offers a means of utilising CO_2 that, when combined with H_2 produced by electrolysis of water, yields zero carbon emissions when methanol is burnt as a fuel) as long as the required energy input comes from renewable sources).[144,147] Therefore, methanol synthesis via CO_2 would provide an avenue for energy storage and recycling of emitted CO_2. Global methanol consumption has risen dramatically in recent decades with the majority used as industrial feedstock for the production of important chemical derivatives such as formaldehyde and acetic acid.[139,144,145] With an octane number of 113 and a volumetric energy density around half that of gasoline, methanol is increasingly considered as a direct fuel for internal combustion engines and fuel cells, or indirectly as a liquid carrier for hydrogen.[138,149,150] Methanol, unfortunately, has a lower gravimetric energy density compared to H_2, but crucially methanol greatly improves on the low volumetric energy density of H_2 which limits the application of H_2 as a fuel.[151] Large industrial plants producing substantial quantities of CO_2 could collect and convert CO_2 to methanol which upon burning as a fuel during operation, will release the CO_2 to be collected once more, hence providing a potential means to prevent net CO_2 emissions from industrial sources (see Figure 4.1).[138,144,147] In 2009, the CO_2-to-Renewable-Methanol Plant was established to do just that and in 2015 reported a production capacity of 4 million litres of methanol a year and 5.5 thousand tonnes of CO_2 was recycled.[144] The need to expand and improve the efficiency of CO_2 recycling to methanol operations has motivated a great deal of research in this area.

Industrial methanol synthesis is typically performed over Cu-based catalysts at 200-300°C and 50-100 bar,[138,140] with ~90% of current production based on the conversion of syngas (CO/H_2 mixture, with <20 at.% CO_2) derived from natural gas.[138,140,152–155] To move away from using fossil fuels as the feedstock for methanol, as mentioned above, its synthesis from CO_2/H_2 has been the main focus of much research. $Cu/ZnO/Al_2O_3$ catalysts are typically used for methanol synthesis from both CO/H_2 and CO_2/H_2 mixtures, as well as for the low temperature water-gas shift (WGS) reaction. Three key reaction pathways are considered in CH_3OH synthesis from $H_2/CO_2/CO$ mixtures (Equations 4.1-4.3); CO_2 hydrogenation, CO hydrogenation, and WGS.[11,13,138,142]

Equation 4.1:

$$CO_2 + 3H_2 \rightleftharpoons CH_3OH + H_2O \qquad \Delta H^0 = -49 \text{ kJ/mol}$$

Equation 4.2:

$$CO + 2H_2 \rightleftharpoons CH_3OH \qquad \Delta H^0 = -90 \text{ kJ/mol}$$

Equation 4.3:

$$CO + H_2O \rightleftharpoons CO_2 + H_2 \qquad \Delta H^0 = -41 \text{ kJ/mol}$$

Isotope-labelling studies with $Cu/ZnO/Al_2O_3$ catalysts have demonstrated that methanol formation predominantly proceeds via the CO_2 hydrogenation route (Equation 4.1) rather than the much slower direct hydrogenation of CO (Equation 4.2).[156–158] This has been shown to remain the case for pure Cu catalysts.[156,159,160] In fact, in a $H_2/CO_2/CO$ reaction mixture the hydrogenation pathway via CO_2 occurs an order of magnitude faster than via CO over a pure Cu catalyst.[159] Even for a CO-rich feed, CO first undergoes a WGS reaction with H_2O (Equation 4.3) to form CO_2 and H_2, and then CO_2 further reacts with H_2 to yield methanol.[138,161] Using a CO_2-rich feed reduces the need for this additional

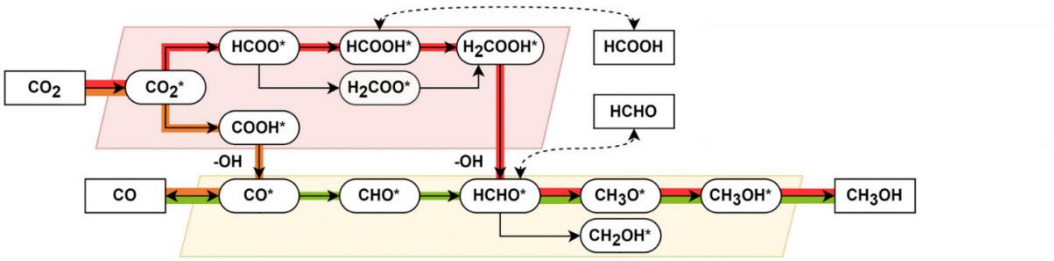


Figure 4.2: *Diagram showing the two possible reaction pathways on a Cu surface for the hydrogenation of CO_2: formate pathway (top), RWGS + CO-Hydro pathway (bottom). Taken directly from Y.-F. Shi* et al.*, EES Catal., 2023, **1**, 921–933.*

WGS step; nevertheless, the presence of CO will increase the methanol production rate at high conversion conditions.[157]

The two possible pathways for hydrogenation of CO_2 are known as: the formate pathway, and the reverse water-gas shift (RWGS) + CO-hydro pathway (Figure 4.2).[142,144,158,162–166] In the formate pathway, H_2 and CO_2 undergo dissociation and create the formate intermediate (HCOO*), the intermediate is hydrogenated further to H_2COOH and the C-O bond is broken to get H_2CO, which can be finally hydrogenated to methanol.[145] In the RWGS + CO-hydro pathway, CO_2 undergoes the RWGS reaction to produce CO* which is hydrogenated via a methoxy intermediate (H_3CO*) to result in methanol.[14] It is widely accepted that the industrially-used $Cu/ZnO/Al_2O_3$ catalyst and pure Cu catalysts mainly proceed via the formate pathway, whereas Cu supported by another metal oxide (e.g. CeO_x, or ZrO_x) will proceed via the RWGS + CO-hydro pathway.[143,166–168]

This chapter will focus on pure Cu catalysts in a CO_2-rich environment, therefore methanol formation mainly proceeds via the formate pathway in this case. The main side reaction expected is the RWGS in Equation 4.3, since it has the same starting products as methanol formation. Industrial conditions are tailored to minimise the RWGS reaction and increase selectivity and activity towards methanol formation. To increase the activity of methanol synthesis, industrial conditions will include a small amount of CO.[169] The exact nature of the beneficial role of CO remains contentious with several mechanisms proposed including: H_2O removal by the WGS reaction which otherwise kinetically inhibits methanol synthesis, regulation of adsorbed oxygen (O*) on the Cu surface, or reduction of ZnO supports to yield oxygen vacancies or Cu^0/Zn^0 alloy sites (specific to the industrial catalyst, see Chapter 6).[55,170]

Methanol formation via the CO_2 hydrogenation route inherently involves the liberation of O* ($CO_2+2H_2 \rightleftharpoons CH_3OH+O$*), which goes on to form H_2O in the overall

reaction of Equation 4.1 ($O^*+H_2 \rightleftharpoons H_2O$). Similarly, the RWGS side reaction (Equation 4.3) liberates O* ($CO_2 \rightleftharpoons CO+O^*$), with exposure of Cu surfaces to CO_2 alone, resulting in deactivation due to O* blocking CO_2 adsorption sites.[170] With H_2 present, O* can be removed by H_2O formation, or the addition of CO to the reaction feed can shift the equilibrium, thereby regulating O* coverage. Critical to rationalising the influence of reaction feed composition, and particularly CO, on methanol productivity is a detailed account of how O* coverage and chemical state of the catalyst surface vary with the balance of reactants under realistic conditions, i.e. approaching the bar-pressure regime used industrially. However, accessing this regime with the required interface sensitivity is a significant challenge due to the dense phases on either side of the solid-gas interface,[19,37,57] with the majority of reports limited either to bulk-sensitive hard X-ray absorption or pressures below a few mbar. The use of E-cells to push to higher pressures and maintain surface sensitivity provides an opportunity to better understand this system.

Herein, this chapter investigates pure Cu catalysts using a combination of NAP-XPS and AtmP-NEXAFS bridging pressures from 0.1 mbar to 1 bar. The coverage of O* and catalyst oxidation state are measured to see how they evolve with the composition of the reaction feed at temperatures (200°C) and pressures (up to 1 bar) more representative of industrial methanol synthesis than prior interface-sensitive studies.[71] For metallic Cu (Cu^0) surfaces exposed to H_2, the addition of a similar CO_2 partial pressure leads to O* formation, confirming CO_2 activation with ongoing H_2 activation regulating the O* coverage and suppressing Cu oxidation. However, at high relative CO_2 partial pressures, excess O* leads to Cu oxidation, poisoning the surface against CO_2 and H_2 activation. On removing CO_2, a Cu^0 surface is not recovered, indicating a high kinetic barrier for H_2 activation on Cu_2O. MS measured at 1 bar corroborates Cu deactivation following CO_2 exposure without H_2 present: a lower H_2O signal is observed when H_2 is reintroduced, indicating the CO_2 hydrogenation and RWGS reactions are

suppressed compared to CO_2 introduction following H_2 pre-treatment. The addition of CO to the feed is able to recover metallic sites which are most active for H_2 dissociation, allowing methanol generation to proceed. This highlights the important function of CO over pure Cu catalysts in industrial methanol synthesis from CO_2-rich feeds, where it serves as a scavenger for adsorbed oxygen, preventing saturation of the catalytically active Cu^0 sites and making the process more robust to variations in reaction conditions. This conclusion provides greater insight into understanding the role of CO in a key industrial process for the future of the Methanol Economy. This study also highlights the benefits of performing measurements at higher (and more representative) pressures which was enabled through the E-cell design.

4.2 Brief Overview of Methods

Three morphological variants of Cu catalyst were used in Chapter 4: foil, thin film, and powder. These different sample geometries were selected to be compatible with the different measurement techniques adopted: Cu foil is an easily workable geometry for NAP-XPS which can be cleaned by sputtering and annealing cycles; Cu thin films can be deposited with low enough thicknesses to allow X-rays to penetrate in the AtmP-NEXAFS cell; Cu powder has a greater surface area to generate a measurable mass signal change in MS. To confirm that the samples were all polycrystalline, so they could be compared in this study, SEM images were collected (see Figure A4.1 in the Appendix). Characterisation of their microstructures confirms that all three morphologies can be considered polycrystalline. Thus, the techniques used herein probe an ensemble of different but comparable model Cu surfaces. Comparisons between the data collected with the different catalyst variants are therefore made in the context of polycrystalline surfaces.

NAP-XPS experiments were performed at the Center for Functional Nanomaterials at Brookhaven National Lab, USA using a lab-based system from SPECS

Surface Nano Analysis GmbH with a PHIOBOS 150 NAP hemispherical analyser and monochromated Al K-α X-ray source (1486.7 eV). NAP-XPS experiments used a polycrystalline Cu foil (Alfa Aesar, 25μm, 99.9999%) as a model catalyst, prepared by cycles of conventional *in situ* Ar^+ ion sputtering (1 kV) and annealing (300°C) until the hydrocarbon signal was below the XPS detection limit. Only Cu, O and C species were detected at the surface during the experiment. High-resolution spectra of the Cu 2p, O 1s, and C 1s core-levels and the Cu LMM AES were collected using a pass energy of 20 eV. The Cu 2p region was only used for energy calibration which showed negligible difference in XPS binding energy between the spectra of Cu^0 and Cu_2O (932.6 eV).[171] The O 1s and C 1s core-level spectra were fitted with pseudo-Voigt functions and Shirley backgrounds.[83] AES in the Cu LMM region are shown after subtraction of a Shirley background and the wide inelastic feature present on the low kinetic energy side. This subtraction is simply to aid visualisation of the data and has no bearing on data interpretation (data subtraction performed by Baran Eren, Weizmann Institute of Science).

AtmP-NEXAFS was performed at beamline B07-C, Diamond Light Source, UK (SI25834).[79,80] A NEXAFS E-cell (as shown in Figure 3.4) was employed which used a continuous SiN_x membrane (500 x 500 μm, 100 nm thick, Silson[128]). Cu (~60 nm) atop a Cr (~5 nm) adhesion layer was deposited onto the SiN_x membrane by RF magnetron sputtering to act as the catalyst. NEXAFS was performed in EY mode by measuring a drain current between the sample and the Au foil electrode in the cell. X-rays in the energy range of 250-2800 eV could be selected, allowing for measurements of the Cu $L_{2,3}$-edges, the O, and the C K-edges to be taken. All AtmP-NEXAFS spectra are shown after subtracting a linear background fitted to the pre-edge region and post-edge normalisation. Energy calibration was performed using the Cu^0 surface obtained by H_2

annealing (main peak set to 933.7 eV).[172] The sample was heated up to 300°C and the gas composition varied to be a mixture of $H_2/CO_2/CO$.

MS measurements were performed using 150 mg of Cu powder (Alfa Aesar, -100 mesh (≤150 μm), 99%) placed in a quartz tube (5 mm inner diameter) between two plugs of quartz wool. Ar was used to balance the gas flow upon changing the composition of the input gas, helping to account for pressure fluctuations which result from the varying pumping efficiency of different gases. Atmospheric pressure was maintained within the reactor throughout the experiment. The sample was initially pretreated by introducing H_2 (20 sccm) and annealed at 275°C for 1 hour. The composition of gas flow into the microreactor was then varied sequentially using $H_2/CO_2/CO$ mixtures at 200°C. MS data is presented with no normalization applied.

4.3 NAP-XPS and AtmP-NEXAFS of Cu

Figure 4.3 and 4.5 (a-c) shows the collected NAP-XPS spectra for the polycrystalline Cu foil surface during sequential exposure to different $H_2/CO_2/CO$ mixtures at 200°C. The chemical state of the Cu surface is obtained by fitting AES of the Cu LMM region shown in Figure 4.3 (a), using similar line-shapes (peak position and width) as those in reference [171]. Peaks corresponding to Cu^0 are shown in blue, whereas those attributed to Cu_2O are shown in red (only apparent in Figure 4.5). Gas phase CO and CO_2 are shown in purple and adsorbed species are shown in green. The O 1s and C 1s regions were fitted with Gaussian-Lorentzian peaks (20-40% Lorentzian). No normalisation was applied to the NAP-XPS data.

Figure 4.3 (a,i) displays AES of the cleaned Cu surface under UHV, where only peaks attributed to Cu^0 are seen (main peak at 918.3 eV, kinetic energy). No C species are discernable (Figure 4.3 (b,i)), indicating low levels of surface contamination, and a single broad peak was seen in the O 1s spectrum (Figure 4.3 (c,i)) at ~531.5 eV. This is

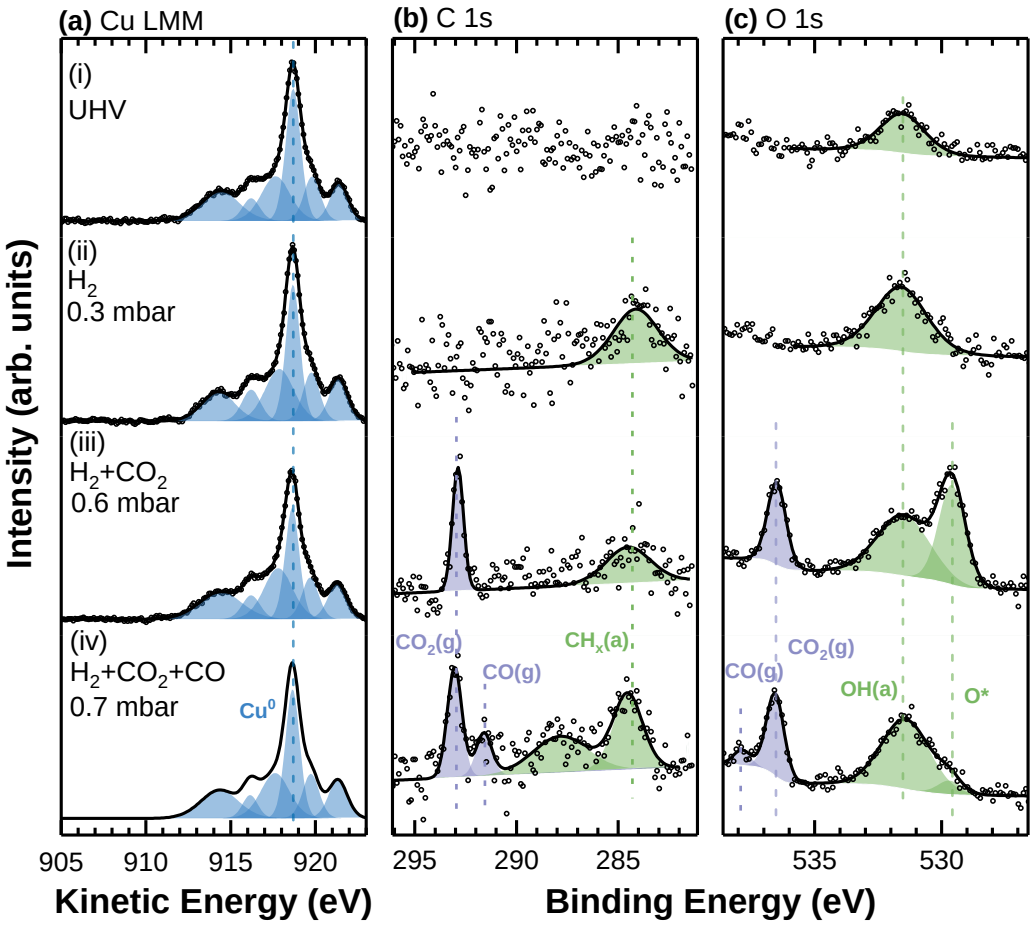


Figure 4.3: *NAP-XPS spectra from the (a) Cu LMM, (b) C 1s, and (c) O 1s regions acquired in (i) UHV, (ii) H_2 (0.3 mbar), (iii) H_2+CO_2 (1:1, 0.6 mbar), (iv) H_2+CO_2+CO (3:3:1, 0.7 mbar). The temperature was fixed at 200°C for all spectra. Spectra collected from pre-treated Cu foil (sputtered and annealed).*

tentatively assigned to potential hydroxylation of the surface, consistent with the binding energy position of OH commonly reported.[173,174] This is typical for polycrystalline surfaces with high-index facets and numerous grain boundaries where trace water vapor from the measurement chamber can adsorb. Some literature has assigned peaks at similar positions to subsurface oxygen species which may form during preparation of the polycrystalline foil.[175,176] However, other literature suggests such species appear at lower binding energies.[177] Even if subsurface oxygen species were present they have not been reported to affect CO_2 adsorption so should not impact the study.[178]

Upon dosing 0.3 mbar of H_2 into the measurement environment, there are no apparent changes in the Cu LMM (Figure 4.3 (a,ii)) spectrum. A very small increase in peak intensity in the O 1s (Figure 4.3 (c,ii)) spectrum is seen. This could be from the additional H_2O introduced upon dosing with H_2 (contamination from gas dosing), increasing the possible OH peak. Alternatively, the peak intensity of subsurface oxygen has been suggested to increase under reducing conditions.[175] A slight increase in peak intensity at ~284.6 eV in the C 1s region (Figure 4.3 (b,ii)) is assigned to small amounts of surface hydrocarbon contamination (CH_x), often referred to as adventitious carbon, although this signal is noisy.[173] When H_2 is present in the gas phase, the Cu surface is expected to dissociate molecular H_2 into chemisorbed hydrogen (H*),[179] which is not detectable with XPS.[180]

Following the addition of 0.3 mbar of CO_2 to the gas mixture, no major changes in the Cu LMM spectrum (Figure 4.3 (a,iii)) are observed, therefore the Cu is not oxidised by the addition of CO_2 (Cu^0 remains). The OH peak and CH_x peak remain (although the surface contamination signal remains very noisy). However, additional peaks emerge in the C 1s (Figure 4.3 (b,iii)) and O 1s (Figure 4.3 (c,iii)) spectra. Those at ~293.0 eV and ~536.5 eV are attributable to CO_2 in the gas phase.[181] Activation of CO_2 is confirmed by the emergence of a peak corresponding to O* at ~529.7 eV.[170] This indicates dissociative

CO_2 adsorption ($CO_2 \rightleftharpoons O^* + CO$) and/or deoxygenation of intermediate species during CO_2 hydrogenation (e.g. $H_2COO^* \rightleftharpoons O^* + H_2CO$, $OH^* + OH^* \rightleftharpoons O^* + H_2O$).[182] The lack of any discernable change in oxidation state in the AES supports the assignment of O* as opposed to lattice oxygen of oxidised Cu. This suggests that O* created from ongoing CO_2 dissociation reacts with H* on the Cu surface to form OH and H_2O, rather than oxidising the Cu surface.[14] Note that the O 1s peak associated with H_2O (surface bound) is likely to overlap with the OH component and may mix to form hydrogen-bonded OH-H_2O hence no additional peak is seen.[174,183] Gas-phase H_2 therefore appears to play an active role in keeping the surface metallic, with a reasonably small O* peak detected in the O 1s spectrum and no obvious Cu_2O in the Cu LMM spectrum. At this stage, the alternative explanation – that competitive adsorption of H_2 suppresses CO_2 adsorption such that the supply of O* is insufficient for Cu oxide formation – cannot be excluded.[184]

Figures 4.3 (a,iv) to (c,iv) show spectra after the addition of 0.1 mbar of CO into the gas mixture. The Cu LMM spectrum (Figure 4.3 (a,iv)) is once again unchanged and the Cu remains completely metallic. However, several changes are apparent in the C 1s and O 1s spectra. Alongside the peaks related to gas phase CO at ~291.8 eV and ~537.9 eV, an additional peak emerges in the C 1s region at ~287.9 eV (Figure 4.3 (b,iv)). This could arise from oxygenated hydrocarbon contaminants,[173] with the corresponding component in the O 1s region convoluted into the broad OH-H_2O peak. The intensity of the CH_x peak in the C 1s region increases slightly as indicated by the less noisy signal. Notably, the O* peak in the O 1s spectrum (Figure 4.3 (c,iv)) is greatly diminished in intensity relative to the other adsorbed and gas phase peaks compared to Figure 4.3 (c,iii). This decrease is consistent with CO scavenging O* from the catalyst surface to form gas phase CO_2, i.e. shifting the equilibrium of dissociative CO_2 adsorption ($CO_2 \rightleftharpoons O^* + CO$). The C 1s data is very noisy, therefore any conclusions made about this data do not rely on assignments in the C 1s region.

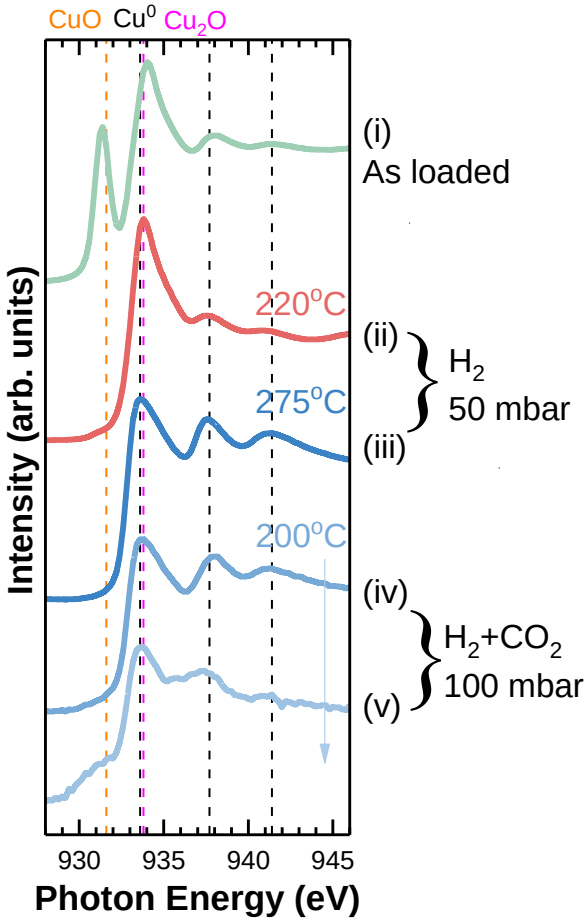


Figure 4.4: *AtmP-NEXAFS spectra from the Cu L_3-edge acquired (i) for the as-deposited sample, (ii) at 220°C with H_2 (50 mbar), (iii) at 275°C with H_2 (50 mbar), (iv) at 200°C with H_2+CO_2 (1:1, 100 mbar), (v) at 200°C with H_2+CO_2 (1:3, 100 mbar). Spectra collected from a Cu film (~60 nm) deposited on the continuous SiN_x membrane.*

Figure 4.4 shows the Cu L_3-edge AtmP-NEXAFS spectra for similar gas dosing steps used for the NAP-XPS experiments in Figure 4.3, but with partial pressures around two orders of magnitude higher. Under vacuum, the as-deposited Cu film exhibits two strong peaks apparent at ~931.3 eV and ~934.0 eV and two smaller features at higher photon energies (Figure 4.4 (i)). NEXAFS probes the unoccupied states of an atom, therefore to understand the origin of these features the occupation of different Cu oxidation states must be considered.[40] The peak at ~931.3 eV is attributed to CuO, which has a distinctly lower energy onset compared to Cu_2O or Cu^0 as it involves a Cu 2p transition to empty 3d states ($3d^9$ configuration in Cu^{2+}).[96,100,185,186] Cu_2O and Cu^0 have fully occupied 3d states, so Cu 2p→4s transitions become dominant, giving rise to a higher absorption onset energy (~934.0 eV).[185,187,188] Cu^0 exhibits distinct fine structure peaks (937.6 eV and 941.3 eV) but is also expected to be more step-like in shape.[187,189] Therefore, the sharp peak at ~934.0 eV in Figure 4.4 (i) must originate partly from Cu_2O, which is known to have a strong peak-like absorption with similar onset energy to Cu^0.[100,172,190] Therefore, the as-deposited sample shows contributions from Cu in three different oxidation states. This is attributed to the gradual oxidation of the initially Cu^0 film due to exposure to air, with Cu_2O and CuO forming at the outermost surface whilst the bulk of the film remains metallic.

Figure 4.4 (ii) shows the Cu film after heating to 220°C in 50 mbar of H_2. All of the CuO has been reduced, as indicated by the complete absence of the peak at ~931.3 eV. The peak at ~934.0 eV remains, as do the resonances at higher energy. These peaks are consistent with a combination of Cu_2O and Cu^0, indicating 220°C is insufficient to fully reduce Cu_2O to Cu in H_2 (50 mbar). Increasing the temperature to 275°C under the same pressure of H_2 (Figure 4.4 (iii)) leads to further reduction of the surface yielding Cu^0 only. This is shown by the step-like spectral shape with a broad absorption onset shifted to slightly lower energy (~933.7 eV) and the relatively stronger fine structure peaks.

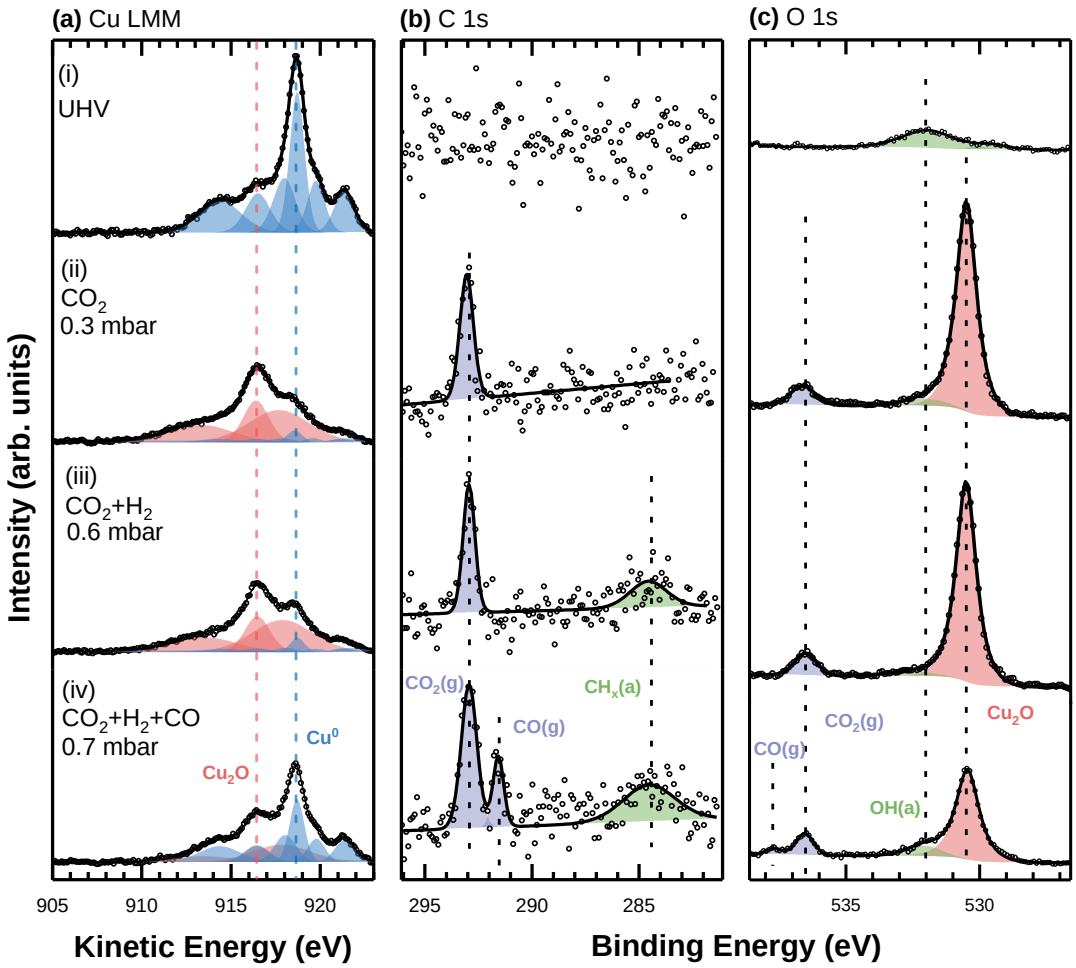


Figure 4.5: *NAP-XPS spectra from Cu LMM, C 1s, and O 1s regions acquired in (i) UHV, (ii) CO_2 (0.3 mbar), (iii) CO_2+H_2 (1:1, 0.6 mbar), (iv) CO_2+H_2+CO (3:3:1, 0.7 mbar). The temperature was fixed at 200°C for all measurements shown. Spectra collected from pre-treated Cu foil (sputtered and annealed).*

After fully reducing the surface to a metallic state, the temperature was reduced to 200°C (reaction temperature) and CO_2 was introduced into the chamber, matching the partial pressure of H_2 (50 mbar of CO_2 + 50 mbar H_2). Figure 4.4 (iv) shows negligible changes to the acquired spectrum, which retains its metallic line shape, confirming the findings of Figure 4.3 hold at higher pressures. Upon increasing the partial pressure ratio to 75 mbar CO_2 + 25 mbar H_2 (Figure 4.4 (v)) the Cu remains predominantly metallic. However, the intensity of the fine structure peaks weakens slightly and a small peak at ~931.5 eV emerges, indicating a small amount of Cu_2O and CuO has formed. Therefore, the ratio of H_2 and CO_2 gas is important, with further increases in CO_2 partial pressure expected to oxidise the Cu surface more. In addition to the Cu L_3-edge, the C K-edge and O K-edge were also acquired during the AtmP-NEXAFS experiment. However, gas phase peaks from CO_2 and CO (after inclusion in the gas mix) dominate these spectra, and gas phase attenuation also modifies these spectra (see Figure A4.2 in the Appendix).

Figure 4.5 and 4.6 shows results of similar NAP-XPS and AtmP-NEXAFS experiments where the order of CO_2 and H_2 introduction are reversed. Prior to the NAP-XPS measurements in Figure 4.5, the Cu foil surface was cleaned by sputtering and annealing. Conversely, for AtmP-NEXAFS in Figure 4.6, the Cu film surface was untreated, with measurements continuing directly from Figure 4.4. Figure 4.5 (a,i) shows the Cu LMM spectrum immediately following surface preparation. This matches the spectrum in Figure 4.3 (a,i), displaying only the features associated with Cu^0. Similarly, no hydrocarbon contamination is seen in the C 1s spectrum (Figure 4.5 (b,i)), and the hydroxyl peak is still visible in the O 1s region (Figure 4.5 (c,i)) due to small and unavoidable water vapor contamination in the NAP measurement chamber. The slightly higher binding energy of this O 1s peak (~532.1 eV) compared to Figure 4.3 (c,i) (~531.5 eV) corresponds more closely to surface OH rather than subsurface oxygen

species.[174,176] A small shoulder peak is also seen here at ~529.5 eV. This could be attributed to a small amount of Cu_2O (not resolved with AES), although its lower binding energy and larger FWHM (~0.5 eV wider) compared to other Cu_2O peaks indicates it is more likely related to O* at the surface.[191,192]

Once 0.3 mbar CO_2 is dosed into the chamber (Figure 4.5 (a,ii)), the Cu LMM spectrum changes significantly. This is accompanied by the emergence of an intense peak at ~530.5 eV in the O 1s region (Figure 4.5 (c,ii)). This indicates Cu_2O formation arising from CO_2 dissociation on the surface. Lattice oxygen in Cu_2O was previously reported to produce a peak at around 530.1-530.4 eV.[171,173,191,193] The small shift in position seen here is within experimental error and could be due to variations in binding strength across different crystal orientations on the polycrystalline sample.[194] Such prominent oxidation of the surface is again consistent with dissociative adsorption of CO_2,[14,170,195] which supplies O* that oxidises Cu^0. CO, which also forms due to CO_2 dissociation, is expected to desorb immediately to the gas phase at 200°C.[196] Thus, no features from adsorbed CO or CO_2 are expected in the C 1s and O 1s spectra of Figures 4.5 (b,ii) and (c,ii), although gas phase CO_2 is still apparent. Similar to the O 1s spectra obtained in vacuum, the surface appears to be partly hydroxylated. There does not appear to be any CuO on the surface from full oxidation of Cu^0/Cu_2O species.

The addition of 0.3 mbar H_2 to the 0.3 mbar CO_2 does not result in any considerable change in the oxidation state of Cu (Figure 4.5 (a,iii)) nor the O 1s peak at ~530.5 eV (Figure 4.5 (c,iii)). Moreover, the addition of H_2 does not change the intensity ratio between the O 1s peaks arising from gaseous CO_2 and lattice Cu_2O. Therefore, H_2 (0.3 mbar) at 200°C is not sufficient to reduce Cu_2O to Cu^0 as the relative amount of Cu_2O is unchanged from that under pure CO_2. In Figure 4.4 (ii) and (iii) to reduce Cu_2O to Cu^0, in 50 mbar of H_2, an increase in temperature from 220°C to 275°C was required. The higher temperature required suggests there is a kinetic barrier for H_2 dissociation

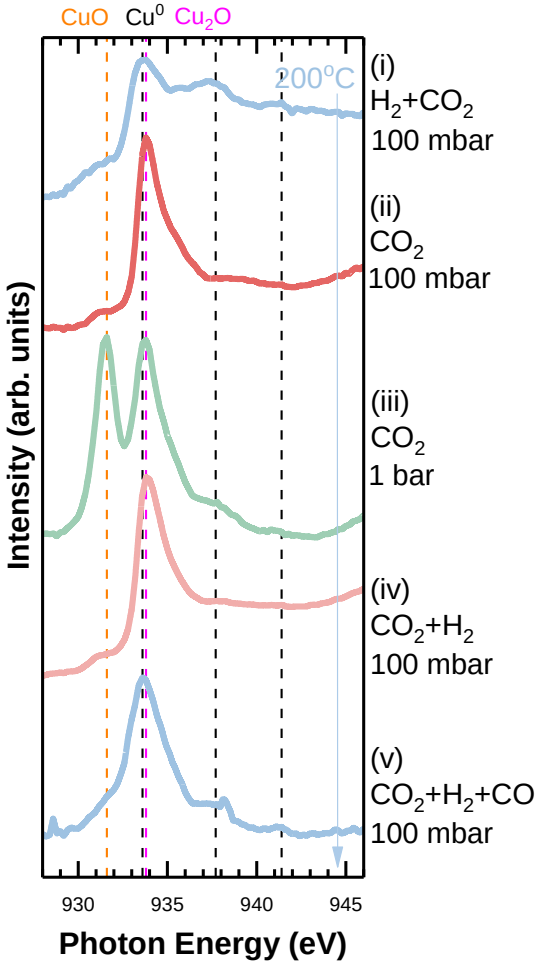


Figure 4.6: *AtmP-NEXAFS spectra from the Cu L_3-edge. Measurements performed at (i) H_2+CO_2 (1:3, 100 mbar), (ii) CO_2 (100 mbar), (iii) CO_2 (1 bar), (iv) CO_2+H_2 (1:1, 100 mbar), (v) CO_2+H_2+CO (9:9:2, 100 mbar). Spectra collected from Cu film (~60 nm) deposited on the continuous SiN_x membrane. The temperature was fixed at 200°C for all measurements shown.*

over Cu_2O and there are no thermodynamic reasons why cannot H_2 cannot reduce Cu_2O. Hence, if left for a long time it would be expected that H_2 would eventually reduce Cu_2O, however to increase the rate of reduction a higher temperature should be used or the addition of a stronger reducing agent. A hydrocarbon peak emerges in the C 1s region (Figure 4.5 (b,iii)), but again the intensity is very weak and the signal is noisy (also seen when H_2 is present in Figure 4.3 (b,ii)).

After the introduction of 0.1 mbar CO into the gas mixture (Figure 4.5 (a,iv)) is a decrease observed in the oxide-to-metallic ratio obtained from the Cu LMM. This is accompanied by a relative reduction in the intensity of the Cu_2O peak at 530.5 eV in the O 1s region (Figure 4.5 (a,iv)). According to XPS measurements of the O 1s region, the intensity ratio between lattice oxygen and oxygen in gas-phase CO_2 decreases compared to when CO was not present. This suggests that CO plays an active role in reducing Cu_2O, increasing the number of metallic adsorption sites available by scavenging oxygen on the surface. The peaks attributed to hydrocarbons and hydroxyl groups persist when CO is dosed; however, oxygenated hydrocarbon contaminants are not discernable. Gas phase CO is clearly seen in both the C 1s and O 1s regions in addition to gas phase CO_2 (Figure 4.5 (b,iv) and Figure 4.5 (c,iv)).

Figure 4.6 shows the Cu L_3-edge NEXAFS following on from the experiment displayed in Figure 4.4, i.e. Figure 4.4 (v) and Figure 4.6 (i) are the same spectrum. In order to simulate the gas dosing protocol used for NAP-XPS in Figure 4.5 (ii) (CO_2 dosed over a clean Cu^0 surface), the flow of H_2 into the cell was stopped, leaving only CO_2 at a pressure of 100 mbar (Figure 4.6 (ii)). A fairly rapid change from Cu^0 to Cu_2O is observed (measurements performed ~30 minutes apart), with a small contribution from CuO also apparent.

Following this initial change, the pressure of CO_2 was increased to 1 bar (Figure 4.6 (iii)), where significant CuO formation was seen. This did not occur at lower CO_2

pressures. This is explained by the increase in partial pressure of CO_2 shifting the chemical equilibrium in favor of increased CO_2 dissociation, thus increasing the supply of O*, which feeds CuO formation. This result highlights the importance of approaching realistic reaction conditions (in this case, high pressures) when studying catalytic reactions, as even under NAP conditions (Figure 4.5 (a,ii)), the catalyst state can differ from that seen at higher pressures (Figure 4.6 (iii)).

After adding H_2 (50 mbar) back into the gas mixture and returning to a total pressure of 100 mbar (Figure 4.6 (iv)), the removal of most CuO is shown by the domination of the Cu_2O peak. However, no features of Cu^0 are apparent. Only after adding CO into the gas mixture (45 mbar CO_2, 45 mbar H_2 and 10 mbar CO) does the line shape become less asymmetric, and the fine structure peaks of Cu^0 emerge (Figure 4.6 (v)), indicating partial reduction of the surface. As observed in Figure 4.5 (a,iv), at this relatively low ratio of CO, the surface does not become fully metallic; however, reduction of the surface by CO is seen. Thus, CO is confirmed to scavenge oxygen on the surface resulting in an increase in the number of metallic sites which are most catalytically active for H_2 and CO_2 dissociation.

4.4 Mass Spectrometry of Cu Powder

So far, only soft X-ray spectroscopy measurements have been considered to follow changes in the chemical state of the catalyst surface with varying gas composition, but the catalyst products generated were not measured. To complement these studies, MS was used to observe how the reaction products vary with the order of H_2 and CO_2 dosing. The H_2O signal is presented here (a product of Equations 4.1 and 4.3) to better determine the possible reactions occurring at the surface; the generated methanol signal is also presented for completeness.

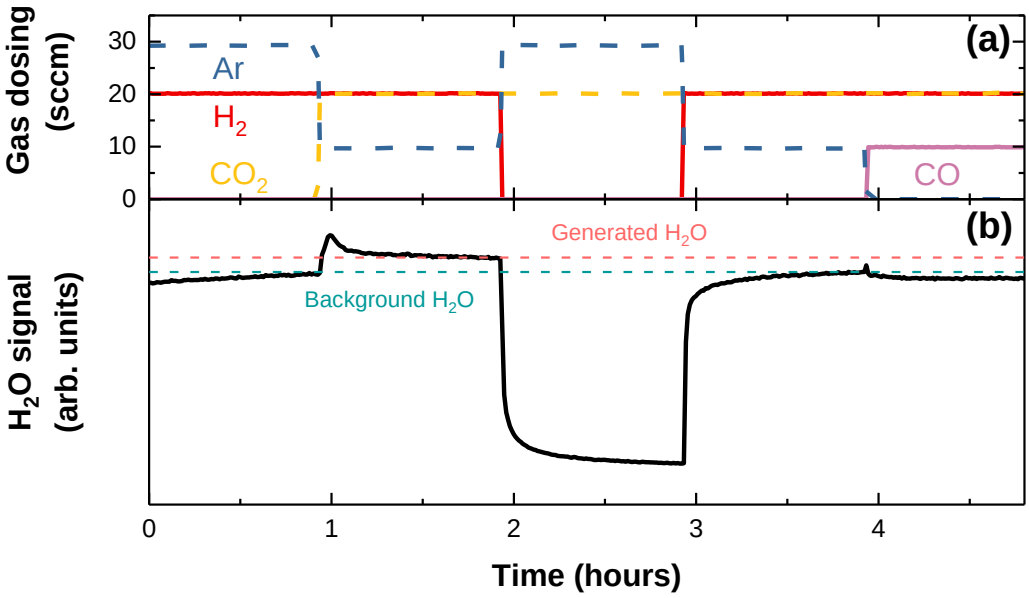


Figure 4.7: *Time evolution of H_2O mass signal for different reaction steps. (a) Flow rates of gases dosed during the reaction. The gas dosing steps proceeded as follows: H_2 (20 sccm), H_2 (20 sccm) and CO_2 (20 sccm), CO_2 (20 sccm), H_2 (20 sccm) and CO_2 (20 sccm), and finally H_2 (20 sccm), CO_2 (20 sccm) and CO (10 sccm). Ar gas was used to balance the chamber pressure and maintain a constant total flow of 50 sccm. (b) H_2O signal during the reaction. The zero of the time scale is set to when the temperature reached 200°C and the pressure is maintained at 1 bar throughout. At t=0 hours, the Cu is expected to be metallic after having been reduced in H_2 at 275°C.*

To prepare the Cu powder it was reduced in H_2 at 275°C (Figure 4.7 (a)) to yield Cu^0. The Cu was determined to be fully reduced once the H_2O signal (Figure 4.7 (b)) decreased to a stable value (~60-90 minutes); this was confirmed by *ex situ* AES as shown in the Appendix (Figure A4.3). Figure 4.7 (b) shows the H_2O signal generated from the Cu powder over time following pre-treatment. The total pressure of gases the powder was exposed to always remained at 1 bar. Figure 4.7 (a) shows how the composition of gas was changed over time. Following pre-treatment, the Cu powder was exposed to H_2 for ~60 minutes at 200°C to determine a base signal of H_2O and allow the temperature to reach an equilibrium. During this first hour in Figure 4.7, a stable H_2O signal is observed whilst dosing H_2, corresponding to a background level of H_2O arising from residual species from the gas lines/reactor walls. For the second hour, CO_2 is introduced alongside H_2. There is a clear peak in the H_2O signal, which decays and stabilises at a higher level than the background signal. The initial increase is characteristic of a transient state brought about by the surface reacting to the change in conditions. The higher level at which the H_2O signal equilibrates can be attributed to H* (from H_2 dissociation) reacting with O* (from CO_2 dissociation) on the Cu surface to form H_2O as part of the CO_2 hydrogenation (Equation 4.1) and/or RWGS reactions (Equation 4.3).[182,197] This can also explain the transient behaviour, the steady-state H* coverage is stabilised during H_2 exposure, serving as a reservoir for reaction with O* when CO_2 is introduced, resulting in an elevated H_2O signal until a new steady-state H* coverage is reached.

In the third hour of the experiment, H_2 is removed from the gas mix and, as expected, the H_2O signal drops to a much lower level. The H_2O signal drops below the background level as seen from H_2 in the first hour. During exposure to CO_2 alone, the surface of the Cu will be oxidised, as shown by the AtmP-NEXAFS measurements in Figure 4.6 (ii) and (iii). When H_2 is reintroduced into the gas mix for the fourth hour, the

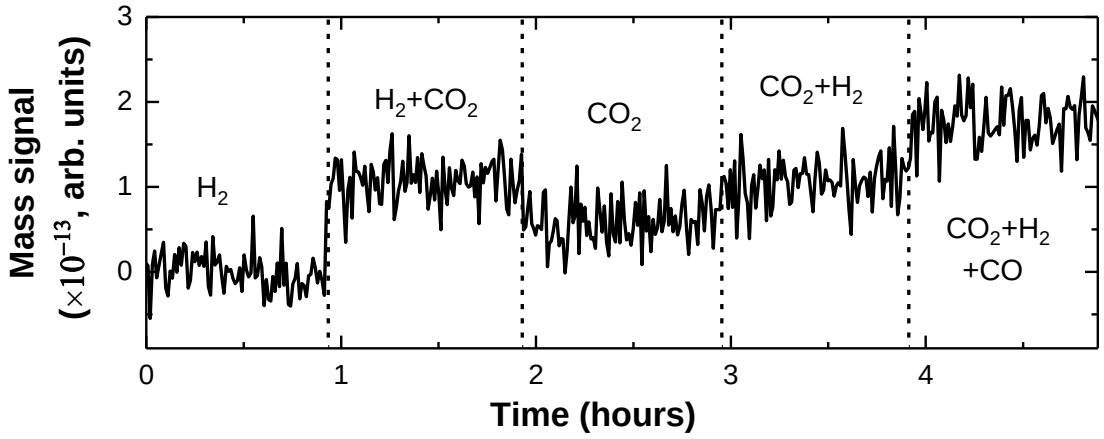


Figure 4.8: *Time evolution of CH_3OH mass signal for different reaction steps at 200°C. The gas dosing steps proceeded in the same manner as described in Figure 4.7 (a).*

H_2O signal returns to the background level seen when only H_2 is present, and no initial peak associated with a transient state is observed. It indicates that CO_2 hydrogenation and RWGS reactions are heavily suppressed compared to when H_2 is dosed onto Cu^0 prior to the CO_2. From Figures 4.3-4.6, the addition of CO is expected to recover the catalytic active metallic sites, this will also cause a shift in the equilibrium of Equation 4.3, suppressing H_2O formation by RWGS. Indeed, a slight drop in the H_2O signal is observed on CO addition, consistent with CO providing an additional pathway for O* removal.

Figure 4.8 shows the methanol signal obtained during the reaction. The methanol yield is small for pure Cu, and the setup used is not well optimised for methanol detection, hence only a very small methanol signal seen. There is a very small increase in methanol signal when CO is introduced. This agrees well with previous literature which had shown CO will increase the activity and selectivity of Cu catalysts towards methanol formation.[169]

4.5 Discussion

Figure 4.9 summarises the main reaction pathways revealed by this study when $H_2/CO_2/CO$ gas mixtures react on Cu surfaces. The ratio of H_2 to CO_2 and the order in which they are introduced can significantly alter the catalyst state and its activity towards methanol synthesis reactions. The C and O K-edge data collected is not discussed, because during the collection of EY-NEXAFS using the conduction of electrons through the gas-phase, the C and O K-edge signals were dominated by the gas-phase signals and distorted by gas absorption for CO_2 and CO when present (see Figure A4.2). An advantage of XPS is the separation of gas-phase and surface species which was demonstrated in NAP-XPS (Figures 4.3 and 4.5) where the surface O* species were not obscured by the gas-phase CO_2 and CO signals.

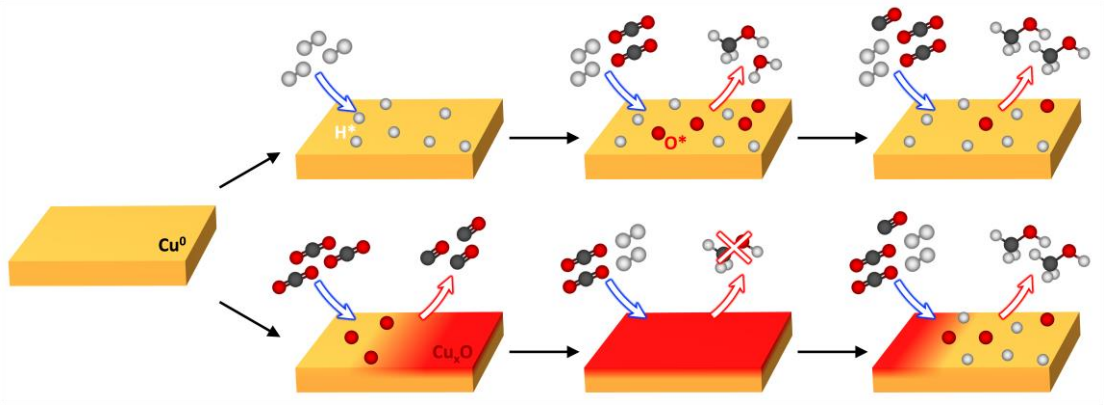


Figure 4.9: *Illustrative diagram of the proposed reaction pathways during exposure of Cu to H_2, CO_2 and CO. The top row corresponds to the gas dosing order in Figures 4.3 and 4.4, i.e. H_2 first, while the bottom row corresponds to the dosing order in Figures 4.5 and 4.6, i.e. CO_2 first. [For the gas molecules: H = grey, O = red, and C = dark grey.]*

During pre-treatment for AtmP-NEXAFS, pure H_2 (50 mbar) at 220°C did not yield a Cu^0 surface, with higher temperatures (275°C) needed to achieve this (see Figure 4.4 (iii)), indicating a large kinetic barrier for H_2 dissociation on Cu oxides.[198,199]

It was found that when H_2 is used as the initial reactant gas (starting from a metallic surface), the Cu surface is maintained in a metallic state, with H_2 acting to remove any residual O* from the Cu surface. When CO_2 is introduced into the gas mix, its activation on the Cu surface is observed through the emergence of O*, but without formation of a distinct Cu oxide phase (apart from at high CO_2:H_2 ratios when Cu^0, Cu_2O, and CuO are found to coexist). The ongoing H_2 dissociation (to H*) on the Cu^0 presumably scavenges O* from CO_2 activation to form OH and H_2O vapor, preventing Cu oxidation.[14,163,165,200] Given that Cu is found to be reduced across a wide pressure range (up to 100 mbar) and the presence of O* in NAP-XPS measurements confirms ongoing CO_2 dissociation, the suppression of Cu oxidation by competitive hydrogen adsorption can be largely excluded. The increase in H_2O signal in the MS (Figure 4.7) upon adding CO_2 following a H_2 pre-treatment further supports this argument, since competitive hydrogen adsorption would not cause this increase in signal. The removal of O* by H* confirms CO_2 and H_2 dissociation on the Cu^0 surface sites, which are both critical to the CO_2 hydrogenation and RWGS reactions that occur under methanol synthesis conditions.[14]

When the ratio of CO_2:H_2 is increased, a small amount of oxide formation is observed, as in Figure 4.4 (v). This oxidation can be rationalised by the amount of O* increasing relative to H* on the surface, such that some excess O* does not react with H* to form H_2O so is available to oxidise Cu. The addition of CO has little effect on the chemical state of the already metallic catalyst. However, the concentration of O* is significantly reduced on the Cu surface, highlighting the role of CO as an oxygen

scavenger (Figure 4.3 (c,iv)).[201] Therefore, CO addition is less crucial when H_2 is dosed prior to CO_2 to maintain catalytically active Cu^0 sites.

On the other hand, if CO_2 is used as the initial reactant gas, then significant oxidation of the Cu surface is observed ($2Cu+O^* \rightleftharpoons Cu_2O$), which can be attributed to O* provided by CO_2 dissociation. CO_2 is found to adsorb as $CO_2^{\delta-}$ on Cu(111) at low pressures (0.01-1 mbar) and room temperature.[170,195] Conversely, on more active Cu(100), Cu(110), and stepped surfaces, CO_2 dissociation is observed through the emergence of chemisorbed oxygen,[202,203] and is even seen on Cu(111) as pressure and temperature are increased.[195] However, O* coverage blocks further CO_2 adsorption on the catalyst surface leading to "self-poisoning".[14,170,195] Although O* coverages of >0.5 monolayers have been observed on Cu(100) during CO_2 exposure through the breakup of the surface into nanoclusters, the Cu subsurface remains predominantly metallic at room temperature.[170] The greater extent of catalyst oxidation observed on polycrystalline Cu is attributed to the higher temperature during CO_2 exposure.

At higher CO_2 pressures of 100 mbar and above, the emergence of CuO at the surface ($Cu_2O + O^* \rightleftharpoons 2CuO$) is observed, which is a significant component at 1 bar. The increase in pressure of CO_2 increases oxidation of Cu through shifting the equilibrium towards CuO ($CO_2 \rightleftharpoons O^* + CO$). On lowering the CO_2 pressure and introducing H_2, the catalyst reduces again to predominantly Cu_2O, but further reduction to Cu^0 is not observed. The rate of H_2 dissociation is very low and insufficient to recover a metallic surface. This is due to a large kinetic barrier for H_2 dissociation on Cu_2O.[198,204] This large barrier is also apparent in the AtmP-NEXAFS measurements in Figure 4.4 (ii) and (iii), where heating to 220°C in H_2 (50 mbar) is insufficient to fully reduce the Cu_2O surface, which only becomes metallic after heating to 275°C. The MS results (Figure 4.7) are also consistent with this, with a similar H_2O signal observed, both when H_2 is added after CO_2 dosing and when only H_2 is dosed. The lack of additional H_2O means the surface is not

reduced to Cu^0. These findings are broadly consistent with prior density functional theory (DFT) calculations suggesting that CuO is easier to reduce than Cu_2O in the presence of H_2.[205]

The differences between Figures 4.3 (iii) and 4.5 (iii) for NAP-XPS, and Figures 4.4 (iv) and 4.6 (iv) for AtmP-NEXAFS emphasise the importance of the order of gas dosing. The oxidation state is different for identical reaction conditions (50:50 mixture of H_2:CO_2 at either a total pressure of 0.6 mbar in NAP-XPS or 100 mbar in AtmP-NEXAFS); the only difference is the order of dosing H_2 and CO_2. If thermodynamic equilibrium is reached, then the final state should be independent of the direction of the approach. To summarise: the Cu surface remains predominantly metallic when H_2 is dosed prior to CO_2 (Figure 4.3 and 4.4), but when CO_2 is introduced first, the Cu surface oxidises towards CuO, with the subsequent addition of H_2 only leading to partial reduction to predominantly Cu_2O (Figure 4.5 and 4.6).

Although the addition of H_2 after CO_2 does not reduce the surface beyond Cu_2O, further reduction can be achieved by the addition of CO ($Cu_2O+CO \rightleftharpoons 2Cu+CO_2$), which is more effective at reducing Cu_2O compared to H_2. CO is thus conclusively shown to behave as an oxygen scavenger, yielding metallic sites which are more catalytically active for CO_2 and H_2 dissociation. Dissociation of H_2 is critical to methanol synthesis, and the results here point towards an important role for CO in the gas mixture: as an oxygen scavenger to maintain Cu^0 sites. The MS data in Figure 4.8 confirms a higher methanol production when CO is present (although conditions are not optimised for methanol synthesis therefore only a small signal is detected).[160] Maintaining these sites allows both H_2 and CO_2 dissociation to proceed, especially as CO_2 activation tends to rapidly oxidise and deactivate the surface unless O* is continuously removed.[170]

Maintaining Cu^0 sites is critical to achieving methanol generation at a significant rate, with an increase in the number of these sites shown to increase activity towards

methanol formation.[169] From Equation 4.3 and Figure 4.7 (b), it is also clear that introducing CO shifts the equilibrium making the RWGS reaction less favorable, such that more CO_2 is directly converted to CH_3OH rather than being converted into CO. Thus, these results demonstrate the importance of using CO in the gas feed for methanol synthesis from CO_2 and H_2 to prevent Cu catalyst deactivation by maintaining metallic sites across a wider range of conditions, including at high CO_2:H_2 ratios.[170] Traditionally CO is produced via steam reforming of natural gas, therefore production of CO is non-renewable.[206] This is a problem as the generation of methanol is motivated by the need to produce a sustainable and greener alternative to fossil fuels, however the manufacture of methanol needs CO for the process to be efficient. CO could alternatively be produced via the electrochemical reduction of CO_2.[207,208] If the CO required in methanol synthesis was produced from CO_2, then this would align with the aim of producing methanol without relying on fossil fuels.

Whilst the focus in this chapter has been the surface of pure Cu catalysts, industrially, ZnO is typically used to support Cu for methanol synthesis. There remains significant debate over the exact nature of the interaction between Cu and ZnO that leads to improved methanol yield.[17,55,209,210] However, it is well accepted that in the presence of ZnO, the Cu remains metallic during methanol synthesis.[55,209] The results in this chapter highlight the importance of Cu remaining metallic in order to dissociate H_2 as well as CO_2. This is important considering the spillover of active H* from Cu^0 to ZnO has been implicated in the formation of reactive intermediates.[209] Recently, there has been much discussion on the nature of reduced Zn species, the species present, and the nature of the interaction between Cu and Zn responsible for the promotional effect of ZnO supports. For example, the formation of a Cu^0/Zn^0 alloy is often considered, but this requires highly reducing conditions.[17,55,210] The inclusion of CO has been shown to help maintain such a Cu^0/Zn^0 alloy,[55] playing a similar role of oxygen scavenger as observed

herein, albeit promoting the reduction of different species (since the presence of Zn already maintains metallic Cu). Hence, the precise role of CO may depend critically on the catalyst composition used. The interaction between Cu and ZnO is investigated in detail in Chapter 6 using $Cu_{70}Zn_{30}$ NPs as a representative system and how the composition of gas (H_2/CO_2/CO) can irreversibly affect the interaction between Cu and ZnO. The results presented in this chapter for pure Cu are important when comparing how the $Cu_{70}Zn_{30}$ system behaves under similar conditions.

4.6 Conclusion

In summary, the results presented in this chapter have shown how the surface chemical state and adsorbates present on Cu vary with the order of gas dosing during CO_2 and H_2 exposure at temperatures typically used for methanol synthesis. Through the complementary NAP-XPS and AtmP-NEXAFS study, the understanding developed is extended to the atmospheric pressure regime whilst still providing surface-sensitive information through soft X-ray spectroscopies. This combined approach proves a practical avenue for studying catalytic reactions at industrially relevant gas pressures. The Cu surface remains metallic in the presence of CO_2 and H_2 when H_2 is dosed first. A small amount of Cu_2O is observed at high CO_2 ratios; however, Cu retains the significant metallic character needed for ongoing CO_2 and H_2 activation. When CO_2 is dosed prior to H_2, the Cu surface readily oxidises to Cu_2O, with significant CuO formation at high CO_2 pressures. The introduction of H_2 only returns the surface to Cu_2O, with further reduction suppressed due to a high kinetic barrier for H_2 dissociation. The addition of CO to the gas feed is found to scavenge oxygen from the Cu surface, thus making Cu^0 sites available for CO_2 and H_2 dissociation. Hence, even though CO_2 has been established as the carbon source for methanol generation,[156] this study demonstrates the importance of including CO in the reactant mixture. This contributes to a process that is more robust to variations in reaction conditions, particularly given that large kinetic

barriers for certain processes (e.g. H_2 dissociation) can lead to effective catalyst deactivation if the desired oxidation state is lost. It is also important to consider the production of CO should ideally not be from traditional routes using natural gas.

This high pressure study was not possible without the development of the E-cell design. These results highlight the importance of studying these phenomena at pressures close to realistic industrial systems, as this can alter both the equilibrium and reaction kinetics, for example the oxidation state behaviour of Cu under different CO_2 pressures. Low pressures of CO_2 (0.3 mbar) only oxidised the surface to Cu_2O, whilst at 100 mbar some further oxidation to CuO and more Cu_2O was observed; at even higher pressures (1 bar), then only CuO was observed. Hence, it is important to continue to extend *in situ* studies to even higher pressures. The majority of the measurements using the E-cell were limited to 100 mbar. The study could be extended by performing all measurements at 1 bar which is more representative of industrial conditions. The pressure limitation came from a combination of: weak signal from EY-NEXAFS at high gas pressure making conduction of electrons through the gas more difficult, and inefficient sealing between Cu and graphite gaskets which was particularly problematic when H_2 was used; H_2 is a small molecule and will leak more easily compared to CO_2 or CO.

The industrial catalyst includes a ZnO support and, as previously mentioned, the role of ZnO and how it promotes the activity and selectivity of the hydrogenation of CO_2 is still not well understood. Thus, another improvement to this study would be to include a more complex catalyst that incorporates Zn. Additionally, the continuous SiN_x membrane used to seal the E-cell was successfully implemented for this initial study. However, SiN_x is not transparent to electrons so the study was limited to EY-NEXAFS, with no high pressure XPS measurements possible.

As a result, the next part of this thesis will address these improvements. First of all, graphene membranes must be reliably manufactured to enable high pressure XPS measurements alongside NEXAFS (Chapter 5). Once this has been achieved a Cu/ZnO catalyst can be studied using an improved E-cell design (Figure 3.6) to elucidate the role of ZnO in the hydrogenation of CO_2 (Chapter 6).

Chapter 5: Graphene as a Window for Ambient Pressure X-Ray Spectroscopy

The development of soft XPS techniques using E-cells relies on the manufacture of graphene membranes. This chapter presents a method of transferring graphene from its growth substrate to a perforated SiN_x membrane window in a clean and reliable way. XPS data from the solid/gas and solid/liquid interface are presented to demonstrate the capabilities of the manufactured graphene membranes. MLG was shown to be capable of enclosing 1 bar of Ar gas within a NAP-XPS system during XPS measurements, whilst BLG enabled XPS measurements of a flowing liquid within a conventional lab-based system. Finally, a summary of the attempts to directly grow graphene onto a perforated SiN_x membrane is presented (greater detail of these attempts can be found in the Appendix).

Some of the content covered in this chapter has been recently published: E. S. Jones, *et al*., *In Situ* Formation of Suspended Graphene Windows for Lab-Based XPS in Liquid and Gas Environments, *ChemCatChem*, published, 2024, 202400239. I performed the majority of experiments detailed in this chapter, and was the lead author on the resulting paper. 2D Raman maps were collected by Robert Weatherup. AtmP-XPS was performed with the help of Jack Swallow, Leanne Jones, Joshua Gibson, and Robert Weatherup. Lab-based XPS of the liquid etching of Au was performed in collaboration with: Charalampos Drivas, Mark Isaacs, and Christopher Parlett.

5.1 Introduction

Graphene is a 2D material made up of an sp^2-hybridised system forming a hexagonal lattice of carbon atoms (Figure 5.1 (a)).[211,212] Electrons in graphene exhibit a high mobility (2.5×10^5 $cm^2V^{-1}s^{-1}$) resulting in a high electrical conductivity.[112,213–215] The high electron mobility originates from the out-of-plane delocalised conjugated π-system

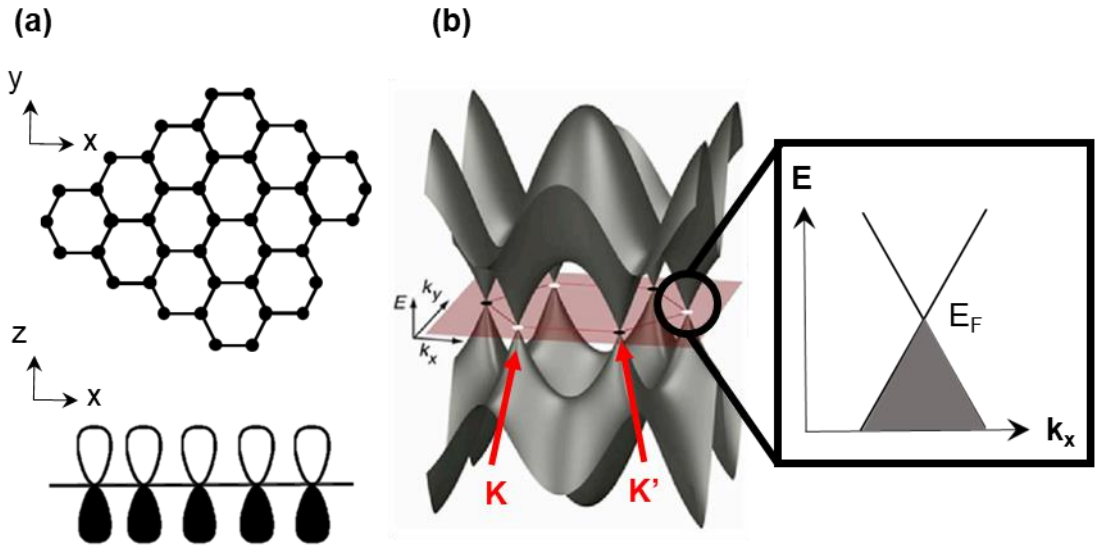


Figure 5.1: *(a) Schematic of hexagonal lattice of carbon atoms (graphene) and a cross-section showing p-orbitals perpendicular to the lattice. (b) Brillouin zone of graphene showing the inequivalent Dirac points (**K** and **K'**) and graphene's dispersion curve which is linear at the Dirac points (emphasised by the inset). (b) Taken from J. Wang* et al.*,* Mater. Today Phys.*, 2017, **3**, 93–117.*

formed of overlapping neighbouring p-orbitals containing lone electrons from each carbon atom. The high electrical conductivity can also be explained by considering the band structure of graphene. At specific points in its Brillouin zone (Dirac points, **K** and **K'** in Figure 5.1 (b)) graphene has a linear dispersion relation where the effective mass of electrons is zero, and thus behave as so-called Dirac fermions (see the Appendix for details).[211,216,217] At these Dirac points the conduction and valence bands touch, therefore graphene is a zero band-gap semiconductor; this can often restrict its applications where doping is required to introduce a band-gap.[218,219]

Graphene has been used as a strong, electron-transparent window for high pressure *in situ* X-ray spectroscopy, such as in E-cells. The strong in-plane sp^2 bonds make it ideal to separate regions with a high pressure difference without bursting. Graphene is also impermeable to gases which prevents the leaking of gases from the E-cell, as long as the graphene is continuous across the window.[119,220–222] Additionally, its thickness of ~1 Å makes it transparent to electrons, therefore electrons emitted from a sample can be measured through graphene which is required for XPS and TEY-NEXAFS measurements.[223] Finally, its high electrical conductivity is useful to minimise charging effects in X-ray spectroscopy.

To utilise graphene as an electron transparent window, a method is required to manufacture high-quality graphene over macroscopic areas (at least mm^2) whilst remaining cost effective. Table 5.2 summarises some graphene production methods.[219,224–231] For most of the methods shown in Table 5.2 there is a trade-off between quality, scalability, and cost.

Chemical vapour deposition (CVD) is capable of producing high-quality graphene on a large scale.[132–134,212,220,232] CVD is preferred to the thermal decomposition of SiC, because the process is highly tunable and can be performed at relatively lower temperatures. In CVD a carbon precursor is heated over a transition metal catalyst,

Method Summary	Advantages	Disadvantages
Mechanical Exfoliation: Repeated peeling of graphite with scotch tape.	• High-quality • Cheap	• Small scale • Small flakes produced
Thermal Decomposition of SiC: Use high temperatures (>1000°C) to growth graphene directly on SiC.	• High-quality • Direct growth on an insulating substrate • Large scale	• Expensive • Difficult to remove graphene from growth substrate
Liquid Phase Exfoliation: Reduction of graphene oxide flakes or liquid-phase exfoliation from graphite.	• Large scale possible • Cheap	• Small flakes • Low-quality
Unzipping carbon nanotubes: Multi-step process involving supports to unzip nanotubes.	• Tunable properties by altering width of nanotubes	• Expensive • Small scale • Difficult
Chemical Vapour Deposition: Dissociation of a carbon precursor over a transition metal catalyst.	• Large scale • High-quality • Tunable	• Expensive • Limited growth substrates

Table 5.2: *Summary of graphene production methods.*

resulting in dissociation of the carbon molecules onto the metal surface which forms graphene.[233,234] The transition metal catalyst is required to lower the high E_A for dissociating the carbon precursor. CVD uses a H_2 pre-treatment to reduce any metal oxides present and ensure the catalyst is metallic and highly active.[232] There are a wide choice of carbon precursors, catalysts, and conditions available. The careful control of CVD growth parameters was relevant to the attempts to directly grow graphene on a perforated SiN_x membrane, as shown in the Appendix. The Appendix also contains a more detailed discussion on the CVD growth mechanism and the effect of adjusting different CVD growth parameters. For the results presented in this chapter: MLG grown on Cu foil was purchased (Graphenea, PI-KEM) to ensure a high degree of consistency between samples.

One of the limiting factors in the application of graphene is the requirement to transfer it from the growth substrate used in CVD to the desired substrate, such as a SiN_x membrane. Transfer methods often introduce defects, tears, wrinkles, and contamination into graphene.[103] Contamination can degrade graphene's properties such as conductivity and contribute to additional X-ray spectroscopy signals; tears and wrinkles can result in leaks and potential weak areas susceptible to bursting under pressure.[134,235,236]

The most common way of transferring graphene (Figure 5.3 (a)) is to use a polymer support (e.g. PMMA) which is applied to the topside of graphene.[59,103,134] The general procedure involves etching the growth substrate using a liquid etchant, followed by washing the PMMA/graphene, before finally adhering the PMMA/graphene to the desired substrate (usually via heating) and removing the PMMA using an acetone and isopropanol (IPA) wash.[19] The support layer provides structural support, preventing the graphene from tearing or crumpling during the transfer due to the high surface tension of the liquid etchant. The substrate can be treated beforehand to make it more

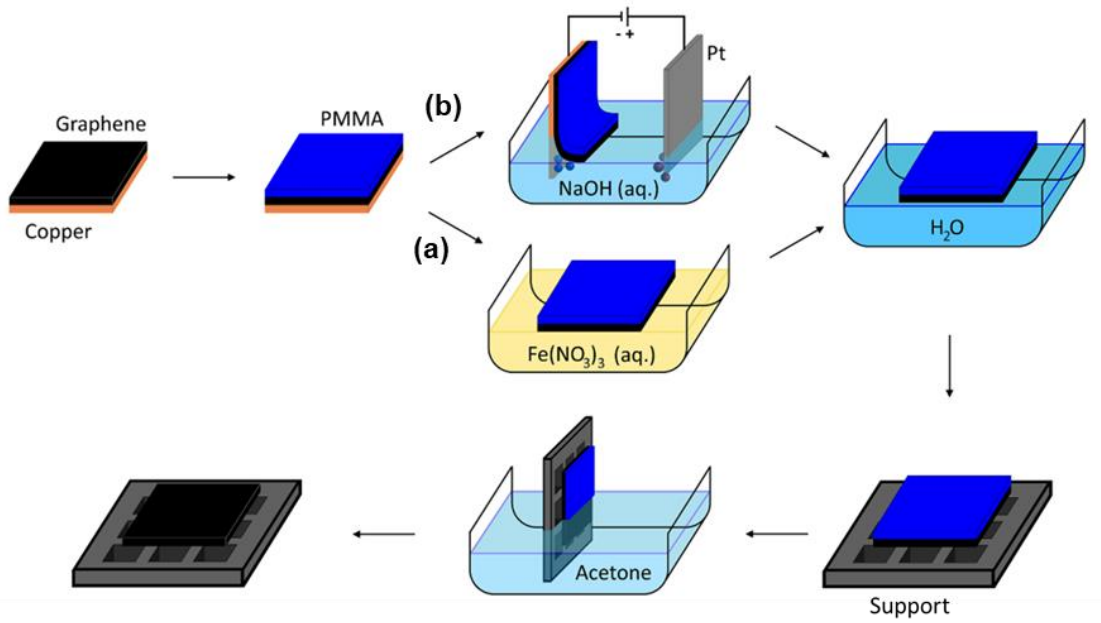


Figure 5.3: *Diagram outlining the transfer of graphene from a Cu foil to another substrate using a PMMA support. Where PMMA/graphene is separated from Cu using either (a) etching of Cu with* $Fe(NO_3)_3$*, or (b) bubbles produced in an electrochemical reaction where Pt is the counter electrode referred to as the bubbling method. (a) and (b) Taken directly from P. Leidinger* et al.*,* J. Phys. D: Appl. Phys.*, 2021,* ***54****, 234001.*

hydrophobic (e.g. annealing or applying hydrophobic self-assembled molecules) and prevent water/bubbles from getting trapped between graphene and the surface which can cause wrinkles.[112,218] Whilst heating PMMA/graphene to adhere it to the substrate, strain and stress can be introduced to graphene due to the different thermal expansion coefficients of graphene and PMMA.[103] Additionally, the growth substrate for CVD is not completely flat, therefore wrinkles inevitably form during the growth process.

Often support transfer methods involve etching the growth substrate which is wasteful and is a particular issue for precious metal catalysts. An alternative method that preserves the catalyst is shown in Figure 5.3 (b), this uses an electrochemical reaction to produce H_2 bubbles at the electrode the metal/graphene is being used as. The bubbles separate the graphene from the metal, thus preserving it, however the bubbles can introduce significant wrinkling and even tearing of the graphene.[103,220,237] Another alternative to preserve the metal catalyst is the stamping method; a polydimethylsiloxane (PDMS) stamp is attached to the graphene which can then be carefully peeled directly from the metal.[238] The adhesion between graphene and Cu metal can be weakened by an oxidising pre-treatment since copper oxides bond more weakly to graphene compared to Cu^0.[239] The contact angle between graphene and the PDMS stamp has to be carefully controlled during peeling.[134] The stamping technique is considered a dry transfer as it avoids any solutions so does not introduce strain into the graphene from the high surface tension of liquid etchants.[239,240] A similar principle is used for large scale graphene production using thermal release tape (TRT). TRT is applied to the graphene, peeled away and transferred to the desired substrate, where heating it will release the graphene.[241] The process of peeling graphene will often introduce significant tears and wrinkles which limits the widespread adoption of stamping techniques.

For all support-based methods it is inevitable that the chosen support will leave some residues and contaminate the graphene being transferred. Therefore, thorough

cleaning steps are often required, but for some polymer residue it can be very difficult to completely clean the graphene without damaging it. To avoid contamination, support-free methods have been developed.[242] This involves the careful use of a frame, or an additional solvent on top of the graphene, as the growth substrate is etched away to prevent the graphene from wrinkling.[19,130,242] The lack of a rigid support means wrinkles are more likely, hence to reduce the surface tension of the liquid, IPA is mixed into the etching solution.[134] This transfer method is particularly difficult and requires a high level of skill to transfer graphene without significant tears and so is often low yield. Tears in graphene would cause a leak in a graphene membrane; a way to overcome this is to transfer MLG twice to get BLG which decreases the chance of multiple tears overlapping between the layers.[21,60,63,67,75]

For the integration of graphene into E-cells it is possible to use a thin metal film which acts as a support for transfer and is the target material to be studied, thus avoiding contamination from a polymer support. For example, the use of a Au support layer where Au is the catalyst to be studied, as seen later in this chapter. In the past Au has been used as a support particularly because common etchants for Cu and Ni do not etch Au. A thin Au layer may not provide sufficient support alone, therefore it could be used in combination with a PDMS stamp for additional rigidity, where the Au barrier would protect graphene from contamination from the PDMS.[226,243,244]

It would be best to avoid a transfer step altogether and grow graphene directly onto the desired substrate. This has been achieved previously by directly growing graphene via CVD on Ni coated grids for TEM (at 1050 °C with a benzene precursor at ambient pressure).[245] The high temperature used resulted in wrinkles in the graphene due to the difference in thermal expansion coefficients of graphene and Ni.[232] Other direct growth methods have been attempted where the catalyst (e.g. Ni[246], Cu[247] or Cu-Ni alloys[248]) is used as a sacrificial layer between graphene and the desired substrate. Often

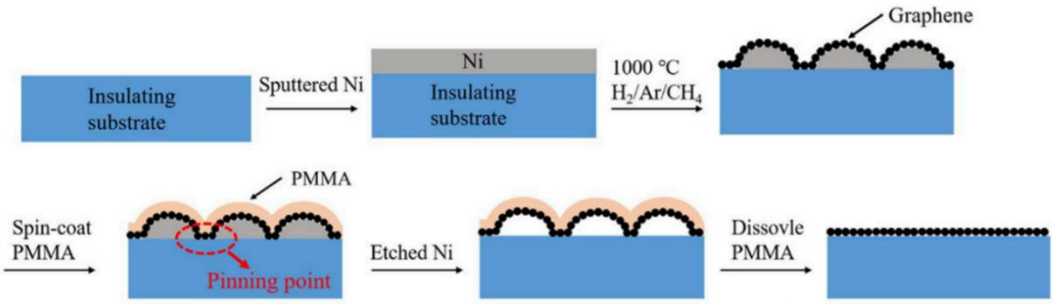


Figure 5.4: *Direct growth of graphene onto an insulating substrate using PMMA as a support and Ni as a catalyst and sacrificial layer. Taken directly from S. Xu* et al.*,* Cell Reports Phys. Sci*., 2021, **2**, 100372.*

an additional support is applied on top of graphene (e.g. PMMA), see Figure 5.4.[249] There are issues with growing directly on insulating substrates, such as very high growth temperatures, high density of defects/grains in graphene, slow growth rates, and poor uniformity.[245,250–258] Whilst there has been significant progress in direct growth methods, this has yet to be successfully applied to perforated SiN_x membranes for use in E-cells. This is because it is difficult to suspend the graphene over the holes and high growth temperatures will likely break the fragile window of the membrane.

Overall, graphene membrane manufacture has primarily relied on the graphene transfer techniques described in this section. However, the unreliable nature of graphene transfer techniques results in small leaks across the membrane window. If the graphene window is too leaky then the UHV environment outside of the cell cannot be maintained, and a differential pumping system may be required to perform XPS.[21,60] In literature so far, graphene membranes have enabled measurements up to 1.5 bar in XPS at synchrotrons which is a significant improvement on the pressures achievable with NAP-XPS alone.[57] Conventional lab-based XPS is far more accessible than synchrotron facilities and the instrumentation is cheaper than a NAP-XPS system. Furthermore, the lower photon flux compared to synchrotron sources means samples are less susceptible to beam damage.[70,259] Therefore, it would be highly beneficial to perform *in situ* XPS measurements with conventional lab-based XPS systems rather than relying on synchrotrons or NAP-XPS systems. To enable high pressure gas or liquid measurements within a conventional lab-based XPS, the reliability of producing leak-free graphene membranes must be improved.

The aim of this chapter is to improve the fabrication of graphene membranes, enabling AtmP-XPS using E-cells. An improved transfer method of graphene from Cu foils to the window of a perforated SiN_x membranes is presented. The transfer method used a 100 nm thick Au support with a PDMS frame, yielding >98% MLG coverage with

a reliability of ~95%. MLG membranes held pressures of 1 bar within a NAP-XPS system to study the changes in the oxidation state of Cu NPs. BLG membranes manufactured using a Au/PDMS support were suitably leak tight. This allowed measurements of the etching of Au in a conventional lab-based XPS using a constant flow of KI/I_2 solution – one of the first instances of using a graphene membrane for liquid-flow measurements in a conventional lab-based XPS. This transfer method shows the potential to extend XPS measurements to pressures above 1 bar at synchrotrons, as well as to perform liquid and high pressure *in situ* measurements within easy-to-access conventional lab-based XPS machines. Furthermore, a short summary of the work done to progress a direct growth method is also discussed. Although the direct growth method was not fully developed, significant steps have been made towards achieving this.

5.2 Transfer of Graphene using a Au/PDMS Support

This section outlines the transfer method which was developed to transfer graphene from a Cu foil to a perforated SiN_x membrane (Silson, 500 x 500 μm window, 200 nm thick SiN_x on Si with an area of 200 x 200 μm hexagonal array of ⌀1 μm holes) using a Au/PDMS support. XPS, SEM, and Raman were used to characterise the transferred graphene and determined that it was clean and continuous with relatively low defects.

5.2.1 Method

Figure 5.5 outlines the method to manufacture graphene membranes used in this thesis. MLG-coated Cu was purchased from Graphenea, PI-KEM (500 μm x 60 mm x 40 mm), shown in Figure 5.5 (i). 100 nm of Au was thermally evaporated onto the graphene side. The Au support protects the graphene from contamination and supports it during the transfer process. Thermal evaporation was chosen because the energy of the impinging Au atoms is low enough so that they do not damage MLG in comparison to RF magnetron sputtering.[114] Au was chosen as a metal support because it is not etched

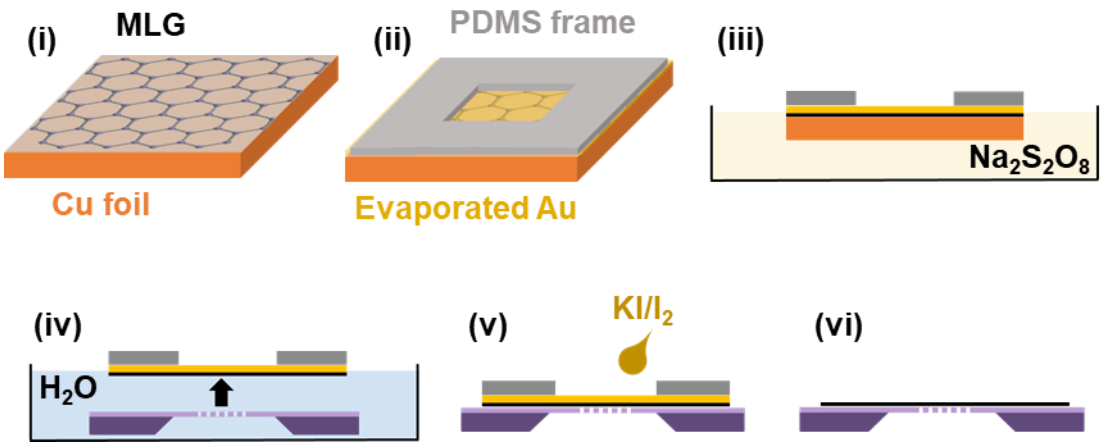


Figure 5.5: *Diagram outlining the key steps in transferring graphene from (i) Cu to (vi) a perforated SiN_x membrane. (ii) Initially 100 nm Au was evaporated onto graphene followed by applying a PDMS frame. (iii) The Cu was then etched in a $Na_2S_2O_8$ solution. (iv) To clean the graphene it was washed in a water bath after etching Cu. MLG/Au/PDMS was then scooped out using a SiN_x membrane and heated at 40°C (30 minutes) then 140°C (30 minutes). (v) The Au can be removed by etching with a KI/I_2 solution leaving MLG suspended over the holes of the membrane in (vi). The graphene membrane was finally washed with a water bath in a similar way to (iv). At step (iv) if a Cu/MLG piece was used to scoop out MLG/Au/PDMS instead and then performing steps (iii)-(vi) yielded BLG on the membrane.*

by $FeCl_3$ or $Na_2S_2O_8$ which are typical etchants used for Cu. The side without Au was cleaned with an O_2 plasma for 15 min to ensure there was no residual MLG. A thin Au support would be insufficient to prevent wrinkling alone, therefore a PDMS stamp was applied to the Au atop the Cu/MLG to minimise wrinkling and ensure graphene remained taught whilst floating on solutions. PDMS was taken from a Gel-Pak box (Agar Scientific, AGG5102-0-10).[226,238,244] The stamp had a hole punched out where the size of that hole was larger than the window of the SiN_x membrane (~⌀3 mm hole) to make a frame (Figure 5.5 (ii)).

The Cu foil was then etched by floating the Cu/MLG/Au/PDMS on a 0.1 M $Na_2S_2O_8$ solution (>98%, Thermo Scientific, 202020010) and left for ~3 hours to remove all of the Cu (Figure 5.5 (iii)).[57,260] To remove any contamination from the etchant, the MLG/Au/PDMS was then transferred to a water bath using a clean piece of Si/SiO_2 wafer and the water bath was refreshed at least three times (Figure 5.5 (iv)).

For MLG membrane manufacture the MLG/Au/PDMS was scooped out of the water using a perforated SiN_x membrane (ensuring the hole in the PDMS was aligned with the membrane window) and heated gently at 40°C for 30 minutes. This dried the surface and removed any residual water trapped between the MLG and SiN_x which would escape through the edges of the MLG/Au/PDMS and help to flatten out any wrinkles. Prior to heating, a gentle stream of Ar gas was applied to the surface to help remove large droplets of water. The membrane was then heated at 140°C to adhere the MLG/Au to the surface to go from step (iv) to (v) in Figure 5.5.[261]

For BLG, once the MLG/Au/PDMS was rinsed with water (Figure 5.5 (iv)) another Cu/MLG piece (with one side cleaned with an O_2 plasma) was used to scoop out the MLG/Au/PDMS instead of a membrane. This was annealed at 40˚C, then 140˚C. The transfer process was continued by etching the Cu once more (from Figure 5.5 (iii)) and proceeding in the same way as for MLG.

Finally, a KI/I_2 solution [4 g KI (>99%, Sigma-Aldrich, 221945) and 1 g I_2 (>99.8%, Sigma-Aldrich, 207772) stirred into 40 ml of distilled water] can be used to remove the Au film if required (Figure 5.5 (v)) followed by rinsing with water and IPA. The final result is a perforated SiN_x membrane with graphene suspended over the holes (Figure 5.5 (vi)).

5.2.2 Characterisation

To initially determine the quality and continuity of transferred MLG, Raman maps and SEM images were collected and are presented in Figure 5.6 and 5.7. The Raman maps in Figure 5.6 (a) are from MLG transferred using a Au support layer only. In comparison the SEM images in Figure 5.7 are from MLG transferred using a Au/PDMS support.

Details of Raman spectroscopy and the origin of these features are outlined in Chapter 2, the Appendix, and in reference [110]. To measure Raman spectroscopy MLG was transferred to a Si/SiO_2 piece. In Figure 5.6 (a) peaks were fitted with a single Lorentzian function to determine the FWHM (Γ_{2D}) and the peak heights. For reference, an example Raman spectrum is included in Figure 5.6 (b). Figure 5.6 (a,i) plots the variation of Γ_{2D} over ~250 × 185 μm^2 area where Γ_{2D} is consistent with MLG over most of the area with a mean value of 29.5 cm^{-1}. I_{2D}/I_G in Figure 5.6 (a,ii) is similarly uniform at ~2 for most of the area. However wrinkles and small spots are apparent where Γ_{2D} exceeds 40 cm^{-1} and there is also an increase in I_{2D}/I_G to above 3 consistent with the effects of strain and stacking of the wrinkled graphene. For the majority of the surface I_D/I_G is ≤0.05 (Figure 5.6 (a,iii)), but at the same wrinkles and spots there is an increase of I_D/I_G to above 0.2. Raman mapping confirms that the majority of the surface is defect-free MLG. The wrinkles are likely caused during the transfer process, particularly as the PDMS support was not used for this sample. The spots may relate to local contamination as well as small tears/defects, with the latter potentially leading to leaks if used to seal

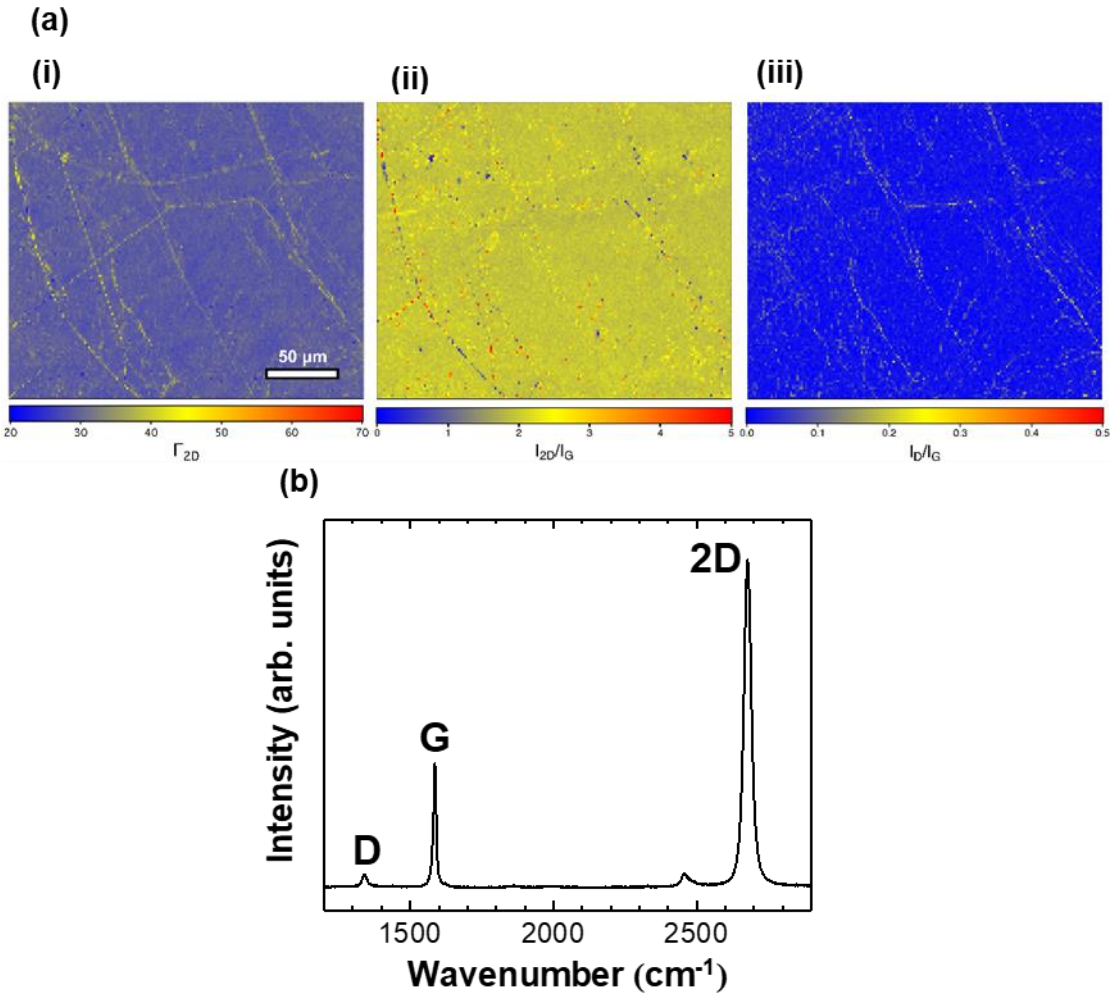


Figure 5.6: *(a) Raman maps of MLG transferred to Si/SiO_2 using a Au support layer (no PDMS), (i) Γ_{2D}, (ii) I_{2D}/I_G, (iii) I_D/I_G. (b) Raman spectrum of MLG on Si/SiO_2 transferred using a Au/PDMS support. The peaks relevant for determining quality and number of layers of graphene have been labelled: D (~1340 cm^{-1}), G (~1580 cm^{-1}), and 2D (~2680 cm^{-1}).*

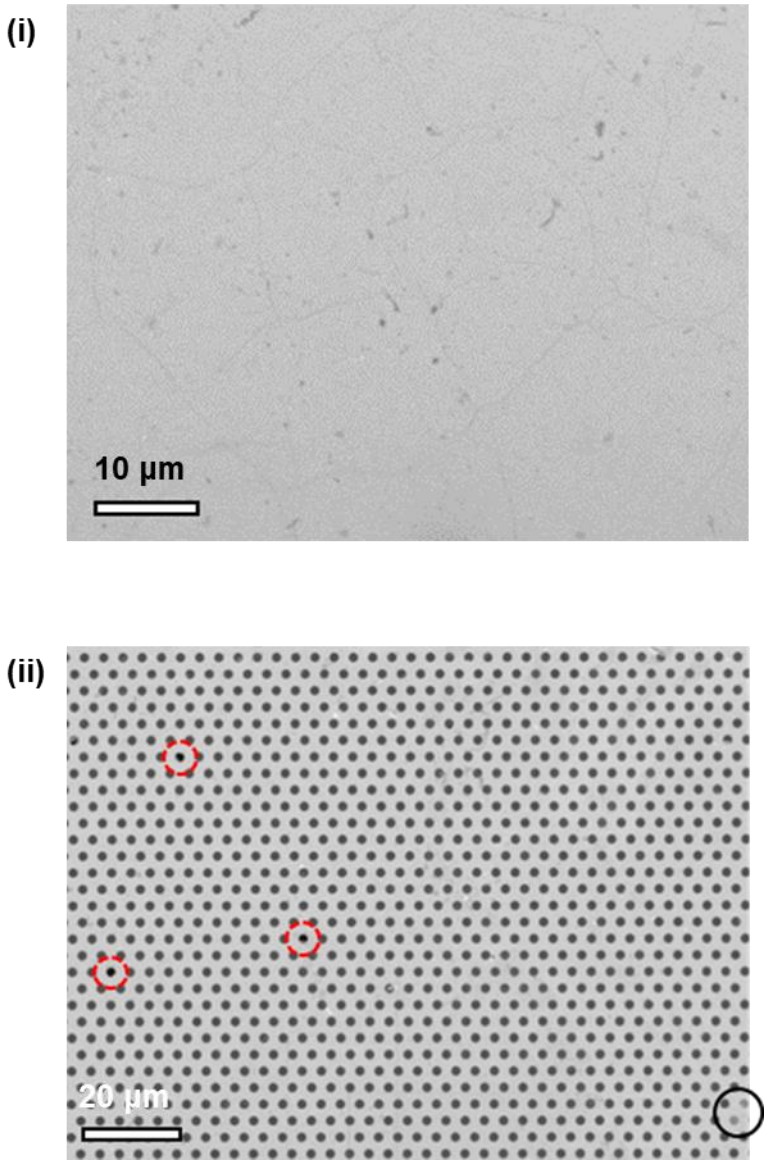


Figure 5.7: *SEM of MLG transferred to a perforated SiN_x membrane using a Au/PDMS support. (i) Area away from the window. (ii) Area of the window showing very few holes (>98% coverage). Dashed red circles indicate holes in the graphene and the black circle indicates BLG coverage.*

the E-cell. The BLG transfer approach therefore helps to minimise such leaks, as the likelihood of the tears being spatially aligned is vanishingly small.

The uniformity of MLG transferred to a perforated SiN_x membrane using a Au/PDMS support was measured using SEM (Figure 5.7). All SEM images in this chapter were collected using a Carl Zeiss EVO SEM with a tungsten electron source with a 2 kV electron beam energy. Figure 5.7 (i) shows a region away from the window which is covered in MLG, where the fine thread-like features correspond to wrinkles which are unavoidable, given the Cu foils used as templates for MLG growth are relatively rough compared to the SiN_x membrane. The dark spots are from additional graphene layers which may include residual graphene from the backside of the Cu which was not fully removed by the O_2 plasma cleaning. Figure 5.7 (ii) shows that the extent of wrinkling is sufficiently low to not significantly impact the coverage of perforations in the SiN_x window. A few holes which are not covered by MLG appear darker and are indicated by the dashed red circles, whilst the black circle indicates some holes that have BLG coverage (as shown by lower contrast with the SiN_x support). Using the image in Figure 5.7 (ii) the approximate coverage of MLG over the holes is >98% and the reliability of producing this coverage was ~95% (sample size of >50 membranes). Comparing Figure 5.6 and 5.7, using the PDMS stamp led to a visibly lower extent of wrinkling (particularly on a large scale), thus demonstrating the improvement the PDMS stamp makes to the transfer process. It was important to leave an area without support from the PDMS, as when the PDMS was removed it also removed the Au/graphene beneath it. Overall, the transferred MLG was of high-quality (low-defect) except at areas of wrinkles or pin-holes. The number of wrinkles and pin-holes was greatly reduced by using a PDMS support resulting in a highly continuous layer of graphene which could be produced reliably. The high coverage and reliability of this transfer method is a great improvement on the methods discussed in section 5.1.

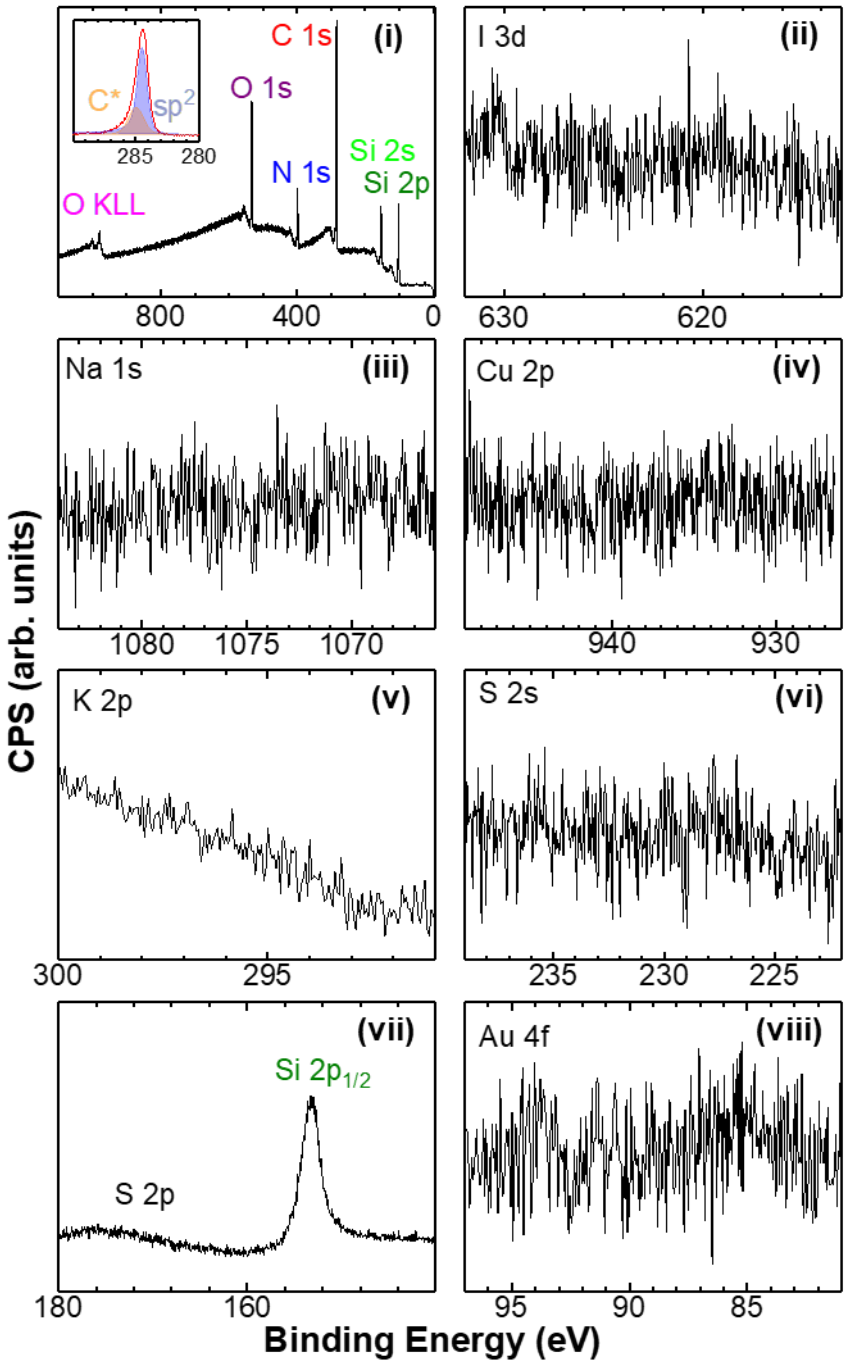


Figure 5.8: *XPS spectra of MLG on a SiN_x window after Au/PDMS support transfer with CPS on the y-axis. (i) Survey spectrum showing no additional peaks from contamination. The inset shows the C 1s region with sp^2 and contamination (C*) components fitted. (ii) - (viii) Detailed regions showing no contamination on the MLG from etching solutions (ii,iii,v,vi,vii) or residual unetched metal (iv and viii).*

Lab-based XPS of the graphene window of the same sample from SEM (Figure 5.7 (ii)) was performed to determine the level of contamination on MLG from the transfer process. XPS in Figure 5.8 was performed in Rex Richards, Oxford using a PHI VersaProbe III system, with a monochromatic Al K-α X-ray source at 1486.7 eV. Survey spectra were collected using a pass energy of 224 eV meanwhile detailed regions utilised a pass energy of 55 eV. The XPS spectra in Figure 5.8 were energy calibrated to the sp^2 peak for graphene at 284.4 eV.[57] The peaks fitted in the C 1s region are Doniach-Šunjić functions with a Shirley background subtracted. Figure 5.8 (i) shows an XPS survey spectrum to determine the extent of contamination from the transfer process. The O KLL Auger features are seen at ~507 eV (kinetic energy) and O 1s core level at 532.5 eV (binding energy) are consistent with the presence of OH and oxidised carbon species associated with exposure to atmosphere and the aqueous solutions used for transfer (see Figure A5.1). The core level peaks of N 1s at ~398 eV, Si 2s at ~153 eV, and Si 2p at ~102 eV are attributed to the SiN_x from the membrane. A strong C 1s core level peak is seen at ~284 eV, and the inset in Figure 5.8 (i) shows a higher resolution scan of this region with two fitted components. The sp^2 hybridised peak (~284.4 eV) arises from the graphene, whilst the peak at ~285.0 eV (C*) is attributed to C-H/C-O species associated with adsorbed surface contaminants e.g. (oxygenated) hydrocarbons.[57,242,262] O and C contamination is very difficult to avoid, especially considering MLG has been exposed to the atmosphere and several solutions during the transfer, but the C contamination is low relative to the sp^2 peak associated with graphene.

Detailed regions in XPS were also collected to check if other contaminants from the transfer process or metal traces from Cu or Au remained (Figure 5.8 (ii-viii)). Figure 5.8 (ii) shows the I 3d region where any iodine species after transfer is beyond the detectable limit of the lab-based XPS, indicating effective removal by thorough washing which is especially important as iodine is highly contaminating. The other relevant

regions relating to contamination from the etchant solutions are Na 1s, K 2p, and S 2s (or S 2p) in Figure 5.8. The S 2p region is very close to the Si $2p_{1/2}$ peak, therefore to confirm there is no detectable sulphur the S 2s region was also collected. The K 2p region has a steep background as this region is at a binding energy just above C 1s, which has a very strong signal from the graphene peak. The XPS spectra in Figure 5.8 (ii) - (viii) show no detectable signal (apart from Si) there is therefore insignificant contamination from the etching solutions and washing with water was sufficient. There is also no detectable residual metal left (Au or Cu) and complete etching was achieved. Hence, Figure 5.8 confirms the transfer graphene is very clean when using a Au/PDMS support. As mentioned in section 5.1, in most transfer processes it is very difficult to prevent any contamination from supports used, particularly if a polymer is used.

The characterisation shown in Figures 5.6-5.8 demonstrates that the Au/PDMS-supported transfer technique, outlined in Figure 5.5, reliably produces high-quality, continuous, and clean graphene, and so is well suited to sealing E-cells for *in situ/operando* studies. This transfer method has the reliability and continuity of other support-based techniques and the cleanliness of support-free techniques, therefore combining the best of both approaches.

5.3 Experimental Applications of Graphene Membranes

To test the capabilities of the transferred graphene to seal E-cells, two main experiments were performed to probe the solid/gas and solid/liquid interfaces. In the first instance it was simpler to test graphene's ability to seal a flowing gas since a NAP-XPS system can easily pump away small volumes of leaked gas. A more difficult task was to seal a flowing liquid within a conventional lab-based XPS system where the UHV chamber will not tolerate any leaks.

5.3.1 Solid/Gas Interface using a NAP-XPS System

A MLG membrane was made using the technique outlined in Figure 5.5. As an initial test Cu NPs were chosen as a standard system. Following graphene membrane manufacture, size-selected Cu NPs (~10 nm) were deposited onto the membrane (see Chapter 2). The graphene membrane was then used to seal an E-cell, see Chapter 3 (Figure 3.6). The graphene membrane was placed on top of a graphite gasket to seal it to the rest of the cell. Although less leak-tight than polymer O-rings, graphite gaskets allow for higher temperature heating and provide an electrical contact to the rest of the cell for EY measurements. This capability was not used in this chapter but is exploited in Chapter 6. The sample was exposed to sequential dosing of Ar, CO_2 and CO at pressures between 50 mbar and 1 bar and at room temperature. The measurements were performed using a NAP-XPS system at B07-C, Diamond Light Source, UK (SI30358-1), meaning some gas leakage through the graphite gasket was manageable. XPS data was collected using a pass energy of 20 eV and excitation energy of 1700 eV. Gases were flowed into the cell in the same way as described in Chapter 4. XPS and TEY-NEXAFS were collected to obtain surface sensitivite measurements.

Figure 5.9 (a) details the changes in oxidation state of Cu in the (a) Cu L_3-edge, and XPS regions: (b) C 1s, (c) O 1s, and (d) Cu $2p_{3/2}$ for Cu NPs exposed to sequential gases (50 mbar) at room temperature. XPS spectra in Figure 5.9 (b-d) have been normalised to the peak maximum in the relevant region and the Cu L_3-edge has been normalised to the post-edge. The Cu L_3-edge spectra have been energy calibrated to have the main peak at 933.7 eV and a linear background subtracted fitted to the pre-edge.[172] The XPS spectra were energy calibrated by setting the sp^2 peak of graphene in the C 1s region to 284.4 eV with a Shirley background subtracted. Gases were flowed to obtain a pressure of 50 mbar in the cell and dosed in the following order at room temperature: Ar, CO_2, CO.

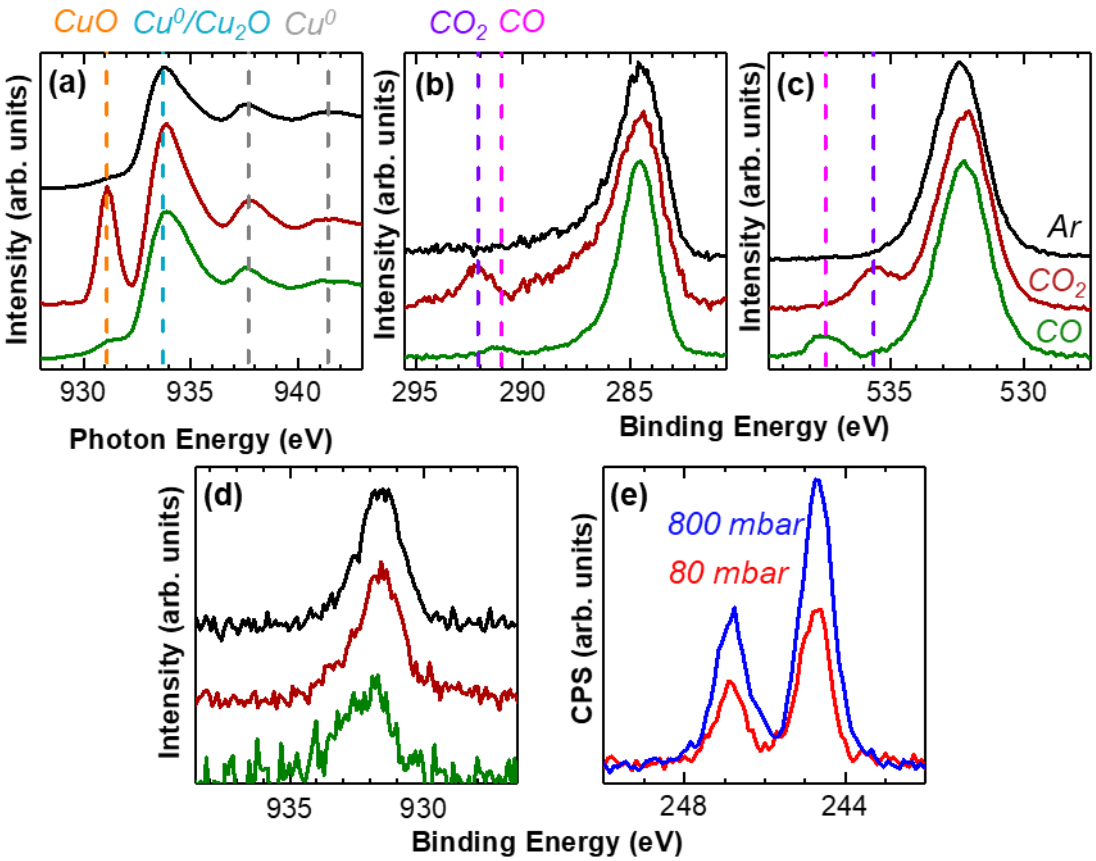


Figure 5.9: *Spectra collected from Cu NPs (~10 nm) on MLG with gas enclosed within the E-cell. (a) Cu L_3-edge, (b) C 1s, (c) O 1s, and (d) Cu $2p_{3/2}$ spectra from Cu NPs (~10 nm) exposed to Ar (black), CO_2 (red), and CO (green) at 50 mbar and room temperature. (e) Ar 2p of Ar gas flowed to obtain a pressure of 80 mbar (red) and 800 mbar (blue).*

Initially, under an Ar atmosphere the Cu L_3-edge (Figure 5.9 (a)) has an edge at 933.7 eV and additional features at 938.0 and 941.8 eV. As explained previously (in Chapter 4), the main peak at 933.7 eV is common for both Cu^0 and Cu_2O.[187] The higher photon energy features only appear for Cu^0 and the absorption edge is more step-like for Cu^0 and peak-like for Cu_2O.[96] Therefore, initially under Ar, the Cu NPs contained a mix of Cu_2O and Cu^0. The Cu NPs were exposed to atmospheric conditions prior to the experiment which would oxidise them. Exposure to the beam under vacuum (during alignment) will reduce CuO to Cu_2O, hence no CuO is seen under Ar.[57] Under Ar gas, both the C 1s and O 1s regions (Figure 5.9 (b) and (c)) show broad peaks at ~285 eV and ~532.2 eV respectively which are primarily attributed to the graphene and surface contamination on the graphene and SiN_x.

Figure 5.9 (d) shows the Cu $2p_{3/2}$ spectra during the gas composition changes, the signal is very weak. Distinguishing between Cu^0 and Cu_2O is very difficult in the Cu $2p_{3/2}$ region as they both appear at the same binding energy (~933 eV). A peak for CuO is slightly easier to distinguish due to it's slight energy shift (~933.5 eV) and appearance of a higher binding energy satellite (~942 eV). The Cu LMM region is more sensitive to Cu oxidation state changes and is therefore often preferred to identify Cu oxidation states in XPS, but the signal from Cu LMM region is even weaker than Cu $2p_{3/2}$, and not detectable in this experiment. The weak signal is attributed to the low loading from Cu NPs resulting in not enough detectable material for XPS. In Chapter 6, XPS signal from Cu/Zn NPs is easily detected when using a higher loading (with no size selection of NPs) at the ALBA synchrotron. Additionally ALBA has an order of magnitude higher photon flux at at these photon energy ranges compared to Diamond Light Source. The discussion in this chapter will hence focus on the Cu L_3-edge to identify oxidation state changes in Cu due its higher sensitivity to oxidation state compared to Cu $2p_{3/2}$.

Upon switching from Ar to CO_2 the Cu L_3-edge shows a new peak at 931.1 eV indicating CuO formation.[186–188] The higher photon energy features from Cu^0 remain, but the edge at 933.7 eV has become more peak-like in shape suggesting more Cu_2O formation. This is consistent with the CO_2 oxidising the accessible outside layer of the Cu NPs to CuO with accompanying Cu_2O formation.[62,170] Some Cu^0 is detected from the centre of the Cu NPs which is not exposed to CO_2, explaining the mixture of Cu^0, Cu_2O, and CuO seen under 50 mbar of CO_2. No change is seen in the Cu $2p_{3/2}$ region. This is unexpected as Cu $2p_{3/2}$ should have a slight peak shift to higher binding energy when CuO forms, but is not detected here because of the weak signal. A new peak also appears in the C 1s (292.1 eV) and O 1s (535.6 eV) regions which can be assigned to the gas-phase CO_2 peak.[71]

Changing the gas composition to pure CO largely removes the CuO feature from the Cu L_3-edge and causes the edge at 933.7 eV to become more step-like. CO is highly reducing so will result in mainly Cu^0 on the surface of Cu NPs. The gas-phase peaks in the C 1s and O 1s regions now appear at 291.0 eV and 537.4 eV respectively, that correspond to the gas phase peaks for CO which are shifted compared to CO_2.[71]

These measurements highlight a key-benefit of XPS, where the gas-phase and surface C and O species are well separated from each other. This is not the case for XAS, where it can be challenging to extract information on surface species in high pressure gas environments (as shown in the Appendix section for Chapter 4). Critical to the detection of these species in the C 1s and O 1s regions herein is the use of graphene windows which are transparent to the low kinetic energy photoelectrons produced by soft X-ray excitation. The photoionisation cross-section of these elements is typically too low at higher photon energies to be reliably detected with hard XPS approaches.[55] However, it is worth noting that the C 1s and O 1s signals of surface species on the NPs can potentially be obscured by peaks related to graphene and adsorbed contamination.

Careful inspection of the O 1s spectrum indicates slight energy shifts in the main broad peak upon changing between different gases. The features of Cu oxide overlap with the broad peak in the O 1s so oxidation/reduction could contribute to these shifts.[171,173,191] Furthermore, the C 1s binding energy of graphene (used here for energy calibration) can vary due to charge transfer doping by the Cu NPs depending on their chemical state, thus can shift the apparent position of the O 1s peaks.[57] Also, a significant portion of the C and O signals likely arise from contamination on the vacuum side of the SiN_x window. These shifts may instead reflect small changes in charge-dissipation of species on the insulating SiN_x.

To test the pressure capabilities of the suspended MLG the gas composition was switched back to Ar and the pressure gradually increased. Figure 5.9 (e) shows the Ar 2p peaks at 80 mbar and 800 mbar, without additional normalisation, with the energy calibrated by setting the gas-phase peak for Ar $2p_{3/2}$ to 244.7 eV and a Shirley background subtracted.[263] The intensity of the Ar 2p peak at 800 mbar is nearly double that when the pressure is 80 mbar, confirming the greater pressure present in the cell. The pressure in the E-cell was further increased to 1 bar with the vacuum chamber pressure remaining at ~$5x10^{-2}$ mbar, whereas under 50 mbar in the E-cell the pressure of the vacuum chamber was ~$1x10^{-2}$ mbar. The pressure and signal increase are not directly proportional as a larger pressure in the cell will increase the scattering of photoelectrons. To perform conventional lab-based XPS gas-phase measurements, leakage through the graphite gasket could be reduced by using Viton O-rings (if heating is not required) or another sealing method. Leakage across the window could also be reduced by using BLG rather than MLG.

5.3.2 Solid/Liquid Interface using a Conventional Lab-based XPS System

Following the success of the gas-phase experiments there was clear scope to extend *in situ* measurements to the solid/liquid interface in a conventional lab-based

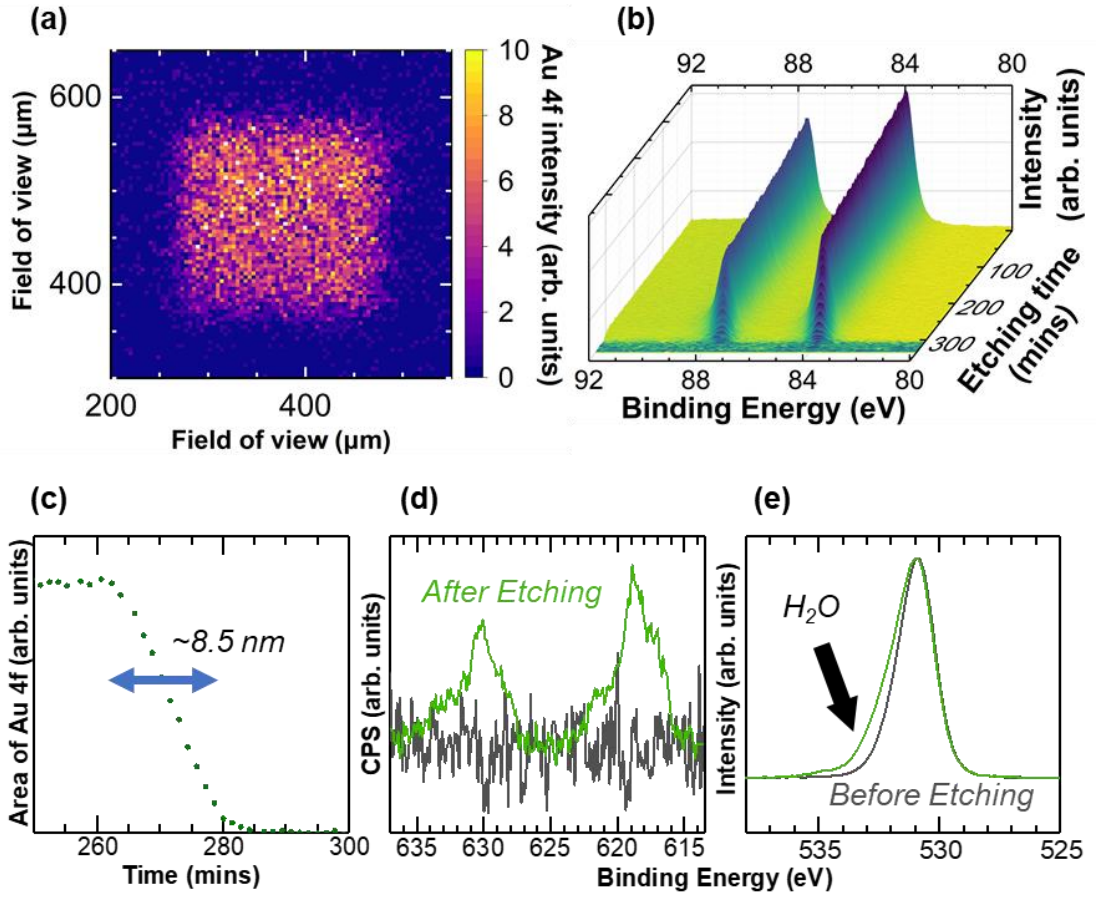


Figure 5.10: *(a) XPS map of the Au 4f signal at 84.0 eV (peak energy after charge calibration) of the SiN_x window covered in Au/BLG. (b) Au 4f region varying over time whilst Au is etched with a KI/I_2 solution. Peak positions have been energy calibrated with the Au $4f_{7/2}$ peak at 84.0 eV. (c) A plot of the area of Au 4f peaks varying over time showing the etching of the final ~8.5 nm of Au. (d) I 3d and (e) O 1s XPS regions comparing before (grey) and after (green) etching the Au with water and KI/I_2 solution flowing through the cell respectively.*

system. A conventional lab-based system will not tolerate the extent of leaking seen in the gas-phase experiment and it is likely that a leak from the liquid will cause complete rupture in the graphene membrane. To minimise the risk of leak/rupture two changes were made; BLG was transferred to the SiN_x window, and a different cell design was used which incorporated Viton O-rings. The consecutive graphene layers in BLG minimise the potential of overlapping tears or pinholes, therefore increase the leak-tightness of the window. A PEEK cell (Figure 3.7) with a Viton O-ring incorporated was used (no heater included). The aim of the experiment was to measure the gradual etching of the Au support layer using a KI/I_2 solution in a conventional lab-based XPS system. After etching was complete, suspended BLG was left over the SiN_x window, through which liquids in the cell can continue to be measured.

The conventional lab-based XPS experiments were performed at the Research Complex at Harwell using a Kratos XPS system. Data was acquired using a Kratos Axis SUPRA using monochromated Al K-α (1486.69 eV) X-rays at 15 mA emission. Detailed region scans were obtained individually with a pass energy of 40 eV. Charge neutralisation was achieved using an electron flood gun. All spectra collected in Figure 5.10 were calibrated to the Au $4f_{7/2}$ peak position of 84.0 eV. XPS map of Au 4f was collected by recording the peak signal in the 77-94 eV range across the surface of the sample. The graphene membrane was prepared by transferring BLG (using the method outlined in Figure 5.5). The Au support layer (100 nm) was not removed as Au was required for the experiment. XPS data in Figure 5.10 has a Shirley background subtracted and the only spectra normalised are in Figure 5.10 (e) using peak heights.

Alignment to the suspended Au/BLG region was achieved by spatially mapping the signal intensity from the Au 4f region (at a fixed binding energy of 84.0 eV, following energy calibration) as shown in Figure 5.10 (a). The presence of Au from the transfer process resulted in a rapid alignment to the graphene window which can otherwise be a

time-consuming task. Following this, distilled water was flowed (1.4 ml/min) into the cell for preliminary testing, with the XPS analysis chamber pressure remaining at ~$3x10^{-7}$ mbar. This chamber pressure is higher than expected for a conventional lab-based XPS system (~10^{-9} mbar) due to the degassing of various components of the flow cell which were not baked prior to introduction into the XPS chamber. The water was then replaced with a Au etching solution: KI/I_2 (0.1 g of KI, 0.025 g of I_2 in 1 L of distilled water).[264,265] Figure 5.10 (b) shows the change in the Au 4f signal over time whilst etching solution was passed through the cell, with energy corrected to the Au $4f_{7/2}$ peak at 84.0 eV. The correction required is found to vary over time, which is likely a result of variations in charging as the cell is not in electrical contact with the spectrometer. The FWHM of the Au 4f peaks did not vary throughout the experiments suggesting no intermediate species were detected. The detection of oxidised Au species was not expected since the etching solution is very dilute; any oxidised Au ions will rapidly dissolve into the solution and be moved away from the X-ray spot by the flow.

During the first ~260 minutes there is a gradual linear decrease in the Au 4f signal with time, attributed to the accumulation of carbon species on the BLG surface due to the relatively high base pressure. A sharper decrease is then observed over ~25 mins until the signal is beyond the detectable limit of XPS, as shown more clearly in Figure 5.10 (c) where the Au 4f peak area is plotted for the final 50 minutes of the experiment. Since the XPS probing depth (5 x IMFP, for ~99.3% of the signal) for Au is ~8.5 nm at this kinetic energy (IMFP ~ 1.7 nm for 1403 eV electrons), no change in the Au signal is expected until the last ~8.5 nm of Au is reached.[34] Considering the final ~8.5 nm takes ~25 minutes to fully etch, this would suggest a rate of ~0.35 nm/min, assuming uniform etching across the Au surface. Therefore, 100 nm should take ~285 minutes, in good agreement with the total time taken for complete etching following the introduction of the Au etchant.

Figure 5.10 (d) and (e) compare the I 3d and O 1s regions respectively before and after the Au film was etched. Note that the cell is filled with water for the pre-etching measurements, whereas post-etching the Au etching solution continued to flow during XPS characterisation, with the chamber pressure remaining at ~$3x10^{-7}$ mbar. In Figure 5.10 (d), prior to etching there is no iodine signal detected, whereas after etching there is a clear iodine signal attributed to the solution beneath the BLG. The I 3d signal shows features of multiple chemical species, most likely as a result of simultaneous detection of I^- and I_3^- ions from the KI/I_2 solution, as well as contributions from species that have precipitated at graphene defects where water may rapidly evaporate into the vacuum chamber.[266–270] *Ex situ* measurements confirm that all of these species can be effectively removed with thorough rinsing in water (see Figure 5.8 (ii)).

In Figure 5.10 (e) both spectra contain a significant contribution at ~530.9 eV, in the O 1s region associated with contamination on the BLG surface such as OH or oxidised carbon species. The O 1s signal post Au etching shows a high binding energy shoulder around ~533 eV, which is tentatively assigned to the liquid-phase water in the cell. The binding energy of water is 538.1 eV relative to the vacuum level from liquid-jet experiments.[271,272] Whereas, the binding energies in Figure 5.10 are referenced to the Fermi level of graphene. The difference between the Fermi and vacuum level is, by definition, the work function of a material.[81] This implies a work function of the Au-BLG membrane of ~5 eV. This is comparable to the work function estimated from previous studies of gas-phase species behind Au-MLG membranes.[57] The difference in binding energy values for water is from reference energy convention and not a physical effect.[81] To be confident that this shoulder is due to water, the ratio of O/Si, O/N, and Si/N before and after etching was calculated (Table 5.11). The atomic ratios were determined from the peak areas after subtracting a Shirley background and accounting for the appropriate relative sensitivity factors (RSFs). The Si/N ratio increased by 1.3%, while the O/Si ratio

	O/Si	*O/N*	*Si/N*
Before Etching	0.49	1.16	2.38
After Etching	0.53	1.25	2.41
Percentage Difference (%)	8.2	7.8	1.3

Table 5.11: *Table showing the ratio of O, Si, and N peak areas to confirm the presence of water in XPS.*

increased by 8.2% and the O/N ratio by 7.8%. This confirms a notable increase in the relative O 1s signal attributed to water being detected behind the BLG.

Overall, Figure 5.10 shows the successful measurements of a graphene encapsulated flowing liquid in a conventional lab-based XPS system. This is the first instance of graphene windows successfully encasing a flowing liquid in a conventional lab-based XPS. Signals from both solute and solvent were recorded through the graphene window whilst the pressure of the vacuum chamber remained at ~$3x10^{-7}$ mbar with no significant increase observed whilst the Au was etched. Given the higher base pressure than typical XPS operating pressures (~10^{-9} mbar), a build-up of contamination was observed over the relatively long measurement period.

5.4 Direct Growth of Graphene onto a Perforated Silicon Nitride Membrane

The Au/PDMS transfer technique was highly successful, but it required a high level of experimental skill and therefore could produce inconsistent results depending on the ability of the person performing the transfer. This section summarises the attempts at developing a method to directly grow graphene onto a perforated SiN_x membrane support which could lower the variability seen with transfer methods and result in much more reliable graphene membrane fabrication. A more detailed analysis of the results from this part of the project is shown in the Appendix for completeness. Figure 5.12 outlines the general method to achieve direct growth of graphene: (i) starting off with a perforated SiN_x membrane; (ii) a catalyst for CVD must be suspended over the holes (e.g. Ni); (iii) following this graphene can be grown via CVD; (iv) finally, the metal catalyst is etched through the holes (herein “holes” will always refer to the holes of a perforated SiN_x membrane) in the membrane to leave only graphene suspended over the holes.

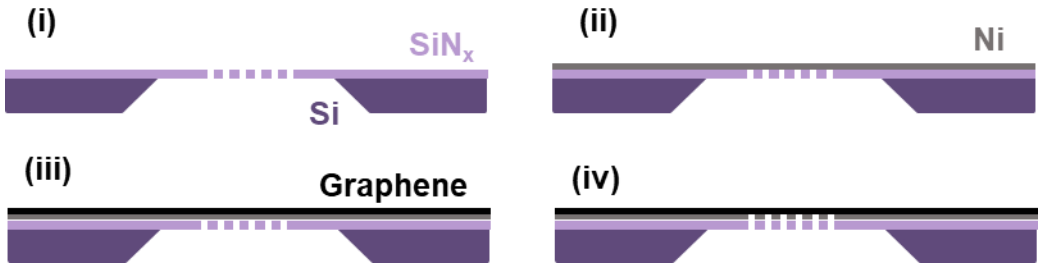


Figure 5.12: *Schematic of method outlining direct growth of graphene over: (i) a perforated SiN_x support. (ii) Initially suspend a catalyst film (Ni) over the holes of the membrane. (iii) Then grow graphene by CVD. (iv) Finally the catalyst can be etched through the holes to leave suspended graphene.*

Ni was chosen as the catalyst film to suspend over the holes since graphene growth via CVD on Ni can be performed at lower temperatures (450-600°C) compared to Cu (850-1000°C).[220,273] Even though the quality of graphene grown on Ni at low temperatures is often lower than on Cu at 1000°C, it is more important that the graphene grown is continuous in order to seal an E-cell.[274] A lower temperature is more desirable as the fragile SiN_x window is likely to break at higher temperatures due to the difference in thermal expansion coefficients between SiN_x and Ni.

A Ni film was successfully suspended over the holes of the SiN_x membrane. The method involved filling the holes in the membrane with poly vinyl (alcohol) (PVA) solution where the membrane was pressed against a small piece of PDMS. By filling the holes a flat surface was created to deposit Ni onto by RF magnetron sputtering. Alternatively, Ni could be directly deposited onto a SiN_x membrane with partially etched holes, but removing the SiN_x underneath the Ni would be difficult.

Growth of graphene by CVD presented an unexpected challenge. The custom-built CVD chamber (see Figure A2.5 in the Appendix) was new at the start of this project and required substantial optimisation. One problem was the over-heating of the sealing Viton O-ring of the CVD chamber, resulting in carbon deposition even when annealing substrates in vacuum. Consequently, it took quite some time to optimise the growth conditions to produce continuous graphene on $Si/SiO_2/Ni$ (with varying Ni film thicknesses) using ethylene (C_2H_4) as a precursor at ~650°C.

Another problem was that, even at a relatively low growth temperature of ~650°C, the Ni suspended SiN_x membranes would consistently break. Therefore, a lower growth temperature was required to avoid this. However, graphene would not grow from ethylene gas below 650°C due to the minimum energy required to dissociate C=C bonds in ethylene. Hence, an alternative carbon precursor was used: acetylene (C_2H_2). The carbon precursor change was accompanied by a new CVD chamber which avoided the

over-heating issues from the previous design; these changes required repeating the optimisation for graphene growth over $Si/SiO_2/Ni$.

Finally, a recipe for graphene growth by CVD at ~550°C was achieved. A small air leak was intentionally introduced in the chamber during annealing to aid the removal of carbon in the bulk of the Ni film. Ni suspended SiN_x membranes did not break at ~550°C and there was some success at growing graphene on these membranes. However, the suspended Ni was unstable for long growth periods where the conditions used to deposit the Ni greatly affected the stability and flatness of the Ni film. A high deposition power resulted in a film with a high degree of stress, which cracked during growth. To decrease the stress a lower deposition power was tested, but films were too rough.

There was insufficient time in the project to develop the technique further. In summary, the unresolved issues are:

- Finding the balance between roughness and stability of a thin Ni film by optimising the deposition conditions. If the power is too high then the film is unstable, but if it is too low then the Ni film is too rough.
- Further optimising CVD growth with C_2H_2 to get a continuous graphene film and reduce the defect level without increasing the temperature of growth.
- Determine a method to remove the suspended Ni (or SiN_x for partially etched membranes) without damaging the graphene.

5.5 Conclusion

The successful transfer of MLG and BLG was achieved using a Au/PDMS support to reliably produce continuous, high-quality and contamination-free suspended graphene over a perforated SiN_x membrane. BLG sealed a flowing liquid for conventional

lab-based XPS and MLG sealed a gas within a NAP-XPS system (up to 1 bar). The measurements presented here suggest XPS could be performed well above 1 bar (particularly with BLG) in a NAP system and that XPS of gas under 1 bar in a conventional lab-based system will be possible in the near future. In Chapter 6, the same graphene membranes are utilised to perform NEXAFS and XPS at 1 bar over a long measurement period within a NAP-XPS system. The application of graphene-sealed E-cells has been an outstanding challenge for *in situ* soft XPS measurements and the work presented here shows a great deal of progress towards making *in situ* XPS more accessible.

To mitigate the need to develop skills to transfer graphene using the Au/PDMS method, there was an attempt to develop a method to directly grow graphene onto a perforated SiN_x membrane. A thin Ni film was successfully suspended over the holes of the window, however a significant amount of time was spent troubleshooting issues with the CVD chamber, the growth temperature, and the roughness and stress in deposited Ni films. Hence, the rest of this thesis uses the Au/PDMS transfer technique to produce graphene membranes. The work completed for a direct graphene growth method showed promising signs and there is scope to continue working towards directly growing graphene on SiN_x membranes. Overall, the time consuming task of optimising CVD growth conditions was unexpected, even though CVD of graphene over Ni is relatively well understood. The difficulties experienced here show how tricky it can be to reproduce results in literature with a custom-built system.

Chapter 6: Investigating the Behaviour of Zn during CO_2 Hydrogenation on Cu/Zn Nanoparticles at Atmospheric Pressure

This chapter investigates the behaviour of Cu and Zn NPs relevant to the hydrogenation of CO_2. Development of the Cu/ZnO catalyst for CO_2 hydrogenation is crucial for its large-scale application and the impact it could have on reducing global CO_2 output. Understanding the catalyst is greatly improved by studying this reaction at as close to industrial conditions as possible. The experiments presented in this chapter are very similar to those in Chapter 4, where a Cu film was used, but the inclusion of Zn and the use of NPs in this chapter makes the catalyst more representative of what is used industrially. Following the reliable synthesis of graphene membranes in Chapter 5, they can now be used alongside an improved E-cell design to perform high pressure NEXAFS and XPS at 1 bar during extended measurement times. This combination of X-ray spectroscopic techniques provides detailed information about the changes to the chemical state of Cu and Zn during the reaction. *Ex situ* STEM-EELS images were also collected to complement the X-ray spectroscopy data.

NAP-XPS data was collected with help from: Ashley Head, and Youngseok Yu. AtmP-XPS and AtmP-NEXAFS was collected alongside: Joshua Gibson, Peixi Cong, Boruch Epstein, and Robert Weatherup. The reference X-ray spectroscopy data used to identify features in the Zn L-edge (as shown in the Appendix) were collected by Virginia Pérez Dieste at the CIRCE beamline at ALBA synchrotron, Spain, on my behalf.[78]

6.1 Introduction

Optimising the catalyst for the hydrogenation of CO_2 is important in converting harmful emissions of CO_2 into useful products e.g. methanol. Chapter 4 discussed the

CO_2 hydrogenation reaction in greater detail and focused on a pure Cu catalyst. The common industrial catalyst is Cu/ZnO/Al_2O_3 (Cu:Zn, 7:3) where the CO_2 hydrogenation reaction is believed to mainly proceed via the formate pathway.[11,144,279,145,162,167,209,275–278] The inclusion of ZnO is known to increase the activity and selectivity of the catalyst compared to Cu alone, but the exact role of ZnO as a promoter is still a topic of much debate in literature.[10,11,24,142–145,276,280,281] Al_2O_3 is believed to mainly act as a support and prevent the sintering of Cu and ZnO particles, however there is some evidence that Al_2O_3 may have another role within the mechanism particularly as different supports (e.g. SiO_2, CeO_2) affect the catalysts' activity and selectivity.[10,13,14,144,145,210,276,282]

The extensive literature on ZnO as a promoter for Cu cannot be covered in detail here, but some of the suggested roles include: ZnO acting as a spacer to increase the surface area of Cu NPs available[283]; partially reduced ZnO with O vacancies (ZnO_x) forming overlayers on Cu NPs resulting in electronic promotion of activity[17,275,284]; migration of Zn into Cu to form a Cu^0/Zn^0 alloy as an active site[209,275,285,286]; the Cu/ZnO interface providing an active site for the reaction[162]; or Cu steps decorated with Zn atoms providing an active site [152,210,275]. The interaction between Cu and ZnO is often described as "synergy" between them, with previous studies probing what conditions yield the greatest degree of synergy, which has been used to explain effects such as the preference for ZnO_x to form overlayers on Cu upon partial reduction of ZnO.[17,152,289–292,275–277,280,284,286–288] The preference for ZnO_x to form overlayers is due to the strong metal-support interaction (SMSI) between Cu and ZnO, as shown in Figure 6.1.[143,277,284] A common result upon which most literature agrees is that the reduction of ZnO is crucial to form the relevant active site during the *in situ* activation step in H_2 (which occurs before exposing the catalyst to reaction conditions).[287,292] However, the exact nature of the active site still remains unclear.[143,275]

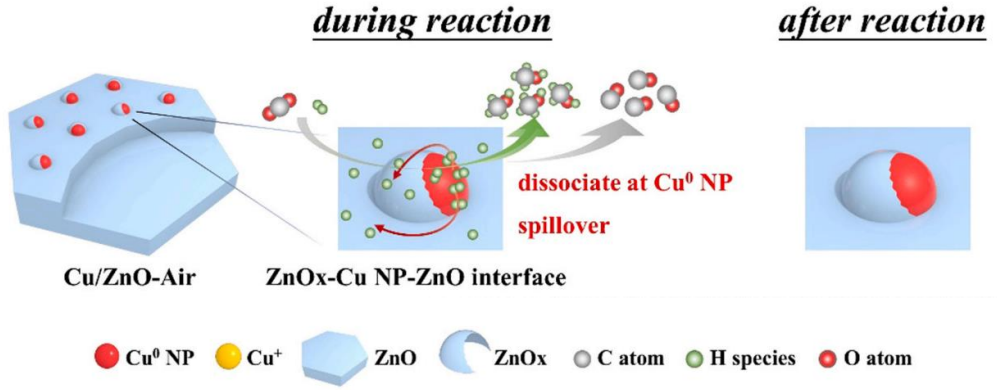


Figure 6.1: *Schematic showing that under reaction conditions a ZnO_x overlayer can form over Cu NPs due to the SMSI. H_2 dissociates at Cu^0 which can spillover to ZnO_x where CO_2 is hydrogenated to give the reaction products. Taken from Z. Chen* et al.*,* Appl. Catal. B Environ.*, 2024, **340**, 123192.*

A large source of inconsistency are the conditions and methods used to study the Cu/ZnO catalyst which provide a different degree of surface sensitivity, and sensitivity to oxidation state and local environment.[17] It is very important to study the catalyst under working conditions, but there is often a trade-off between studying the catalyst at realistic high pressures and the surface sensitivity of measurements.[11,12,95,287,293] The pressure of the gas, as well as the composition, is important as it will affect how oxidising or reducing the gas is. Hence, pressure and composition of the gas will greatly influence the chemical state and structure of the catalyst which is a source of the inconsistency seen in literature.[145,287,294] For example, the pressure of the gas will affect the degree to which ZnO is reduced to either metallic Zn (Zn^0) or ZnO_x, with pressures in excess of 1 bar of H_2 typically needed to reduce ZnO.[11,17,145,284] How reducing the gas is will, therefore, affect whether Cu^0/ZnO_x or Cu^0/Zn^0 species are present; there is much debate over which species is the source of increased catalytic activity. Cu^0/Zn^0 alloy is favoured by reducing conditions, whereas Cu^0/ZnO_x sites are thought to be favoured by more oxidising conditions.[14] Furthermore, a highly oxidising environment can destroy the synergy between Cu and Zn and create segregated phases of CuO and ZnO.[287,295] The loss of Cu^0 sites under oxidising conditions would decrease the activity of the catalyst since Cu^0 is thought to be a crucial part of the active site for this reaction.[276,287] Results in Chapter 4 demonstrated that Cu^0 sites could be maintained in a more reducing environment through the addition of CO, for a pure Cu catalyst.[71] The significant influence of gas composition on the catalyst motivated the high pressure study performed in this chapter where the relative amounts of H_2 and CO_2 were carefully controlled to investigate the influence this had on the catalyst.

The preference of H_2 or CO_2 to bond and dissociate on Cu or Zn is heavily affected by the oxidation state of each species and hence, the composition of the gas. CO_2 can bind strongly to Zn^0 and ZnO_x and dissociate over these sites, where the

presence of O vacancies stabilises CO_2 and intermediates that form (e.g. the formate intermediate will lose an O atom during hydrogenation which can occupy the vacancies in ZnO_x).[11,14,296–298] If only ZnO is present, then CO_2 may preferentially bond to Cu^0 instead.[276] Hence, once the Zn^0/ZnO_x sites are completely oxidised, then Cu^0 sites will become oxidised too. In comparison, H_2 dissociation occurs preferentially over Cu^0 sites to create active H* species which can take part in the reaction, or can spillover to ZnO and reduce it (Figure 6.1).[167,277,290] ZnO is sometimes referred to as a H* reservoir which can result in reverse spillover of H* back to oxidised Cu sites to recover Cu^0 and can take part in the reaction. If the catalyst is heavily oxidised then heterolytic dissociation of H_2 (into H^+ and H^-) over ZnO rather than CuO/Cu_2O can occur.[277] The heterolytically-dissociated H species are thought to be less active for hydrogenation but can still aid the reduction of oxidised Cu species.[276,277]

Soft XAS is a valuable tool to study the oxidation state changes in a surface sensitive manner. The application of *operando* XAS has mainly been limited to bulk-sensitive hard X-ray regions to perform measurements of pressures up to 40 bar.[209,210,299] The high pressures achieved make these measurements representative of industrial conditions, but do not yield the desirable surface sensitivity for studying heterogeneous catalysis. Zabilskiy *et al.* observed the formation of a Cu^0/Zn^0 alloy under a H_2 pre-treatment which oxidises to ZnO and Zn formate (Cu^0 is unchanged) under reaction conditions, and hence suggested Zn formate to be a crucial intermediate.[209] Other studies have also correlated the degree of Cu^0/Zn^0 alloying to the activity of the catalyst.[143] However, when performing further high pressure XAS measurements, Zabilskiy *et al.* demonstrated that the Cu^0/Zn^0 alloy is not important for a high activity.[299] Instead, the interplay between Cu and Zn oxides is important, especially since the Cu^0/Zn^0 alloy is thought to be oxidised upon the introduction of CO_2.[279,285,286,294,299,300] Other high pressure XAS studies have demonstrated a support-dependent (e.g. Cu/ZnO

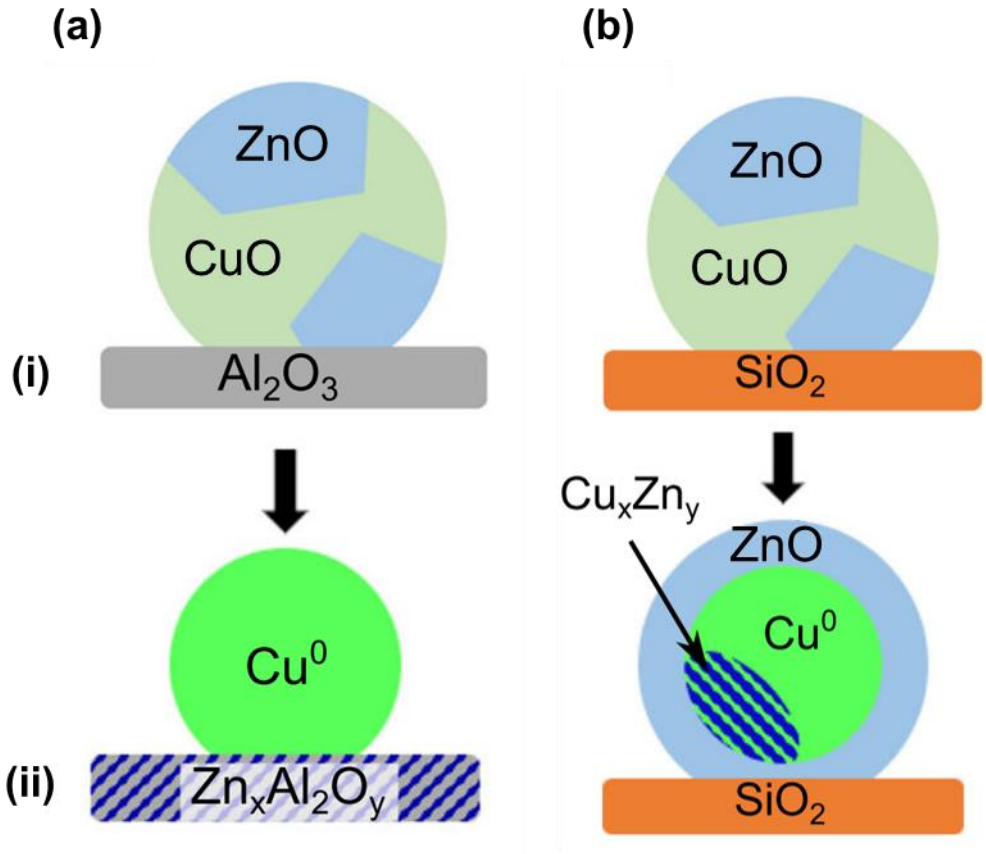


Figure 6.2: *Schematic showing (i) as-received $Cu_{70}Zn_{30}$ NPs supported on (a) Al_2O_3 and (b) SiO_2. There is initially segregation between different metal elements. (ii) Rearrangement and change in oxidation state following exposure to reaction conditions (H_2+CO_2, 220°C): (a) Cu^0 NPs atop Zn incorporated into the aluminium oxide support, (b) Zn incorporates into the Cu^0 NP to obtain regions of alloying with an oxidised Zn overlayer atop SiO_2. (a) and (b) Adapted from N. J. Divins* et al.*,* Nat. Commun.*, 2021, **12**, 1435.*

on Al_2O_3 vs on SiO_2) behaviour where some Cu^0/Zn^0 alloy may be present alongside ZnO_x species under reaction conditions (Figure 6.2).[210] Therefore, it is difficult to be conclusive as to which species are important or even present under reaction conditions, where the same technique (at representative industrial pressures) can show different results.

XPS has traditionally been used for more surface sensitive measurements at lower pressures. Amann *et al.* performed grazing incidence hard XPS of the Cu(211)/Zn/ZnO model catalyst at pressures up to 500 mbar.[55] They did not use the Zn 2p region to measure oxidation state changes since it undergoes very small shifts (<1 eV) between Zn^0 and ZnO. They could not use the Zn LMM region either since the signal strength was too low through the high gas pressure.[301,302] Identification of Zn's oxidation state was therefore challenging and the Zn 3d region was used, but the signal was very noisy. CO was determined to be crucial for maintaining some amount of Cu^0/Zn^0 alloy whilst a CO_2-rich environment will favour more ZnO.[55,275,294,303] This further emphasises the changes in species observed with gas composition, but these findings would greatly benefit from performing measurements at higher pressures and with improved signal-to-noise ratio.[17]

The results presented in this chapter probe the oxidation state and speciation of Zn and Cu to determine the species present under different reaction conditions. A sequential gas dosing study using $H_2/CO_2/CO$ mixtures was performed (similar to Chapter 4) over $Cu_{70}Zn_{30}$ NPs, which is a representative ratio of Cu:Zn used in the industrial catalyst.[145] Herein, for simplicity, $Cu_{70}Zn_{30}$ is referred to as brass. A combination of surface sensitive AtmP-XPS and AtmP-NEXAFS using soft X-rays at 1 bar provided extensive detail on the oxidation state and local environment. *Ex situ* STEM-EELS images were also collected to show the structural changes in the NPs. Under reaction conditions, the NPs contain a mixture of Cu^0/Zn^0 alloy with a ZnO_x overlayer

where the amount of this structure is increased by using a H_2 pre-treatment or through the addition of CO. If an oxidising pre-treatment is used, then under reaction conditions there is a completely different structure including Cu^0 which strongly interacts with ZnO_x, and there is no Zn^0 present. These results would be greatly enhanced by performing some catalytic activity tests using different pre-treatments and gas mixtures.

6.2 Brief Overview of Methods

NAP-XPS measurements were performed at the Center for Functional Nanomaterials at Brookhaven National Lab using a lab-based system from SPECS Surface Nano Analysis GmbH, with a PHIOBOS 150 NAP hemispherical analyser and monochromated Al K-α X-ray source (1486.7 eV). A brass foil (Alfa Aesar, 1 mm, 45221) was used for NAP-XPS measurements. The sample was heated using a laser and gases were dosed into the analysis chamber using manual leak valves. The brass surface was prepared using cycles of Ar^+ sputtering (1.5 kV) and annealing (200-250°C) until the AES spectra of Cu and Zn showed only metallic features. High resolution spectra of Zn 2p, Cu 2p, O 1s, C 1s, and AES spectra of Cu and Zn (Cu LMM and Zn LMM) were collected using a pass energy of 20 eV. The energy was calibrated using the Cu^0 peak at 932.6 eV in the Cu 2p spectra, where Cu_2O shows negligible shift in binding energy and CuO contains an additional peak at ~933.8 eV (the Cu $2p_{3/2}$ region was fitted with Doniach-Šunjić peaks). All NAP-XPS data has a Shirley background subtracted and is normalised to the peak heights. Following energy calibration, the Cu LMM region was fitted in the same way as in Chapter 4, using parameters from reference [171]. The Zn LMM region was not fitted as there was not sufficient literature for ZnO, Zn^0, and particularly ZnO_x to enable a meaningful fit, therefore conclusions were drawn based on peak position.

AtmP-XPS and AtmP-NEXAFS measurements were performed using the E-cell design shown in Figure 3.6. The E-cell was sealed with a graphene membrane. MLG was transferred to a perforated SiN_x membrane (500 x 500 μm, 200 nm thick, an array

of ⌀1 μm holes arranged in a hexagonal grid at a pitch of 2μm, Silson[128]) using the Au/PDMS transfer technique outlined in Chapter 5. The pressure of the cell was maintained at 1 bar and the flow of gases was controlled using MFCs. The cell was heated using a graphite heater. Brass NPs were deposited onto graphene membranes with no size selection imposed (~5-20 nm) and with a deposition time of ~30 minutes. Brass NPs provided a more realistic catalytic system compared to the brass foil due to their increased surface-to-volume ratio. Brass NPs were not used for NAP-XPS due to the low signal strength from a conventional lab-based X-ray source, whereas the higher photon flux at synchrotrons provided sufficient signal strength to detect changes in the brass NPs. The brass NPs underwent no treatment prior to data collection.

AtmP-XPS was performed at the CIRCE beamline at the ALBA synchrotron, Spain (2022097065-rweatherup).[78] XPS and TEY-NEXAFS were collected through the analyser cone owing to the electron transparency of graphene. The regions collected were: Zn 2p, Cu 2p, O 1s, C 1s, Cu LMM, Zn LMM, and the Cu L_3-edge, using X-ray photon energies in the 850-1500 eV range. The photon energy for core-level regions was selected to maintain a constant kinetic energy range and the photon energy used for AES regions was optimised for signal strength, and the same pass energy (20 eV) was used for all regions. Unfortunately, the degree of charging observed for Zn 2p and Cu 2p was different to Cu LMM and Zn LMM regions, so the core levels could not be used for energy calibration. The C 1s and O 1s regions were dominated by the graphene signal and contamination from the SiN_x membrane, therefore were also not used for energy calibration; this is a disadvantage with probing through the graphene membrane since overlapping species in the C 1s and O 1s regions makes determining the adsorbed species challenging. Energy calibration was, therefore, performed using the Cu LMM and the same shift was applied to Zn LMM. This is not ideal, as the Cu LMM is expected to change during the reaction. Cu^0 was identified in the Cu LMM region when a main

peak and shoulder peak were present with a 3 eV separation, which is not observed for Cu_2O or CuO, and in this case the main peak was set to 918.6 eV (kinetic energy).[77] If Cu^0 was oxidised and the shape of the Cu LMM changed, the collected Cu L_3-edge was used to determine the oxidation state, where the peak in the Cu LMM region was calibrated to a position of 917.7 eV for CuO and 916.6 eV for Cu_2O.[304,305] A Shirley background was subtracted from XPS data and normalised to peak intensities. The Cu LMM region was fitted after energy calibration in the same way as for NAP-XPS, which confirmed the assignment of the Cu oxidation state and showed any minor contributions from other oxidation states. The Cu L_3-edge was treated in the same manner as the AtmP-NEXAFS data (detailed below).

AtmP-NEXAFS data was collected at the B07-C beamline at Diamond Light Source, UK (SI33490).[79,80] EY-NEXAFS was recorded using the drain current between the sample and a gold mesh electrode within the cell and the Cu L_3-edge and Zn L_3-edge were collected. Background subtraction was performed by fitting two splines or linear fits: one to the pre-edge and one to the post-edge. A linear fit is often suitable for the pre-edge as it accounts for the variation of absorption coefficient with photon energy which, over a small range, is approximately linear. In EY-NEXAFS, the amount of absorption is measured via secondary electron emission processes. The electrons leaving the sample can be scattered by the gas in the cell where the degree of electron scattering is affected by gas pressure, temperature, and the energy of the emitted electrons. Therefore, the drain current in the post-edge region can vary non-linearly with photon energy, hence requiring a spline fitting. Complicated backgrounds are often observed when measuring the drain current through the gas in the cell as small variations in pressure and temperature will alter the background. Background subtraction used Thorondor data treatment software (based in *Jupyter* notebook).[306] It is common to normalise NEXAFS data to the post-edge, but due to the difficult background subtraction the post-edge was

deemed to be an insufficient reference point. Therefore, the data was normalised to the peak height instead. Energy calibration was achieved by setting the Cu absorption edge to 933.7 eV for the Cu^0 peak under 1 bar of H_2 (200°C) where the same shift was then applied to all other edges. The complex post-edge background was not observed to the same extent in Chapter 4 since the pressure in the E-cell was maintained at a lower pressure (100 mbar), hence the degree of electron scattering was lower.

STEM-EELS images were collected from brass NPs deposited on holey carbon covered, Au-coated TEM grids. The NPs were pre-treated in a tube furnace and inertly transferred to the STEM via a glovebox. During the pre-treatment, the tube furnace was initially purged in Ar (1 bar) for 30 minutes at room temperature before heating to 200°C (10°C/min). The sample was then exposed to sequential treatments of H_2 and/or O_2 (1 bar, 2-3 hours) where, between sequential doses, the atmosphere was purged with Ar for 30 minutes. Finally, the sample was cooled to room temperature in an Ar atmosphere (10°C/min). Fresh brass NP samples were used for each different sequential gas dosing experiment. STEM-EELS images show the EELS map collected where only Cu (blue) and Zn (red) regions are shown. The corresponding EELS spectra have been energy calibrated such that the Cu L_3-edge is at 933.7 eV for Cu^0, following a linear background fitted to the pre-edge and normalisation to the post-edge. The Zn L_3-edge signal in EELS was too weak relative to the large background from the nearby Cu L_3-edge, so it was not collected.

Reference measurements of Zn and brass foils are discussed in the Appendix alongside an assignment of the features in the Zn L_3-edge (Figures A6.3 and A6.4).

6.3 NAP-XPS vs AtmP-XPS of Brass

Figure 6.3 (a,b) shows NAP-XPS collected from a brass foil when exposed to $H_2/CO_2/CO$ mixtures at 200°C. The Cu LMM region for the cleaned brass foil under UHV

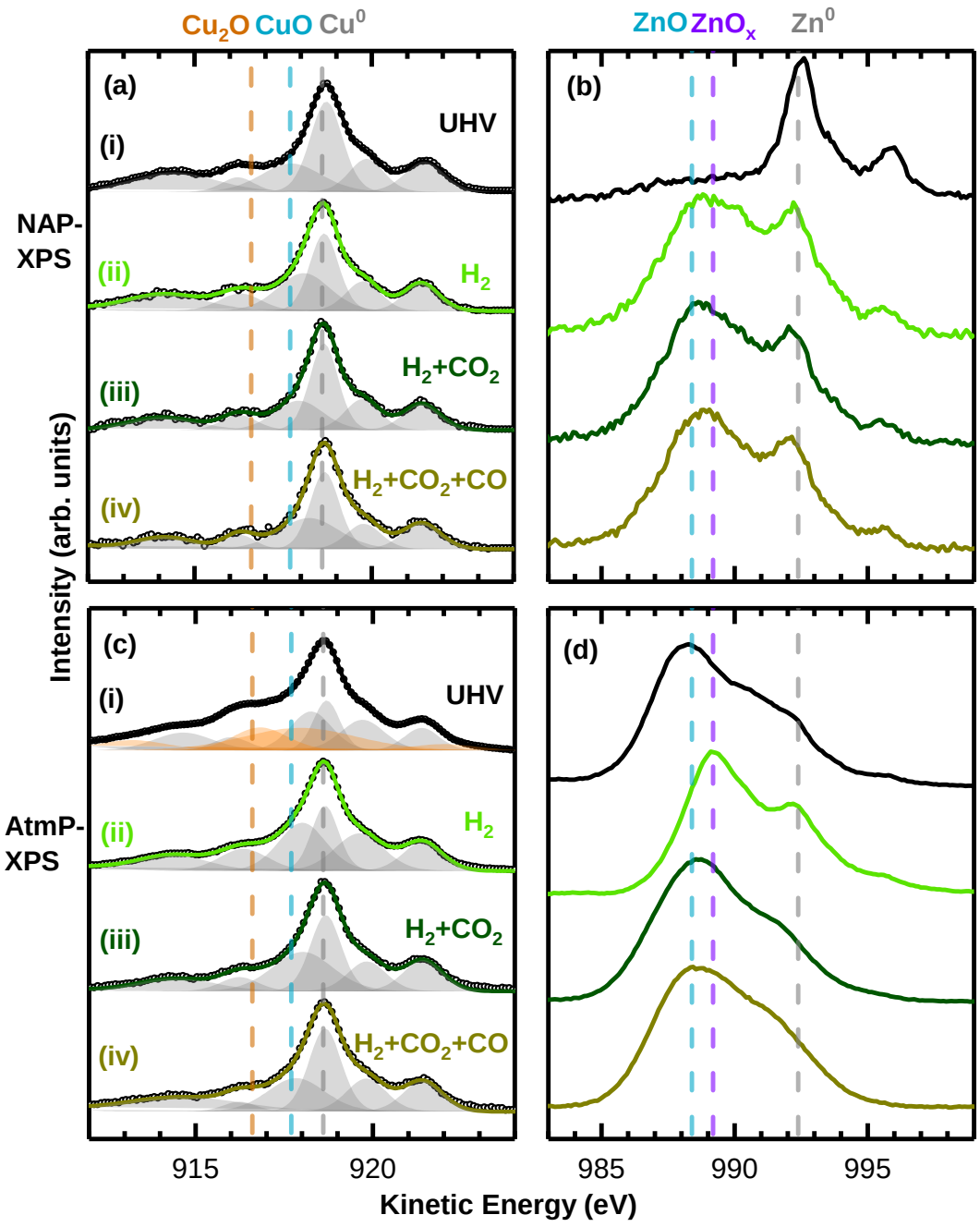


Figure 6.3: *(a) Cu LMM and (b) Zn LMM from NAP-XPS of a brass foil under the following conditions: (i) UHV, (ii) H_2 (0.3 mbar), (iii) H_2+CO_2 (1:1, 0.6 mbar), and (iv) H_2+CO_2+CO (3:3:1, 0.7 mbar) all at 200°C. (c) Cu LMM and (d) Zn LMM from AtmP-XPS of brass NPs under (i) vacuum at room temperature, then (ii) H_2, (iii) H_2+CO_2 (1:1), and (iv) H_2+CO_2+CO (3:3:1) at 1 bar and 200°C.*

conditions is shown in Figure 6.3 (a,i). The colour of fitted peaks corresponds to a specific oxidation state of Cu. Under UHV there are only peaks related to Cu^0 (grey). In the corresponding Zn LMM region (Figure 6.3 (b,i)) the peak at 992.4 eV and the shoulder at 995.9 eV suggests Zn^0 is present. The starting state of the brass foil is metallic as a result of the sputtering and annealing pre-treatment.

Upon dosing H_2 at 0.3 mbar (200°C) there are no changes in the Cu LMM (Figure 6.3 (a,ii)) whilst in the Zn LMM (Figure 6.3 (b,ii)) there is a new peak at ~989 eV, associated with the oxidation of Zn, alongside remaining Zn^0 features. Although oxidation is not expected from pure H_2, this likely results from water contamination in the H_2 gas lines which is difficult to minimise. Cu^0 is not oxidised suggesting Zn protects Cu in a sacrificial manner, where water preferentially oxidises Zn^0 since Zn is more oxophilic.[55] The position of the peak at ~989 eV is at a higher kinetic energy and is broader than expected for pure ZnO, usually located at 988.4 eV.[285,307–312] A peak at 989.2 eV is tentatively attributed to an additional species: ZnO_x ($0<x<1$). ZnO_x is often referred to in literature as a partially reduced ZnO with O vacancies present.[152,276,277,284,294,307,311,313] A peak in the Zn LMM region has been observed previously in literature at ~989.2 eV, either via mild oxidation of Zn^0 or via severe reduction of ZnO. However, it has not been formally assigned.[285,294,307,313,314] The identification of ZnO_x at 989.2 eV is demonstrated in lab-based XPS sputtering experiments of a Zn and brass foil in the Appendix (Figures A6.1 and A6.2). Since the peak at ~989 eV is very broad there must be a mix of ZnO and ZnO_x. Overall, under 0.3 mbar of H_2 there is a mix of Zn^0/ZnO_x/ZnO and Cu^0 on the surface of the brass foil.

0.3 mbar of CO_2 was then added to create a 1:1 mix of H_2 and CO_2. Figure 6.3 (a,iii) and (b,iii) show little change in the oxidation state of Cu and Zn. Cu remains metallic and Zn still contains a mix of Zn^0/ZnO_x/ZnO, with the broad peak at ~989 eV becoming slightly narrower towards lower kinetic energies, indicating some oxidation of ZnO_x to

ZnO. The introduction of CO_2 does not oxidise Cu^0, similar to the observation made in Chapter 4 over a pure Cu foil. For a pure Cu foil, dissociated H_2 protects the surface from O* (from dissociated CO_2) by reacting to form H_2O via the RWGS reaction, thus preventing oxidation.[71] For brass NPs, H* may protect Cu^0 in the same way as observed for pure Cu foil, or O* may not attack Cu^0 since it is bound more strongly to Zn, or a combination of both mechanisms. The small amount of oxidation observed for Zn^0/ZnO_x suggests O* does not attack Cu^0, however without MS measurements it cannot be conclusively stated which mechanism is protecting Cu^0 from oxidation. Finally, 0.1 mbar of CO was added and no notable changes are seen in Figure 6.3 (a,iv) and (b,iv) consistent with the pressure of CO not being sufficient to reduce ZnO.[315]

AtmP-XPS at 1 bar is shown in Figure 6.3 (c) and (d) which provides more industrially relevant measurements due to the higher pressure used compared to NAP-XPS. Under vacuum conditions (room temperature), Cu^0 is identified in the Cu LMM region (Figure 6.3 (c,i)). After fitting the Cu LMM region, there are peaks for both Cu^0 and Cu_2O (orange). Cu will oxidise to Cu_2O and CuO when exposed to ambient conditions.[71] CuO is not detected but this is unsurprising as it is easily reduced to Cu_2O when exposed to X-rays under vacuum.[57] The Zn LMM (Figure 6.3 (d,i)) has a peak at ~988.2 eV suggesting it is mostly ZnO. However, the peak is broad towards lower kinetic energies, attributed to a small amount of $Zn(OH)_2$ present on the surface. ZnO, when exposed to atmospheric conditions, is known to form a small amount of $Zn(OH)_2$.[316–318] The assignment of a $Zn(OH)_2$ peak at 987.4 eV is confirmed in the Appendix (Figure A6.1).[69,305]

The sample was heated to 200°C and 1 bar of H_2 was introduced. The fitted peaks for Cu_2O vanish and only Cu^0 peaks remain, indicating the reduction of Cu_2O to Cu^0 as expected in H_2 (Figure 6.3 (c,ii)). Meanwhile the Zn LMM region (Figure 6.3 (d,ii)) has two new peaks at 989.2 eV and 992.4 eV from ZnO_x and Zn^0 respectively (a very

small shoulder at 995.9 eV is also observed from Zn^0).[77,305,319] 1 bar of H_2 at 200°C is sufficient to reduce ZnO to Zn^0.[17,285] High pressures are crucial to enable the reduction of ZnO, where ZnO does not reduce in NAP-XPS at 0.3 mbar of H_2 (Figure 6.3 (b,ii)). ZnO_x may form via partial reduction from ZnO in H_2 or from partial oxidation from Zn^0 in water. At 200°C, when Cu^0 and Zn^0 are present, they form an α-phase brass alloy (Cu^0/Zn^0).[320]

Whilst maintaining a pressure of 1 bar and at a temperature of 200°C, CO_2 was added to achieve a 1:1 mix of H_2 and CO_2. Cu^0 is not oxidised as shown by the unchanged shape of the Cu LMM region (Figure 6.3 (c,iii)). The peak at 992.4 eV for Zn^0 (Figure 6.3 (d,iii)) vanishes and the main peak position in Zn LMM shifts to 988.6 eV, with a small shoulder peak at 991.5 eV corresponding to ZnO formation. The slightly higher position of the main ZnO peak (988.6 eV instead of 988.4 eV) indicates some ZnO_x is still present, but XPS is unable to easily separate small amounts of ZnO_x from significant ZnO due to their close peak positions. Similar to NAP-XPS, it is not clear whether oxidation of Zn^0/ZnO_x to ZnO or H_2 dissociation is responsible for Cu remaining metallic.

Finally, CO was introduced to achieve a 3:3:1 ratio for H_2:CO_2:CO. The Cu LMM shape once again remains unchanged with only Cu^0 present (Figure 6.3 (c,iv)). In the Zn LMM region the main peak shifts to a slightly higher kinetic energy and shows some broadening towards 989.2 eV (Figure 6.3 (d,iv)). This suggests more reducing conditions convert some ZnO to ZnO_x, therefore CO's role may be to help recover reduced ZnO species which could be important in maintaining good catalytic activity (as suggested by literature).[55,275]

Figure 6.4 shows the results of similar NAP-XPS and AtmP-XPS experiments but where the order of CO_2 and H_2 introduction was reversed. Prior to the NAP-XPS measurements in Figure 6.4, a fresh piece of brass foil was cleaned by sputtering and

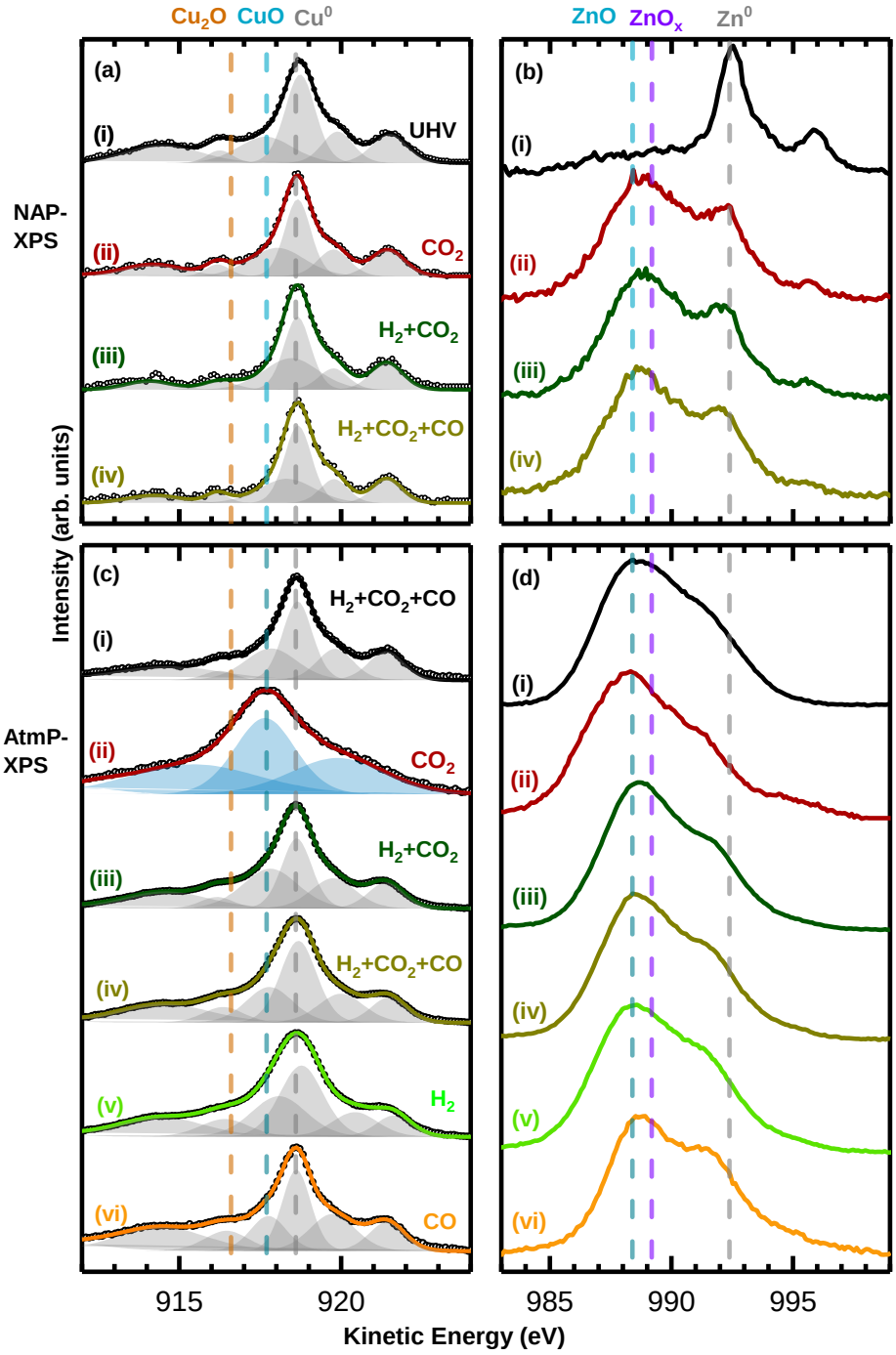


Figure 6.4: *(a) Cu LMM and (b) Zn LMM from NAP-XPS of a brass foil under the following conditions: (i) UHV, (ii) CO_2 (0.3 mbar), (iii) H_2+CO_2 (1:1, 0.6 mbar), and (iv) H_2+CO_2+CO (3:3:1, 0.7 mbar) all at 200°C. (c) Cu LMM and (d) Zn LMM from AtmP-XPS of brass NPs under the following conditions: (i) H_2+CO_2+CO (3:3:1), (ii) CO_2, (iii) H_2+CO_2 (1:1), (iv) H_2+CO_2+CO (3:3:1), (v) H_2, and (vi) CO all at 1 bar and 200°C.*

annealing. On the other hand, for AtmP-XPS, the brass NPs were untreated, with the measurements continuing directly from Figure 6.3 (for convenience, spectra in Figure 6.3 (c,iv) and (d,iv) are repeated in Figure 6.4 (c,i) and (d,i)).

Figure 6.4 (a,i) and (b,i) show the Cu LMM and Zn LMM regions, respectively, immediately following surface preparation (UHV, 200°C) in NAP-XPS where both spectra show a metallic starting state identical to in Figure 6.3. When CO_2 (0.3 mbar) is introduced at 200°C, Cu remains metallic (Figure 6.4 (a,ii)). In Figure 6.4 (b,ii), the Zn LMM region shows a prominent feature at ~988.6 eV indicating oxidation to ZnO. The peak at 992.4 eV (and shoulder at 995.9 eV) shows that Zn^0 remains. There is also a slight broadening of the ZnO peak towards 989.2 eV corresponding to ZnO_x. Therefore, CO_2 at this low pressure does not fully oxidise Zn^0 to ZnO. In Chapter 4, under the same conditions, Cu foil was oxidised to Cu_2O.[71] As previously mentioned, Zn^0 is preferentially oxidised over Cu^0. The only mechanism explaining how Cu^0 sites are not oxidised in this instance is the preference for O* to remain on Zn sites, since there is no significant H* available to remove O* via the RWGS reaction. The results presented here cannot conclusively determine whether CO_2 dissociates at Zn^0/ZnO_x or Cu^0 sites, only that O* preferentially attacks Zn^0/ZnO_x rather than Cu^0. However, literature suggests CO_2 binds more strongly on Zn^0/ZnO_x sites compared to Cu^0, hence most likely dissociates at Zn^0/ZnO_x sites.[276,296,298]

0.3 mbar of H_2 was then introduced (Figure 6.4 (a,iii) and (b,iii)) followed by adding 0.1 mbar of CO (Figure 6.4 (a,iv) and (b,iv)). No change is observed across the AES spectra. The low pressure of H_2 and CO is insufficient to reduce ZnO so there is no increase in the amount of ZnO_x or Zn^0 species, hence the mix of $ZnO/ZnO_x/Zn^0$ is constant. [152,276,277,284,294,307,311,313] Similarly, the oxidation state of Cu^0 is unchanged as it cannot be reduced further.

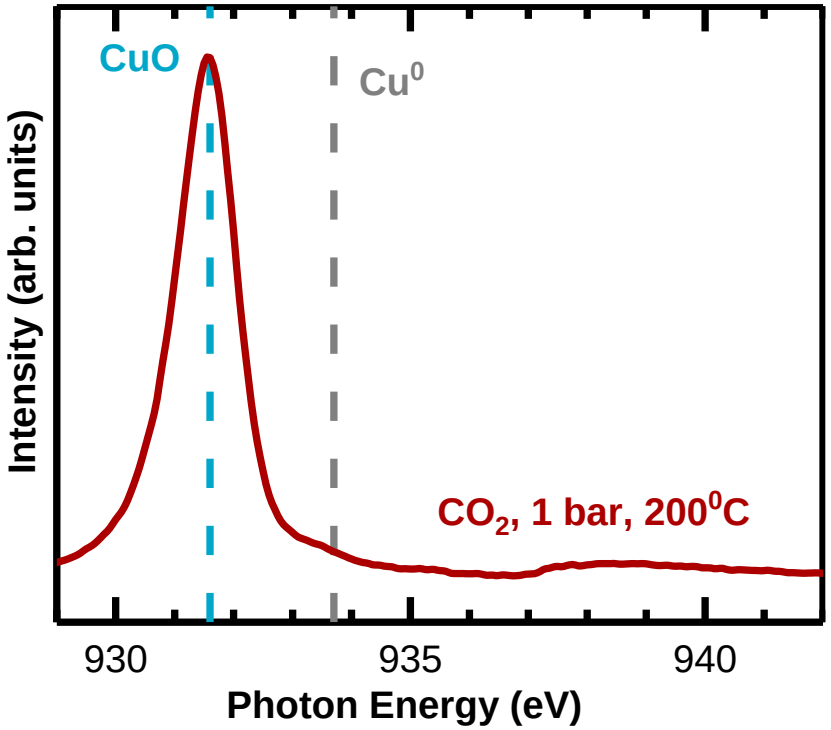


Figure 6.5: *Cu L_3-edge of brass NPs exposed to CO_2, 1 bar, 200°C during AtmP-XPS measurements shown in Figure 6.4 (c,ii).*

In AtmP-XPS measurements the sample was exposed to CO_2 at 1 bar (Figure 6.4 (c,ii) and (d,ii)) following the $H_2/CO_2/CO$ mix used in the experiment in Figure 6.3 (c,iv) and (d,iv). When exposed to 1 bar of CO_2 the Cu LMM region changes significantly indicating Cu^0 has been oxidised (Figure 6.4 (c,ii)). NEXAFS data collected under the same conditions (see Figure 6.5) is used for energy calibration. The Cu L_3-edge shows a single peak at 930.8 eV which is only observed for CuO, therefore the Cu LMM is shifted to 917.7 eV, where fitted peaks are for CuO (blue) only. Cu^0 has therefore been fully oxidised under 1 bar of CO_2 whereas, in NAP-XPS, CO_2 at 0.3 mbar did not oxidise Cu^0, demonstrating the importance of performing high pressure measurements. The Zn LMM (Figure 6.4 (d,ii)) peak shifts to a higher kinetic energy (988.2 eV) and has a shoulder at 991.5 eV suggesting all Zn species have been oxidised fully to ZnO. Cu is not protected from oxidation since all of the Zn species are oxidised to ZnO, therefore O* will then oxidise Cu. The peak position is at a slightly lower kinetic energy than expected for pure ZnO (988.4 eV). This is similar to that seen in vacuum in Figure 6.3 (d,i); suggesting a small amount of $Zn(OH)_2$ is present. This is unexpected as there should be no H_2 present in pure CO_2. However, it is possible a very small amount of residual H_2 (or H_2O from the gas lines) is present which forms a small amount of $Zn(OH)_2$.

H_2 was then added to obtain a 1:1 mixture of H_2 and CO_2. The CuO is fully reduced to Cu^0 in Figure 6.4 (c,iii), so the Cu LMM is calibrated to 918.6 eV, and fittings show only Cu^0 peaks (grey). Meanwhile the shape of the Zn LMM has broadened towards ~989 eV corresponding to a small amount of ZnO_x, but there is still a substantial amount of ZnO seen in Figure 6.4 (d,iii). The oxidation state of Cu in Figure 6.3 (c,iii) and 6.4 (c,iii) under a 1:1 mix of H_2:CO_2 is the same (Cu^0) regardless of the order of dosing H_2 and CO_2. Similarly, the relative amount of ZnO and ZnO_x is the same regardless of the order of dosing H_2 and CO_2 (Figure 6.3 (d,iii) and 6.4 (d,iii)). Whereas for Cu alone (in Chapter 4), the Cu oxidation state depended on the order of dosing H_2 and CO_2.

CO was added to get a 3:3:1 mixture of H_2:CO_2:CO. The Zn LMM region experiences a greater extent of broadening of the main peak towards ~989 eV (Figure 6.4 (d,iv)). The broadening to higher kinetic energies increases even further when the gas composition is switched to pure H_2 (Figure 6.4 (d,v)) suggesting there is more ZnO_x present. There is additional broadening to higher kinetic energies indicating some $Zn(OH)_2$ formation too. When comparing Figure 6.3 (d,ii) to Figure 6.4 (d,v), the oxidation state of Zn is different depending on whether H_2 is dosed prior to or after oxidation respectively; Zn^0 and ZnO_x are not fully recovered under pure H_2 following exposure to pure CO_2 in Figure 6.4. The gas composition was made even more reducing by switching to pure CO. The Zn LMM peak narrows and shifts towards 989.2 eV and the peak at 992.4 eV also starts to return (Figure 6.4 (d,vi)), indicating more reduction to ZnO_x and Zn^0.

The experiments shown in Figure 6.3 and 6.4 indicate the possible role CO has in maintaining Zn^0 and ZnO_x sites that may be responsible for the increase in catalytic activity. Zn^0 and ZnO_x sites are not fully recovered in H_2 following oxidation in CO_2. It is worth noting under industrially relevant conditions the catalyst would not be exposed to such severe oxidising conditions as done here (pure CO_2 at 1 bar), therefore pure CO would not likely be required to recover the catalyst and less CO would be sufficient. Additionally, comparing Figure 6.3 and 6.4 it appears the order of dosing H_2 and CO_2 when approaching a 1:1 ratio of H_2:CO_2 does not affect the oxidation state of Cu (Cu^0) or Zn (ZnO mainly with a small amount of ZnO_x). The difference between NAP-XPS and AtmP-XPS measurements demonstrates the importance of studying reactions as close to reaction pressures as possible such that the chemical potentials of the gases are representative, since this strongly affects the chemical state of the surface.

6.4 STEM-EELS of Brass Nanoparticles

To further investigate the irreversible changes following oxidation of Zn, STEM-EELS images were collected for brass NPs exposed to H_2 and O_2 in different orders (Figure 6.6). O_2 was used rather than CO_2 due to safety limitations for the tube furnace.

Figure 6.6 (a,i) shows the STEM-EELS image collected from as-deposited brass NPs where the red and blue regions correspond to Zn and Cu respectively. This data was collected by obtaining an EELS spectrum at each pixel where the software (Gatan) then extrapolates the relative intensity of the Cu and Zn signal within the relevant L_3-edge range (~920-1040 eV), and finally this information is displayed using a 2D colour map. There is some mixing between Cu and Zn with a slight preference for Zn towards the centre and Cu towards the edge of the particles. The Cu L_3-edge from the EELS spectrum collected simultaneously is shown in Figure 6.6 (b,i). Peaks for Cu^0 and Cu_2O both appear at 933.7 eV, but they can be distinguished by a step-like or peak-like shape, respectively, as well as the appearance of high-energy resonances for Cu^0.[185,189,190] However, the low resolution of EELS means the high-energy resonances for Cu^0 are not visible. There is not a sharp peak or step at 933.7 eV, but instead a mix between the two. Therefore, the as-deposited brass NPs contain both Cu^0 and Cu_2O. The peak at ~931 eV indicates CuO is also present. Hence, the as-deposited brass NPs contain a mix of Cu^0/Cu_2O/CuO from exposure to ambient conditions prior to measurement.

Figure 6.6 (ii) shows the STEM-EELS for brass NPs exposed to H_2 only (200°C). As expected CuO and Cu_2O are fully reduced to Cu^0, shown by the step-like absorption edge at 933.7 eV in the Cu L_3-edge (Figure 6.6 (b,ii)). The STEM-EELS image in Figure 6.6 (a,ii) shows a clear change in the distribution of Cu and Zn compared to the as-deposited particles. There is a greater degree of alloying between Cu and Zn in the centre of the particle with an overlayer of Zn. According to AtmP-XPS (Figure 6.3 (d,ii)), the oxidation state of Zn is a mix of Zn^0 and ZnO_x. It is well documented that ZnO_x forms

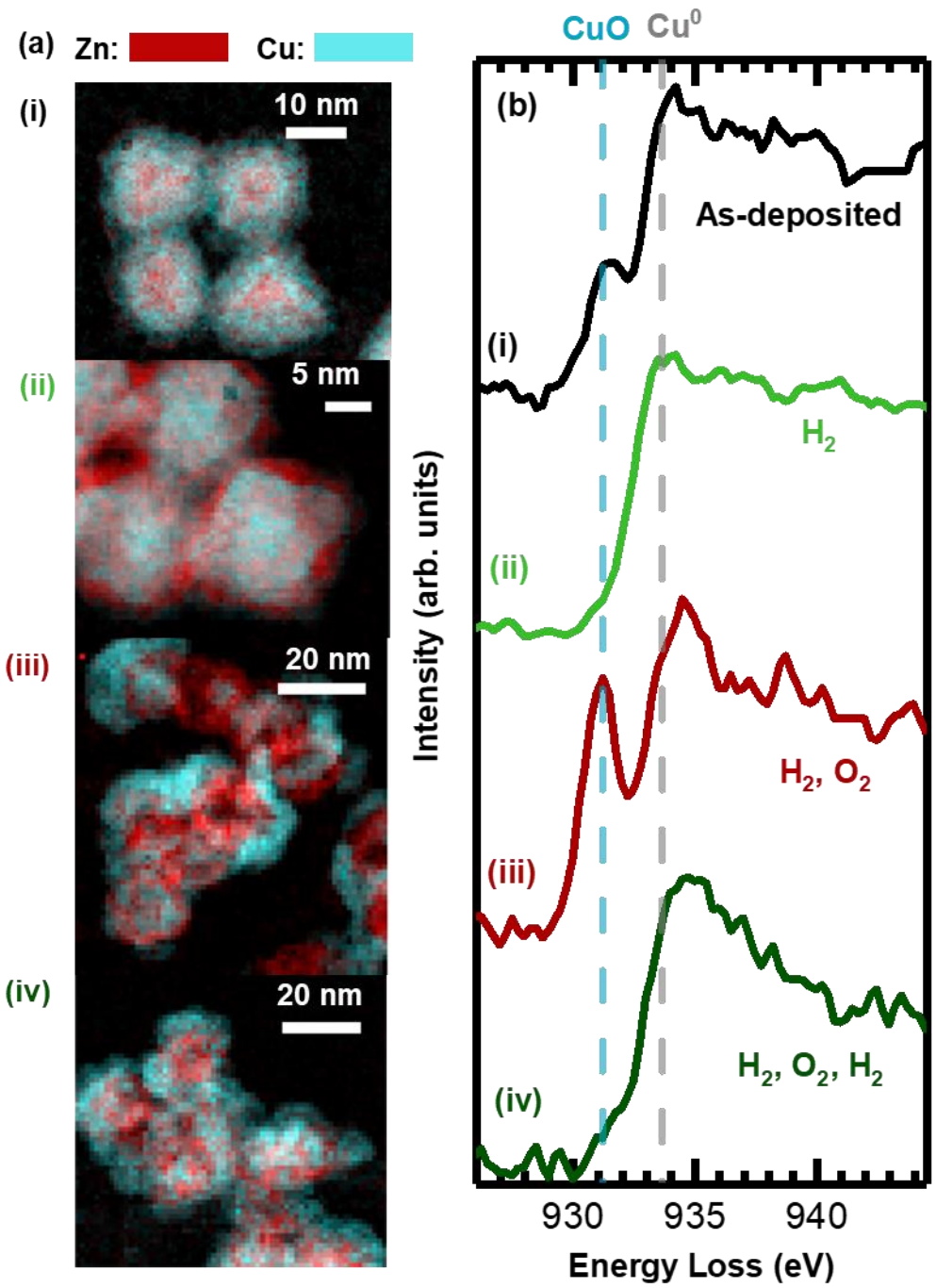


Figure 6.6: *(a) STEM-EELS images collected brass NPs for (i) as-deposited and after exposed to different pre-treatments: (ii) H_2, (iii) H_2, O_2, and (iv) H_2, O_2, H_2, at 1 bar and 200°C. Cu is shown in blue and Zn in red. Samples were treated in a tube furnace and inertly transferred for measurements. (b) EELS for the Cu L_3-edge collected from the regions shown in (a).*

overlayers on Cu under reducing conditions, the red shell around the particles confirms this. [152,275–277,284,287] Therefore, Zn^0 is most likely mixed with Cu^0 at the centre of the particle, forming an α-phase Cu^0/Zn^0 alloy surrounded by a ZnO_x overlayer.[302,311,320] A similar result was observed by S. Yue *et al.* in recent experiments, however they did not record *in situ* high pressure XPS to support the conclusions made unlike the results presented here.[295]

Figure 6.6 (iii) shows brass NPs after a H_2 and subsequent O_2 treatment. Clear segregation is now observed between areas of Cu and Zn with a slight preference for Cu on the outside of the particles.[287] EELS confirms oxidation to CuO and Cu_2O as indicated by the reappearance of a strong peak at ~931 eV and a peak-like feature at ~933.7 eV. In AtmP-XPS (Figure 6.4 (c,ii)), under 1 bar of CO_2, only CuO is detected. EELS detects transmitted electrons compared to XPS which detects electrons originating from the surface, consequently EELS is more bulk sensitive. Therefore, there is a CuO shell with Cu_2O nearer the centre of the NPs, which explains why Cu_2O was detected in EELS and not in XPS. Also, under 1 bar of CO_2, Zn is completely oxidised to ZnO (Figure 6.4 (d,ii)), therefore it is reasonable to assume ZnO forms under 1 bar of O_2. Overall, following a H_2 and O_2 treatment, brass NPs separate into CuO/Cu_2O and ZnO regions with no alloying and a potential CuO shell encasing the NPs (as also observed by S. Yue *et al.*).[295]

Figure 6.6 (iv) shows brass NPs after treatment in H_2, then O_2, then H_2 again; this experiment will determine if the distribution of Cu and Zn can be recovered by H_2 following complete oxidation. Figure 6.6 (a,iv) shows some small regions of mixing between Cu and Zn, but the mixing is not to the same extent as seen in Figure 6.6 (a,ii) when H_2 is dosed prior to O_2. Additionally, no ZnO_x overlayer is present on the particles, instead there is a slight preference for Cu on the outside of the particles. The EELS spectrum in Figure 6.6 (b,iv) suggests all of the CuO has been reduced and some Cu_2O

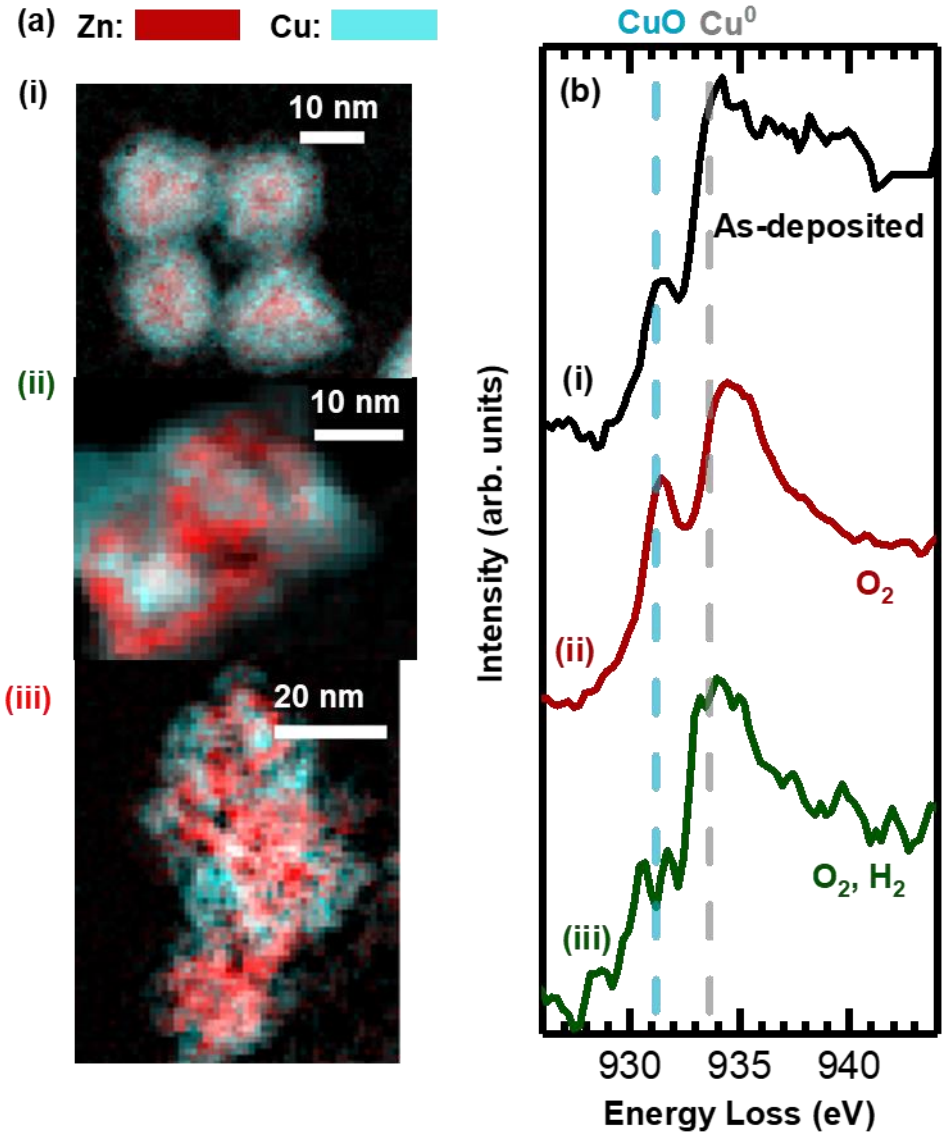


Figure 6.7: *(a) STEM-EELS images collected from brass NPs for (i) as-deposited and after exposed to different pre-treatments: (ii) O_2, and (iii) O_2, H_2, at 1 bar and 200°C. Cu is shown in blue and Zn in red. Samples were treated in a tube furnace and inertly transferred for measurements. (b) EELS for the Cu L_3-edge collected from the regions shown in (a).*

remains since the edge at 933.7 eV is more peak-like. From AtmP-XPS (Figure 6.4 (c,v)), Cu^0 is recovered when the surface is exposed to pure H_2 after oxidation in CO_2. The discrepancy between XPS and EELS could be due to the more highly oxidising conditions used (O_2 in STEM-EELS vs CO_2 in AtmP-XPS), or because of the different probing depths of the techniques.[295] Unfortunately this difference was unavoidable, since dosing CO_2 was not possible for the tube furnaces. Furthermore, from AtmP-XPS, in Figure 6.4 (d,v), ZnO_x did reform to some extent under pure H_2, following oxidation. The STEM-EELS images suggest that any ZnO_x present must be mixed in with Cu and ZnO rather than forming a distinguished overlayer on the particles. The conclusions made about the changes in the structure of Cu and Zn, when exposed to O_2, are still relevant to the CO_2 case, and agree with the irreversible oxidation state changes seen for Zn with AtmP-XPS and AtmP-NEXAFS.

Figure 6.7 shows brass NPs which underwent a pre-treatment in (ii) O_2 and (iii) O_2, then H_2 (the data from the as-deposited brass NPs from Figure 6.6 (i) is repeated in Figure 6.7 (i) for convenience). In Figure 6.7 (ii) the Cu and Zn segregate when O_2 is dosed and Cu oxidises to CuO and Cu_2O, also observed in Figure 6.6 (iii). In Figure 6.7 (iii), upon dosing O_2 then H_2 there is a greater amount of mixing between Cu and Zn and partial reduction to Cu_2O occurs with some CuO remaining. In comparison, in Figure 6.6 (iv) the contribution at 931 eV for CuO is much lower, this suggests a H_2 pre-treatment somewhat aids reduction after oxidation.

Overall, the STEM-EELS images further demonstrate the irreversible behaviour seen with AtmP-XPS, where the Cu/Zn structure seen during a H_2 pre-treatment is not recovered after severe oxidation. This will likely impact the activity of the catalyst.

6.5 AtmP-NEXAFS of Brass Nanoparticles

AtmP-NEXAFS data was also collected from brass NPs to reveal more details about the irreversible changes that occur following oxidation. Reference data was collected for Zn and brass foils and is discussed in the Appendix (Figure A6.3 and A6.4). In summary peaks in the Zn L_3-edge are assigned to: 1024.1 eV (ZnO_x), 1026.0 eV and ~1031 eV (Zn^0), and 1026.8 eV, 1028.9 eV, and 1033.1 eV (ZnO).

AtmP-NEXAFS spectra of the Cu L_3-edge are shown in Figure 6.8 and Zn L_3-edge in Figure 6.9 for brass NPs when exposed to different ratios of H_2 and CO_2 at 1 bar, 200°C. Initially, pure H_2 was dosed and the relative amount of CO_2 was gradually increased until eventually reaching pure CO_2 (Figure 6.8 (i) and 6.9 (i)). The process was then reversed by slowly introducing more H_2 until reaching pure H_2 again (Figure 6.8 (ii) and 6.9 (ii)). In Figure 6.8 and 6.9, the darker green spectra were taken in H_2-rich conditions (bottom spectrum is under pure H_2), whereas spectra shown in darker red were in CO_2-rich conditions (top spectrum is under pure CO_2). Figure 6.10 shows a detailed key of the exact ratio of H_2:CO_2 used and the composition each colour corresponds to.

Under pure H_2 (Figure 6.8 (i)) the Cu L_3-edge has a step-like absorption edge at 933.7 eV, with a resonance at ~938.0 eV corresponding to Cu^0 that agrees with AtmP-XPS (Figure 6.3 (c,ii)). In Chapter 4, a higher temperature (275°C) was required to reduce Cu_2O to Cu^0 for a Cu film under 100 mbar of H_2.[71] The higher pressure of 1 bar in Figure 6.8 could explain the lower temperature needed for reduction. However, Figure 6.11 shows the Cu L_3-edge for a Cu film under 1 bar of H_2 at 220°C which contains a mixture of Cu_2O and Cu^0, so even at 1 bar of H_2 a pure Cu film is not completely reduced at ~200°C. This suggests ZnO is responsible for the lower temperature to dissociate H_2 and reduce Cu_2O. However, the data in Figure 6.11 does not fully rule out the possibility of sample variation (thin film vs NPs) affecting the temperature required to dissociate H_2.

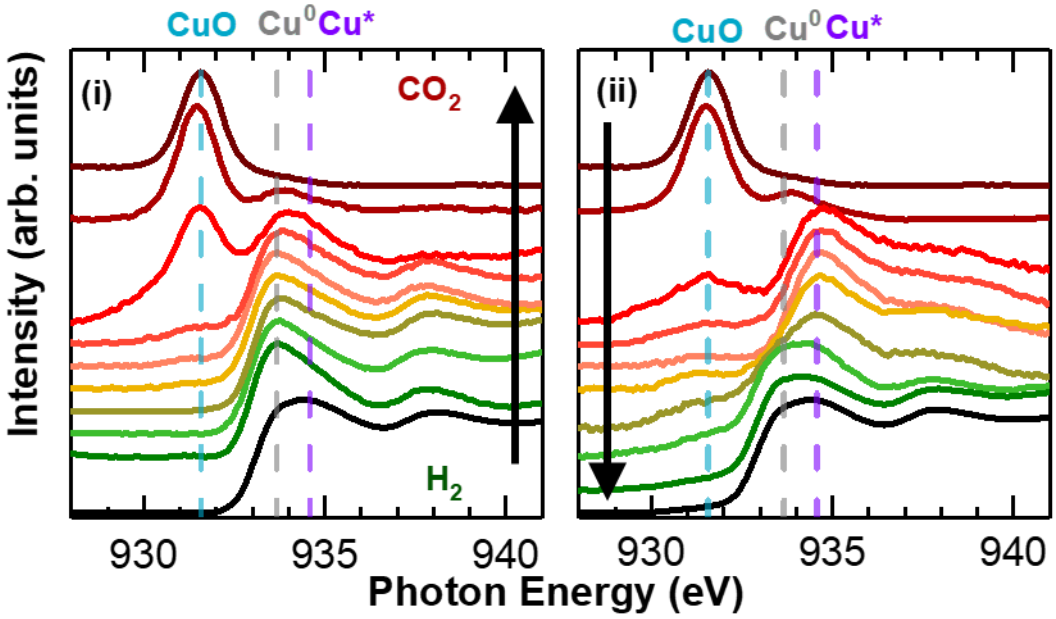


Figure 6.8: *Cu L_3-edge from brass NPs suspended on graphene collected at 1 bar and at 200°C. (i) Starting from the bottom, pure H_2 was dosed and the composition was slowly changed to decrease the H_2:CO_2 ratio, until pure CO_2 (the top spectrum). (ii) The same sample initially under pure CO_2 where H_2 was slowly reintroduced until pure H_2 was achieved once again. The colours of each spectra in (i) and (ii) correspond to identical H_2:CO_2 ratios where the darker red spectra indicates more CO_2 and darker green indicates more H_2.*

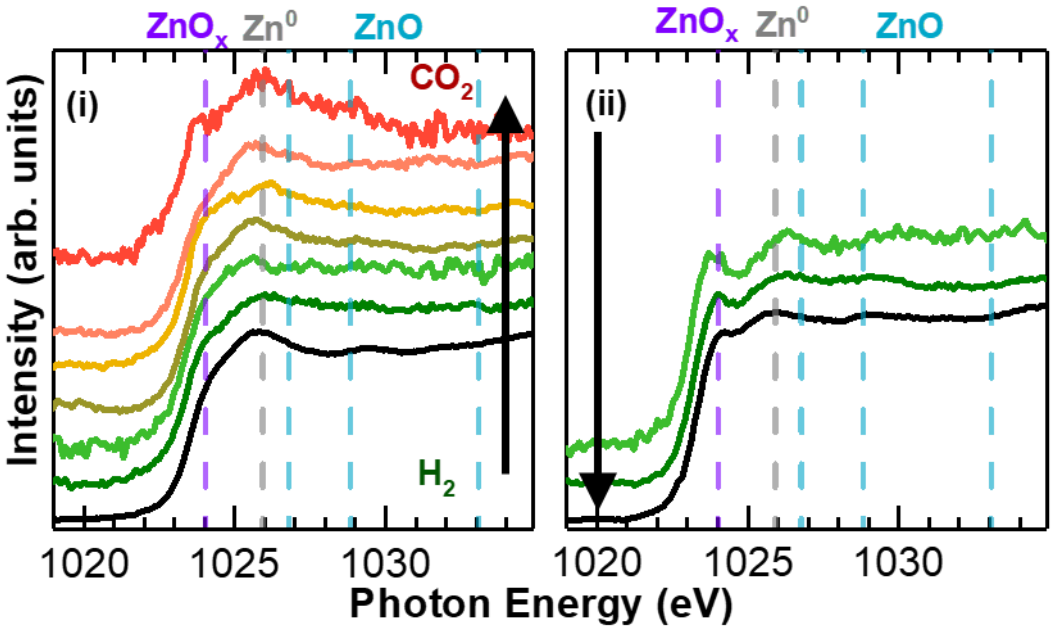


Figure 6.9: *Zn L_3-edge from brass NPs suspended on graphene collected at 1 bar and at 200°C. (i) Starting from the bottom, pure H_2 was dosed and the composition was slowly changed to decrease the H_2:CO_2 ratio, until pure CO_2. (ii) The same sample initially under pure CO_2 where H_2 was slowly reintroduced until pure H_2 was achieved once again. The colours (matching Figure 6.8) of each spectra in (i) and (ii) correspond to identical H_2:CO_2 ratios where the darker red spectra indicates more CO_2 and darker green indicates more H_2.*

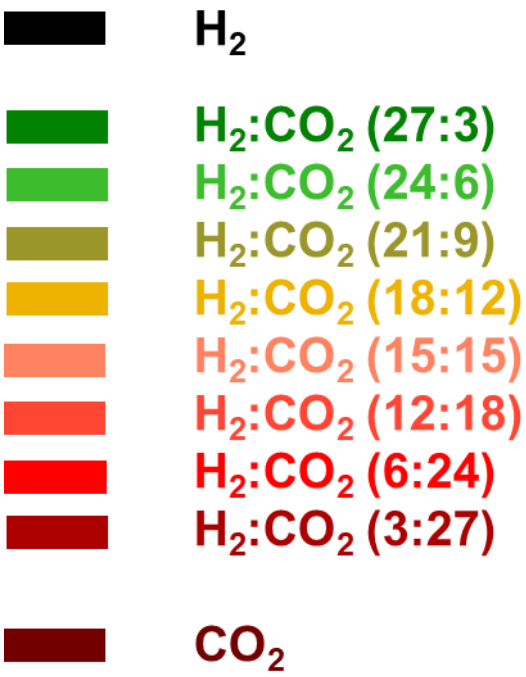


Figure 6.10: *Key for AtmP-NEXAFS measurements in Figures 6.8 and 6.9 showing the exact composition for each colour. Total flow of 30 sccm was maintained using*

Under 1 bar of H_2, the Cu L_3-edge for brass NPs contains another feature at 934.6 eV (Cu*) which causes the edge to broaden. Under 1 bar of H_2 in the Cu LMM region (Figure 6.3 (c,ii)), there are no additional features, except those expected for Cu^0. Since Cu* and Cu^0 are indistinguishable with XPS this indicates Cu* is a metallic species. A change in hybridisation of unoccupied states with neighbouring atoms could alter the energy of the transition measured in the Cu L_3-edge, explaining the different absorption energies for Cu^0 and Cu*.[185,321] Makarova *et al.* have previously observed that a shift in the Cu L_3-edge can be caused by hybridisation of orbitals in more atomic-like samples rather than in the bulk, which agrees with the assignment of Cu* to hybridisation of unoccupied orbitals.[321] The reference data collected for the metallic and partially oxidised brass foil in Figure A6.3 (b,ii) shows no Cu* feature, which agrees with Makarova *et al.* that this interaction is only seen for atomic-like samples and not in bulk foils. An interaction between Cu and Zn may account for Cu*.[152,286,321] A shift in the Cu L_3-edge has also been attributed to a change in the local potential of an atom which alters the core-hole potential and thus the transition energy.[189] The change in local potential can result in a much lower relative intensity of resonance peaks compared to the main peak (for more detail see reference [189]). When Cu* is observed alone (Figure 6.8 (ii)), the resonance features for Cu^0 are not observed. Therefore the shift observed for Cu* could be due to hybridisation of orbitals or, more generally, a change in the local environment.

Cu* is tentatively assigned to an interaction between Cu^0 and ZnO_x. The interaction between Cu^0 and ZnO_x may result in hybridisation or changes in local potential, causing this energy shift.[189,321] Cu* cannot be from an interaction between Cu^0 and ZnO, since under 1 bar of H_2 there is no ZnO present (as shown in AtmP-XPS in Figure 6.3 (d,ii)). It is possible an interaction between Cu^0 and Zn^0 could cause the Cu* feature; this is ruled out by careful inspection of Figure 6.8 (ii) where, at a 1:1, H_2:CO_2 ratio, there is a pure Cu* signal in the Cu L_3-edge. In the corresponding Zn LMM under

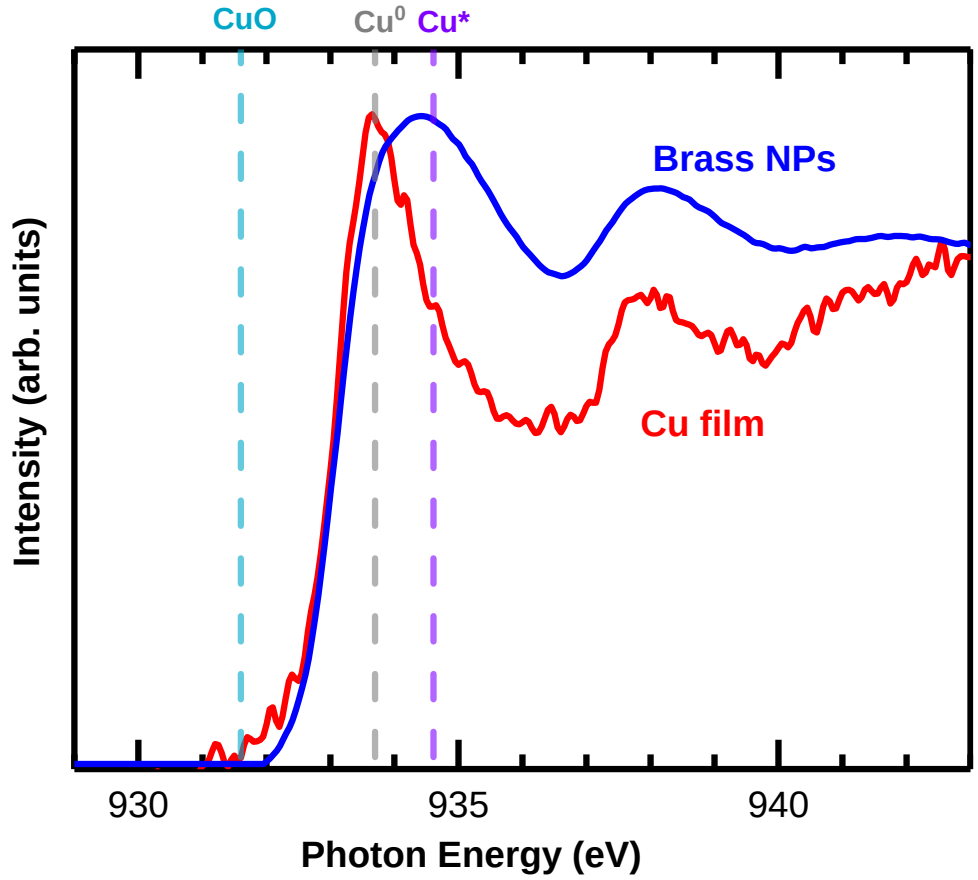


Figure 6.11: *Cu L_3-edge for brass NPs (blue) and a Cu film, ~4 nm, (red) at 1 bar of H_2 and temperatures of 200°C and 220°C respectively.*

the same conditions (H_2:CO_2, 1:1 mix following pure CO_2 dose in Figure 6.4 (d,iii)) there is a mix of ZnO and ZnO_x with no Zn^0. This suggests, Cu* does not arise from an interaction between Cu^0 and Zn^0. ZnO_x is consistently detected alongside Cu* under different conditions. It is possible the O vacancies in ZnO_x enable intimate contact with Cu^0 which causes a strong interaction.[10,278] Cu* is therefore an indicator of the strong interaction ("synergy") between Cu^0 and ZnO_x, previously believed to be important for catalytic activity as a potential active site.[17,144,152,280,286,290,291,322]

Herein, the peak at 934.6 eV is labelled Cu* and assigned to the presence of Cu*/ZnO_x species. The Cu*/ZnO_x peak thus indicates a strong interaction between metallic Cu and ZnO_x, implying there is a strong degree of mixing between Cu* and ZnO_x. The peak at 933.7 eV (with a resonance at ~938.0 eV) will be labelled Cu^0 and corresponds to either: Cu^0 similar to bulk Cu (as seen in Cu foil); or Cu^0 in brass NPs that is not strongly interacting with ZnO_x (e.g. in the Cu^0/Zn^0 alloy). Both Cu^0 and Cu* are metallic, where the different notation clarifies the local environment of the Cu. It is interesting to note the interaction between Cu^0 and Zn^0 does not appear to alter the Cu L_3-edge, suggesting the nature of the interactions in the Cu^0/Zn^0 alloy is different to Cu*/ZnO_x. The details of these interactions are not discussed in this thesis, but could be explored further using DFT calculations or EXAFS measurements.

Upon introducing CO_2, the Cu* species disappears, corresponding to a weakening of the Cu*/ZnO_x interaction (Figure 6.8 (i)). At intermediate H_2:CO_2 ratios (27:3 to 15:15) Cu^0 remains with a step-like edge at 933.7 eV and associated resonance feature at ~938 eV. At a high proportion of CO_2 (12:18, H_2:CO_2) the absorption edge is more peak-like and shifts to a slightly higher photon energy indicating Cu_2O formation. The appearance of a peak at 931.6 eV indicates CuO formation. Once at a H_2:CO_2 ratio of 3:27 and in pure CO_2 then only CuO is detected.

Figure 6.8 (ii) directly follows from Figure 6.8 (i), where the same sample starts at pure CO_2 at the top, and H_2 is slowly reintroduced until reaching pure H_2 once again at the bottom of Figure 6.8 (ii). CuO is relatively easily reduced resulting in the disappearance of the peak at 931.6 eV at a 12:18 ratio of H_2:CO_2. At this composition there is some discrepancy in how reduced Cu is between Figure 6.8 (i) and (ii), which is most likely caused by some variability in gas composition from pumping the cell. In Figure 6.8 (ii), at intermediate H_2:CO_2 ratios, the chemical state of Cu is purely Cu* with no Cu^0 (no resonance feature is observed). Hence, all Cu is metallic and interacts strongly with ZnO_x (only Cu*/ZnO_x species are present) under these conditions. Cu^0 away from ZnO_x begins to return at a 21:9 ratio of H_2:CO_2 as shown by the broadening of the Cu L_3-edge towards 933.7 eV and return of the resonance feature at 938 eV. Eventually at pure H_2 the chemical state of Cu is identical to when H_2 was dosed first. This confirms Cu can be fully reduced after exposure to pure CO_2, unlike in STEM-EELS when O_2 was used. Even though the chemical state of Cu is reversible after heavy oxidation, the intermediate Cu states are very different when going from H_2 to CO_2 (Cu^0 exists only away from ZnO_x) compared to going from CO_2 to H_2 (only Cu*/ZnO_x species exist). This suggests there are irreversible structural changes after oxidation, as shown in STEM-EELS.

The Zn L_3-edge spectra for the same sample exposed to the conditions in Figure 6.8 are shown in Figure 6.9. Figure 6.9 (i) shows the changes from pure H_2 to CO_2 and Figure 6.9 (ii) shows the reverse changes back to H_2.

Under initially reducing conditions (H_2, 1 bar, 200°C), at the bottom of Figure 6.9 (i) the main peak is at 1026.0 eV, with a small shoulder at 1024.1 eV, therefore Zn^0 and ZnO_x are detected respectively. This concurs with the AtmP-XPS data collected under the same conditions (Figure 6.3 (d,ii)). However, no peak at ~1031 eV is detected for Zn^0 in brass NPs which is seen in the reference data (Figure A6.4 (b,ii)). The loss of higher

energy resonance peaks for Zn^0 could be from a change in local potential, similar to what was seen for Cu* in Figure 6.8.

Upon adding CO_2, the relative intensity of the peak at 1026.0 eV decreases compared to the peak at 1024.1 eV. This agrees with the observation in AtmP-XPS that Zn^0 is oxidised to ZnO_x when CO_2 is added (Figure 6.3 (d,iii)). No Zn L_3-edge signal is detectable at high CO_2 concentrations. ZnO is a large band gap semiconductor whose electrical conductivity at 200°C is ~$1x10^{-6}$ S/m. Therefore, its insulating nature prevents the collection of a drain current from the sample and thus no signal in EY-NEXAFS.[323] The Zn L_3-edge signal becomes noisier as the CO_2 concentration increases, because of the increasing amount of insulating ZnO. In Figure 6.4 (d,ii), ZnO forms under pure CO_2 during AtmP-XPS measurements, therefore it can be assumed that ZnO also forms under the same conditions for AtmP-NEXAFS measurements. The Zn L_3-edge signal is lost at the same ratio of H_2:CO_2 (12:18) at which Cu oxidises in Figure 6.8 (i).

Figure 6.9 (ii) continues from Figure 6.9 (i) where the same sample started in pure CO_2, and H_2 was slowly reintroduced. The Zn L_3-edge signal is only detectable at a H_2:CO_2 ratio of 21:9; the same ratio at which the Cu^0 peak at 933.7 eV returns in Figure 6.8 (ii). The shape of the Zn L_3-edge is very different compared to before pure CO_2 was dosed in Figure 6.9 (i). There is a more intense peak at 1024.1 eV and a relatively weak peak at 1026.0 eV following oxidation, corresponding to mostly ZnO_x. Thus, ZnO has been reduced to ZnO_x but has not been fully reduced to Zn^0, even at high H_2 concentrations. This agrees with the AtmP-XPS data in Figure 6.4 (d,v), further demonstrating the irreversibility of Zn's chemical and structural changes.

AtmP-NEXAFS was also collected for fresh brass NPs exposed to: pure CO_2, with H_2 slowly added until the gas was purely H_2, before the composition was reversed back to pure CO_2. The AtmP-NEXAFS data is shown in Figure A6.5 and A6.6 in the Appendix. The data is not shown in the main text because the changes for the Cu L_3-

edge in Figure A6.5 are very similar to Figure 6.8. This demonstrates that the Cu oxidation state is recoverable regardless of whether a H_2 pre-treatment is used. Also, the changes in Figure A6.6 for the Zn L_3-edge are very similar to Figure 6.9 (ii) after CO_2 is dosed, reinforcing that there are irreversible changes in Zn after being completely oxidised.

6.6 Discussion

Figure 6.12 shows a schematic illustrating the observed structural and oxidation state changes for brass NPs when going from pure H_2 to pure CO_2 based on the results of AtmP-XPS, STEM-EELS, and AtmP-NEXAFS.

As-deposited brass NPs are shown in Figure 6.12 (i). The core of the NP contains ZnO with a mix of Cu^0 and Cu_2O towards the edge of the particle, and an outer layer of CuO. AtmP-XPS data also suggests some $Zn(OH)_2$ is present, which is not included for simplicity. CuO is observed in STEM-EELS (Figure 6.6 (b,i)) but not in AtmP-XPS (Figure 6.3 (c,i)) consistent with the X-ray induced reduction of CuO to Cu_2O in vacuum. [57] There is a preference for CuO to form at the surface which has been exposed to ambient conditions.[302]

Under H_2 (1 bar, 200°C) the structure in Figure 6.12 (ii) includes a Cu^0/Zn^0 alloy at the centre of the particle and a ZnO_x overlayer, which agrees with a recent TEM study performed by S. Yue *et al*.[295] Cu^*/ZnO_x species are also detected, and although their location is not directly resolved herein, their presence can be attributed to the interface between the central Cu^0/Zn^0 alloy and the ZnO_x overlayer. The ZnO_x overlayer is expected as its occurrence is well-documented in literature under highly reducing conditions.[152,275–277,284,287,295] Although, it cannot be ruled out that water contamination in the H_2 could partially oxidise Zn^0 to form ZnO_x rather than via direct reduction of ZnO, as seen at low pressures in NAP-XPS (Figure 6.3 (b,ii)).

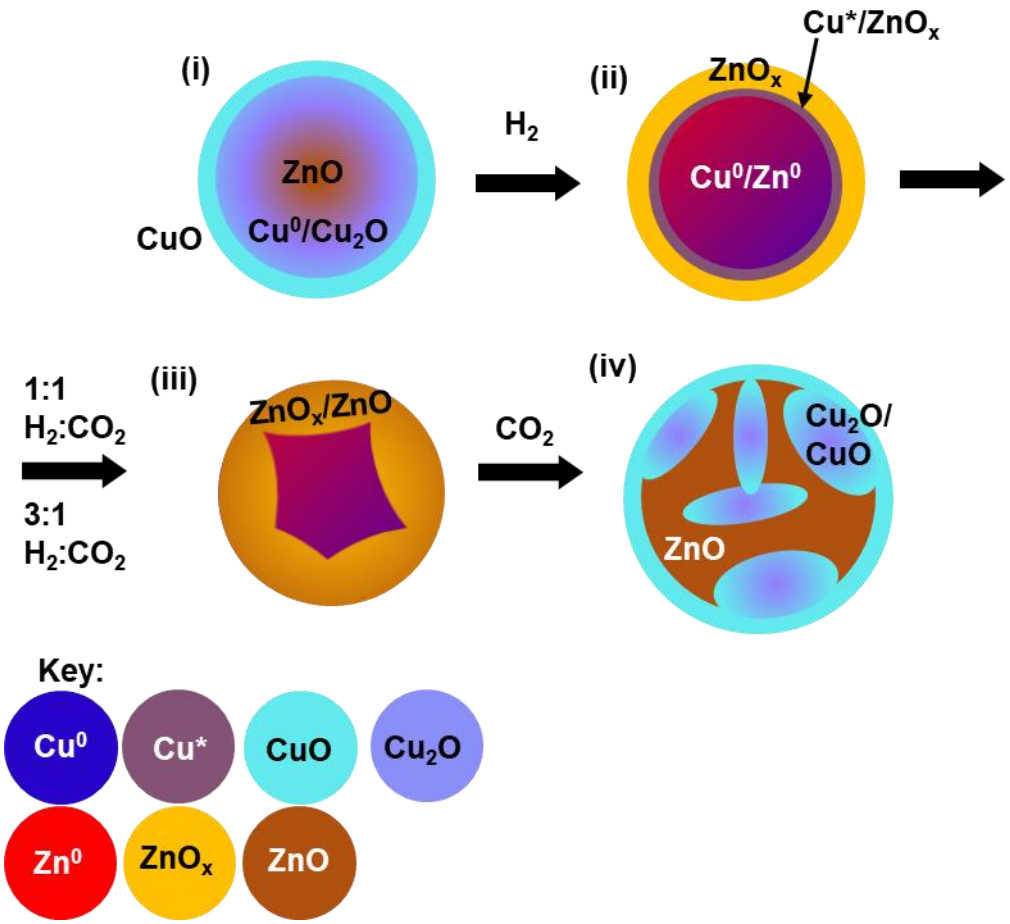


Figure 6.12: *Schematic suggesting the changes seen in brass NPs under different H_2 and CO_2 exposure using AtmP-XPS, STEM-EELS, and AtmP-NEXAFS data. This schematic shows the changes when H_2 is dosed prior to CO_2: (i) as-deposited, (ii) H_2, (iii) H_2+CO_2 (1:1 or 3:1), and (iv) CO_2. All gases are considered at a total pressure of 1 bar and at 200°C.*

1 bar of H_2 reduces all Cu_2O/CuO species to Cu^0 at 200°C for brass NPs (Figure 6.4 (c,iii) and Figure 6.6 (b,ii)), whereas Cu alone requires a higher temperature (~275°C) to be fully reduced.[71] A possible explanation of how ZnO decreases the temperature for reduction of Cu is via heterolytic dissociation of H_2 to form H^+ and H^-, which can spillover to Cu_2O to aid reduction.[14,277,324] This leads to reduction of Cu species initially, because of the higher oxophilicity of Zn.[55] Significant heterolytic dissociation of H_2 over ZnO is only expected at high pressures, and when Cu^0 sites are recovered at the NP surface then homolytic H_2 dissociation to active H* at Cu^0 sites is expected to dominate.[277,290,324,325] Heterolytically dissociated H_2 is not expected to be active for CO_2 hydrogenation, hence it is important to have Cu^0 sites to form active H* species.[277] Once these sites are present at the NP surface, the active H* species can spillover to ZnO and aid reduction to ZnO_x, with literature suggesting ZnO_x can also store this H* and act as a reservoir.[144,209,290,322] Alternatively, Zn^0/ZnO_x could aid reduction of Cu_2O by being preferentially oxidised, however this is unlikely to be the case here given the as-deposited brass NPs do not contain detectable amounts of Zn^0/ZnO_x. Nevertheless, it is possible a combination of the two mechanisms occurs where heterolytic dissociation of H_2 on ZnO forms some ZnO_x that can then remove O from Cu_2O. The O 1s region could potentially help in determining the amount of O* present during the reaction, however it is dominated by surface contamination from the graphene and topside of the SiN_x membrane. This is a disadvantage of probing samples through the graphene membrane, particularly given that an assumed advantage of using soft X-rays is the large photoionisation cross-section for C and O.[37]

The structure of the NPs could be quite different if another support was used. As shown in Figure 6.2, when Al_2O_3 is used as a support then Zn can integrate into Al_2O_3, whereas when using a more weakly interacting support (e.g. SiO_2, or graphene) then a

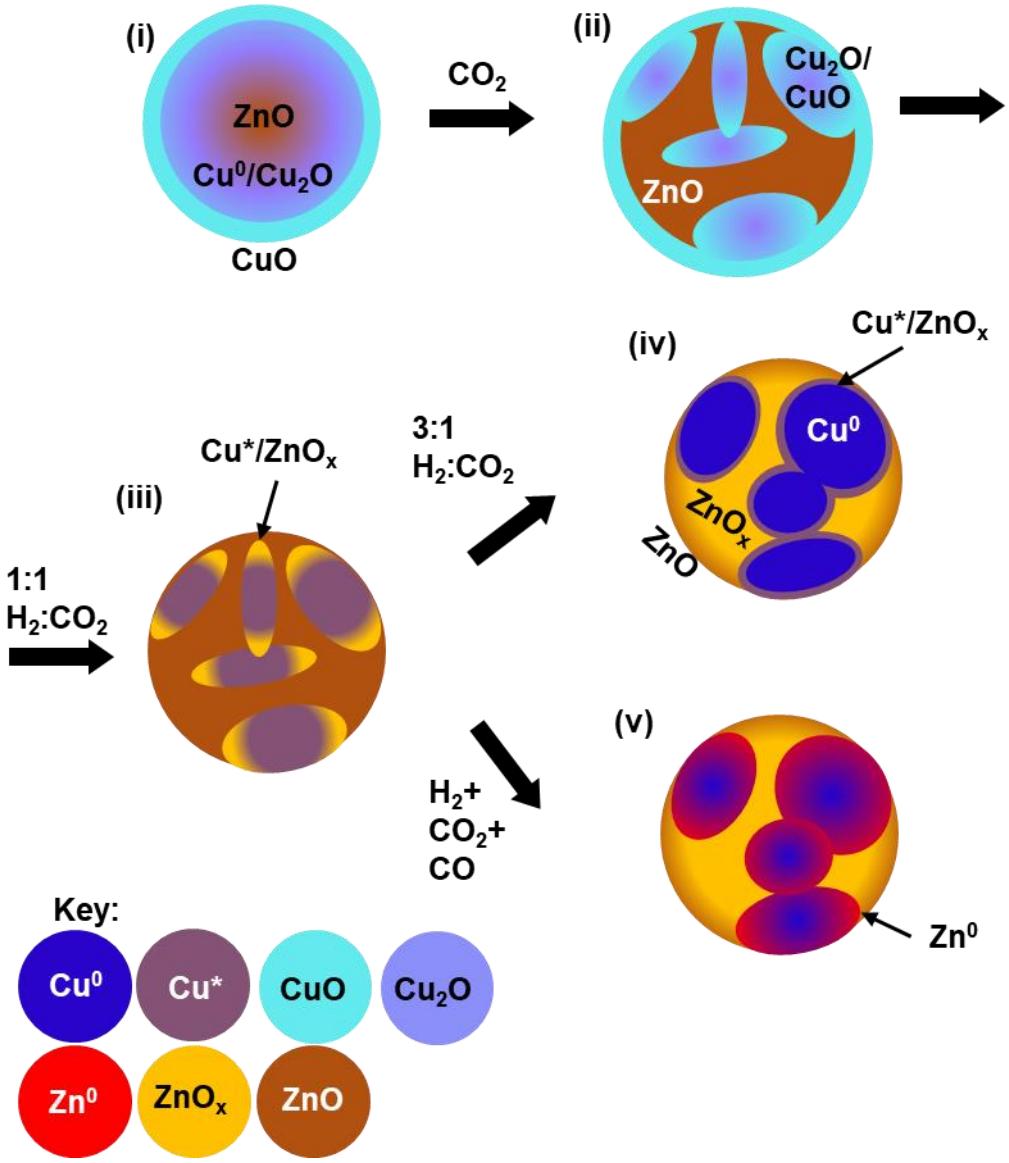


Figure 6.13: *Schematic suggesting the changes seen in brass NPs under different H_2 and CO_2 exposure using AtmP-XPS, STEM-EELS, and AtmP-NEXAFS data. This schematic shows the changes when CO_2 is dosed prior to H_2: (i) as-deposited, (ii) CO_2 (which is the same as Figure 6.12 (iv)), (iii) H_2 + CO_2 (1:1), (iv) H_2 + CO_2 (3:1), and (v) H_2 + CO_2 + CO (3:3:1). All gases are considered at a total pressure of 1 bar and at 200°C.*

central Cu^0/Zn^0 alloy surrounded by oxidised Zn forms (as seen in the results presented here).[210] However, support effects are not investigated in this study.

Figure 6.12 (iii) indicates two relevant ratios of H_2:CO_2; 1:1 and 3:1 and shows an overlayer of ZnO/ZnO_x covering the remaining Cu^0/Zn^0 alloy. The 1:1 ratio is relevant to the AtmP-XPS data and 3:1 is relevant to industrial conditions for methanol synthesis (for AtmP-NEXAFS the data used for the 3:1 ratio has an actual ratio of 21:9 as this was the closest approximation). No STEM-EELS images were collected from brass NPs under a H_2:CO_2 mix, but the lack of Cu* species seen with AtmP-NEXAFS (Figure 6.8 (i)) suggests there is no strong interaction between Cu* and ZnO_x under these conditions. The partial oxidation of the ZnO_x overlayer to ZnO may decrease the synergy between Cu and ZnO_x. As mentioned earlier, the results presented do not determine where CO_2 dissociates, but they do confirm that O* will preferentially oxidise Zn^0/ZnO_x rather than Cu^0. From literature, it is thought that CO_2 may dissociate over ZnO_x where the O vacancies can stabilise CO_2 adsorption and any intermediates that form, which may be important in the reaction mechanism.[11,276,296]

Common practice for methanol synthesis is to approach reaction conditions after a H_2 pre-treatment. Figure 6.12 (iii) suggests in this case Cu^0/Zn^0 alloy dominates with no significant Cu^*/ZnO_x interactions even though ZnO_x is present under these conditions.[11,145,287,292] This has an important implication on the possible active sites for the reaction since there is debate in literature as to which is active: Cu^0/Zn^0 alloy or the interaction between Cu* and ZnO_x. This data suggests Cu^0/Zn^0 alloy is present and potentially active, but does not interact strongly with neighbouring ZnO_x. However, ZnO_x may still be important for the dissociation of CO_2 through its O vacancies.[276,294,297]

Figure 6.13 details the structural and oxidation state changes when CO_2 is dosed prior to introducing H_2. The changes shown are the same regardless of whether CO_2 is dosed on a fresh sample or on a sample following a H_2 pre-treatment, hence Figure 6.12

(iv) and Figure 6.13 (ii) are the same. Distinct regions of CuO and ZnO are shown, where there is some Cu_2O in the centre of the Cu regions. EELS spectra (Figure 6.6 (b,iii)) detected some Cu_2O as well as CuO which was not detected with AtmP-XPS (Figure 6.4 (c,ii)). In contrast, only Cu^0 was detected in NAP-XPS, because the low pressure was insufficient to oxidise Cu^0. EELS is more sensitive to the bulk which suggests Cu_2O is nearer the centre of the particle, or alternatively it may have formed during the cool down and sample transfer. Crucially, following oxidation with CO_2 there is no alloying or interaction between Cu and Zn species and there is a large change in the structure compared to under reaction conditions in Figure 6.12 (iii).[287,295]

Figure 6.13 (iii) shows the arrangement of Cu and Zn once H_2 was slowly re-introduced to a 1:1, H_2:CO_2 ratio. There are separated ZnO and Cu regions that remain from treatment in pure CO_2, but Cu*/ZnO_x regions are now shown instead of Cu_2O/CuO regions. A substantial amount of ZnO is still detected under these conditions in AtmP-XPS (Figure 6.4 (d,iii)), so this region is thought to remain largely unchanged. AtmP-NEXAFS (Figure 6.8 (ii)) shows that all Cu species are fully reduced and strongly interact with ZnO_x (i.e. Cu*/ZnO_x). As suggested earlier, ZnO can aid the reduction of Cu_2O via heterolytic dissociation of H_2. This reduction mechanism would cause preferential reduction of Cu at the interface between Cu and ZnO and result in a significant amount of mixing between Cu and Zn species. The formation of ZnO_x (Figure 6.4 (d,iii)) is most likely as a result of spillover of H* from metallic Cu once formed. [277,324] It is unlikely heterolytic H_2 dissociation is able to maintain ZnO_x sites, since any ZnO_x sites will be oxidised by CO_2. Whereas, once metallic Cu sites form, H_2 dissociation over metallic Cu occurs more readily than heterolytic dissociation, so could compete with oxidation from CO_2. Therefore, ZnO_x near metallic Cu sites can be maintained and Figure 6.13 (iii) shows regions of Cu*/ZnO_x. Reverse spillover of H* stored in ZnO (from earlier exposure to H_2) is ruled out as a reduction mechanism, since at a high pressure of CO_2 all of the

stored H* will react via the RWGS reaction to form water and deplete the H* reservoir.[277,290] Furthermore, when no H_2 pre-treatment was used (Figure A6.5 and A6.6), going from pure CO_2 and introducing H_2 still yielded a rapid reduction of Cu_2O. The proposed structure is supported in literature where the Cu*/ZnO_x interface is expected to form under oxidising conditions.[14]

Figure 6.13 (iv) shows the brass NP structure when at a higher H_2 ratio (3:1, H_2:CO_2), closer to conditions relevant to industrial methanol formation. The more reducing environment favours more ZnO_x formation so the Zn region now contains a mix of ZnO and ZnO_x. Additionally, the stronger reducing conditions means the Cu regions grow to include Cu^0 atoms separated from ZnO_x that are only surrounded by other Cu^0 atoms (more bulk-like). Cu^0 and Cu* are detected with AtmP-NEXAFS (Figure 6.8 (i)), so there must still be some Cu* remaining which is interacting with ZnO_x at the boundary between bulk-like Cu^0 and ZnO_x. This is similar to what was observed at the boundary between Cu^0/Zn^0 and ZnO_x when H_2 was dosed initially in Figure 6.12 (ii). It is worth noting that under pure H_2 following oxidation, STEM images (Figure 6.6 (iv)) showed a slight preference for Cu^0 on the outside of the particle and these conditions are not shown in Figure 6.13.

Under industrially relevant conditions (~3:1 ratio of H_2:CO_2), the oxidation state of Cu is metallic for brass NPs, regardless of direction of approach from either pure H_2 or CO_2. In contrast, for Cu alone then CO was required to maintain catalytically active Cu^0 sites (Chapter 4).[276,287] Figure 6.12 (iii) and 6.13 (iv) show that the oxidation state of Zn and the NP structure vary depending on the direction of approach to reaction conditions. Introducing CO_2 first favours formation of a ZnO_x/ZnO mixture, and the H_2/CO_2 gas mix is unable to recover Zn^0 since CO_2 will continually oxidise the exposed ZnO_x to ZnO.[11,14,276,296] The ZnO can be reduced to ZnO_x again via spillover of H* from Cu^0 sites.[277,290] Hence, under reaction conditions there is a dynamic change between

ZnO and ZnO_x.[275] The same result is not observed when approaching from H_2-rich conditions because the structure is very different. When H_2 is dosed first, a ZnO_x overlayer forms which is exposed to the external environment and is oxidised to ZnO when CO_2 is added, protecting the Zn^0 sites within the NP (Figure 6.12 (iii)). The results herein suggest the different behaviour with dosing order is the result of difficulty in reversing large changes in structure under oxidising conditions where CuO and ZnO become segregated. Addition of H_2 encourages mixing of Cu and Zn once again, but is insufficient to fully reverse the segregation which occurs.

Since the direction of approaching reaction conditions affects the structure and species present, it will also impact the active sites, and hence, the activity of the catalyst.[277,279,285–287,300,326] After a H_2 pre-treatment, there is a preference for the Cu^0/Zn^0 alloy surrounded by ZnO_x/ZnO, whereas when approaching from CO_2-rich conditions then the Cu*/ZnO_x species and strong synergy between Cu* and ZnO_x is preferred. There is potential to further investigate the catalytic activity of these species and potential active sites. Brass powder could be prepared using a H_2 or CO_2 pre-treatment before exposing it to reaction conditions (3:1, H_2:CO_2 ratio) and measuring the catalytic activity. It would be expected that the H_2 pre-treated sample would perform better, as this is done industrially, suggesting the Cu^0/Zn^0 alloy alongside the ZnO_x species is more catalytically active. These measurements would complement this study well; however, there was not enough time to access the required setup to perform them.

Finally, Figure 6.13 (v) shows how the structure may change when CO is added to the H_2 and CO_2 mixture to give a more reducing environment. Zn^0 is detected in AtmP-XPS (Figure 6.4 (d,vi)) so there is now alloying between Cu^0 and Zn^0. CO is a stronger reducing agent than H_2 so will enable reduction of ZnO_x to Zn^0. If the Cu^0/Zn^0 alloy is important for activity, then CO is vital to regenerate these sites should they be oxidised, and to encourage mixing between Cu and Zn again. [55,294] This observation agrees with

other studies which have also suggested CO_2-rich conditions favour Cu^0/ZnO_x species and the addition of CO will favour the formation of the Cu^0/Zn^0 alloy.[55] Similar to Chapter 4, where CO was important for maintaining Cu^0 sites, for brass NPs, the addition of CO is important for maintaining Cu^0/Zn^0 sites which, once oxidised, cannot be recovered by H_2 alone.[275]

6.7 Conclusion

The results presented in this chapter follow on from Chapter 4. Graphene membranes integrated into an E-cell enabled high pressure XPS and NEXAFS measurements of brass NPs to provide a greater understanding of the structure and oxidation state changes Cu and Zn experience under different gas compositions. STEM-EELS images complimented X-ray spectroscopy data.

Once again, the importance of studying a catalytic system under as near to realistic pressures as possible was demonstrated. In brass, Cu^0 did not oxidise at 0.3 mbar of CO_2, whereas at 1 bar of CO_2, Cu^0 oxidised to CuO. Similarly, the oxidation state of Zn under H_2 was influenced by pressure: under 0.3 mbar there was a mix of $ZnO/ZnO_x/Zn^0$, under 1 bar there was a mix of ZnO_x/Zn^0, demonstrating high H_2 pressures are required to reduce ZnO.

The temperature required for H_2 to reduce CuO/Cu_2O to Cu^0 was lower using brass compared to Cu alone. This was thought to most likely be from heterolytic dissociation of H_2 over ZnO when Cu_2O/CuO species are present. A low pressure of CO_2 was insufficient to oxidise the Cu in brass, in contrast to Cu alone. This is because CO_2 leads to preferential oxidation of Zn^0 and ZnO_x sites first. Only at high pressures of CO_2, once all of the Zn sites are oxidised, will Cu^0 then be oxidised.

The direction of approaching reaction conditions from either pure H_2 or pure CO_2 affected the chemical state, structure, and therefore active sites in brass. A H_2 pre-

treatment resulted in a Cu^0/Zn^0 alloy encased in a ZnO_x/ZnO overlayer under reaction conditions with no strong interaction between Cu* and ZnO_x. A pure CO_2 pre-treatment instead resulted in a significant change in structure and complete segregation of CuO and ZnO. Subsequently, under reaction conditions there were mainly Cu^*/ZnO_x sites present and no alloy, and H_2 could not recover the structure seen during a H_2 pre-treatment. This suggests the strong synergy between Cu* and ZnO_x was only present after more oxidising conditions. The introduction of CO began to recover the Cu^0/Zn^0 alloy and potentially a more mixed structure.

To further explore the most active phases, catalytic tests could be performed on brass powder under reaction conditions where different samples are exposed to either a H_2 or CO_2 pre-treatment. Depending on whether a H_2 or CO_2 pre-treatment yields a greater catalytic activity would help determine whether Cu^0/Zn^0 or Cu^*/ZnO_x sites are more active, respectively. DFT calculations would also be beneficial to better understand the features in the Zn L_3-edge.

Overall, this high pressure X-ray spectroscopy study has revealed information about the species present under reaction conditions which have not been observed before. In particular, the strong interaction between Cu* and ZnO_x after heavy oxidation in contrast to Cu^0/Zn^0 alloy after a H_2 pre-treatment. The *in situ* measurements whilst the gas composition was altered demonstrated that Cu^0/Zn^0 alloy and ZnO_x could both be present under reaction conditions, rather than one or the other as sometimes suggested by literature.

Chapter 7: Summary and Future Work

7.1 Summary

This thesis has focused on the development of techniques to enable high pressure, and, therefore, more industrially relevant *in situ*/*operando* studies of heterogeneous catalysis using soft X-ray spectroscopy. Chapter 1 detailed the benefits of using soft X-rays for surface sensitive studies, but also the limitations they can impose on experiments. The chosen method for extending X-ray spectroscopy to high pressure was the use of E-cells sealed with an X-ray or electron transparent window. The material the window is made from can be selected depending on the needs of the experiment. In this thesis, an X-ray transparent continuous SiN_x window was used for XAS and an electron transparent graphene window (suspended over a perforated SiN_x frame) was used for XPS. Chapter 3 presented the different E-cell designs used throughout studies included in this thesis and how they were adapted and improved for each experiment. Results across Chapters 4-6 demonstrated the scope of high pressure and liquid measurements possible with E-cells. They also highlight some of the drawbacks of the E-cell approach: that an appropriate membrane can be difficult to manufacture and using graphene windows can obscure O and C signals of interest.

The catalytic system studied in this thesis was the hydrogenation of CO_2 to methanol, which is relevant to the potential production of net-zero carbon fuel. In the first instance, as shown in Chapter 4, the role of CO in the gas mixture over a pure Cu catalyst was investigated. An E-cell sealed with a continuous SiN_x membrane enabled high pressure (100 mbar) XAS studies of the catalyst whilst varying the order of dosing H_2/CO_2/CO gas mixtures. Complementary NAP-XPS and MS data were also collected from analogous polycrystalline Cu materials. The order of dosing H_2 and CO_2, when approaching reaction conditions, affected the oxidation state of Cu. When approaching

from pure H_2 then Cu^0 was favoured, whereas when approaching from pure CO_2 then Cu_2O/CuO was observed. It was determined that CO acts as an O* scavenger to recover active Cu^0 sites which, if oxidised, could not be recovered in a reasonable timescale using H_2 alone at 200°C.

To extend high pressure measurements to include XPS, it was vital to develop a reliable method to produce graphene membranes. Chapter 5 showed a transfer technique using a Au/PDMS support to produce graphene membranes with >98% coverage of MLG and a reliability of ~95%. MLG membranes successfully sealed 1 bar of Ar gas within a NAP-XPS system, demonstrating that XPS measurements could be performed at high pressures. Furthermore, by producing BLG membranes the leak-tightness of the E-cell was improved, enabling measurements of the etching of Au with a flowing liquid within conventional lab-based XPS. However, the transfer technique required a high level of skill to obtain the reliability and coverage achieved in this thesis. Therefore, to make these approaches more widely accessible, a method to directly grow graphene on perforated SiN_x membranes was explored. The method involved depositing a thin and flat Ni film onto a perforated membrane followed by growing graphene via CVD. There was some success in the preliminary stages of developing this technique, however there remain issues still to be resolved.

Finally, in Chapter 6, brass NPs were investigated using a similar methodology as used in Chapter 4, but with a more representative NP catalyst for the hydrogenation of CO_2 which included Zn as well as Cu. H_2/CO_2/CO gas mixtures were sequentially dosed over the catalyst at 1 bar. The integration of graphene membranes enabled high pressure simultaneous XPS and XAS measurements. The aim of the study was to determine the role of Zn in improving the catalytic activity of Cu, a highly debated topic in literature. NAP-XPS and STEM-EELS data were also collected from brass to complement the high pressure study. The order of dosing H_2 and CO_2, upon approaching

reaction conditions, significantly influenced the structure of the brass NPs and the oxidation state of Zn, whereas the oxidation state of Cu was the same regardless of the direction of approach (Cu^0). When H_2 was dosed first, a Cu^0/Zn^0 alloy dominated under reaction conditions with a ZnO_x/ZnO overlayer. In comparison, when CO_2 was dosed first, mixing between metallic Cu and ZnO_x was favoured, resulting in a strong interaction between them; no Zn^0 was detected. The difference in structure and composition depending on the pre-treatment was attributed to the large structural change the NPs experienced when exposed to pure CO_2 where the Cu^0/Zn^0 alloy segregates into separate Cu and Zn species. Addition of CO appeared to aid the reduction of ZnO_x to Zn^0, encouraging more Cu^0/Zn^0 alloy formation, thus partly reversing the segregation that occurred during exposure to pure CO_2. These results suggest the possible active species for this catalyst is the Cu^0/Zn^0 alloy surrounded by ZnO_x/ZnO, where there is not a strong interaction between Cu and ZnO_x, and CO is important to recover and maintain these active sites.

The application of E-cells and graphene membranes (manufactured using the Au/PDMS technique) to perform *in situ* X-ray spectroscopy has continued within the Weatherup research group beyond the work outlined in this thesis. Most notably, high pressure XPS and NEXAFS measurements are now routinely performed at the CIRCE beamline (ALBA synchrotron, Spain) at 4 bar over long measurement periods to study other heterogeneous catalysts, such as a zeolite powder catalyst for the Fischer-Tropsch reaction. This demonstrates the potential wide-range applicability of the E-cell technique combined with graphene membranes to performed high pressure X-ray spectroscopy studies of other heterogeneous catalysts, other than those outlined in this thesis. The limitation of 4 bar is due to the maximum operating pressures of regulators used for gas cylinders, and not a limitation of the sealing capability of the E-cell or suspended graphene.

However, to pursue even higher pressures the sealing of the E-cell must be improved by replacing the graphite gaskets with a more leak-tight and heat-resistant alternative. It is an exciting prospect that the pressure capabilities of the E-cell are not currently limited by the performance of the graphene membranes, considering previous efforts have been restricted by unreliable manufacture of electron transparent windows. Additionally, a huge success of this project was that other members of the research group have reproduced the continuity of transferred graphene outlined in Chapter 5, therefore the Weatherup group can continue to perform high pressure X-ray spectroscopy far beyond this project.

The work presented in this thesis on the catalyst for the hydrogenation of CO_2 has added significantly to existing literature. In particular, the results presented here indicate the species present under reaction conditions are Cu^0/Zn^0 alloy and a weakly interacting ZnO_x/ZnO overlayer. Additionally, results show the introduction of CO helps maintain metallic Zn and Cu sites. This conclusion agrees with other soft X-ray studies, but disagrees with many hard X-ray studies. The wide range of conditions and measurement methods used to study this catalytic system can make it incredibly difficult to make any general and meaningful conclusions. The reason so much literature focuses on the $Cu/ZnO/Al_2O_3$ catalyst for CO_2 hydrogenation is the implication this has on the future of developing cleaner energy and decreasing global CO_2 output. But, too often the results shown in literature are not linked back to this motivation. The results shown here could be improved on by increasing the pressure and by using the industrial catalyst as a powder, thus making the results more representative of industrial conditions. Ultimately, even with greater understanding of this system, the question must be asked: how could this knowledge potentially improve the activity or selectivity of the process to make it feasible on a large scale? The next step must be to start using the vast amount of knowledge available in literature to optimise the process further with this

understanding, rather than all efforts continuing to focus on measuring the system as it is.

Overall, this thesis has demonstrated the application of E-cells to high pressure XPS and NEXAFS, and that this is a powerful tool to investigate the changes that catalysts undergo under industrially relevant reaction conditions.

7.2 Future Work

As mentioned in section 7.1, there were attempts to directly grow graphene onto a perforated SiN_x membrane that were not completed in this project. The main issues were:

1. Improving the deposition of Ni thin films to increase their stability and decrease their roughness.
2. Optimising the growth of graphene using acetylene (C_2H_2) to reduce the level of defects without increasing the growth temperature.
3. Improving the suspension of Ni such that the film is not damaged during CVD.

Suggested solutions are:

1. The power and Ar gas flow during PVD could be optimised methodically for film stability and roughness. There is also scope to try heating the substrate during PVD to reduce the stress that occurs at high temperatures in CVD.
2. The introduction of Au has previously been used to reduce the levels of defects in CVD-grown graphene on Ni.[327] A thin (1-3 nm) layer of Au could be evaporated atop Ni and the growth optimised on this new catalyst composition.
3. Depositing Ni films on partially etched SiN_x membranes is the most convenient method to ensure the Ni remains stable throughout the CVD process. However, removing the SiN_x beneath the Ni without damaging the graphene could be challenging. Suspending a thin layer of Ni over the holes of a perforated SiN_x

membrane avoids this issue, but this is difficult to achieve and the thin Ni is likely to be damaged during the heating steps in CVD. Further discussion of membrane fabrication with the manufacturer (Silson[128]) could be valuable to see if thicker, and more stable Ni could be deposited during the perforated membrane production.

Overall, the task to produce directly grown graphene on perforated SiN_x membranes is challenging. If the quality of the transferred graphene using the Au/PDMS support technique is adequate, and there is appropriate time to learn how to transfer graphene in this way, then the Au/PDMS transfer method is currently the most efficient way of producing graphene membranes.

The results in Chapter 6 could be further enhanced with catalytic testing and DFT modelling. A catalytic reactor could be used to probe the activity of brass powder to compare when reaction conditions are approached from either a H_2-rich or CO_2-rich environment. It is expected a H_2 pre-treatment would yield greater activity, as in industry, thus Cu^0/Zn^0 alloy sites surrounded by ZnO_x/ZnO are more active than Cu^*/ZnO_x sites. This would be an important conclusion in the context of the literature in this area, since the strong synergy between Cu and ZnO_x is thought to be important. The effect of the addition of CO on activity could also be tested, where in the case of a CO_2 pre-treatment it is expected that CO will increase the activity by increasing the available Cu^0/Zn^0 sites. DFT simulation of the Zn L_3-edge in brass for Zn^0 and ZnO_x would aid interpretation of the Zn L_3-edge, but was not essential, as reference data collected in this thesis was sufficient.

Overall, the results presented in this thesis demonstrate the potential of E-cells to extend X-ray spectroscopy to atmospheric pressures and the accessibility of *in situ*/*operando* techniques has been enhanced. In particular, XPS could be performed at

pressures in excess of 1 bar within NAP-XPS system and up to 1 bar within lab-based XPS systems.

Appendix

Chapter 2: Characterisation Techniques

Origin of Signals in SEM

Figure A2.1 (a) shows the interaction volume for incident electrons and the approximate origin depth of emitted electrons and X-rays which can be used to form an image.

SE come from inelastic scattering of incident electrons when they interact with weakly bound valence electrons in the sample.[328] SE typically have very low energy due to the inelastic scattering events and are often defined as being in the <50 eV range. To escape the sample surface the SE must have enough energy to overcome the work function of the material. Additionally, excited electrons will undergo further inelastic collisions before reaching the surface. Therefore, SE originate from very near the sample surface (few nms for most materials), since excited electrons from deeper in the sample will undergo more inelastic scattering and lose too much energy so cannot escape the sample surface.[328]

Incident electrons can also interact more weakly with the sample and be deflected via elastic scattering forming the BSE signal. BSE can be described using a “billiard-ball” model where the mass of the electron is significantly lower than the nuclei of an atom hence will be scattered by the nucleus with almost no energy loss.[328] Heavier nuclei will appear brighter in the BSE signal since the scattering will be stronger. Similar to SE, when escaping the sample, electrons will undergo some inelastic scattering such that they lose a small amount of energy. BSE are approximately defined as having energy >50 eV.[328] It is important to consider the contribution of BSE to the SE signal, since BSE from very deep into the sample could undergo enough inelastic scattering such that their energy is <50 eV. By using a lower energy incident electron beam, the distortion of the

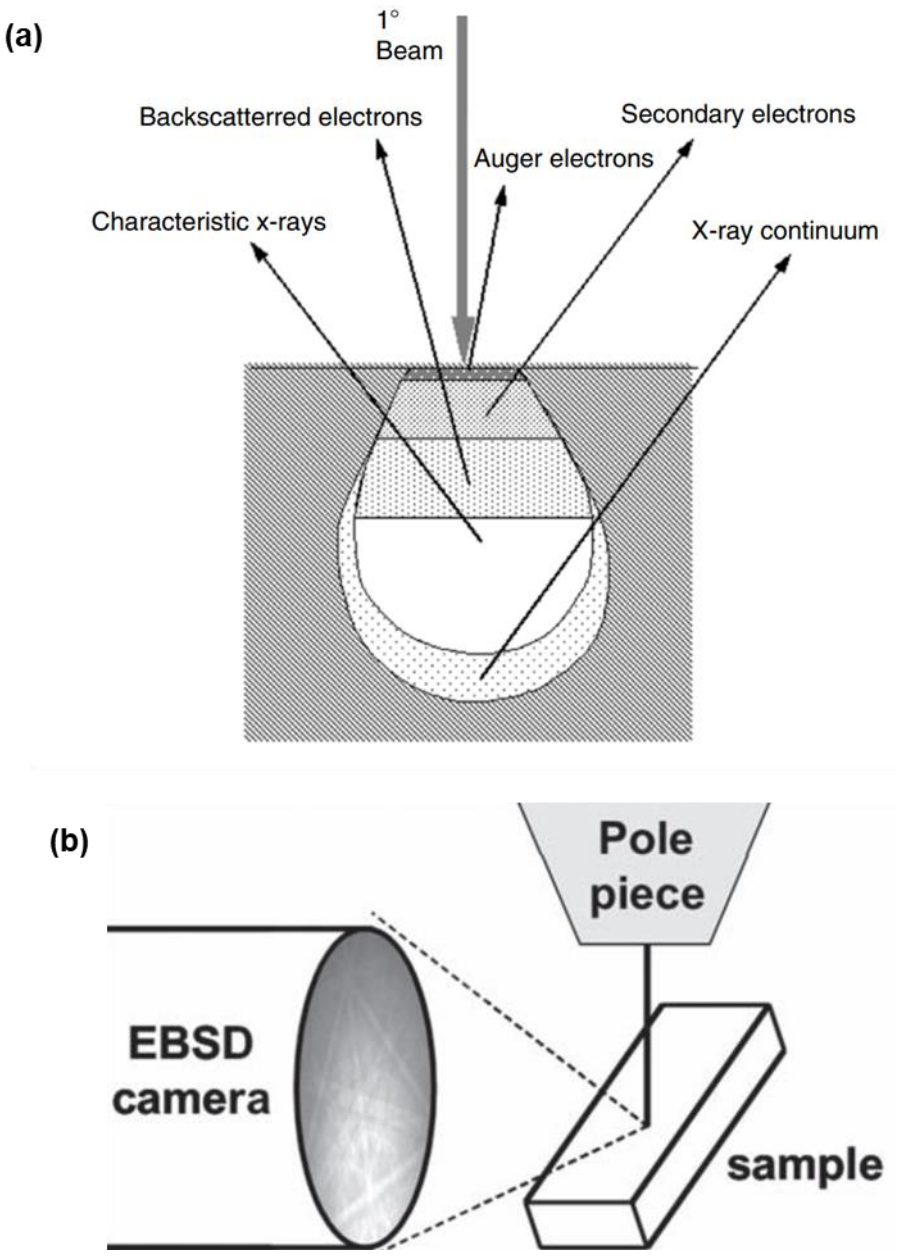


Figure A2.1: *(a) Schematic showing the interaction volume for the incident electron beam in SEM and the depths from which different signals originate. (b) Diagram showing how EBSD is collected from a sample in SEM. (a) Taken directly from W. Zhou et al., in* Scanning Microscopy for Nanotechnology: Techniques and Applications*, 2007, pp. 1–40. (b) Taken directly from D. Stojakovic,* Process. Appl. Ceram.*, 2012, **6**, 1–13.*

SE signal from BSE can be minimised. Lower energy electrons will not penetrate as deeply into the sample and decrease the BSE signal, whereas the SE signal is less dependent on the incident electron beam energy.

BSE can also be used in EBSD experiments as shown in Figure A2.1 (b). When the sample contains a well-defined crystal structure the elastically scattered electrons will undergo constructive and destructive interference as a result of scattering from consecutive layers within the crystal as described by Bragg's Law.[329] During EBSD experiments the sample is tilted at 70° with respect to the horizontal and the diffraction signal is collected at the EBSD camera. The diffraction pattern can be used to identify different crystal orientations which can be mapped to the surface.

Optical Microscopy

Optical microscopy is primarily used in this thesis to characterise graphene layers transferred to Si/SiO_2 wafers. A Nikon Eclipse LV100ND microscope was used for all images collected with 5x, 20x, 50x, and 100x magnification lenses available. It was possible to view the sample either using reflected light or transmitted light through the sample. Transmission mode was particularly useful for viewing suspended films over perforated SiN_x membranes.

Figure A2.2 shows graphene transferred to a Si/SiO_2 wafer viewed under the 50x magnification lens. There is a clear contrast between the graphene (blue) and underlying Si/SiO_2 substrate (light orange). Stacked graphene layers result in a darker blue colour as shown in Figure A2.2. The visibility of graphene can be optimised by altering the thickness of the SiO_2 layer and the wavelength of the incident light.[330] The optical contrast between SiO_2 and graphene occurs due to the increased optical path and the opacity of graphene.[330] Under white visible light, graphene is visible on ~100 nm and ~300 nm thick SiO_2.[330] Hence, throughout this thesis all optical microscope images are from graphene

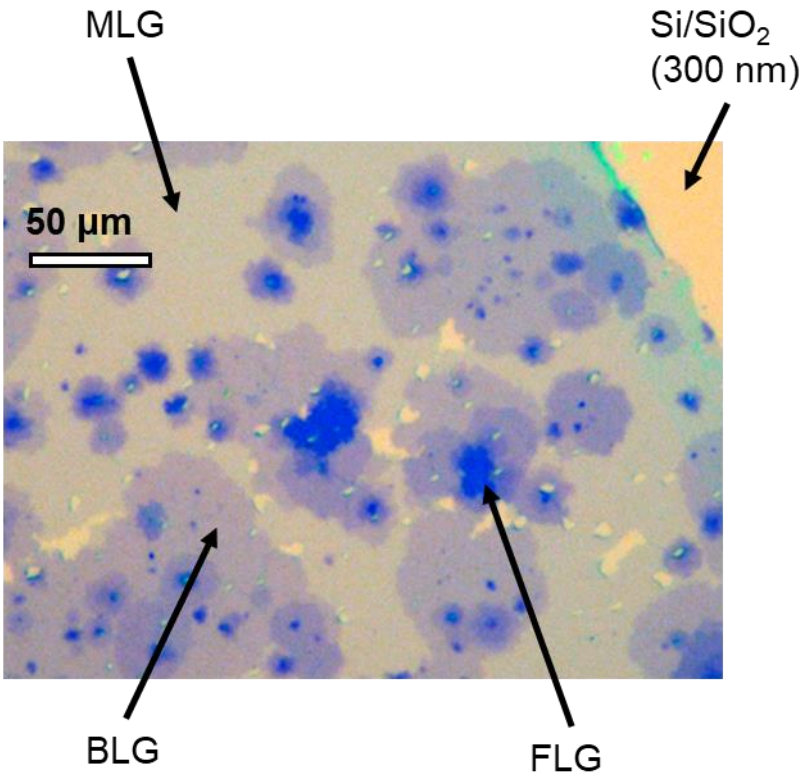


Figure A2.2: *Optical microscope image at 50x magnification. The image shows graphene grown via CVD and transferred to a Si/SiO₂ wafer. Regions of the underlying wafer, MLG, BLG, and FLG have been indicated.*

transferred to Si/SiO_2 with a thickness of 300 nm. If a different wavelength of light is used then a different thickness of SiO_2 would be required, e.g. 200 nm thick for blue light.[330]

Origin of Features in Raman Spectroscopy for Graphene

To understand how Raman spectroscopy provides valuable information about graphene it is useful to first consider the fundamentals of vibrational spectroscopy.

When a sample is irradiated with a laser the vibrational modes (phonons) of a molecule can be excited or de-excited via an imaginary vibrational state resulting in inelastic scattering of the incident photons.[331] Figure A2.3 shows the different inelastic scattering events which can occur. When a molecule is excited to a higher vibrational level it creates a phonon (Figure A2.3 (c) Stokes scattering) and will release a photon with energy lower than the incident laser. Or a phonon can be annihilated when the molecule de-excites to the vibrational ground state (Figure A2.3 (a) Anti-Stokes scattering) thus releasing a photon with energy higher than the incident laser.[110,331] The intense Rayleigh feature in Raman is from elastic scattering of photons, which does not contain any information about the vibrational modes of a molecule (Figure A2.3 (b)). Generally only the Stokes scattering events are detected since they are more intense than the Anti-Stokes features, because the vibrational ground state is more highly occupied compared to the vibrational excited states needed for Anti-Stokes scattering. Raman spectroscopy measures the energy change of incident photons for all vibrational modes which result in a change in polarizability of the molecule (Raman active).[331]

In solids, the process is slightly more complex as the incident photon can also excite electrons to create an electron-hole pair. A similar process to that described above will occur to produce a Raman spectrum, but it can involve an electron-hole pair and is, thus, influenced by the electronic structure of the material too. Electronic excitations are particularly important in Raman spectroscopy of graphene, because graphene is a semiconductor with a well-defined band-gap that is very small. Hence, the incident laser

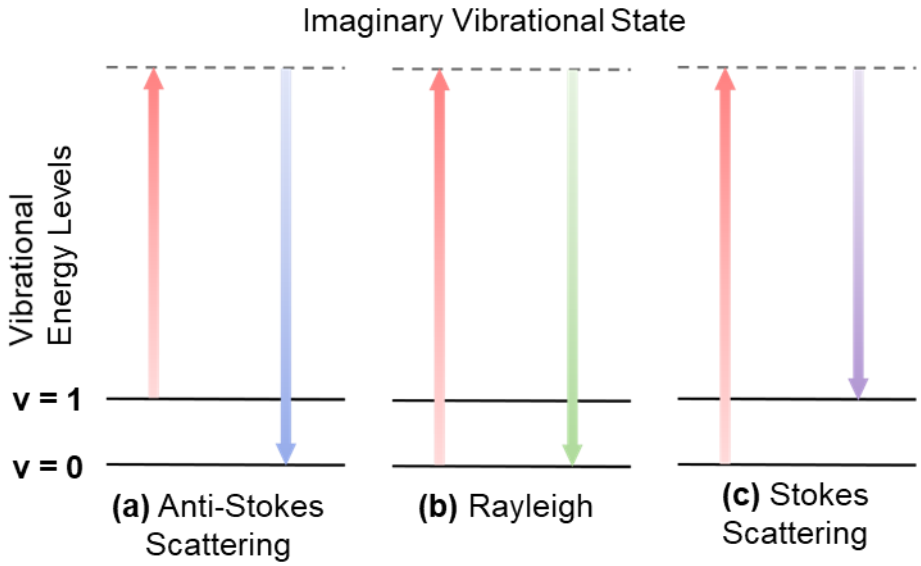


Figure A2.3: *Basic vibrational energy level diagram demonstrating the different processes leading to features in Raman.*

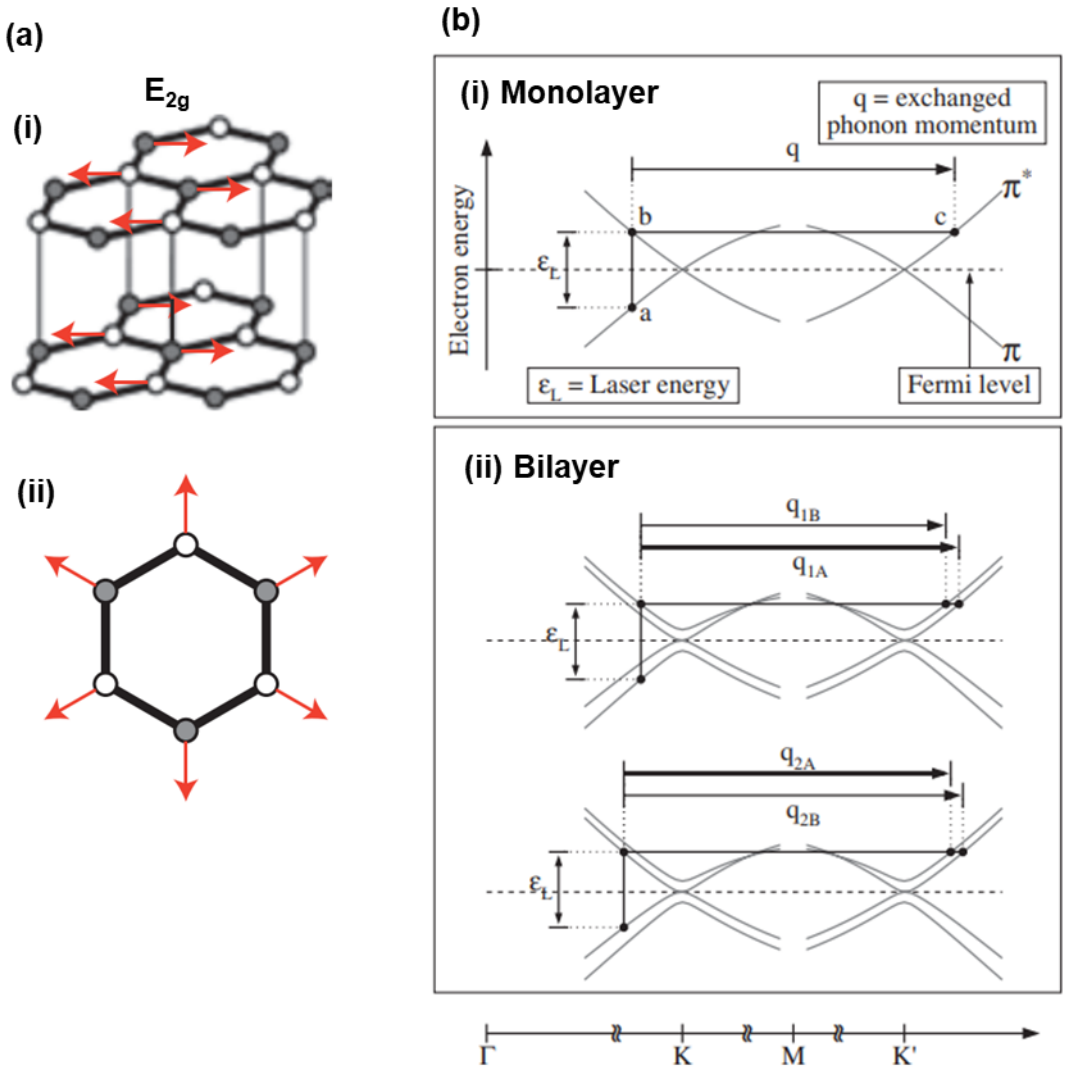


Figure A2.4: *Diagrams explaining the origin of features in Raman spectroscopy for graphene. (a) (i) The E_{2g} degenerate in-plane transverse optical mode responsible for the G peak and (ii) the breathing vibrational mode responsible for the D peak. (b) The band structure and the interaction between an electron-hole pair and phonons result in: (i) a single 2D peak for MLG and (ii) four 2D peaks in BLG. (a) Taken from A. C. Ferrari* et al.*,* Nat. Nanotechnol.*, 2013, **8**, 235–246. (b) Taken from A. C. Ferrari* et al.*,* Phys. Rev. Lett.*, 2006, **97**, 187401.*

energy is sufficient to excite electrons from the valence to the conduction band and will influence the vibrational excitations.

The three main peaks observed in a Raman spectrum of graphene are: D (~1350 cm^{-1}), G (~1580 cm^{-1}), and 2D (~2700 cm^{-1}). As mentioned in the main text, a G peak is indicative of sp^2 hybridised carbons where the position is affected by the particular sp^2 structure present. The vibrational mode responsible for the G peak in graphene is shown in Figure A2.4 (a,i), this is the E_{2g} degenerate in-plane transverse optical mode.[112]

The vibrational mode responsible for the 2D and D peaks is the breathing mode shown in Figure A2.4 (a,ii). The 2D peak is the result of a double resonant process where there is an exchange between phonon momentum and the electronic structure, as shown in Figure A2.4 (b,i) for MLG. An electron-hole pair is created, the electron is then scattered by a phonon (with momentum **q**, b→c), the electron is then scattered again by another phonon (with momentum -**q**, c→b), before finally the electron-hole pair recombine.[110,111] The exchange of two phonons allows momentum and therefore energy to be conserved. The D peak is formed via a similar process but where only one phonon is exchanged, hence the D peak is at half of the excitation energy of 2D. To ensure momentum is conserved when only one phonon is exchanged it must interact with a defect in graphene.[109–111] Therefore, the intensity of the D peak correlates directly with the presence of defects in graphene and this peak does not appear for defect-free graphene.[107] In highly defective samples other peaks such as: D', D+D", and D+D' can also appear. [109,110]

MLG has a linear dispersion curve which is not retained when two graphene layers are stacked on top of each other (Figure A2.4 (b,ii)) and instead, through Van der Waal's interactions between layers, the band splits to contain 4 components for BLG.[211] This splitting results in 4 possible phonon exchanges with different momentum in BLG compared to one value of momentum for MLG.[110,111] This means the 2D peak in MLG

can be fitted with a single Lorentzian and BLG requires 4 Lorentzian peaks. The more layers of graphene present, the more the electronic structure changes, thus the 2D peak changes with this. Therefore, the FWHM of the 2D peak can be used to determine the number of graphene layers present.

Chemical Vapour Deposition Chamber

Low pressure CVD of graphene was performed in a custom-built vacuum chamber made from 304 stainless steel (Figure A2.5). The CVD chamber was newly built at the start of this project. Pumping was achieved using a combination of: a rotary vane (roughing) pump containing a gas ballast to help pump away H_2 (Leybold, SCROLLVAC plus), and a turbomolecular (turbo) pump (Leybold, TURBOVAC 450i). The roughing pump alone pumped from ambient pressure to ~10^{-2} mbar. The turbo pump operated at a maximum of ~10^{-3} mbar for long durations and could achieve a base pressure of ~10^{-8} mbar.

Process gases were dosed into the chamber using Swagelok tubing (6 mm) and computer-operated MFCs (Bronkhorst, EL-FLOW Select), see Figure A2.5 (i). The relevant gases for CVD were H_2, C_2H_4, and C_2H_2; a single MFC was used for H_2, whilst another single MFC was sufficient for either C_2H_4 or C_2H_2 since the gases were never dosed simultaneously. From previous work, it was known that MFCs are susceptible to leaking (~$2x10^{-6}$ mbar) even when fully closed (0 sccm).[327] Swagelok quarter turn manual plug valves were placed either side of the MFC to enable full control of gas dosing and to account for the small leak across the MFCs.

Heating was achieved using a graphite heater coated with an insulating layer of boron nitride (Boroelectric, tectra) and temperature was recorded using a type C thermocouple placed at one end of the heater (Figure A2.5 (ii)). The heater power was controlled and temperature was monitored using a PID control unit (Yudian, AI-516 Artificial Intelligence Industrial Controller). Samples were placed as near to the centre as

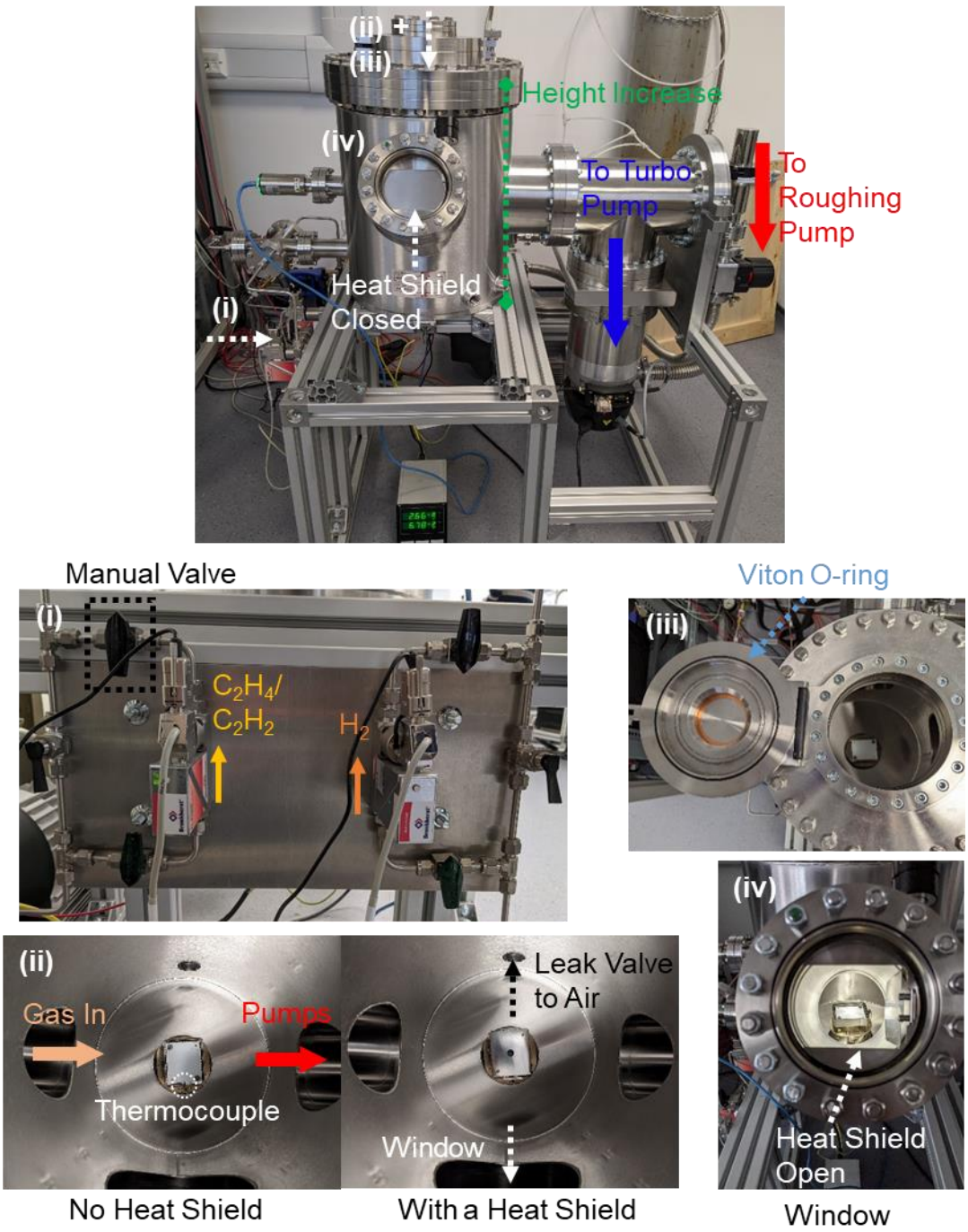


Figure A2.5: *Pictures of the custom-built CVD chamber used for graphene growth. Top: whole chamber indicating location of pumps and other relevant components. (i) MFCs for gas dosing. (ii) Top-down view of the inside of the chamber showing the heater with and without a heat shield. (iii) Top-down view of the lid of the chamber indicating the sealing Viton O-ring. (iv) The window of the chamber with its heat shield open.*

possible to ensure uniform heating, however there was likely some discrepancy between the temperature recorded at the edge using the thermocouple and the temperature at the centre of the heater where the samples were placed.

The picture shown in Figure A2.5 was the second design of this CVD chamber where the distance between heater and lid was increased to prevent the Viton O-ring from overheating (Figure A2.5 (iii)). When the first, smaller chamber was used then a heat shield was incorporated over the heater to protect the lid as shown in Figure A2.5 (ii). The hole in the centre of the heat shield ensured samples beneath were still exposed to the gases dosed into the chamber. The window at one of the ports for the CVD chamber was used to check on samples during growth. An additional heat shield was added here to prevent the window from overheating and potentially cracking at higher temperatures during long growth processes (Figure A2.5 (iv)).

During graphene growth optimisation, it was determined that a small leak of air was beneficial to remove adventitious carbon during heating. A leak valve was added to one of the ports of the chamber which was open to the atmosphere, thus an air leak could be introduced in a controlled manner (position indicated in Figure A2.5 (ii), but is not visible).

Chapter 3: Environmental Cells

Choice of Window Material – Transparency

From section 3.2, the choice of window typically involves balancing a variety of factors including the need for X-ray and/or electron transparency, the pressure difference which must be maintained, spectroscopic overlap of elemental signals with those being measured, compatibility with the reaction environment, and cost. This section will consider two important factors in more detail to compare window materials: transparency and stability.

Whether X-rays or photoelectrons can be transmitted by the window is determined by the attenuation length or IMFP of X-rays or photoelectrons respectively.[34,36,41–44] Different materials will scatter X-rays/photoelectrons by different amounts. For a specific material to be used as an effective window the thickness should be less than the attenuation length/IMFP in that material. In Chapter 1 it was mentioned that the attenuation length/IMFP can be increased by increasing the energy of the incident photons in X-ray spectroscopy. Figure A3.1 shows how the (a) IMFP of photoelectrons and (b) attenuation length of X-rays varies in common window materials for (a) XPS and (b) NEXAFS.[34,41,43] It is clear from these figures that increasing photon energy (i.e. using hard X-rays) will increase attenuation length/IMFP, therefore allowing a thicker window.

For XPS, however, making the choice to use hard X-rays is not that simple. Chapter 1 also mentioned the need to consider photoionisation cross-section which rapidly decreases with increasing photon energy, therefore the probability of an ionisation event releasing an electron decreases with increasing photon energy. The intensity of photoelectrons being generated per second from a material for a given spectral peak (I) can be determined as:[77]

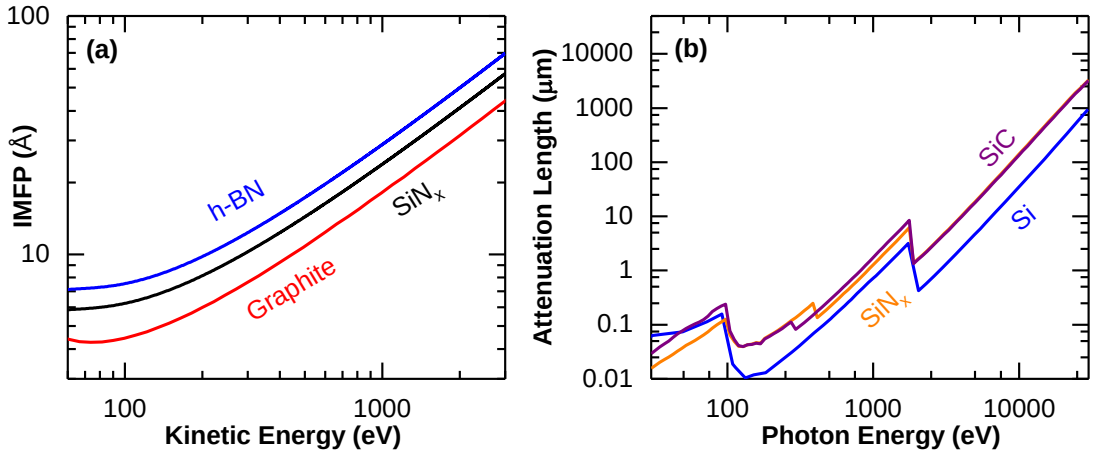


Figure A3.1: *(a) IMFP of electrons varying with the kinetic energy of photoelectrons in possible XPS window materials: SiN_x, graphite, and h-BN. (b) Attenuation length of X-rays varying with incident X-ray energy. Shown for possible NEXAFS window materials: Si, SiN_x, and SiC. The large decreases in attenuation length correspond to the absorption edges of: Si L-edge at 100 eV, C K-edge at 280 eV, N K-edge at 400 eV and Si K-edge at 1840 eV. (a) Plotted using data from S. Tanuma et al.,* Surf. Interface Anal.*, 2011, **43**, 689–713 and H. Shinotsuka et al.,* Surf. Interface Anal.*, 2019, **51**, 427–457. (b) Plotted using data from B. L. Henke et al.,* At. Data Nucl. Data Tables*, 1993, **54**, 1–168.*

Equation A3.1:

$$\mathrm{I(E)} \propto \sigma_S(\mathrm{E})\, \lambda_S(\mathrm{E})$$

Where σ_S is the photoionisation cross section[45,332] and λ_S is the IMFP[333] of photoelectrons in the sample material, and E is photoelectron kinetic energy. Higher energy incident photons will generate photoelectrons of higher kinetic energy, therefore E is proportional to incident photon energy. Hence, σ_s is dependent on E. As incident photon energy is increased, E and λ_s increase whilst σ_s decreases, therefore a peak intensity for a given photoelectron kinetic energy (and corresponding incident photon energy) could be calculated for a specific material (λ_s is material dependent) and core level excitation (σ_s is excitation dependent). As shown in Figure 3.1, in the main text, the sample material is usually deposited onto the window and photoelectrons must travel through the window to be detected. In the context of photoelectron detection through a window material an additional term must be included in Equation A3.1 to include the attenuation of photoelectrons by the window. The fractional loss of intensity of photoelectrons can be calculated using the Beer-Lambert law, hence an additional exponential term is included to give:

Equation A3.2:

$$\mathrm{I(E)} \propto \sigma_S(\mathrm{E})\, \lambda_S(\mathrm{E})\, e^{-\frac{t}{\lambda_W(E)}}$$

Where t is the thickness of the window and λ_W is the IMFP of photoelectrons in the window material. For the purposes of this model: the electron analyser is assumed to be normal to the sample surface, attenuation length of incoming photons is neglected (as it will be 1000 times greater than the IMFP, see Figure A3.1) so no sharp discontinuities from absorption edges are seen, and instrument-related factors have been omitted.

Figure A3.2 (a) and (b) show the variation in photoelectron intensity with kinetic energy of photoelectrons (based on Equation A3.2) for Cu 2p and Cu 3p core levels for several representative window materials (graphene[334], Si (15 nm)[72], and SiN_x (5 nm)[66]).[45,332,333] Cu was chosen due to its relevance to experiments in this thesis. Single electron photoionisation cross section values were taken from literature and the IMFP was calculated using the formula from Powell and Jablonski.[45,332,333] This figure demonstrates the trade-off between IMFP and photoionisation cross section, yielding a peak in the intensity of photoelectrons. The photoelectron intensity does not continue to increase with increasing kinetic energy of photoelectrons (and therefore incident photon energy), as would be expected if it was only IMFP dependent. The thinner the window material the higher the maximum photoelectron signal reaching the detector. Furthermore, the maximum intensity is at lower kinetic energies for thinner windows, highlighting that these may be most suitable at the energies typically available in conventional lab-based XPS systems (e.g. 1486 eV). Additionally, due to the variation of photoionisation cross section between Cu 2p and Cu 3p core levels, the peak intensity occurs at a lower kinetic energy when measuring the Cu 3p compared to Cu 2p.

The observed variations in Figure A3.2 highlight the importance of carefully selecting a suitable combination of core level, incident photon energy, and window to obtain a measurable signal in XPS. For XPS measurements it is not simply the case that by increasing photon energy that a more intense signal will be obtained. Following the discussion in Chapter 1, surface sensitive information is desired for studying the interface of heterogeneous catalysts, hence soft X-rays are preferred for both NEXAFS and XPS. Therefore, thinner windows are required for E-cells performing *in situ/operando* measurements of catalysts to enable the effective use of soft X-rays.

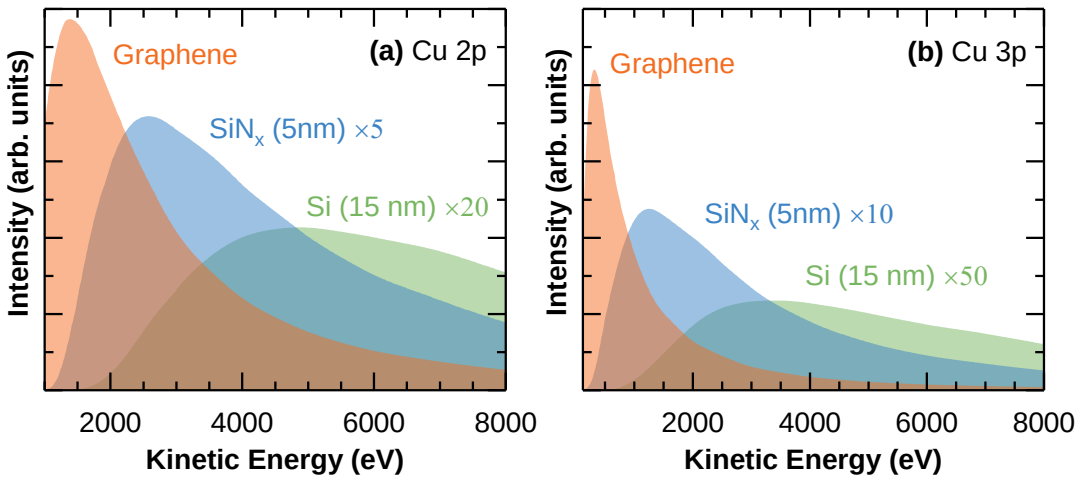


Figure A3.2: *Variation in photoelectron intensity ($I(E) = \sigma_S(E)\,\lambda_S(E)\,e^{-\frac{t}{\lambda_W(E)}}$), with photoelectron kinetic energy (E) for a sample (S) through the window (W) for the: (a) Cu 2p and (b) Cu 3p core levels. The thinner the window material, the lower the photoelectron kinetic energy (hence incident photon energy) required to achieve the strongest signal. Photoionisation cross section data taken from J. J. Yeh* et al*.,* At. Data Nucl. Data Tables*, 1985, **32**, 1–155 and J. H. Scofield, Lawrence Livermore Lab., 1973, 5–6. IMFP was calculated using C. J. Powell* et al*., NIST Electron Inelastic-Mean-Free-Path Database, 2000.*

Choice of Window Material – Stability

A theoretical treatment demonstrates that thinner windows are preferred to optimise signal strength for soft X-ray spectroscopy. Practically, however, it is not suitable to use the thinnest possible material as mechanical strength must also be considered. The mechanical strength reflects the material's ability to maintain a pressure difference across it, as required in an E-cell. The following equations relate a material to the pressure difference across it which will initiate rupture: [334]

Equation A3.3:

$$\delta = a\sqrt{1.5(1-\nu)\,\sigma'/E'}$$

Equation A3.4:

$$\Delta P = \frac{8E't\delta^3}{3(1-\nu)a^4}$$

Where: ΔP is the pressure difference that can be maintained, a is the radius of aperture the material is maintaining a pressure difference over, δ relates to the deformation of a material under pressure before breaking, and t is the thickness of the material (see Figure A3.3). The material specific quantities are: E' (Young's modulus), σ' (tensile strength), and ν (Poisson's ratio).

The variation of pressure difference before rupture with aperture size and window material is shown in Figure A3.4. As expected, the smaller the size of the aperture it must seal, the more stable the window is. Figure A3.4 (a) was calculated using Equations A3.3 and A3.4 from Leidinger *et al.*[334] and material specific properties were taken from references [222,334–336] using δ = 0.1a for graphene.[334] Figure A3.4 (b) combines calculated data from (a), and values taken from reference [129]. The window dimensions were chosen to resemble those used in representative E-cell studies and those used in this

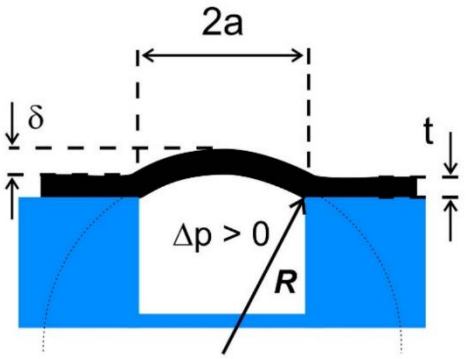
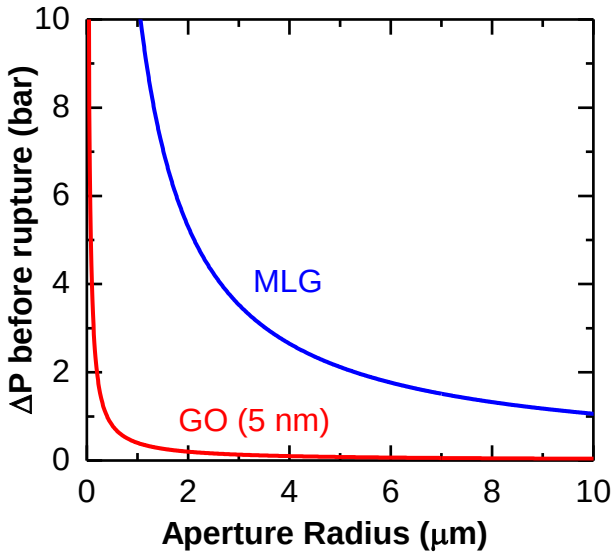


Figure A3.3: *Diagram demonstrating the parameters in Equations A3.3 and A3.4 to calculate the pressure difference a material can sustain over an aperture before bursting. Taken from P. Leidinger* et al*.,* J. Phys. D: Appl. Phys*., 2021,* ***54****, 234001.*

(a)



(b)

Material	Monolayer Graphene	Graphene Oxide	SiN_x
Thickness (nm)	~0.3	~5	~100
Relevant Aperture Dimensions (μm)	⌀1	⌀3	500 x 500
ΔP for Rupture (bar)	21	0.4	>4.0

Figure A3.4: *(a) The pressure difference required to rupture a window varying with radius of aperture for MLG and 5 nm thick GO. Data in (a) was calculated using Equations A3.3 and A3.4, and the values for material properties were taken from references in the main text. (b) Table summarising rupture pressures of some example windows chosen to correspond to E-cell reports in literature. The values for MLG and GO were calculated in the same way as for (a) at fixed radii. The rupture pressure for SiN_x was taken from: Silson - Differential Pressure Windows, https://www.silson.com/product/pressure-windows-vacuum-windows/, (accessed 22 March 2024), and is representative of membrane dimensions used in this thesis.*

thesis.[57,58] This comparison emphasises the potential for using graphene to cover small aperture sizes (often with multiple apertures in an array) due to its ability to maintain a large pressure difference at thicknesses where it is suitably electron transparent. Figure A3.4 (b) shows that the perforated SiN_x window will most likely break before graphene does, especially as perforations will weaken the window further (not included in this model). Although continuous SiN_x (100 nm) can maintain large pressure differences for large aperture sizes (0.5 × 0.5 mm), at these thicknesses it is not suitably electron transparent for use in XPS measurements. Instead a smaller aperture size with a thinner window material is preferable.

To conclude, graphene appears to be the best option for applications requiring both high transparency and high stability, under the assumption that the graphene is continuous and defect-free. As discussed in Chapter 5, this is very difficult to achieve in practice.

Examples of Applications of Membranes – Continuous Membranes

As mentioned previously the typical material used for windows in continuous membranes is SiN_x due to its robust and relatively cheap nature.[25,61,126,127,62,64,101,121–125] For example, it has been used to investigate the preferential oxidation of CO gas over a Co catalyst.[15,25] NAP-XPS and NAP-NEXAFS measurements were used to study behaviour up to 0.5 mbar, but to achieve much higher pressures (1 bar) a gas-flow E-cell sealed by a membrane with a 100 nm thick SiN_x window was needed. For this window thickness, soft X-rays could be used and data was collected using EY-mode, therefore surface sensitive information was collected.[102,137] Figure A3.5 shows the design of the E-cell used which was made mainly from PEEK and shows how a drain current for EY measurements was collected. This enabled the investigation of the effect of introducing V into the Co catalyst where it was determined V aided in preventing the

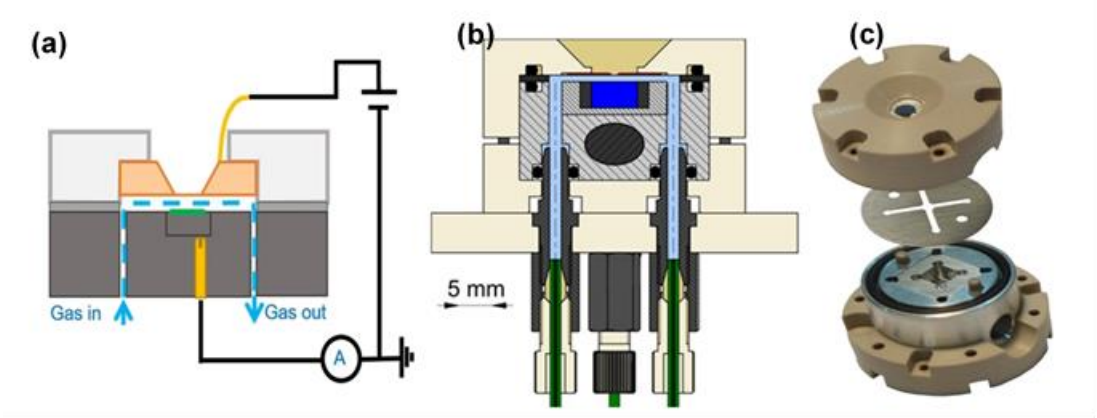


Figure A3.5: *(a) Schematic demonstrating the electrical circuit which enables drain current measurement needed for EY collection in NEXAFS. (b) Schematic of the cell design with an outer casing of PEEK (beige and green) encasing aluminium (grated light grey) and a molybdenum centre (grated black at the centre) where gas is fed through the stainless steel tubes (grated dark grey) and the cell is sealed with Viton O-rings (black) and a continuous* SiN_x *membrane. (c) Picture of the cell. (a-c) Taken from C. Castán-Guerrero* et al., Rev. Sci. Instrum.*, 2018,* ***89****, 054101.*

oxidation of the CoO active sites to the inactive Co_3O_4 species, confirming the catalyst is more active when V is incorporated.[15]

SiN_x membranes can also be used to study the solid-liquid interface through either a static or flow E-cell. Beam damage was observed when using a SiN_x sealed liquid-flow cell to measure NEXAFS of a Cu film exposed to alkali halide solutions (pH 13.0).[62] In this example both EY and FY were collected to probe the surface and bulk respectively. By using soft X-rays, the Cu L_3-edge from EY was collected showing oxidation of Cu to CuO when exposed to the X-ray beam. The Pourbaix diagram of Cu at a pH of 13.0 suggests Cu should not undergo significant dissolution to Cu^{2+}.[62] Furthermore, the extent of oxidation increases over time suggesting it is a direct consequence of exposure to the X-ray beam.[62] Further evidence for beam induced effects were seen when, using the same setup as liquid measurements, Cu was exposed to air under the X-ray beam. EY measurements showed the Cu surface started with a mixture of Cu_2O/CuO (from surface oxidation after being stored in air) where the CuO component increased over time when exposed to the X-ray beam. FY measurements initially showed a Cu^0 bulk where the proportion of Cu_2O also grew over time. This behaviour indicates beam induced effects where the Cu surface was oxidised in air more rapidly in the presence of the X-ray beam compared to without, such that eventually the bulk started oxidising too.[62] Therefore, it is important to consider beam damage in experiments using E-cells.

More recently there have been design developments to attempt to minimise beam damage. A SiN_x membrane was once again used in soft X-ray NEXAFS experiments, but in this case it sealed PDMS containing microfluidic channels to study the complexation of Ca with ethylenediaminetetraacetic acid as a standard reaction.[337] By altering factors such as flow rate, the X-ray beam size and flux, exposure time, and

concentrations of the solution, the beam damage effects were minimised.[337] The stability of SiN_x was important to allow long term measurements.

Finally, as previously mentioned SiN_x has also been used for XPS measurements. SiN_x sealed a static volume of different concentrations of CsCl solutions within an E-cell. Through using a lab-based XPS system with an Al-Kα source (1486.7 eV) Cs 4d peaks were observed and their intensity varied with concentration as expected.[66] This experiment did not require a NAP system because SiN_x sufficiently sealed the cell resulting in no leaks. However, due to the short IMFP of electrons a combination of a very thin SiN_x window (5 nm) and long exposure times were needed and the signal strength was still very weak.[66] Hence, most examples of soft XPS have used graphene membranes instead.

Examples of Applications of Membranes – Perforated Membranes

One of the first implementations of membranes using graphene as a window came in 2011 when A. Kolmakov *et al.* suspended GO flakes over a small single-hole (Figure A3.6 (a)).[58] GO was deposited using a Langmuir-Blodgett technique and they measured Au NPs in XPS with an aqueous salt solution behind the window.[58,338] However, an issue with this design is the single-hole meaning any leaks will result in complete rupture and failure of the cell. Additionally, the design does not allow for the flow of liquid, therefore when probing a chemical reaction the concentrations will change and the reagents will not be replenished resulting in variations in reaction rate over time.

An adaptation of this is: incorporated multichannel arrays, which are typically sealed with BLG where each channel is an individual reaction cell (Figure A3.6 (b)).[59,63,67,75] This setup has been used to collect photoemission electron microscopy (PEEM) images whilst applying a potential across electrodes. Therefore, enabling *in situ* data collection to determine the effect of an applied potential on the oxidation state of Cu in the $CuSO_4$ electrolyte contained in the cell.[67] PEEM provides surface sensitive

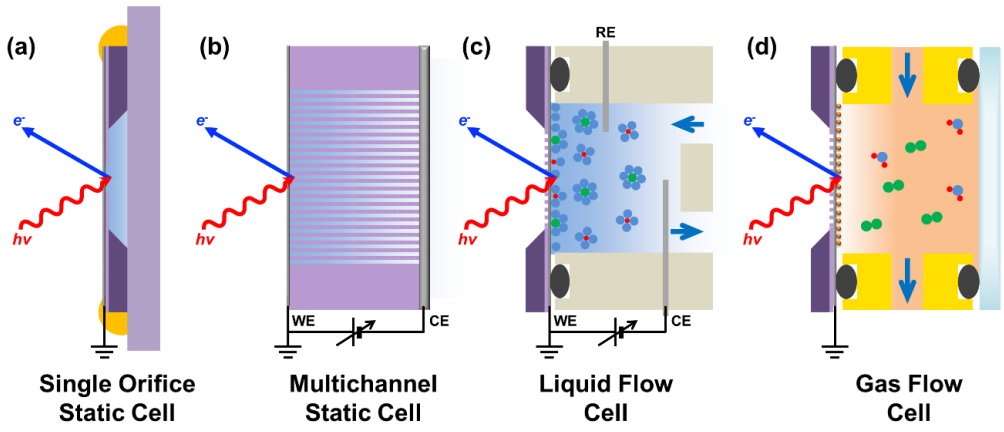


Figure A3.6: *(a) Single aperture static cell, coated in graphene or GO. (b) Multichannel array used in a static cell, coated with BLG. Perforated SiN_x membrane coated in MLG in a flow cell configuration for (c) liquids and (d) gases.*

information to determine oxidation states near the electrode since it measures electrons with a fixed kinetic energy and therefore relies on these electrons not being scattered which provides the surface sensitivity. Graphene's conductivity meant it acted as an electrode and this experiment was only possible since graphene could seal the liquid whilst maintaining electron transparency. Some beam damage to the solution was observed in this case.[62] The manufacture of these windows can still be somewhat unreliable, but the multichannel array has a significant benefit. Failure to seal one channel does not cause a complete failure across all channels as the other channels remain sealed and are independent of each other. The use of BLG decreased the likelihood of a tear or wrinkle resulting in the membrane leaking, since it is unlikely consecutive tears will align across two layers. In modern X-ray spectroscopy the typical beam size (e.g. 100 μm) is large enough such that multiple channels are illuminated at once. The potential drawback of this is it cannot be known if burst or sealed channels are being illuminated.

A further development of this technique is to incorporate a flow of either a liquid or gas (see Figure A3.6 (c) and (d)). A flow can reduce possible beam damage effects and replenishes any reactants used in an *in situ* experiment.[19,60] Previous examples of flow cells have been sealed with either MLG or BLG suspended over perforated SiN_x membranes transferred using PMMA from its growth substrate (Cu).[21,57] In the case of liquid flow cells then, typically, BLG is preferred, for example BLG was used when probing Co as a catalyst for the oxygen evolution reaction. Co on graphene helped to stabilise a $Co(CO)_x$ species which increased the reduction of Co^{3+} to Co^{2+} (the active site).[60] MLG was sufficient, in another example, to hold a gas pressure up to 1 bar enabling measurement of the oxidation of Cu under O_2 and spontaneous reduction under vacuum, as well as gas-phase XPS measurements of Ar, CO, CO_2, N_2, O_2 and even H_2.[57] The small perforations in the SiN_x window limited the graphene area that was

required to produce a good seal, thus increasing the success rate of difficult transfer techniques. Although, if the holes were not adequately covered by graphene then the cell would leak and the use of a flow could increase the likelihood of damaging UHV equipment. This risk can be reduced by limiting experiments to NAP-XPS systems which can handle the low pressures arising from small leaks.[21,57,60]

Chapter 4: Revealing the Role of CO during CO_2 Hydrogenation on Cu Surfaces

Microstructural Characterisation of Cu Catalysts using SEM

For *ex situ* characterisation using SEM: Cu powder was loaded into a ceramic boat and placed in a glass tube with inlet and outlet valves within a tube furnace. The inlet of the glass tube was supplied with a H_2:Ar (5%:95%) gas mixture. The outlet was connected to the exhaust through a bubbler, with gas flow monitored by the extent of bubble formation. The furnace temperature was increased at 5°C/min to 270°C and then held for an hour before cooling to room temperature. The inlet and outlet valves of the work tube were subsequently sealed and transferred into a glovebox. For SEM the Cu powder was exposed to air prior to measurements. For SEM imaging of the thin Cu film (~60 nm) a similar surface treatment to AtmP-NEXAFS was performed in the custom-built CVD chamber (Figure A2.5): H_2 flowed at a pressure of 50 mbar with the temperature held at 275°C for 30 minutes. The powder and thin film were measured using a Carl Zeiss Merlin field emission gun SEM, while the foil was measured using a Carl Zeiss EVO SEM with a tungsten electron source. EBSD was performed using a Bruker Quantax e-Flash1000 system with an acceleration voltage of 20 kV.

Figure A4.1 (a) shows an SEM image of the annealed powder. The low magnification image in Figure A4.1 (a,i) shows a bimodal distribution of Cu particles sizes, some with diameters of ~100 µm, while smaller particles have diameters of <10 µm, consistent with the -100 mesh of the purchased powder (i.e. all particles have diameters ≤150 µm). The high magnification image in Figure A4.1 (a,ii) shows a somewhat porous surface, with grain sizes of tens to hundreds of nanometres. This is consistent with previous reports where the reduction of copper oxide yields a similar porous morphology, and thus a larger Cu surface area that exhibits many different surfaces.[339]

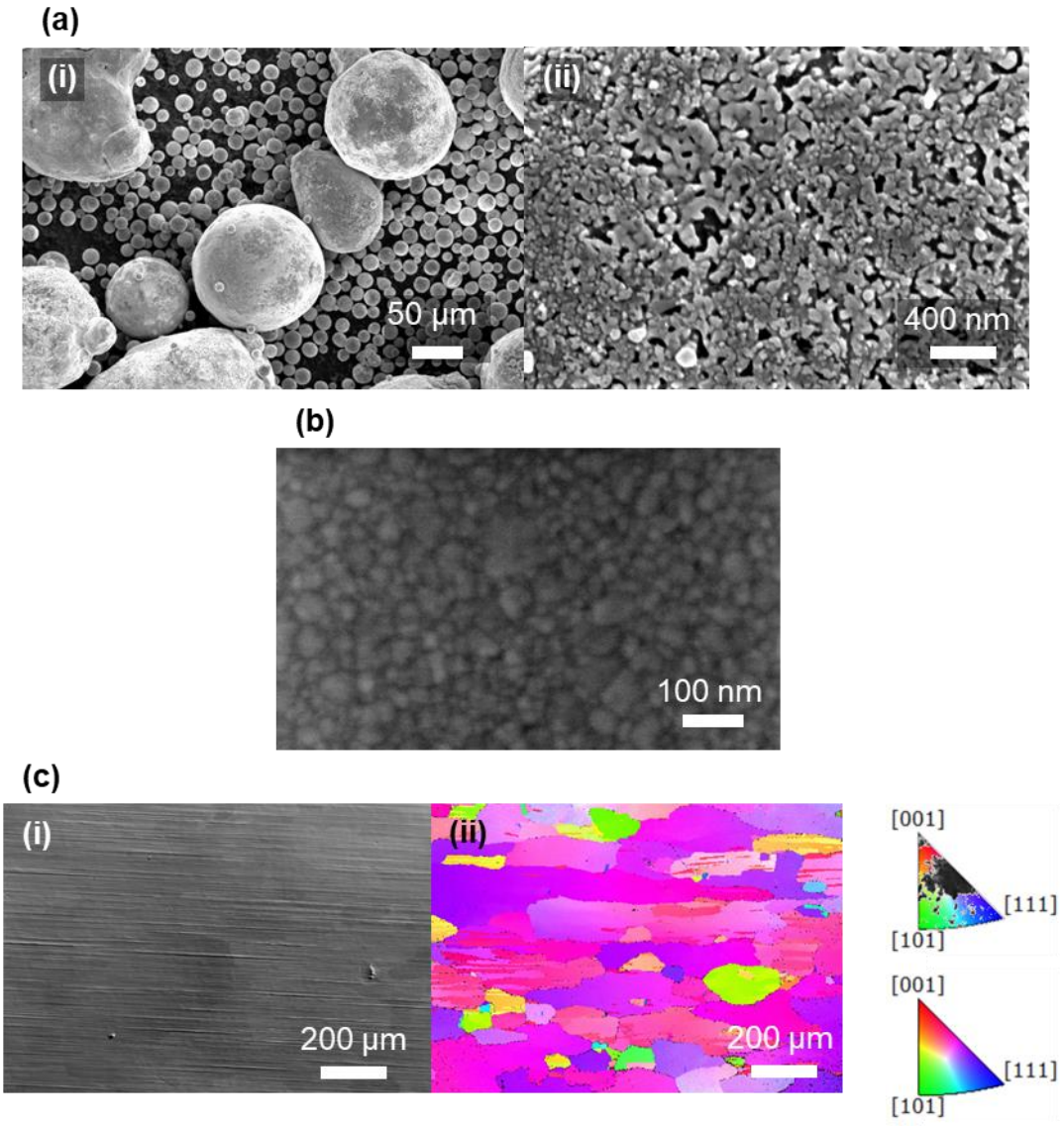


Figure A4.1: *(a) SEM images (5 kV accelerating voltage) of annealed Cu powder at (i) low and (ii) high magnification. (b) SEM image (2 kV accelerating voltage) of annealed Cu thin film (~60 nm). (c) (i) SEM image (20 kV accelerating voltage) of Cu foil (25 µm) following Ar^+ ion sputtering and annealing (300°C), (ii) EBSD map of the same Cu foil in (i). The inverse pole figure colour code with and without grain orientation data plotted is displayed to the right. Note that SEM and EBSD images in (c) are not taken in the same region.*

Figure A4.1 (b) shows an SEM image of the sputter-deposited Cu (60 nm) thin film on SiN_x, following the pre-treatment described above. Many small grains can be seen in the image, with similar lateral dimensions to the film's thickness and comparable dimensions to those observed for the Cu powder. The film appears amorphous with no preference for a particular crystal orientation, hence is polycrystalline.

Figure A4.1 (c,i) shows the SEM image of a Cu foil piece after sputtering and annealing. Clear rolling striations are seen across the sample surface associated with manufacture of the Cu foil. Figure A4.1 (c,ii) shows an EBSD map of grain orientations in the direction of the surface normal, with the inverse pole figure colour code also shown. A variety of orientations are present, but some preferential <112> texture is apparent. The topography associated with the rolling striations on the Cu foil mean even individual grains will not have a single well-defined surface orientation, but instead contain a variety of surfaces which will be simultaneously probed in the NAP-XPS measurements. Therefore, a high density of low coordination sites is expected on the surface of the Cu foil. It is worth noting the much lower annealing temperatures used in this work, compared to other studies where a Cu<111> surface forms by repeated sputter annealing of polycrystalline Cu.[177]

C K-edge and O K-edge from AtmP-NEXAFS

Figure A4.2 shows the C K-edge and O K-edge from AtmP-NEXAFS of the Cu film (~60 nm) deposited on a continuous SiN_x membrane. The signal is dominated by the gas-phase signal since the detection of NEXAFS using EY through a drain current relies on conduction of electrons through ionisation events in the gas. Hence, the C K-edge and O K-edge cannot be used for interpretation related to chemistry at the solid/gas interface.

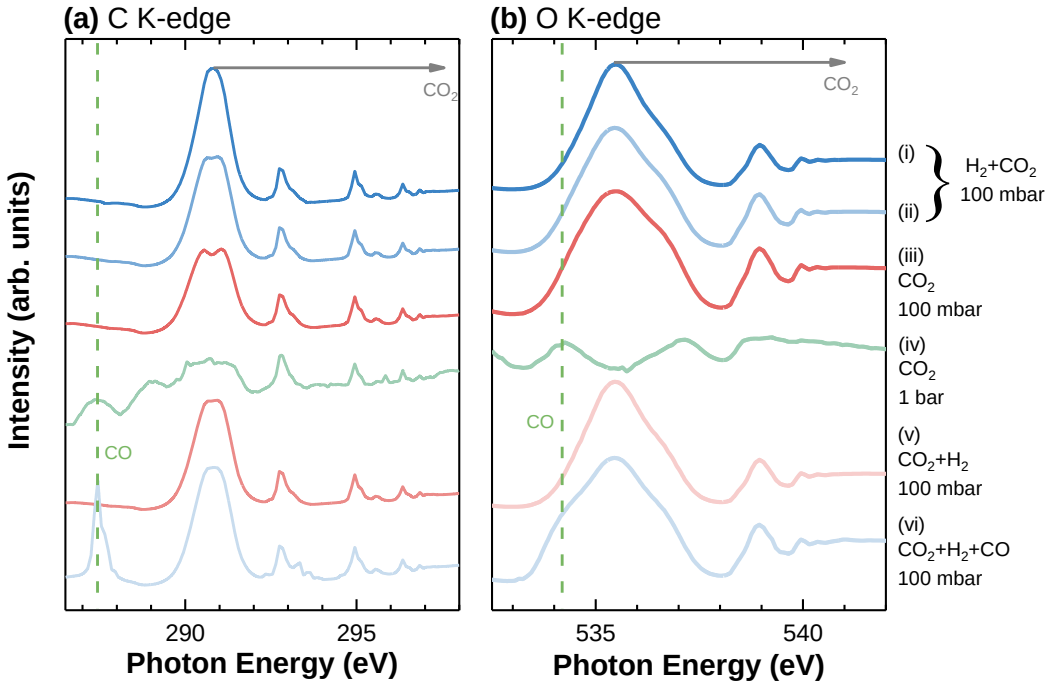


Figure A4.2: *AtmP-NEXAFS spectra from the (a) C K-edge and (b) O K-edge acquired in (i) H_2+CO_2 (1:1, 100 mbar), (ii) H_2+CO_2 (1:3, 100 mbar), (iii) CO_2 (100 mbar), (iv) CO_2 (1 bar), (v) CO_2+H_2 (1:1, 100 mbar), (vi) CO_2+H_2+CO (9:9:2, 100 mbar). All spectra are shown in the order they were collected in. Spectra were collected from the Cu film (~60 nm) deposited on the continuous SiN_x membrane and all at a temperature of 200°C.*

Ex Situ *XPS of Cu Powder for MS Measurements*

The Cu powder for *ex situ* XPS measurements was prepared using the same preparation as for SEM for microstructural characterisation of Cu, but unlike for SEM, the Cu powder was inertly transferred to the XPS system. Lab-based XPS was performed in Rex Richards, Oxford using a PHI VersaProbe III system with a monochromatic Al X-ray source at 1486 eV. Peaks were energy calibrated to a Au foil standard (Au $4f_{3/2}$ at 84.0 eV) and data was collected using a pass energy of 23 eV.

The difference between the as-received and annealed powder is shown in Figure A4.3 (a). The as-received material is a dull-brown colour initially, which becomes a brighter pink-orange after annealing, characteristic of Cu^0. The as-received powder shows the spectral features of Cu^{2+} (CuO) in both the Cu LMM and Cu 2p regions, with the Cu LMM spectrum in Figure A4.3 (b) showing a prominent peak at ~917.0 eV with a broad but defined shoulder towards lower kinetic energy. Meanwhile the Cu $2p_{3/2}$ peak is located at ~933.9 eV in Figure A4.3 (c) with a pronounced satellite structure at a higher binding energy relative to the main peak. The Cu LMM of the annealed powder is consistent with Cu^0, having a sharper main peak at lower kinetic energy (918.6 eV). The Cu 2p region shows a much weaker satellite structure compared to the as-received powder and the main Cu $2p_{3/2}$ peak is found to be at slightly lower binding energy of ~932.8 eV. This confirms the surface of the powder is metallic following annealing. Therefore, this data shows that the pretreatment process for the MS measurements yields a Cu^0 surface and can be compared to other Cu^0 surfaces (following a H_2 pre-treatment) investigated in Chapter 4.

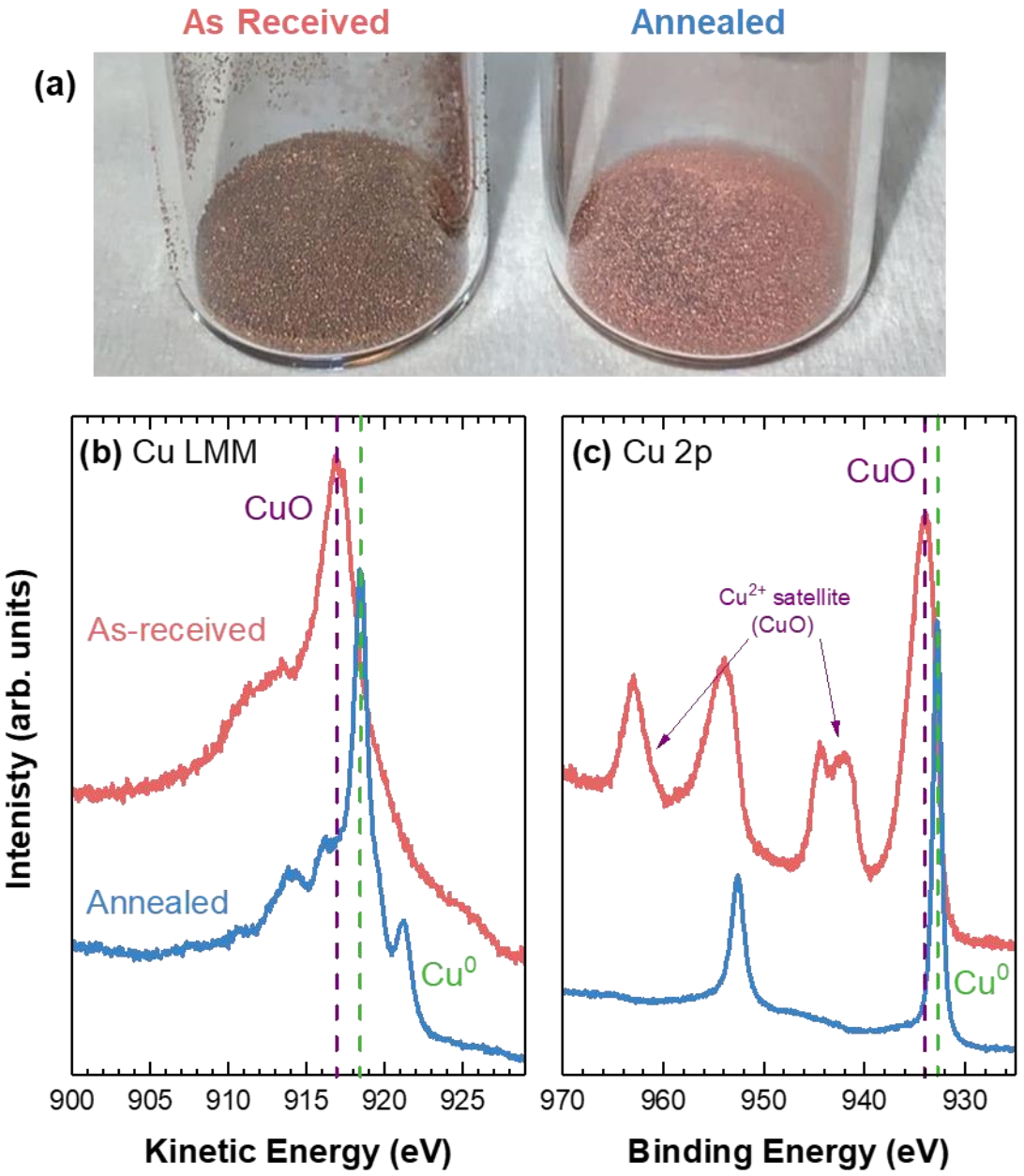


Figure A4.3: *(a) Cu powder as-received (left) and annealed to 275°C in 5%:95% H_2:Ar for 60 minutes (right). (b) Cu LMM and (c) Cu 2p XPS regions of the same as-received and annealed Cu powder as shown in (a).*

Chapter 5: Graphene as a Membrane for Ambient Pressure X-ray Spectroscopy

Linear Dispersion Relation of Graphene

For a non-relativistic particle a parabolic dispersion curve would be expected (Equation A5.1) where the effective mass of the particle can be calculated by considering the second derivative (Equation A5.2). As seen in Figure 5.1 (b) in the main text, graphene has a linear dispersion curve at its Dirac points. Therefore, for the case of electrons in graphene, the effective mass is zero.[217] Electrons in graphene can be described as Dirac fermions as they appear to be massless and have a high mobility.

Equation A5.1:

$$E = \frac{p^2}{2m^*}, \qquad p = \frac{h}{\lambda} = \hbar k:$$

$$E = \frac{\hbar^2 k^2}{2m^*}$$

Equation A5.2:

$$\frac{\partial^2 E}{\partial k^2} = \frac{\hbar^2}{m^*}$$

O 1s of Graphene Transferred using Au/PDMS

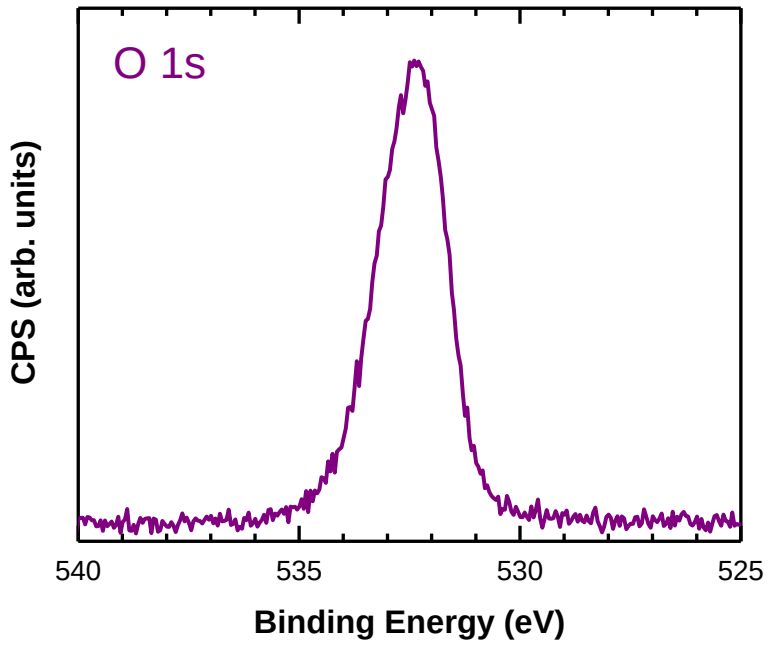


Figure A5.1: *O 1s region collected from graphene transferred to a perforated SiN_x membrane. Signal originates from exposure to atmosphere and aqueous solutions during the transfer process. Multiple peaks with similar binding energies will overlap to create a broad O 1s peak. This has not been fitted since distinguishing between these species is very difficult. The O KLL region was not collected.*

CVD Growth Mechanism and Parameters

Traditionally Cu is the preferred catalyst for CVD as it is relatively cheap and readily forms MLG due to its low carbon solubility. Although, through careful control of precursor pressure, catalyst thickness, exposure time, and the cooling rate it is possible to obtain MLG from high carbon solubility catalysts, such as Ni,[132,340] more detail can be found in reference [340] and is presented in Figure A5.2 (a). In summary, by controlling these factors the carbon flux incident on the catalyst surface (J_I) can be balanced by the carbon flux diffusing through the bulk (J_D), which acts as a carbon reservoir, to ensure a supersaturation of carbon at the surface is maintained and MLG formation occurs. The difference between J_I and J_D is the carbon flux which forms graphene on the catalyst surface (J_G), see Figure A5.2 (b). FLG formation occurs when there is a significant carbon reservoir which has accumulated in the bulk of the transition metal. Upon cooling the direction of J_D will reverse and precipitation of carbon can occur, resulting in additional layers of graphene. Precipitation upon cooling can be minimised through rapid cooling or by minimising the accumulation of a bulk carbon reservoir during the isothermal growth period.

The realisation that MLG formation was possible on catalysts apart from Cu encouraged more research into different catalysts for graphene growth. For example, an advantage of growing graphene on Ni compared to Cu is the lower growth temperatures that can be used; Cu often requires temperatures of 850-1000°C whereas Ni-based catalysts have been shown to grow graphene at temperatures as low as 450°C.[327] A lower temperature reduces costs involved and is important if growing on fragile substrates (e.g. SiN_x membranes). However, due to the lower temperature the levels of defects in graphene grown on Ni is greater than on Cu.

The temperature of CVD growth and hence quality of graphene is also determined by the carbon precursor used. Gaseous precursors are the most common

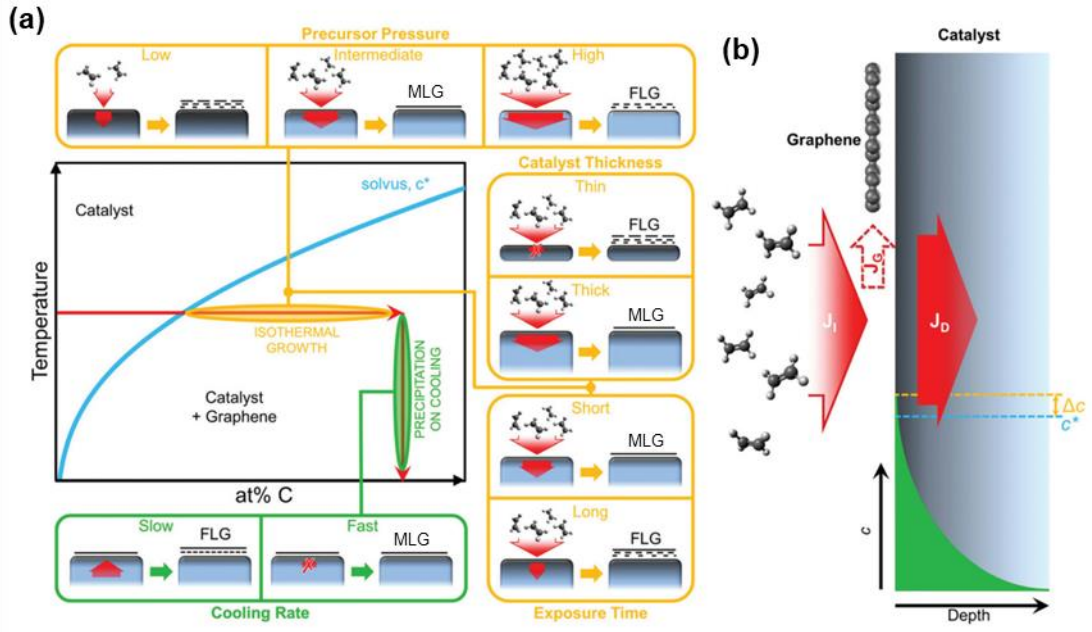


Figure A5.2: *(a) Schematic outlining how precursor pressure, catalyst thickness, exposure time, and cooling rate can influence the thickness of graphene grown during CVD and how each factor contributes to either isothermal growth or precipitation upon cooling. (b) The different carbon fluxes (J) which must be balanced to ensure a supersaturation of carbon is accumulated near the surface of the catalyst. (a) and (b) Taken from A. Cabrero-Vilatela* et al., Nanoscale*, 2016,* ***8****, 2149–2158.*

(e.g. methane[341], ethylene[342], acetylene[240,255]) but there are some examples of solids (e.g. PMMA[343]) or liquids (e.g. benzene[344]) being used.[112] Methane is commonly used over Cu to obtain high-quality MLG. The required temperature is >850 °C to dissociate methane, where the temperature of CVD is limited by the energy required to break the C-H bond.[273] Ethylene can be used at a slightly lower temperature, as C=C double bonds require a lower temperature to dissociate compared to C-H bonds, whilst still maintaining a high quality of graphene. Acetylene can be used at a much lower temperature as the C≡C triple bond is the most easy to dissociate. For example, using acetylene over a Ni-Au alloy catalyst, MLG growth was achieved at temperatures as low as 450°C.[327] Low temperature growth processes often incorporate two-steps: nucleation and domain growth. An initial low pressure step will create nucleation sites where small carbon domains begin to form, followed by a higher pressure step which encourages domain growth until neighbouring domains impinge on each to create a continuous layer of graphene.[327]

Suspending a Ni Film over a Perforated Silicon Nitride Membrane

To suspend a Ni film over a perforated SiN_x membrane, initially, a stamping transfer method was attempted, similar to that used for graphene in Chapter 5. A PDMS stamp was applied to a Ni thin film (~100 nm) to transfer it from one Si/SiO_2 piece to another where heating PDMS to ~100-120°C will release the Ni.[236,345] However, the Ni was significantly wrinkled during the transfer and would not completely cover the holes of the window. A PVA stamp was also attempted, similar to that in reference [239]. To make the PVA solution: high molecular mass PVA (high Mr PVA, average molecular weight: 85,000-124,000, 87-89% hydrolysed, Sigma Aldrich) and low molecular mass PVA (low Mr PVA, average molecular weight: 9,000-10,000, 80% hydrolysed, Sigma Aldrich) were stirred together and dissolved in water whilst heating at 80°C. The consistency of the PVA solution can be altered by changing the relative amount of high Mr PVA and low Mr

PVA such as increasing the amount of high Mr PVA to make the solution more viscous.[239] The properties of the PVA solution can also be changed by altering the relative amount of water, for example, more water will increase the surface tension of the PVA solution. A drop of PVA solution (3 g high Mr, 7 g low Mr, 65 ml water) was applied to a glass slide and pressed onto the Ni thin film to adhere the film to the PVA. To release the Ni film, PVA can be dissolved in water heated to 80°C.[239] But this method had the same issues as the PDMS stamp, where the Ni was too wrinkled after the transfer.

Figure A5.3 shows a schematic of the successful method used to suspend Ni over the holes. Firstly, a perforated SiN_x membrane was applied to a clean square of PDMS (cleaned with ethanol and IPA), ensuring the window was over the PDMS whilst leaving an edge to help remove the membrane later. A drop of PVA solution was then added onto the window (Figure A5.3 (i)) of the membrane and before the PVA dried it was checked under the optical microscope for bubbles. If there were bubbles this meant that the PVA had not filled all of the holes, therefore not forming a flat surface for Ni deposition later, and the PVA was then removed using water and reapplied. If there were no bubbles then the PVA was left to dry in air for ~2 hours. The PVA solution used contained only low Mr PVA (2.5 g) mixed with 10 ml water. Water is a relatively high surface tension liquid, so a concentrated PVA solution was made to ensure the surface tension of the solution was low enough to pass through the small holes (⌀1 µm) in the membrane. No high Mr PVA was used to prevent the solution becoming too viscous which would also stop PVA from filling the holes.

To remove the membrane from the PDMS it was heated on a hotplate at ~100°C to reduce the adhesion of the PDMS. The membrane could then be slowly and carefully peeled away so as not to break the window (Figure A5.3 (iv)). Ni was then deposited onto the flat side of the membrane using RF magnetron sputtering. Sputtering was preferred as it more easily covers rough surfaces compared to evaporation, which

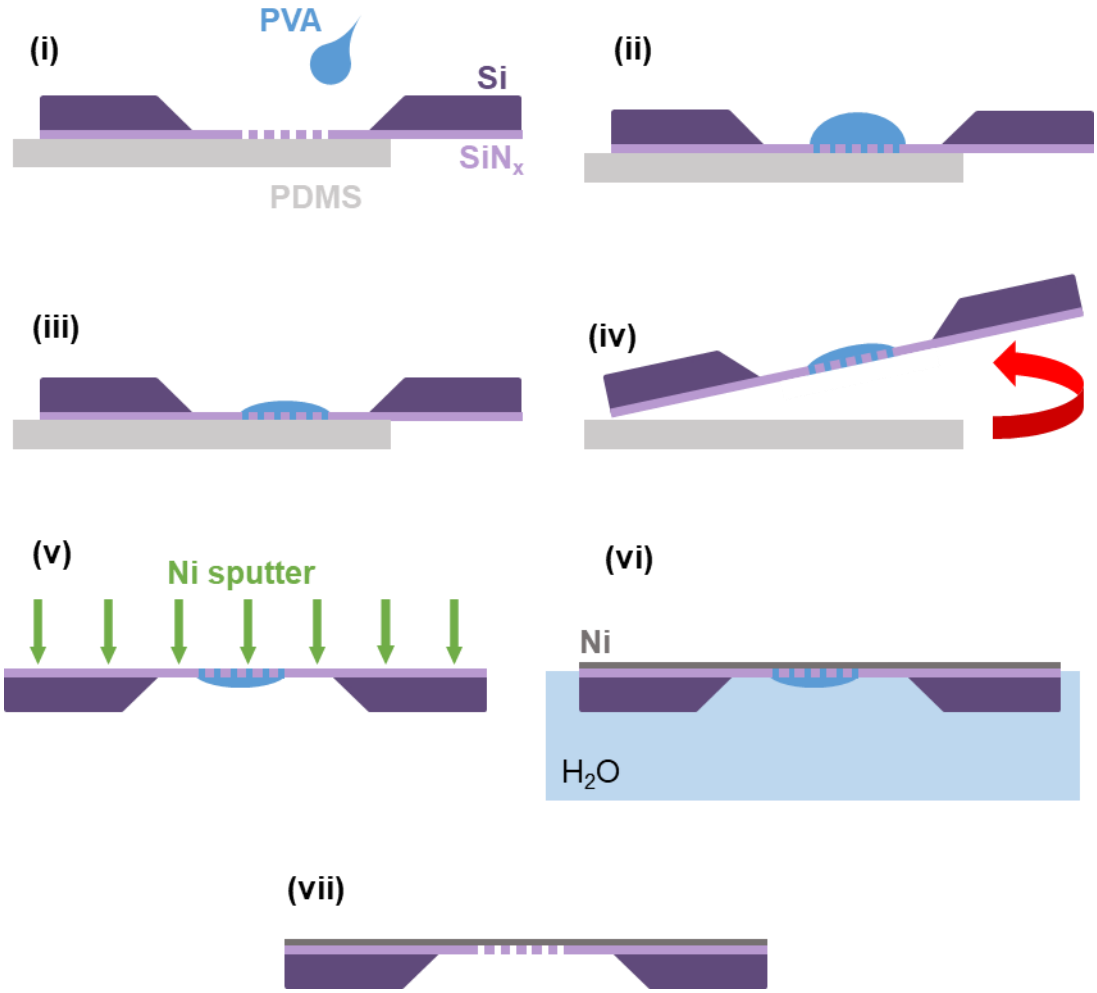


Figure A5.3: *Schematic of suspension of Ni thin film over the holes of a perforated SiN_x membrane. (i) PVA solution is dropped into the holes of the membrane whilst supported on PDMS to create a flat surface. (ii) Before the PVA is dry it is checked under the optical microscope for any bubbles. If there are bubbles the PVA is removed with water and reapplied as in (i), if not the PVA is left to dry in air as in (iii). (iv) Once the PVA is dry the PDMS/membrane is heated to ~100°C for ~10 minutes to release the membrane from the PDMS. (v) Ni is then deposited onto the flat surface of the membrane using RF magnetron sputtering. (vi) PVA is removed by floating the membrane on water (80°C) and left for ~30 minutes, before finally cleaning with IPA to leave Ni suspended over the holes as in (vii).*

only covers the surface in the direct line-of-sight of the source. The Ni deposition required some optimisation to deposit a thin film which was flat and would not delaminate. A high sputtering power will deposit a flat surface, but with more stress in the film meaning it is more likely to delaminate. For most depositions 100 W was used. However, in some later depositions, 50 or 75 W was used to prevent delaminating of the film.

Finally, PVA was removed by floating the membrane on water (heated at 80°C) for ~30 minutes and cleaned with IPA (Figure A5.3 (vi)). Figure A5.4 shows the optical microscope images of (a) an unsuccessful attempt and (b) a successful attempt at suspending Ni over the holes. In Figure A5.4 (a) the PVA solution was too dilute so did not fill the holes; the Ni film is not continuous across the surface and light can be seen through the holes. Whereas in Figure A5.4 (b), the PVA solution (2.5 g low Mr PVA and 10 ml water) did fill the holes, resulting in a continuous Ni film and no light being transmitted through the window, which demonstrates complete coverage. There is some surface residue in Figure A5.4 (b,i) which is most likely from the PDMS stamp which easily picks up dust. This was avoided through more thorough cleaning of the PDMS stamp.

Optimisation of CVD Growth of Graphene – Ethylene Precursor

The next step to achieve direct growth of graphene over a perforated SiN_x membrane was to optimise graphene growth over Ni. The custom-built vacuum chamber used for CVD growth is described earlier in the Appendix (Figure A2.5). The CVD chamber was newly installed, therefore required significant optimisation to grow continuous graphene on Ni. Ethylene (C_2H_4) was chosen as a precursor because the temperature of growth is lower than methane (ethylene dissociates at ~600°C) whilst still maintaining a relatively low level of defects in graphene.[112,273] The graphene was characterised using optical microscopy and Raman in Figures A5.5–A5.8. Graphene was transferred from Ni to Si/SiO_2 for characterisation using a PMMA support and etching the

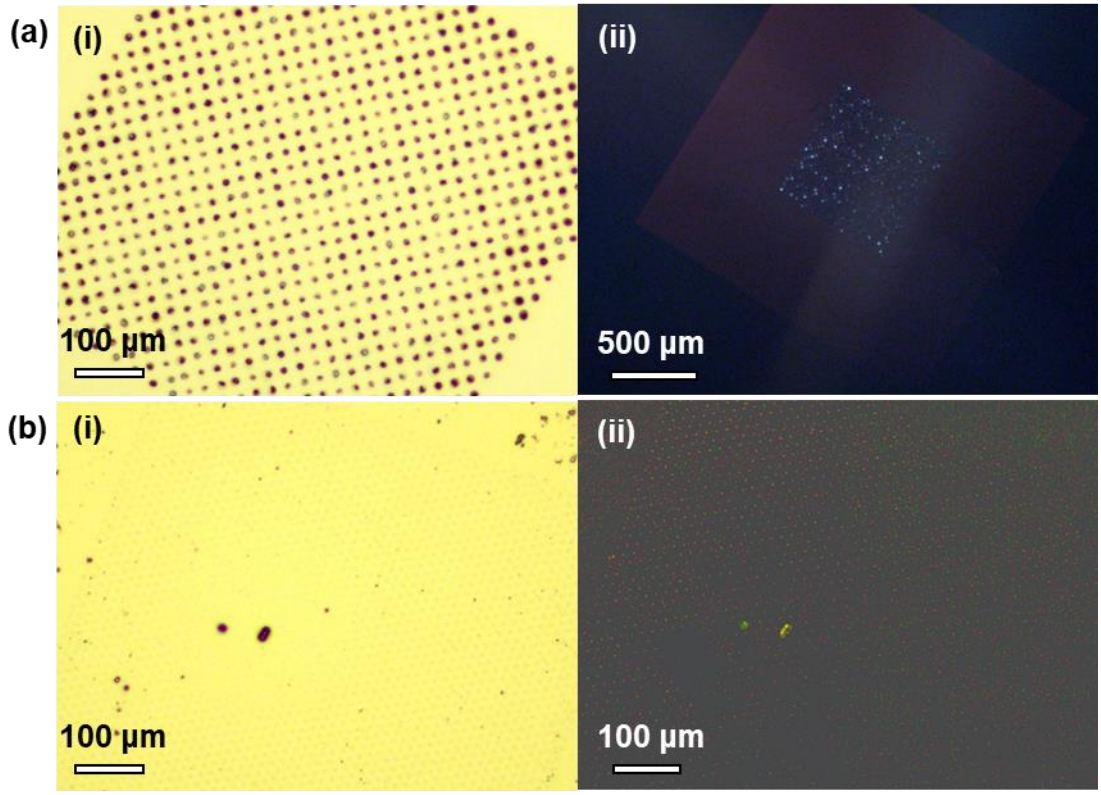


Figure A5.4: *Optical microscope images taken in (i) reflection and (ii) transmission mode. (a) The suspended Ni is not covering the holes of the membrane so the holes are visible in (i) and light is seen through the holes in (ii). (b) Suspended Ni completely covers the holes such that there is a flat surface in (i) and no light is seen through the holes in (ii).*

Ni using $FeCl_3$ solution (3.2 g in 40 ml, 97%, Sigma Aldrich), and PMMA was removed using acetone.

However, some PMMA residue can still be seen in the optical microscope images (green/very light blue marks). All SEM images of graphene were collected with graphene still on Ni following growth using a Carl Zeiss EVO SEM with a tungsten electron source and 2 kV electron beam energy.

Initial CVD optimisation did not use a membrane, due to their expense, and instead was carried out on $Si/SiO_2/Ni$ (100 nm) samples. The general CVD procedure used throughout involved heating the sample in H_2 (1 mbar) to the desired growth temperature (at 20°C/min). The sample was then annealed in H_2 for a further 20 minutes at the growth temperature. H_2 was then replaced with the carbon precursor and held at the growth pressure and temperature for a certain time. The sample was then cooled to room temperature under vacuum (~30°C/min). The H_2 pre-treatment reduced the metal catalyst to make it active for dissociating the carbon precursor.

Figure A5.5 (a) shows an image from an initial growth attempt in the CVD chamber using $Si/SiO_2/Ni$ (100 nm), and conditions: C_2H_4 at 600°C, $5x10^{-5}$ mbar (7 minutes) followed by $3x10^{-4}$ mbar (3 minutes). Figure A5.5 (d,i) shows the corresponding Raman spectra for this growth. The purple circle encasing a light blue area is a region of highly defective MLG (I_{2D}/I_G is 1.9, I_{2D}/I_G is ~2.5 and a Γ_{2D} of 36 cm^{-1}). The darker blue patches in the image correspond to thicker areas of graphene. In the region encased by the red circle, the Raman spectrum suggests this is amorphous, graphitic carbon. Non-optimised growth conditions should yield patchy areas of graphene with no growth between those areas.[327] The behaviour in Figure A5.5 (a), therefore cannot be explained by a lack of optimisation, but instead is most likely caused by an issue with the CVD chamber.

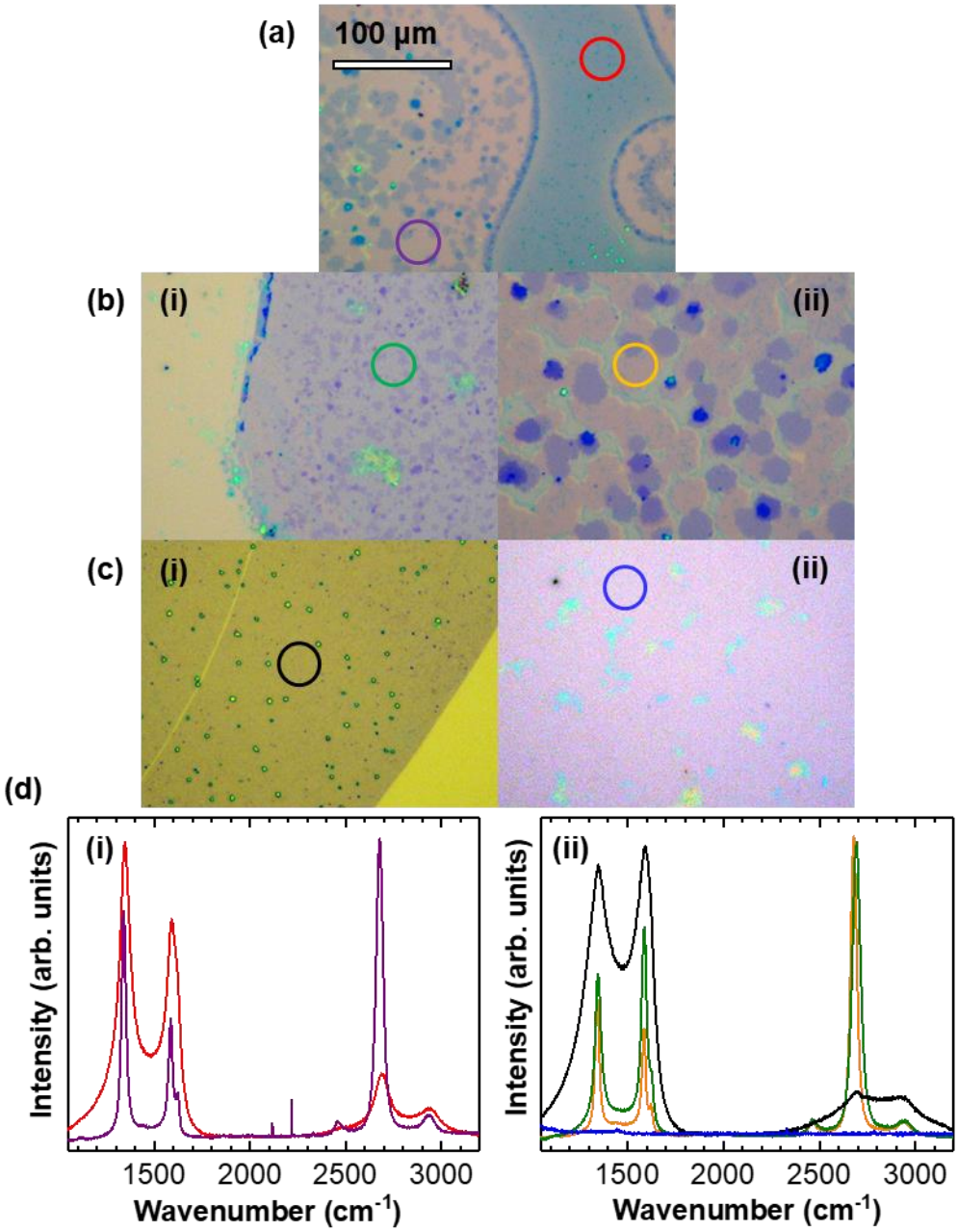


Figure A5.5: *(a-c) Optical microscope images of transferred films grown by different exposure conditions. (a) Graphene growth: 600°C, C_2H_4 at 5x10^{-5} mbar (7 minutes), then 3x10^{-4} mbar (1 minute) with no heat shield. (b) Tests of chamber with no heat shield and (c) Tests of chamber with heat shield for: (i) annealing in vacuum (600°C for 20 minutes) and (ii) H_2 only (600°C, 1 mbar for 20 minutes). (d) Raman spectroscopy of areas indicated on images (a-c) where the coloured spectra correspond to each region.*

To determine the reasons for formation of amorphous, graphitic carbon, two tests were performed with Si/SiO_2/Ni (100 nm): annealing in vacuum at 600°C (20 minutes), and annealing in H_2 (1 mbar) at 600°C (20 minutes). Without a carbon precursor in both cases it is expected there should be no graphene growth. Figure A5.5 (b) shows the results of these tests and in both instances graphene is present on the surface, Raman spectroscopy (Figure A5.5 (d,ii), green and orange lines) confirms this, which suggests there is another source of carbon from the chamber itself. During testing it was noticed that the lid of the chamber was very hot, which meant the Viton O-ring sealing the lid to the rest of the chamber was heating up during each process. The heater was placed directly below the lid and, due to needing to open the lid frequently to add and remove samples, a Viton O-ring was chosen to seal the lid since it is reusable (compared to Cu gaskets). However, when Viton O-rings are heated to elevated temperatures they can start to decompose and de-gas. The degassing of the O-ring was thus suspected to be the source of the carbon during the tests. Figure A5.5 (c) shows the same annealing and H_2 test, but with a tantalum heat shield placed over the heater to protect the lid of the chamber. The heat shield had a hole in the centre such that samples beneath it were still exposed to the dosed gases. With the heat shield, the vacuum annealing experiment resulted in amorphous carbon and the H_2 annealing experiment showed no carbon on the surface (Figure A5.5 (d,ii)). The surface carbon from the vacuum annealing experiment most likely comes from the bulk of the film and accumulates during Ni deposition. The addition of H_2 removes this amorphous carbon, confirming that carbon in Figure A5.5 (c) came from deposition of Ni and not the chamber. Therefore, the heating of the Viton O-ring was the original source of carbon contamination on the Ni resulting in graphene growth. For future growth attempts a heat shield was needed to prevent degassing of the Viton O-ring.

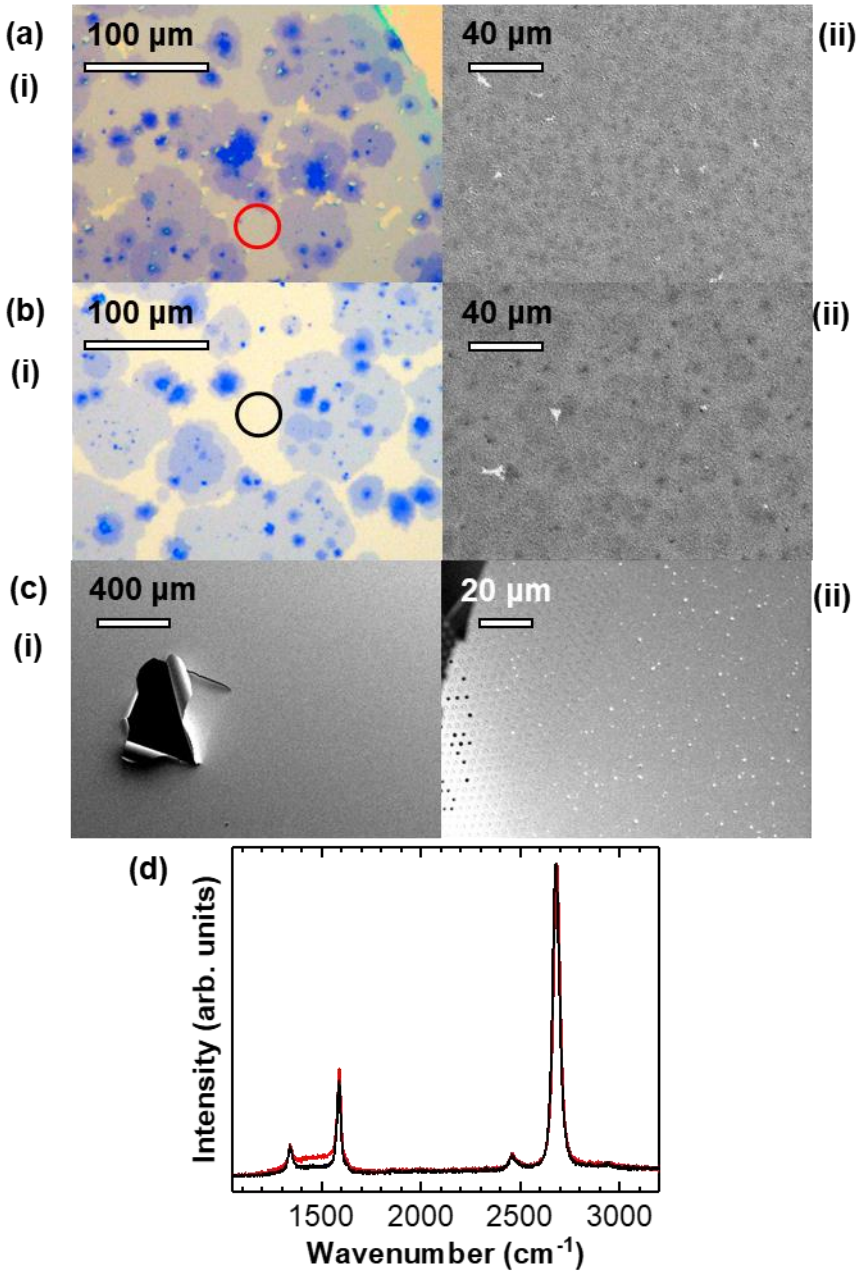


Figure A5.6: *(a) and (b): (i) Optical microscope and (ii) SEM images of graphene after CVD on Si/SiO_2/Ni (300 nm). Conditions for (a): 650°C, C_2H_4 at $7x10^{-6}$ mbar (1 minute) followed by $3x10^{-4}$ mbar (30 minutes). Conditions for (b): 650°C, C_2H_4 at $7x10^{-6}$ mbar (1 minute) followed by $3x10^{-4}$ mbar (15 minutes). (c) SEM images of a burst partially etched SiN_x membrane coated in Ni after CVD which followed the same procedure as in (b). (d) Raman spectra from regions of graphene indicated by the coloured circles in (a,i) and (b,i).*

The conditions of graphene growth could then be optimised and Figure A5.6 (a) and (b) show two examples of continuous graphene growth on Si/SiO_2/Ni (300 nm). The conditions for each growth were: (a) 650°C, C_2H_4 at $7x10^{-6}$ mbar (1 minute) followed by $3x10^{-4}$ mbar (30 minutes) and for (b) 650°C, C_2H_4 at $7x10^{-6}$ mbar (1 minute) followed by $3x10^{-4}$ mbar (15 minutes). A higher growth temperature of 650°C was used, compared to 600°C in testing, as this was found to increase the extent of dissociation of the C_2H_4 precursor and aid graphene growth. The only difference between the two growths was the duration of the second growth step (domain growth). Figure A5.6 (d) shows the quality of graphene in the MLG (light blue) regions does not vary signficantly between the growth conditions: Γ_{2D} of ~38 cm^{-1} and I_D/I_G ratio of 0.38. The shorter domain growth time (Figure A5.6 (b)) has a slightly higher I_{2D}/I_G ratio of 3.0 compared to 2.7 for the longer domain growth run. Therefore, the different growth times mainly affects the extent of MLG and BLG growth, where a longer domain growth time results in a greater amount of BLG, as expected.[340] The important result from these growths is the continuous nature of graphene over the whole surface as shown in SEM (Figures A5.6 (a,ii) and (b,ii)) where only a few, small pinholes are seen. The number of pinholes is not reduced by using a longer growth time, therefore the source of pinholes is likely from roughness of the Ni surface which is consistent across both samples.

This stable growth recipe was next tested on a SiN_x membrane, as shown in Figure A5.6 (c). The SiN_x membrane was not perforated, but instead had the holes only partially etched through, therefore leaving a flat side of SiN_x which Ni was deposited on without using the PVA filling technique. This membrane was stronger and easier to use in testing as fewer preparation steps were required. The window of the membrane broke during growth (Figure A5.6 (c,i)). The higher magnification SEM image in Figure A5.6 (c,ii) suggests there may be some graphene growth based on the grey colour, compared to the whiter dots which relate to roughness. The cause of the window breaking is the

difference in thermal expansion coefficients between Ni and SiN_x. The growth temperature was lowered and cooling rate decreased, but at lower temperatures no graphene growth was observed. Overall, the temperature needed to sufficiently dissociate the C_2H_4 precursor will result in the window of the SiN_x membrane breaking.

Optimisation of CVD Growth of Graphene – Acetylene Precursor

Given the need for a lower graphene growth temperature, an alternative carbon precursor was tested: acetylene (C_2H_2). C_2H_2 will dissociate at much lower temperatures, however the resulting graphene is more defective.[273,274,346] For graphene membranes it is more important to have continuous graphene than an absence of defects, therefore acetylene offers a viable alternative. It is worth noting that at the same time as changing carbon precursor, the CVD chamber design was updated. The updated design moved the lid further away from the heater to protect the Viton O-ring from overheating, therefore a heat shield was not needed for growths using this chamber.

As with the previous chamber, an initial test was performed to see if graphene grew when just H_2 was dosed. As shown in Figure A5.7 (a,i), there are small patches of graphene (Si/SiO_2/Ni (500 nm) heated to 550°C and annealed in H_2 (1 mbar) for 20 minutes). Heating of the O-ring could not be an issue. Instead, it was thought there could be too much carbon imbedded in the Ni during deposition, which the H_2 was incapable of cleaning. To address this, rather than heating the Si/SiO_2/Ni in H_2, a small air leak (~$6x10^{-6}$ mbar) was introduced through a leak valve in the chamber. Then, once at growth temperature, the air leak was stopped and the surface was annealed in H_2 (1 mbar) for 20 minutes, as done previously. The O_2 in the air would be more effective at removing carbon from the Ni compared to H_2, although it would result in oxidation of Ni. Hence, a treatment in H_2 was needed afterwards to reduce the Ni to a metallic state and make it active for graphene growth. Figure A5.7 (a,ii) shows the optical microscope image from a Ni surface which underwent an air/H_2 pre-treatment and confirms there is now no

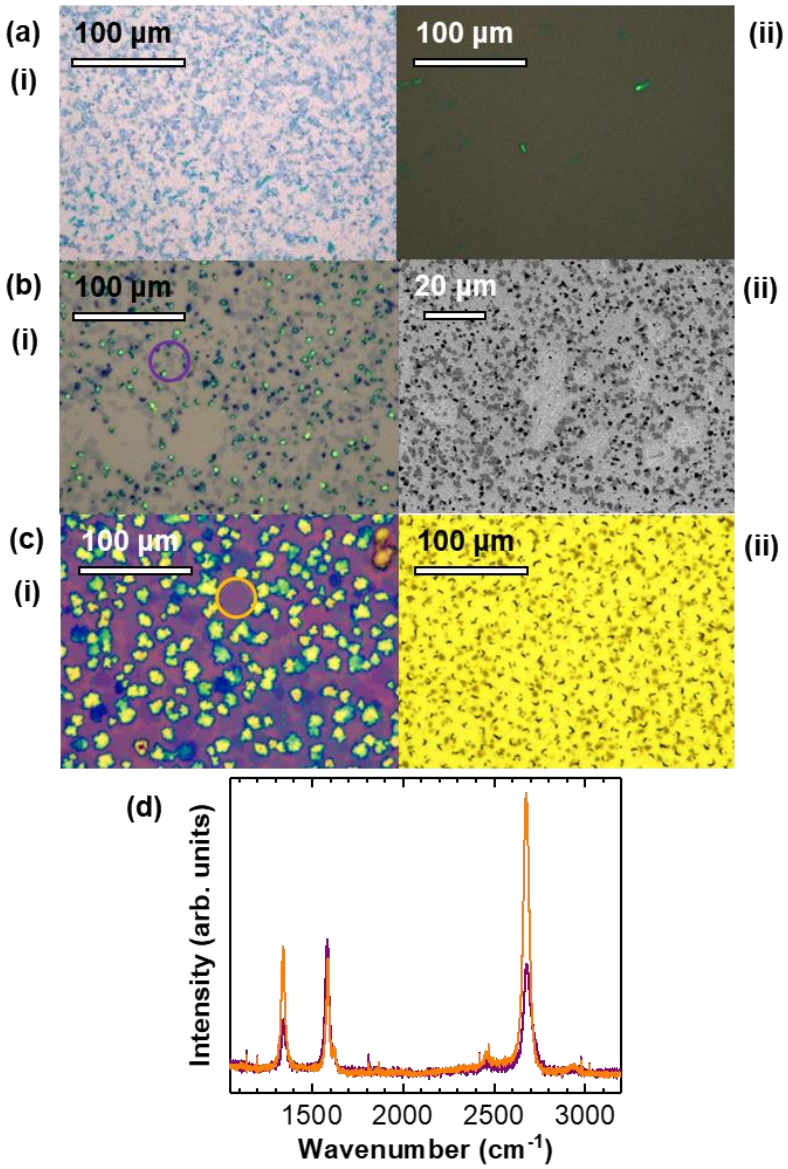


Figure A5.7: *(a) Optical microsocpe images for H_2 annealing (550°C, 1 mbar for 20 minutes) for (i) heating up in H_2, and (ii) heating up in a small air leak (~6x10^{-6} mbar). (b) Graphene growth using C_2H_2 (550°C, 2x10^{-6} mbar for 15 minutes) on Si/SiO_2/Ni (350 nm): (i) Optical microscope and (ii) SEM images. (c) Optical microsocpe images from graphene growth using C_2H_2 (550°C, 2x10^{-6} mbar for 15 minutes) on a perforated SiN_x membrane with a 350 nm suspended Ni film: (i) transferred to Si/SiO_2 and (ii) directly of membrane following growth. (d) Raman spectra from regions of graphene indicated by the coloured circles in (b,i) and (c,i).*

carbon. Therefore, all growths using C_2H_2 used the same pre-treatment: heating in air, followed by annealing in H_2.

Figure A5.7 (b) shows an initial growth attempt using C_2H_2 with the air/H_2 pre-treatment conditions: 550°C, C_2H_2 at $2x10^{-6}$ mbar (15 minutes) using Si/SiO_2/Ni (350 nm). The optical microscope image shows patchy coverage of graphene and this is confirmed by the SEM image, where there are only small patches of graphene. Raman spectroscopy (Figure A5.7 (d)) shows that the small patches of graphene are very thick with an I_{2D}/I_G ratio of 0.8 and a Γ_{2D} of 49.2 cm^{-1}. The coverage is very poor so a longer C_2H_2 exposure time of 75 minutes is shown in Figure A5.7 (c). This CVD run used Si/SiO_2/Ni (350 nm) and a perforated SiN_x membrane with Ni suspended (350 nm) via the PVA method. The optical microscope image and Raman spectroscopy of the transferred graphene (Figure A5.7 (c,i) and (d)) confirm good coverage of MLG, with an I_{2D}/I_G ratio of 2.2 and a Γ_{2D} of 36.4 cm^{-1}. However, there are some spaces which are not covered with graphene and, as expected when using C_2H_2 at this temperature, the MLG is highly defective (I_D/I_G of 1.1). In Figure A5.7 (c,ii) the optical microscope image shows the window does not break during growth, thus 550°C is a suitably low enough temperature to prevent the window from breaking. Unfortunately, the suspended Ni does not remain over the holes. This could be because the Ni film is too thin or too unstable due to the high power used for deposition (100 W) which introduces stress into the film.

To decrease the stress in the Ni film, a lower deposition power was used for sputtering Ni (75 W). As a test, a partially etched SiN_x membrane was used (as in Figure A5.6), and the C_2H_2 growth time was increased to 90 minutes to improve coverage. Figure A5.8 (a) shows the optical microscope image of transferred graphene from a longer C_2H_2 growth (550°C, $2x10^{-6}$ mbar for 90 minutes) and confirms better coverage, with thicker graphene present. However, the graphene coverage is not completely continuous. Raman spectroscopy (Figure A5.8 (c)) yields an I_{2D}/I_G ratio of 1.5 and a Γ_{2D}

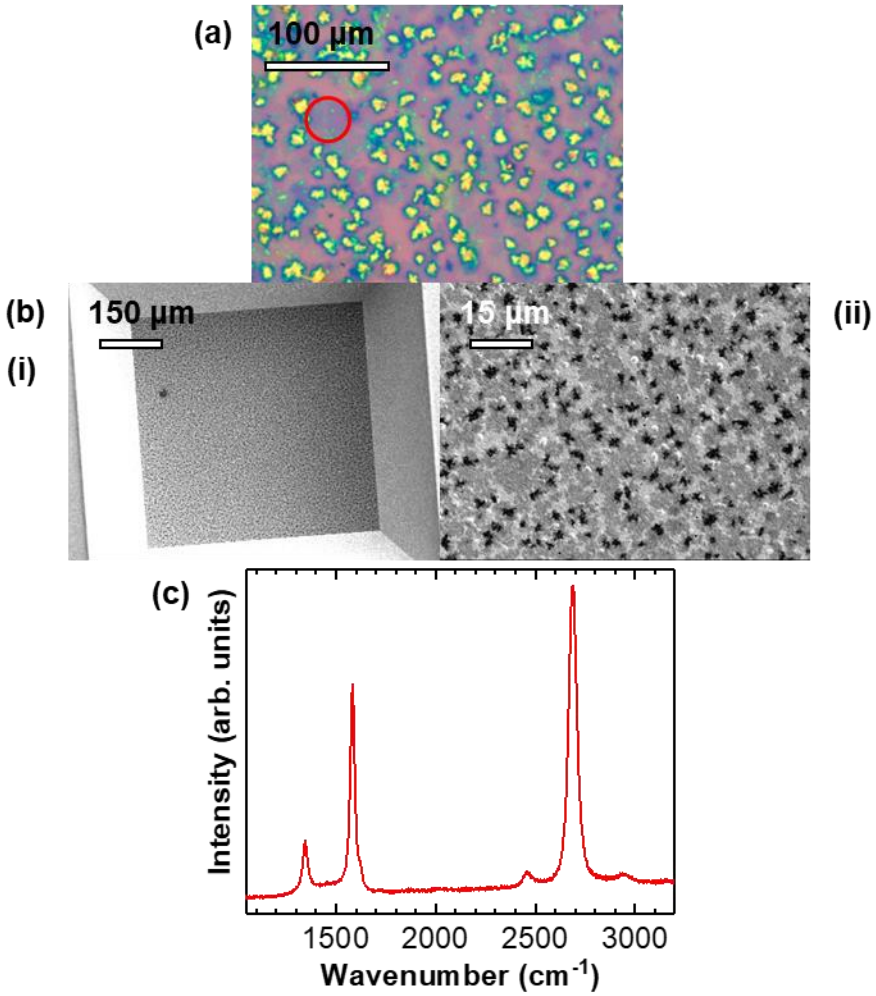


Figure A5.8: *Graphene growth using C_2H_2 (550°C, $2x10^{-6}$ mbar, 90 minutes) over $Si/SiO_2/Ni$ (350 nm) and a partially etched SiN_x membrane with deposited Ni (350 nm). A lower power of 75 W was used to deposit the Ni. (a) Optical microscope image of transferred graphene. (b) SEM images of the partially etched SiN_x membrane after growth, showing good coverage and the Ni still intact. (c) Raman spectrum from region as indicated in (a).*

of 46.5 cm^{-1}, showing this is BLG, or even FLG. The defect level is lower than in Figure A5.7, with an I_D/I_G value of 0.3. The decrease in the I_D/I_G ratio is not necessarily due to a decrease in defects from growth, but could be because BLG/FLG is present in Figure A5.8 instead of MLG in Figure A5.7. Overlapping graphene layers will decrease I_D, due to the stacking of layers, which minimises the chance of consecutive defects. The SEM images in Figure A5.8 (b) demonstrate the window and Ni are still intact and the graphene coverage is similar to the optical microscope image. The lower power increased the stability of the Ni film, although the Ni is very rough.

Chapter 6: Investigating the Behaviour of Zn during CO_2 Hydrogenation on Cu/Zn Nanoparticles at Atmospheric Pressure

Lab-based XPS: Sputtering Profiles of Zn and Brass Foils

XPS data was collected at Rex Richards, Oxford using a PHI VersaProbe III system with a monochromatic Al Kα X-ray source at 1486 eV, and a photoelectron emission angle of 45°. Energy calibration was performed using the adventitious carbon peak at 285.0 eV in the C 1s region and spectra were collected using a pass energy of 55 eV. Peaks in the O 1s region were fitted with a Gaussian-Lorentzian (70:30) function. Samples underwent *in situ* sputtering with Ar^+ (500 V) with 2 minutes cycles between measurements.

Figure A6.1 shows the surface of the Zn foil (99.994%, Alfa Aesar) that initially has a layer of $Zn(OH)_2$, as seen in the (i) O 1s and (ii) Zn LMM regions, with a peak at 532 eV and 987.4 eV respectively.[316–318] After a short sputter (4 minutes, 500 V, Ar^+) this thin $Zn(OH)_2$ layer has been removed and leaves ZnO (988.4 eV in the Zn LMM and 529.9 eV in the O 1s). Over time more O is removed via sputtering which makes the surface more metallic, as shown by the growing peak at 992.4 eV in the Zn LMM, during which the ZnO peak begins to broaden towards 989.2 eV. The peak at 989.2 eV is identified as ZnO_x since, during sputtering, O is removed to create vacancies resulting in defective ZnO (i.e. ZnO_x).

Similarly, in Figure A6.2, the brass foil (alloy 260, Alfa Aesar) initially had a very thick layer of $Zn(OH)_2$, as well as a significant amount of CuO (917.7 eV in Figure A6.2 (iii)). After ~22 minutes of 500 V Ar^+ sputtering, the Cu LMM peak has shifted to 918.6 eV indicative of Cu^0 formation. The Zn LMM peak at 988.4 eV shows there is still a significant amount of ZnO. Similarly to Figure A6.1, as the foil is sputtered, it removes O to create ZnO_x, as shown by a broadening at 989.2 eV, and an increase in the peak at

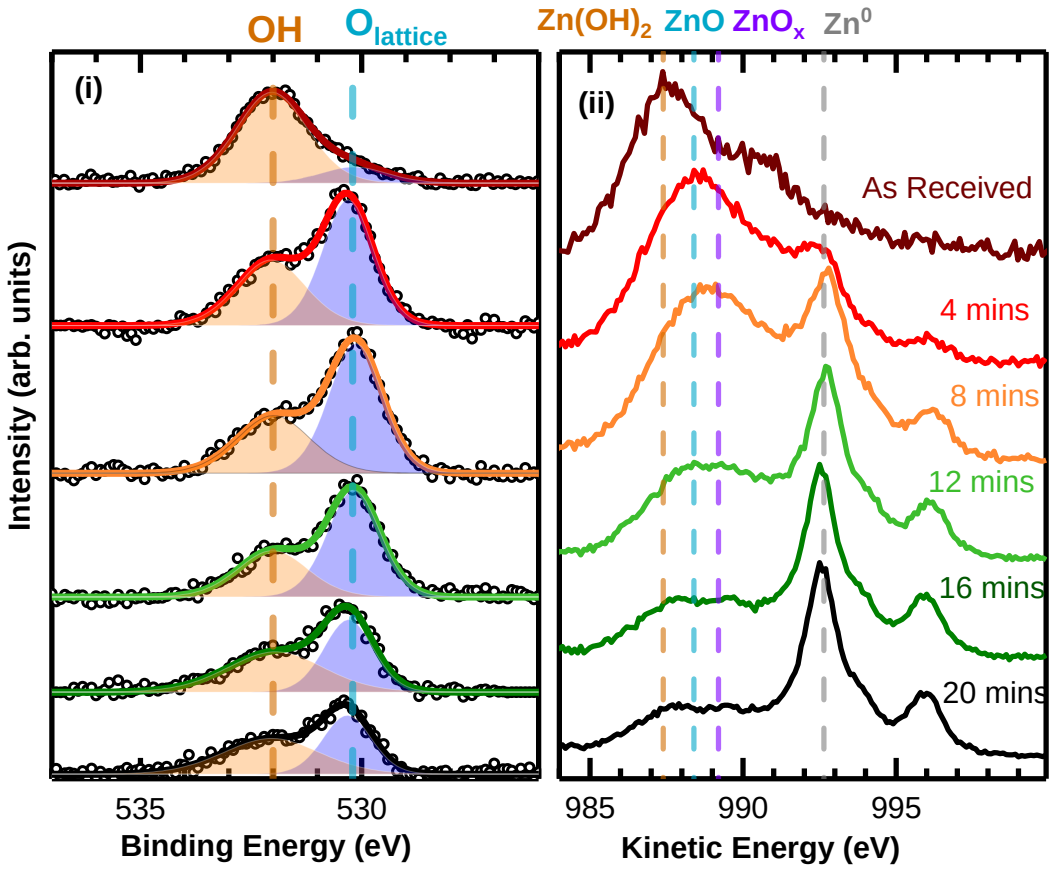


Figure A6.1: *Zn foil sputtered using 2 minute cycles of Ar^+ (500 V). (i) O 1s and (ii) Zn LMM regions.*

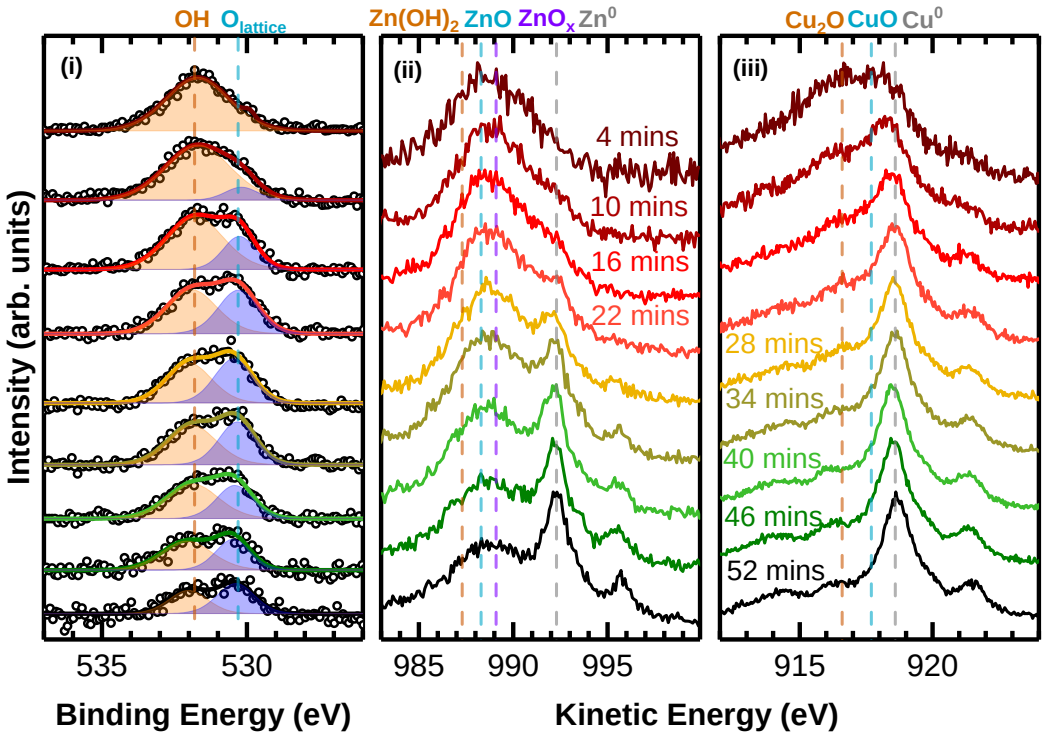


Figure A6.2: *Brass foil sputtered using 2 minute cycles of Ar^+ (500 V). (i) O 1s, (ii) Zn LMM, and (iii) Cu LMM regions.*

992.4 eV showing the formation of Zn^0 during O removal. It is worth noting that Zn^0 does not contain any features at 989.2 eV.[77] Therefore, a feature at 989.2 eV can be assigned to ZnO_x. The ZnO/ZnO_x layer in the brass foil is not completely removed even after almost an hour of sputtering. As expected, the O 1s region is initially dominated by OH, from $Zn(OH)_2$. However, during sputtering, it is unclear whether the $O_{lattice}$ peak is from ZnO or CuO, since it is likely that their peaks will be very close together. Therefore, it is difficult to utilise the O 1s region to distinguish between ZnO and CuO in brass. The broad features would make distinguishing adsorbed species also very challenging.

Reference Data for the Cu L_3-edge and Zn L_3-edge

The oxidised Zn foil was prepared by heating in an oven under ambient conditions at 250°C for 1 hour. Partially oxidised and metallic samples were cleaned via Ar^+ sputtering (1.5 kV) in a preparation chamber and inertly transferred to the analysis chamber a NAP-XPS system. XPS spectra were collected at an excitation energy of 1600 eV and pass energy of 20 eV. Samples were determined to be metallic once a well-defined metallic spectrum in the Zn LMM region was measured. Partially oxidised spectra were taken when sputtering had yet to achieve a completely metallic surface in the Zn LMM region. A Shirley background was subtracted from the XPS data and the Cu $2p_{3/2}$ region was used for energy calibration by setting Cu^0 to 932.6 eV. If no Cu region was available then the Zn^0 peak in Zn LMM at 992.4 eV was used for energy calibration. XPS data was normalised to peak heights. NEXAFS data was treated in the same manner as described for AtmP-NEXAFS in Chapter 6.

For reference data from a pure Cu foil, see reference [171] for the Cu LMM, and see reference [71] and Chapter 4 for the Cu L_3-edge.

Reference Cu L_3-edge and Cu LMM data from a brass foil are shown in Figure A6.3. XPS and NEXAFS were collected from the same sample. XPS shown in Figure A6.3 (i) confirms Cu^0 is present.[77] The Cu L_3-edges appears step-like at 933.7 eV, which

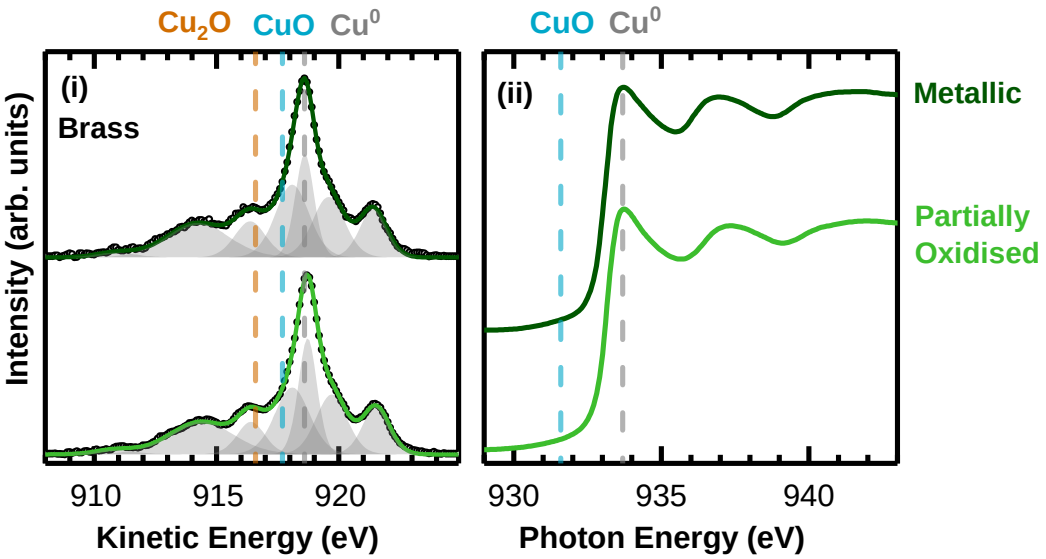


Figure A6.3: *Reference data for Cu in a brass foil for (i) Cu LMM region in XPS and (ii) Cu L_3-edge in NEXAFS under different conditions. Data in (i) and (ii) were collected from the same sample. Partially oxidised state was achieved via incomplete sputtering. Metallic reference data was collected by sputtering until a metallic shape was seen in the corresponding Zn LMM region.*

is associated with Cu^0 as described in Chapter 4.[189] The high energy resonances are at 937.0 eV and 941.2 eV as expected.[71] Figure A6.3 (b) also shows a partially oxidised brass foil where the Cu LMM and Cu L_3-edge indicate the Cu is fully metallic. Therefore, via sputtering, the Cu is more quickly reduced in comparison to Zn (see Figure A6.4 (b), where the Zn is still oxidised following the same sputtering treatment).

Previous high pressure measurements of Zn have utilised hard X-rays and measured the Zn K-edge.[14,17,209,210,276,278,281] The use of soft X-rays in the experiments in Chapter 6 meant the Zn L_3-edge was collected. Most instances of the Zn L_3-edge in literature measure ZnO, which exists under ambient conditions.[40,347–352] Therefore, there is a gap in literature where soft X-rays have not been used to probe more reduced ZnO species which require highly reducing conditions (i.e. high pressure), so there is very limited literature on the Zn L_3-edge for reduced ZnO species.

To understand the changes in the Zn L_3-edge used in this thesis, reference Zn L_3-edge and Zn LMM data were collected for a (a) Zn foil and (b) brass foil, as shown in Figure A6.4. The oxidised Zn foil primarily contains ZnO as shown in XPS (Figure A6.4 (a,i)) with a main peak at 988.4 eV and a shoulder at 991.5 eV. The Zn L_3-edge (Figure A6.4 (a,ii)) for ZnO has three main peaks at: 1026.8, 1028.9, and 1033.1 eV.[349] Zn^{2+} has an unoccupied 4s state. However, the 4s orbital is highly delocalised, so the probability of a transition to 4s is low.[347,352–354] The three main peaks in ZnO are from the 2p to 4d transition; the different transition energies are from orbitals of different symmetry (e.g. e and t_2) and the probability of transition to each orbital varies with coordination number and geometry.[348,353] There is also a shoulder peak at 1024.1 eV for ZnO due to the low probability transition from 2p to the delocalised 4s states.[348] It is worth noting that the energy value for the ZnO peaks varies in literature.[350,355] Therefore, energy calibration of the Zn L_3-edge cannot easily use literature values. In this thesis, the Zn L_3-edge is calibrated using the same energy shift applied to the corresponding Cu L_3-edge for brass,

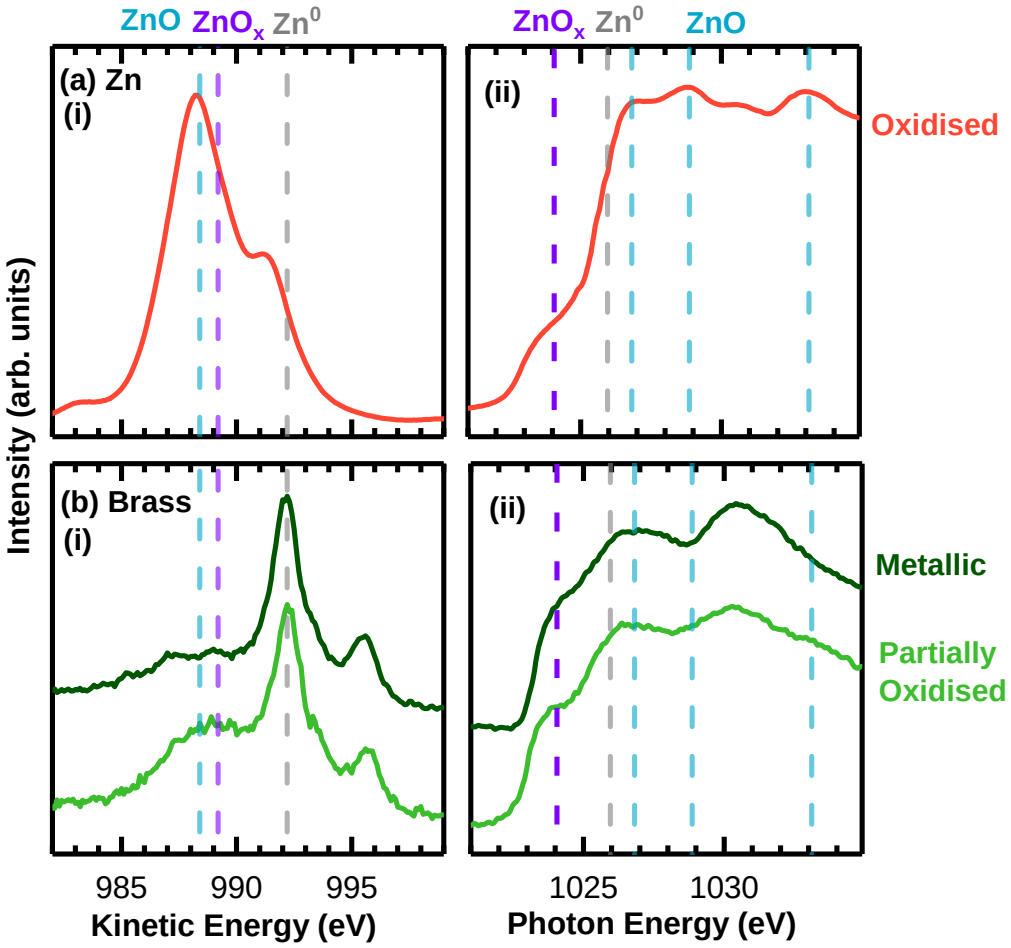


Figure A6.4: *Reference data for Zn in (a) Zn foil and (b) Brass foil for (i) Zn LMM region in XPS and (ii) Zn L_3-edge in NEXAFS under different conditions. Data in (i) and (ii) were collected from the same sample. Partially oxidised state was achieved via incomplete sputtering. Metallic reference data was collected by sputtering until a metallic shape was seen in the Zn LMM region. Oxidised spectra were collected following heating at 250°C at ambient pressure for 1 hour.*

where the position of the Cu L_3-edge is well-defined. In Figure A6.4 (a,ii), there is no Cu L_3-edge to calibrate to since it is a pure Zn foil. Therefore, calibration is performed to the shoulder at 1024.1 eV which is shared with brass (for the 2p to 4s transition).

In Figure A6.4 (b), the partially oxidised brass foil shows a more intense peak at 1024.1 eV. From the Zn LMM region (Figure A6.4 (b,i)) there is a mixture of Zn^0 and ZnO_x present (peaks at 992.4 eV and 989.2 eV respectively). The increase in the intensity of the peak at 1024.1 eV means there is a corresponding increase in the probability of a transition to the 4s orbital. Partial occupation or hybridisation of the 4s orbital in a partially oxidised Zn species (e.g. ZnO_x) could increase the localisation of the 4s orbital, increasing the probability of a transition to 4s.[356] Therefore, a strong feature at 1024.1 eV is tentatively assigned to the ZnO_x species. The metallic brass foil (Figure A6.4 (b,ii)) has a lower intensity peak at 1024.1 eV in the Zn L_3-edge. This corresponds to a decrease in intensity of the ZnO_x peak in Zn LMM at 989.2 eV, which supports the assignment of ZnO_x to the peak at 1024.1 eV.

The Zn LMM region for both brass foil reference samples in Figure A6.4 (b,i) suggests Zn^0 present (peak at 992.4 eV and shoulder at 995.9 eV). In the Zn L_3-edge there are peaks at 1026.0 eV and ~1031 eV in both Zn L_3-edges, which are not seen in the ZnO spectrum in Figure A6.4 (a,ii).[351] These peaks are tentatively attributed to Zn^0. Zn^0 has a full 4s orbital so a 2p to 4d transition is favoured over a transition to 4s; hence, the peak positions are at a higher energy than the peak for ZnO_x. This assignment is supported by the increase in relative intensity of the peaks at 1026.0 eV and ~1031 eV once a fully metallic surface is seen in XPS. No reference data was collected for a pure Zn foil, therefore the Zn^0 peaks could be due to a Cu^0/Zn^0 alloy rather than pure Zn^0. For convenience, the peaks will be assigned to Zn^0 in this thesis.

Overall, the identification of features in the Zn L_3-edge is challenging, as there is little available literature with well-defined references. An approximate assignment of

peaks has been made: 1024.1 (ZnO_x), 1026.0 eV and ~1031 eV (Zn^0), and 1026.8 eV, 1028.9 eV, and 1033.1 eV (ZnO). This agrees with literature, where peaks in the 1020-1025 eV range are attributed to 2p to 4s transitions, whereas peaks >1025 eV are due to transitions to the 4d orbitals.[350,355]

AtmP-NEXAFS of Brass Nanoparticles: $CO_2 \rightarrow H_2 \rightarrow CO_2$

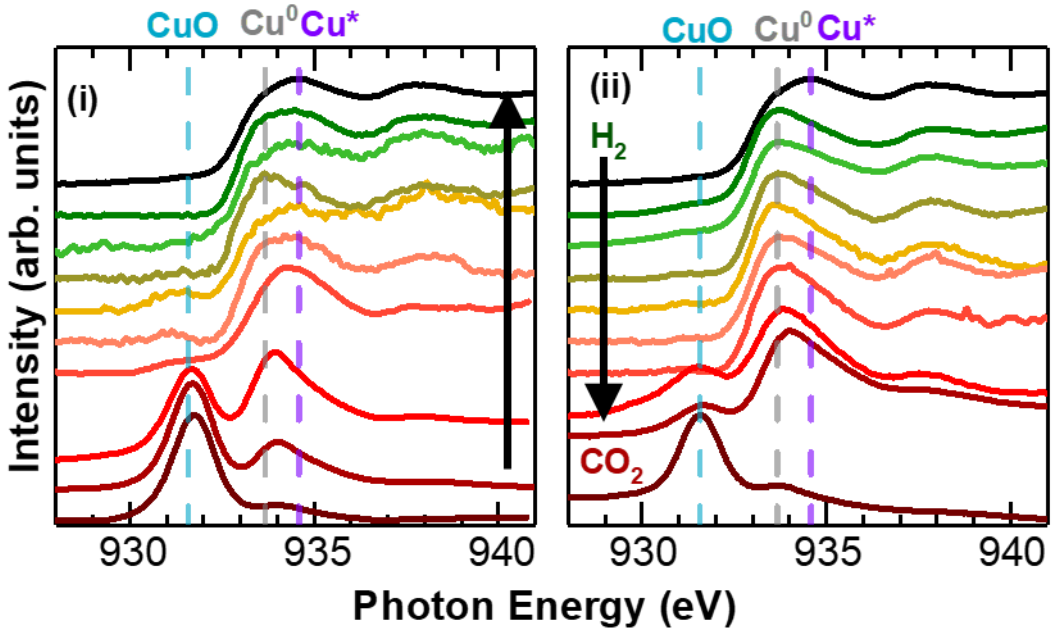


Figure A6.5: *Cu L_3-edge from brass NPs suspended on graphene, collected at 1 bar and 200°C. (i) Starting from the bottom, pure CO_2 was dosed and the composition was slowly changed to increase the H_2:CO_2 ratio until pure H_2 (the top spectrum). (ii) The same sample initially under pure H_2 where CO_2 was slowly reintroduced until under pure CO_2 once again. The colours of each spectra in (i) and (ii) correspond to identical H_2:CO_2 ratios, where the darker red spectra indicates more CO_2, and darker green indicates more H_2. See Figure 6.10 for a detailed key for exact H_2:CO_2 ratios.*

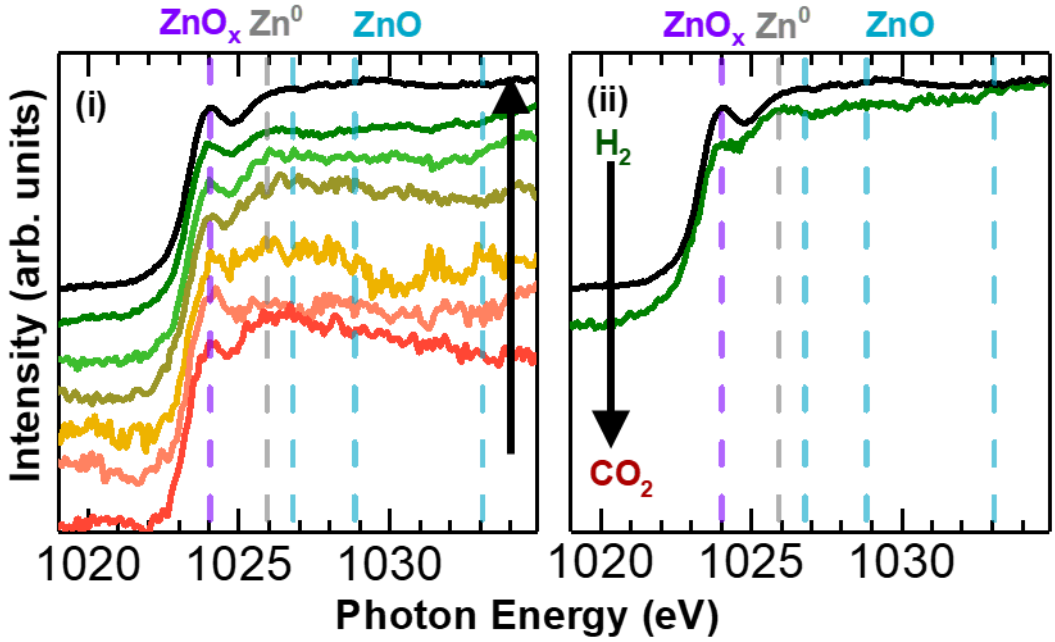


Figure A6.6: *Zn L_3-edge from brass NPs suspended on graphene, collected at 1 bar and 200°C. (i) Starting from the bottom, CO_2 was dosed and the composition was slowly changed to increase the H_2:CO_2 ratio, until pure H_2 (the top spectrum). (ii) The same sample initially under pure H_2 where CO_2 was slowly reintroduced until under pure CO_2 once again. The colours of each spectra in (i) and (ii) correspond to identical H_2:CO_2 ratios, where the darker red spectra indicates more CO_2, and darker green indicates more H_2. See Figure 6.10 for a detailed key for exact H_2:CO_2 ratios.*

References

1 J. Schnadt et al., Present and new frontiers in materials research by ambient pressure x-ray photoelectron spectroscopy, *J. Phys. Condens. Matter*, 2020, **32**, 413003.

2 C. H. Wu et al., Probing electrode/electrolyte interfaces in situ by X-ray spectroscopies: Old methods, new tricks, *Phys. Chem. Chem. Phys.*, 2015, **17**, 30229–30239.

3 K. A. Stoerzinger et al., Insights into Electrochemical Reactions from Ambient Pressure Photoelectron Spectroscopy, *Acc. Chem. Res.*, 2015, **48**, 2976–2983.

4 X. Li et al., In Situ/Operando Characterization Techniques to Probe the Electrochemical Reactions for Energy Conversion, *Small Methods*, 2018, **2**, 1700395.

5 R. Schlögl, Heterogeneous catalysis, *Angew. Chemie - Int. Ed.*, 2015, **54**, 3465–3520.

6 D. Liu et al., Review of Recent Development of In Situ/Operando Characterization Techniques for Lithium Battery Research, *Adv. Mater.*, 2019, **31**, 1806620.

7 E. Roduner, Understanding catalysis, *Chem. Soc. Rev.*, 2014, **43**, 8226–8239.

8 J. R. H. Ross, *Heterogeneous Catalysis Fundamentals and Applications*, Elsevier B. V., 2012.

9 L. Pandit et al., Versatile in situ/operando Setup for Studying Catalysts by X-Ray Absorption Spectroscopy under Demanding and Dynamic Reaction Conditions for Energy Storage and Conversion, *Chemistry–Methods*, 2022, **2**, 202100078.

10 S. Navarro-Jaén et al., Highlights and challenges in the selective reduction of carbon dioxide to methanol, *Nat. Rev. Chem.*, 2021, **5**, 564–579.

11 Y. Li et al., A review of in situ/operando studies of heterogeneous catalytic hydrogenation of CO2 to methanol, *Catal. Today*, 2023, **420**, 114029.

12 Y. Han et al., In Situ Characterization of Catalysis and Electrocatalysis Using APXPS, *ACS Catal.*, 2021, **11**, 1464–1484.

13 T. Kamsuwan et al., Comparative study on the effect of different copper loading on catalytic behaviors and activity of Cu/ZnO/Al2O3 catalysts toward CO and CO2 hydrogenation, *Heliyon*, 2021, **7**, 07682.

14 S. C. Qi et al., Causation of catalytic activity of Cu-ZnO for CO2 hydrogenation to methanol, *Chem. Eng. J.*, 2022, **430**, 132784.

15 L. Zhong et al., Improving the Catalytic Performance of Cobalt for CO Preferential Oxidation by Stabilizing the Active Phase through Vanadium Promotion, *ACS Catal.*, 2021, **11**, 5369–5385.

16 T. Kamsuwan et al., Differences in Deterioration Behaviors of Cu/ZnO/Al2O3Catalysts with Different Cu Contents toward Hydrogenation of CO and CO2, *ACS Omega*, 2022, **7**, 25783–25797.

17 A. Beck et al., Following the structure of copper-zinc-alumina across the pressure gap in carbon dioxide hydrogenation, *Nat. Catal.*, 2021, **4**, 488–497.

18 A. Kolmakov et al., Recent Approaches for Bridging the Pressure Gap in Photoelectron Microspectroscopy, *Top. Catal.*, 2016, **59**, 448–468.

19 R. S. Weatherup, 2D Material Membranes for Operando Atmospheric Pressure Photoelectron Spectroscopy, *Top. Catal.*, 2018, **61**, 2085–2102.

20 H. Bluhm et al., In Situ X-Ray Photoelectron Studies of Gas–Solid Interfaces at Near-Ambient Conditions, *MRS Bull.*, 2007, **32**, 1022–1030.

21 J. J. Velasco-Vélez et al., Atmospheric pressure X-ray photoelectron spectroscopy apparatus: Bridging the pressure gap, *Rev. Sci. Instrum.*, 2016, **87**, 053121.

22 F. Tao et al., Break-up of stepped platinum catalyst surfaces by high CO coverage, *Science*, 2010, **327**, 850–853.

23 J. Kim et al., Operando Surface Studies on Metal-Oxide Interfaces of Bimetal and Mixed Catalysts, *ACS Catal.*, 2021, **11**, 8645–8677.

24 X. Lian et al., Unraveling Catalytic Reaction Mechanism by In Situ Near Ambient Pressure X-ray Photoelectron Spectroscopy, *J. Phys. Chem. Lett.*, 2022, **13**, 8264–8277.

25 S. K. Beaumont, Soft XAS as an: In situ technique for the study of heterogeneous catalysts, *Phys. Chem. Chem. Phys.*, 2020, **22**, 18747–18756.

26 G. A. Somorjai et al., Determination of molecular surface structure, composition, and dynamics under reaction conditions at high pressures and at the solid-liquid interface, *Angew. Chemie - Int. Ed.*, 2011, **50**, 10116–10129.

27 J. F. Li et al., Shell-isolated nanoparticle-enhanced Raman spectroscopy, *Nature*, 2010, **464**, 392–395.

28 A. S. Malkani et al., Operando Spectroscopic Investigations of Copper and Oxide-Derived Copper Catalysts for Electrochemical CO Reduction, *ACS Catal.*, 2019, **9**, 474–478.

29 L. J. Falling et al., Graphene-Capped Liquid Thin Films for Electrochemical Operando X-ray Spectroscopy and Scanning Electron Microscopy, *ACS Appl. Mater. Interfaces*, 2020, **12**, 37680–37692.

30 S. Chenna et al., Operando transmission electron microscopy: A technique for detection of catalysis using electron energy-loss spectroscopy in the transmission electron microscope, *ACS Catal.*, 2012, **2**, 2395–2402.

31 B. L. Mehdi et al., Observation and quantification of nanoscale processes in lithium batteries by operando electrochemical (S)TEM, *Nano Lett.*, 2015, **15**, 2168–2173.

32 M. Gu et al., Demonstration of an electrochemical liquid cell for operando transmission electron microscopy observation of the lithiation/delithiation behavior of Si nanowire battery anodes, *Nano Lett.*, 2013, **13**, 6106–6112.

33 F. A. Stevie et al., Introduction to x-ray photoelectron spectroscopy, *J. Vac. Sci. Technol. A Vacuum, Surfaces, Film.*, 2020, **38**, 063204.

34 S. Tanuma et al., Calculations of electron inelastic mean free paths. IX. Data for 41 elemental solids over the 50 eV to 30 keV range, *Surf. Interface Anal.*, 2011, **43**, 689–713.

35 S. Tanuma et al., Calculations of Electron Inelastic Mean Free Paths, *Surf. Interface Anal.*, 1993, **21**, 165–176.

36 M.P.Seah et al., Quantitative Electron Spectroscopy of Surface: A Standard Data Base for Electron Inelastic Mean Free Paths in Solids, *Surf. Interface Anal.*, 1979, **1**, 2–11.

37 E. S. Jones et al., Enclosed Cells for Extending Soft X-ray Spectroscopies to Atmospheric Pressures and above, *ACS Symp. Ser.*, 2021, **1396**, 175–218.

38 M. Salmeron et al., Ambient pressure photoelectron spectroscopy: A new tool for surface science and nanotechnology, *Surf. Sci. Rep.*, 2008, **63**, 169–199.

39 C. Escudero et al., From solid-vacuum to solid-gas and solid-liquid interfaces: In situ studies of structure and dynamics under relevant conditions, *Surf. Sci.*, 2013, **607**, 2–9.

40 B. Gilbert et al., X-ray absorption spectroscopy of the cubic and hexagonal polytypes of zinc sulfide, *Phys. Rev. B - Condens. Matter Mater. Phys.*, 2002, **66**, 245205.

41 H. Shinotsuka et al., Calculations of electron inelastic mean free paths. XII. Data for 42 inorganic compounds over the 50 eV to 200 keV range with the full Penn algorithm, *Surf. Interface Anal.*, 2019, **51**, 427–457.

42 P. J. Cumpson et al., Elastic scattering corrections in AES and XPS. II. Estimating attenuation lengths and conditions required for their valid use in overlayer/substrate experiments, *Surf. Interface Anal.*, 1997, **25**, 430–446.

43 B. L. Henke et al., X-ray Interactions: Photoabsorption, Scattering, Transmission and Reflection, *At. Data Nucl. Data Tables*, 1993, **54**, 1–168.

44 M. P. Seah, Simple universal curve for the energy-dependent electron attenuation length for all materials, *Surf. Interface Anal.*, 2012, **44**, 1353–1359.

45 J. J. Yeh et al., Atomic Subshell Photoionization Cross Sections and Asymmetry Parameters, *At. Data Nucl. Data Tables*, 1985, **32**, 1–155.

46 H. Siegbahn et al., ESCA applied to liquids, *J. Electron Spectrosc. Relat. Phenom.*, 1973, **2**, 319–325.

47 K. Siegbahn et al., *ESCA applied to free molecules*, North-Hollan Publishing Company: Amsterdam-London, 1969.

48 D. E. Starr et al., Investigation of solid/vapor interfaces using ambient pressure X-ray photoelectron spectroscopy, *Chem. Soc. Rev.*, 2013, **42**, 5833–5857.

49 D. F. Ogletree et al., A differentially pumped electrostatic lens system for photoemission studies in the millibar range, *Rev. Sci. Instrum.*, 2002, **73**, 3872–3877.

50 D. Frank Ogletree et al., Photoelectron spectroscopy under ambient pressure and temperature conditions, *Nucl. Instruments Methods Phys. Res. Sect. A Accel. Spectrometers, Detect. Assoc. Equip.*, 2009, **601**, 151–160.

51 C. Schlueter et al., The new dedicated HAXPES beamline P22 at PETRAIII, *AIP Conf. Proc.*, 2019, **2054**, 040010.

52 T. Masuda, Various spectroelectrochemical cells for in situ observation of electrochemical processes at solid–liquid interfaces, *Top. Catal.*, 2018, **61**, 2103–2113.

53 K. Kobayashi et al., Development of a laboratory system hard X-ray photoelectron spectroscopy and its applications, *J. Electron Spectrosc. Relat. Phenom.*, 2013, **190**, 210–221.

54 H. Kiuchi et al., Operando hard X-ray photoelectron spectroscopy of LiCoO2 thin film in an all-solid-state lithium ion battery, *Electrochem. Commun.*, 2020, **118**, 106790.

55 P. Amann et al., The state of zinc in methanol synthesis over a Zn/ZnO/Cu(211) model catalyst, *Science*, 2022, **376**, 603–608.

56 E. J. Crumlin et al., X-ray spectroscopy of energy materials under in situ/operando conditions, *J. Electron Spectrosc. Relat. Phenom.*, 2015, **200**, 264–273.

57 R. S. Weatherup et al., Graphene Membranes for Atmospheric Pressure Photoelectron Spectroscopy, *J. Phys. Chem. Lett.*, 2016, **7**, 1622–1627.

58 A. Kolmakov et al., Graphene oxide windows for in situ environmental cell photoelectron spectroscopy, *Nat. Nanotechnol.*, 2011, **6**, 651–657.

59 J. Kraus et al., Photoelectron spectroscopy of wet and gaseous samples through graphene membranes, *Nanoscale*, 2014, **6**, 14394–14403.

60 J. J. Velasco-Velez et al., Photoelectron Spectroscopy at the Graphene-Liquid Interface Reveals the Electronic Structure of an Electrodeposited Cobalt/Graphene Electrocatalyst, *Angew. Chemie - Int. Ed.*, 2015, **54**, 14554–14558.

61 J. J. Velasco-Velez et al., The structure of interfacial water on gold electrodes studied by x-ray absorption spectroscopy, *Science*, 2014, **346**, 831–834.

62 R. S. Weatherup et al., Environment-Dependent Radiation Damage in Atmospheric Pressure X-ray Spectroscopy, *J. Phys. Chem. B*, 2018, **122**, 737–744.

63 H. Guo et al., Enabling Photoemission Electron Microscopy in Liquids via Graphene-Capped Microchannel Arrays, *Nano Lett.*, 2017, **17**, 1034–1041.

64 I. J. Drake et al., An in situ cell for characterization of solids by soft x-ray absorption, *Rev. Sci. Instrum.*, 2004, **75**, 3242–3247.

65 G. D. Moggridge et al., Environmental cells for in situ X-ray diffraction and X-ray absorption spectroscopic studies of heterogeneous catalysts, *Nucl. Instruments Methods Phys. Res. B*, 1995, **97**, 28–32.

66 R. Endo et al., In situ X-ray photoelectron spectroscopy using a conventional Al-Kα source and an environmental cell for liquid samples and solid-liquid interfaces, *Appl. Phys. Lett.*, 2019, **114**, 173702.

67 S. Nemšák et al., Interfacial Electrochemistry in Liquids Probed with

Photoemission Electron Microscopy, *J. Am. Chem. Soc.*, 2017, **139**, 18138–18141.

68 Y. Zhang et al., Real-Time Characterization of the Fine Structure and Dynamics of an Electrical Double Layer at Electrode-Electrolyte Interfaces, *J. Phys. Chem. Lett.*, 2021, **12**, 5279–5285.

69 J. Duchoslav et al., XPS study of zinc hydroxide as a potential corrosion product of zinc: Rapid X-ray induced conversion into zinc oxide, *Corros. Sci.*, 2014, **82**, 356–361.

70 C. Arble et al., Radiation damage of liquid electrolyte during focused X-ray beam photoelectron spectroscopy, *Surf. Sci.*, 2020, **697**, 121608.

71 J. E. N. Swallow et al., Revealing the Role of CO during CO2 Hydrogenation on Cu Surfaces with In Situ Soft X-Ray Spectroscopy, *J. Am. Chem. Soc.*, 2023, **145**, 6730–6740.

72 T. Masuda et al., In situ x-ray photoelectron spectroscopy for electrochemical reactions in ordinary solvents, *Appl. Phys. Lett.*, 2013, **103**, 111605.

73 E. Tsunemi et al., Hard x-ray photoelectron spectroscopy using an environmental cell with silicon nitride membrane windows, *J. Appl. Phys.*, 2015, **117**, 234902.

74 F. F. Settembrini et al., Anisotropic straining of graphene using micropatterned SiN membranes, *APL Mater.*, 2016, **4**, 116107.

75 A. Yulaev et al., Graphene Microcapsule Arrays for Combinatorial Electron Microscopy and Spectroscopy in Liquids, *ACS Appl. Mater. Interfaces*, 2017, **9**, 26492–26502.

76 L. Wang et al., Single-Layer Graphene Membranes Withstand Ultrahigh Applied Pressure, *Nano Lett.*, 2017, **17**, 3081–3088.

77 J. F. Moulder et al., Handbook of X-ray Spectroscopy, 1992, 1–261.

78 V. Pérez-Dieste et al., Near ambient pressure XPS at ALBA, *J. Phys. Conf. Ser.*, 2013, **425**, 072023.

79 G. Held et al., Ambient-pressure endstation of the Versatile Soft X-ray (VerSoX) beamline at Diamond Light Source, *J. Synchrotron Radiat.*, 2020, **27**, 1153–1166.

80 D. C. Grinter et al., The Versatile Soft X-Ray (VerSoX) Beamline at Diamond Light Source, *Synchrotron Radiat. News*, 2022, **35**, 39–47.

81 S. Axnanda et al., Direct work function measurement by gas phase photoelectron spectroscopy and its application on PbS nanoparticles, *Nano Lett.*, 2013, **13**, 6176–6182.

82 G. R. Khan, Crystallographic, structural and compositional parameters of Cu–ZnO nanocrystallites, *Appl. Phys. A Mater. Sci. Process.*, 2020, **126**, 311.

83 N. Fairley et al., Systematic and collaborative approach to problem solving using X-ray photoelectron spectroscopy, *Appl. Surf. Sci. Adv.*, 2021, **5**, 100112.

84 G. Greczynski et al., X-ray photoelectron spectroscopy: Towards reliable binding energy referencing, *Prog. Mater. Sci.*, 2020, **107**, 100591.

85 S. Evans, Curve synthesis and optimization procedures for X-ray photoelectron spectroscopy, *Surf. Interface Anal.*, 1991, **17**, 85–93.

86 G. H. Major et al., A detailed view of the Gaussian–Lorentzian sum and product functions and their comparison with the Voigt function, *Surf. Interface Anal.*, 2022, **54**, 262–269.

87 S. Doniach et al., Many-electron singularity in X-ray photoemission and X-ray line spectra from metals, *J. Phys. C Solid State Phys.*, 1970, **3**, 285–291.

88 J. J. Pireaux et al., Core-electron relaxation energies and valence-band formation of linear alkanes studied in the gas phase by means of electron spectroscopy, *Phys. Rev. A*, 1976, **14**, 2133–2145.

89 S. Axnanda et al., Using 'Tender' X-ray Ambient Pressure X-Ray Photoelectron Spectroscopy as A Direct Probe of Solid-Liquid Interface, *Sci. Reports*, 2015, **5**, 09788.

90 J. J. Yeh et al., Atomic subshell photoionization cross sections and asymmetry parameters: 1 ≤ Z ≤ 103, *At. Data Nucl. Data Tables*, 1985, **32**, 1–155.

91 J. J. Velasco-Velez et al., A comparative study of electrochemical cells for in situ x-ray spectroscopies in the soft and tender x-ray range, *J. Phys. D: Appl. Phys.*, 2021, **54**, 124003.

92 Y. Tamenori, Electron yield soft X-ray photoabsorption spectroscopy under normal ambient-pressure conditions, *J. Synchrotron Radiat.*, 2013, **20**, 419–425.

93 G. T. Seidler et al., A laboratory-based hard x-ray monochromator for high-resolution x-ray emission spectroscopy and x-ray absorption near edge structure measurements, *Rev. Sci. Instrum.*, 2014, **85**, 113906.

94 N. Isomura et al., Depth-selective X-ray absorption spectroscopy by detection of energy-loss Auger electrons, *Appl. Surf. Sci.*, 2015, **355**, 268–271.

95 B. Mei et al., In situ catalytic cells for x-ray absorption spectroscopy measurement, *Rev. Sci. Instrum.*, 2023, **94**, 051501.

96 A. Jonas et al., Towards Poisson noise limited optical pump soft X-ray probe NEXAFS spectroscopy using a laser-produced plasma source, *Opt. Express*, 2019, **27**, 36524–36537.

97 R. J. Nicholls, Advances in modelling electron energy loss spectra from first principles, *J. Phys. Mater.*, 2021, **4**, 024008.

98 A. J. Achkar et al., Determination of total X-ray absorption coefficient using non-resonant X-ray emission, *Sci. Reports*, 2011, **1**, 182.

99 W. Błachucki et al., High energy resolution off-resonant spectroscopy for X-ray absorption spectra free of self-absorption effects, *Phys. Rev. Lett.*, 2014, **112**, 173003.

100 F. Tavani et al., Structural and mechanistic insights into low-Temperature CO oxidation over a prototypical high entropy oxide by Cu L-edge operando soft X-ray absorption spectroscopy, *Phys. Chem. Chem. Phys.*, 2021, **23**, 26575–26584.

101 F. Zheng et al., In-situ X-ray Absorption Study of Evolution of Oxidation States

and Structure of Cobalt in Co and CoPt Bimetallic Nanoparticles (4 nm) under Reducing (H2) and Oxidizing (O2) Environments, *Nano Lett.*, 2011, **11**, 847–853.

102 S. L. M. Schroeder et al., What determines the probing depth of electron yield XAS?, *Surf. Sci.*, 1995, **324**, L371–L377.

103 M. Chen et al., Advances in transferring chemical vapour deposition graphene: A review, *Mater. Horizons*, 2017, **4**, 1054–1063.

104 C. Y. Tang et al., *Transmission Electron Microscopy (TEM)*, Elsevier B.V., 2017.

105 D. B. Williams et al., *Transmission electron microscopy*, 2009.

106 Introduction to TEM (MyScope), https://myscope.training/TEM_Introduction_to_TEM, (accessed 22 March 2024).

107 F. Tuinstra et al., Raman Spectrum of Graphite, *J. Chem. Phys.*, 1970, **53**, 1126–1130.

108 C. Thomsen et al., Double resonant raman scattering in graphite, *Phys. Rev. Lett.*, 2000, **85**, 5214–5217.

109 J. Bin Wu et al., Raman spectroscopy of graphene-based materials and its applications in related devices, *Chem. Soc. Rev.*, 2018, **47**, 1822–1873.

110 A. C. Ferrari et al., Raman spectroscopy as a versatile tool for studying the properties of graphene, *Nat. Nanotechnol.*, 2013, **8**, 235–246.

111 A. C. Ferrari et al., Raman spectrum of graphene and graphene layers, *Phys. Rev. Lett.*, 2006, **97**, 187401.

112 H. C. Lee et al., Review of the synthesis, transfer, characterization and growth mechanisms of single and multilayer graphene, *RSC Adv.*, 2017, **7**, 15644–15693.

113 M. Al-Mansoori et al., Effects of gas flow rate on the structure and elemental composition of tin oxide thin films deposited by RF sputtering, *AIP Adv.*, 2017, **7**, 125105.

114 J. S. Gibson et al., Gently does it!: in situ preparation of alkali metal-solid electrolyte interfaces for photoelectron spectroscopy, *Faraday Discuss.*, 2022, **236**, 267–287.

115 P. Jia et al., Effect of oxygen plasma etching on graphene's mechanical and electrical properties, *IOP Conf. Ser. Mater. Sci. Eng.*, 2017, **182**, 012030.

116 M. G. Lemaitre et al., Improved transfer of graphene for gated schottky-junction, vertical, organic, field-effect transistors, *ACS Nano*, 2012, **6**, 9095–9102.

117 Nikalyte Ltd., https://www.nikalyte.com/nl-uhv/, (accessed 22 March 2024).

118 J. Maibach et al., Toward Operando Characterization of Interphases in Batteries, *ACS Mater. Lett.*, 2023, **5**, 2431–2444.

119 J. S. Bunch et al., Impermeable atomic membranes from graphene sheets, *Nano Lett.*, 2008, **8**, 2458–2462.

120 J. Schnadt et al., The new ambient-pressure X-ray photoelectron spectroscopy instrument at MAX-lab, *J. Synchrotron Radiat.*, 2012, **19**, 701–704.

121 C. Escudero et al., A reaction cell with sample laser heating for in situ soft X-ray absorption spectroscopy studies under environmental conditions, *J. Synchrotron Radiat.*, 2013, **20**, 504–508.

122 D. K. Bora et al., An ultra-high vacuum electrochemical flow cell for in situ / operando soft X-ray spectroscopy study, *Rev. Sci. Instrum.*, 2014, **85**, 043106.

123 J. H. Guo et al., The interaction of cations and liquid water studied by resonant soft-X-ray absorption and emission spectroscopy, *J. Electron Spectrosc. Relat. Phenom.*, 2005, **144**–**147**, 287–290.

124 H. Yuzawa et al., In situ soft X-ray absorption spectroscopy applied to solid-liquid heterogeneous cyanopyrazine hydration reaction on titanium oxide catalyst, *J. Phys. Chem. C*, 2015, **119**, 7738–7745.

125 P. Jiang et al., In situ soft X-ray absorption spectroscopy investigation of electrochemical corrosion of copper in aqueous NaHCO3 solution, *Electrochem. Commun.*, 2010, **12**, 820–822.

126 J. Forsberg et al., System for in situ studies of atmospheric corrosion of metal films using soft x-ray spectroscopy and quartz crystal microbalance, *Rev. Sci. Instrum.*, 2007, **78**, 083110.

127 T. Herranz et al., Influence of the cobalt particle size in the CO hydrogenation reaction studied by in situ X-ray absorption spectroscopy, *J. Phys. Chem. B*, 2009, **113**, 10721–10727.

128 Silson - SiN Membranes, https://www.silson.com/product/silicon-nitride/, (accessed 22 March 2024).

129 Silson - Differential Pressure Windows, https://www.silson.com/product/pressure-windows-vacuum-windows/, (accessed 22 March 2024).

130 G. Zhang et al., Versatile Polymer-Free Graphene Transfer Method and Applications, *ACS Appl. Mater. Interfaces*, 2016, **8**, 8008–8016.

131 L. H. Li et al., Strong oxidation resistance of atomically thin boron nitride nanosheets, *ACS Nano*, 2014, **8**, 1457–1462.

132 S. Hofmann et al., CVD-enabled graphene manufacture and technology, *J. Phys. Chem. Lett.*, 2015, **6**, 2714–2721.

133 X. Zhang et al., Recent progress in low-temperature CVD growth of 2D materials, *Oxford Open Mater. Sci.*, 2023, **3**, itad010.

134 L. P. Ma et al., Transfer Methods of Graphene from Metal Substrates: A Review, *Small Methods*, 2019, **3**, 1900049.

135 J. W. Elmer et al., Diffusion bonding and brazing of high purity copper for linear collider accelerator structures, *Phys. Rev. Spec. Top. - Accel. Beams*, 2001, **4**, 053502.

136 B. Eren et al., Identifying the catalyst chemical state and adsorbed species during methanol conversion on copper using ambient pressure X-ray spectroscopies, *Phys. Chem. Chem. Phys.*, 2020, **22**, 18806–18814.

137 C. Castán-Guerrero et al., A reaction cell for ambient pressure soft x-ray

absorption spectroscopy, *Rev. Sci. Instrum.*, 2018, **89**, 054101.

138 A. Goeppert et al., Recycling of carbon dioxide to methanol and derived products-closing the loop, *Chem. Soc. Rev.*, 2014, **43**, 7995–8048.

139 K. A. Ali et al., Recent development in catalytic technologies for methanol synthesis from renewable sources: A critical review, *Renew. Sustain. Energy Rev.*, 2015, **44**, 508–518.

140 F. Dalena et al., *Methanol Production and Applications: An Overview*, Elsevier B.V., 2018.

141 J. P. Lange, Methanol synthesis: A short review of technology improvements, *Catal. Today*, 2001, **64**, 3–8.

142 S. Zhang et al., A Short Review of Recent Advances in Direct CO2 Hydrogenation to Alcohols, *Top. Catal.*, 2021, **64**, 371–394.

143 C. Wu et al., Understanding and Application of Strong Metal-Support Interactions in Conversion of CO2to Methanol: A Review, *Energy and Fuels*, 2021, **35**, 19012–19023.

144 X. Jiang et al., Recent Advances in Carbon Dioxide Hydrogenation to Methanol via Heterogeneous Catalysis, *Chem. Rev.*, 2020, **120**, 7984–8034.

145 Y.-F. Shi et al., Copper-based catalysts for CO2 hydrogenation: a perspective on active sites, *EES Catal.*, 2023, **1**, 921–933.

146 M. Bowker et al., The photocatalytic window: Photo-reforming of organics and water splitting for sustainable hydrogen production, *Catal. Lett.*, 2015, **145**, 214–219.

147 A. Goeppert et al., *Toward a Sustainable Carbon Cycle: The Methanol Economy*, Elsevier Inc., 2018.

148 BBC - 2023 Hottest Year on Record Worldwide, https://www.bbc.co.uk/news/science-environment-67861954, (accessed 22 March 2024).

149 G. A. Olah, Towards oil independence through renewable methanol chemistry, *Angew. Chemie - Int. Ed.*, 2013, **52**, 104–107.

150 G. A. Olah, Beyond oil and gas: The methanol economy, *Angew. Chemie - Int. Ed.*, 2005, **44**, 2636–2639.

151 R. Rajasegar et al., in *ASME International Mechanical Engineering Congress and Exposition, Proceedings (IMECE)*, 2017, vol. 6.

152 M. Behrens et al., The Active Site of Methanol Synthesis over Cu/ZnO/Al2O3 Industrial Catalysts, *Science*, 2012, **759**, 893–898.

153 J. C. Frost, Junction effect interactions in methanol synthesis catalysts, *Nature*, 1988, **334**, 577–580.

154 M. Behrens, Heterogeneous Catalysis of CO2 Conversion to Methanol on Copper Surfaces, *Angew. Chemie - Int. Ed.*, 2014, **53**, 12022–12024.

155 F. Pontzen et al., CO2-based methanol and DME - Efficient technologies for industrial scale production, *Catal. Today*, 2011, **171**, 242–250.

156 G. C. Chinchen et al., Mechanism of methanol synthesis from CO2/CO/H2 mixtures over copper/zinc oxide/alumina catalysts: use of 14C-labelled reactants, *Appl. Catal.*, 1987, **30**, 333–338.

157 N. D. Nielsen et al., The roles of CO and CO2 in high pressure methanol synthesis over Cu-based catalysts, *J. Catal.*, 2021, **393**, 324–334.

158 M. Bowker, Chemisorption and industrial catalytic processes, *Vacuum*, 1983, **33**, 669–685.

159 N. D. Nielsen et al., Bifunctional Synergy in CO Hydrogenation to Methanol with Supported Cu, *Catal. Lett.*, 2020, **150**, 1427–1433.

160 J. Nerlov et al., Methanol synthesis from CO2, CO, and H2 over Cu(100) and Ni/Cu(100), *J. Catal.*, 1999, **181**, 271–279.

161 A. Y. Rozovskii et al., Fundamentals of methanol synthesis and decomposition, *Top. Catal.*, 2003, **22**, 137–150.

162 S. Kattel et al., Active sites for CO2 hydrogenation to methanol on Cu/ZnO catalysts, *Science*, 2017, **355**, 1296–1299.

163 L. C. Grabow et al., Mechanism of methanol synthesis on Cu through CO2 and CO hydrogenation, *ACS Catal.*, 2011, **1**, 365–384.

164 S. Kattel et al., Optimizing Binding Energies of Key Intermediates for CO2 Hydrogenation to Methanol over Oxide-Supported Copper, *J. Am. Chem. Soc.*, 2016, **138**, 12440–12450.

165 Y. Yang et al., Fundamental studies of methanol synthesis from CO2 hydrogenation on Cu(111), Cu clusters, and Cu/ZnO(0001), *Phys. Chem. Chem. Phys.*, 2010, **12**, 9909–9917.

166 P. B. Rasmussen et al., Methanol synthesis on Cu(100) from a binary gas mixture of CO2 and H2, *Catal. Lett.*, 1994, **26**, 373–381.

167 R. Burch et al., The role of hydrogen in methanol synthesis over copper catalysts, *Catal. Lett.*, 1990, **5**, 55–60.

168 Q. L. Tang et al., CO2 fixation into methanol at Cu/ZrO2 interface from first principles kinetic Monte Carlo, *J. Catal.*, 2009, **263**, 114–122.

169 J. Yoshihara et al., Methanol synthesis and reverse water-gas shift kinetics over Cu(110) model catalysts: Structural sensitivity, *J. Catal.*, 1996, **161**, 776–782.

170 B. Eren et al., Dissociative Carbon Dioxide Adsorption and Morphological Changes on Cu(100) and Cu(111) at Ambient Pressures, *J. Am. Chem. Soc.*, 2016, **138**, 8207–8211.

171 M. C. Biesinger, Advanced analysis of copper X-ray photoelectron spectra, *Surf. Interface Anal.*, 2017, **49**, 1325–1334.

172 P. Jiang et al., Experimental and theoretical investigation of the electronic structure of Cu2O and CuO thin films on Cu(110) using x-ray photoelectron and absorption spectroscopy, *J. Chem. Phys.*, 2013, **138**, 024704.

173 L. Trotochaud et al., Water Adsorption and Dissociation on Polycrystalline Copper Oxides: Effects of Environmental Contamination and Experimental Protocol, *J. Phys. Chem. B*, 2018, **122**, 1000–1008.

174 K. Andersson et al., Autocatalytic water dissociation on Cu(110) at near ambient conditions, *J. Am. Chem. Soc.*, 2008, **130**, 2793–2797.

175 A. Eilert et al., Subsurface Oxygen in Oxide-Derived Copper Electrocatalysts for Carbon Dioxide Reduction, *J. Phys. Chem. Lett.*, 2017, **8**, 285–290.

176 H. Bluhm et al., Methanol oxidation on a copper catalyst investigated using in situ X-ray photoelectron spectroscopy, *J. Phys. Chem. B*, 2004, **108**, 14340–14347.

177 M. Favaro et al., Subsurface oxide plays a critical role in CO2 activation by Cu(111) surfaces to form chemisorbed CO2, the first step in reduction of CO2, *Proc. Natl. Acad. Sci. U. S. A.*, 2017, **114**, 6706–6711.

178 P. A. Taylor et al., Carbon dioxide chemistry on Cu(100), *J. Vac. Sci. Technol. A Vacuum, Surfaces, Film.*, 1992, **10**, 2570–2575.

179 L. Österlund et al., Bridging the pressure gap in surface science at the atomic level: H/Cu(110), *Phys. Rev. Lett.*, 2001, **86**, 460–463.

180 J. Q. Zhong et al., Synchrotron-based ambient pressure X-ray photoelectron spectroscopy of hydrogen and helium, *Appl. Phys. Lett.*, 2018, **112**, 091602.

181 T. G. Avval et al., Carbon dioxide gas, CO2(g), by near-ambient pressure XPS, *Surf. Sci. Spectra*, 2019, **26**, 014022.

182 Y. F. Zhao et al., Insight into methanol synthesis from CO2 hydrogenation on Cu(1 1 1): Complex reaction network and the effects of H2O, *J. Catal.*, 2011, **281**, 199–211.

183 S. Yamamoto et al., In situ x-ray photoelectron spectroscopy studies of water on metals and oxides at ambient conditions, *J. Phys. Condens. Matter*, 2008, **20**, 184025.

184 H. Tissot et al., Interaction of Atomic Hydrogen with the Cu2O(100) and (111) Surfaces, *J. Phys. Chem. C*, 2019, **123**, 22172–22180.

185 M. Grioni et al., Studies of copper valence states with Cu L3 x-ray-absorption spectroscopy, *Phys. Rev. B*, 1989, **39**, 1541–1545.

186 D. D. Sarma et al., Electronic structure of high-Tc superconductors from soft-x-ray absorption, *Phys. Rev. B*, 1988, **37**, 9784–9787.

187 P. Thakur et al., Electronic structure of Cu-doped ZnO thin films by x-ray absorption, magnetic circular dichroism, and resonant inelastic x-ray scattering, *J. Appl. Phys.*, 2010, **107**, 103915.

188 P. F. Schofield et al., Cu 2p absorption spectroscopy as a probe for the site occupancy of (ZnxCu1-x)WO4 solid solution, *Phys. Chem. Miner.*, 1993, **20**, 375–381.

189 M. Grioni et al., Unoccupied electronic structure and core-hole effects in the x-ray absorption spectra of Cu2O, *Phys. Rev. B*, 1992, **45**, 3309–3318.

190 K. O. Kvashnina et al., Electronic structure of complex copper systems probed by resonant inelastic X-ray scattering at Cu L3 edge, *Phys. B Condens. Matter*, 2009, **404**, 3559–3566.

191 B. Eren et al., Catalyst Chemical State during CO Oxidation Reaction on

Cu(111) Studied with Ambient-Pressure X-ray Photoelectron Spectroscopy and Near Edge X-ray Adsorption Fine Structure Spectroscopy, *J. Am. Chem. Soc.*, 2015, **137**, 11186–11190.

192 B. Eren et al., Reaction of CO with Preadsorbed Oxygen on Low-Index Copper Surfaces: An Ambient Pressure X-ray Photoelectron Spectroscopy and Scanning Tunneling Microscopy Study, *J. Phys. Chem. C*, 2015, **119**, 14669–14674.

193 B. H. Liu et al., Ambient pressure X-ray photoelectron spectroscopy study of room-temperature oxygen adsorption on Cu(1 0 0) and Cu(1 1 1), *Appl. Surf. Sci.*, 2022, **583**, 152438.

194 M. D. Higham et al., Mechanism of CO2 conversion to methanol over Cu(110) and Cu(100) surfaces, *Dalton Trans.*, 2020, **49**, 8478–8497.

195 T. Yang et al., Surface orientation and pressure dependence of CO2 activation on Cu surfaces, *J. Phys. Chem. C*, 2020, **124**, 27511–27518.

196 S. Vollmer et al., Determination of site specific adsorption energies of CO on copper, *Catal. Lett.*, 2001, **77**, 97–101.

197 H. W. Lim et al., Modeling of the kinetics for methanol synthesis using Cu/ZnO/Al 2O3/ZrO2 catalyst: Influence of carbon dioxide during hydrogenation, *Ind. Eng. Chem. Res.*, 2009, **48**, 10448–10455.

198 J. Y. Kim et al., Reduction of CuO and Cu2O with H2: H embedding and kinetic effects in the formation of suboxides, *J. Am. Chem. Soc.*, 2003, **125**, 10684–10692.

199 K. H. Schulz et al., Surface hydride formation on a metal oxide surface: the interaction of atomic hydrogen with Cu2O(100), *Surf. Sci.*, 1992, **278**, 9–18.

200 U. J. Etim et al., Improving the Cu/ZnO-Based Catalysts for Carbon Dioxide Hydrogenation to Methanol, and the Use of Methanol As a Renewable Energy Storage Media, *Front. Earth Sci.*, 2020, **8**, 545431.

201 J. Szanyi et al., Methanol synthesis on a Cu(100) catalyst, *Catal. Lett.*, 1991, **10**, 383–390.

202 S. S. Fu et al., Interactions of O2, CO, CO2, and D2 with the stepped CU(311) crystal face: Comparison to CU(110), *Surf. Sci.*, 1992, **262**, 68–76.

203 I. A. Bönicke et al., A study on CO2 dissociation on a stepped (332) copper surface, *Surf. Sci.*, 1994, **307**–**309**, 177–181.

204 S. Sakong et al., Dissociative adsorption of hydrogen on strained Cu surfaces, *Surf. Sci.*, 2003, **525**, 107–118.

205 Y. Maimaiti et al., Reduction mechanisms of the CuO(111) surface through surface oxygen vacancy formation and hydrogen adsorption, *Phys. Chem. Chem. Phys.*, 2014, **16**, 3036–3046.

206 M. Fowles et al., Steam Reforming of Hydrocarbons for Synthesis Gas Production, *Top. Catal.*, 2021, **64**, 856–875.

207 T. Zheng et al., Recent Advances in Electrochemical CO2-to-CO Conversion on Heterogeneous Catalysts, *Adv. Mater.*, 2018, **30**, 1802066.

208 S. Jin et al., Advances and Challenges for the Electrochemical Reduction of CO2 to CO: From Fundamentals to Industrialization, *Angew. Chem.*, 2021, **133**, 20795–20816.

209 M. Zabilskiy et al., The unique interplay between copper and zinc during catalytic carbon dioxide hydrogenation to methanol, *Nat. Commun.*, 2020, **11**, 2409.

210 N. J. Divins et al., Operando high-pressure investigation of size-controlled CuZn catalysts for the methanol synthesis reaction, *Nat. Commun.*, 2021, **12**, 1435.

211 J. Wang et al., Magnetics and spintronics on two-dimensional composite materials of graphene/hexagonal boron nitride, *Mater. Today Phys.*, 2017, **3**, 93–117.

212 G. Synthesis et al., Chemical Vapour Deposition of Graphene Synthesis, Characterisation, and Application: A Review, *Molecules*, 2020, **25**, 3856.

213 A. S. Mayorov et al., Micrometer-scale ballistic transport in encapsulated graphene at room temperature, *Nano Lett.*, 2011, **11**, 2396–2399.

214 A. A. Balandin, Thermal properties of graphene and nanostructured carbon materials, *Nat. Mater.*, 2011, **10**, 569–581.

215 K. S. Novoselov et al., A roadmap for graphene, *Nature*, 2012, **490**, 192–200.

216 M. I. Katsnelson, Graphene: carbon in two dimensions, *Mater. Today*, 2007, **10**, 20–27.

217 K. S. Novoselov et al., Two-dimensional gas of massless Dirac fermions in graphene, *Nature*, 2005, **438**, 197–200.

218 A. J. Watson et al., Transfer of large-scale two-dimensional semiconductors: Challenges and developments, *2D Mater.*, 2021, **8**, 032001.

219 K. S. Novoselov et al., Electric Field Effect in Atomically Thin Carbon Films, *Science*, 2004, **306**, 666–669.

220 R. S. Weatherup et al., Kinetic control of catalytic CVD for high-quality graphene at low temperatures, *ACS Nano*, 2012, **6**, 9996–10003.

221 C. Lee et al., Measurement of the Elastic Properties and Intrinsic Strength of Monolayer Graphene, *Science*, 2008, **321**, 385–388.

222 D. G. Papageorgiou et al., Mechanical properties of graphene and graphene-based nanocomposites, *Prog. Mater. Sci.*, 2017, **90**, 75–127.

223 R. R. Nair et al., Fine structure constant defines visual transparency of graphene, *Science*, 2008, **320**, 1308.

224 E. Escobedo-Cousin et al., Local solid phase growth of few-layer graphene on silicon carbide from nickel silicide supersaturated with carbon, *J. Appl. Phys.*, 2013, **113**, 114309.

225 K. V. Emtsev et al., Towards wafer-size graphene layers by atmospheric pressure graphitization of silicon carbide, *Nat. Mater.*, 2009, **8**, 203–207.

226 S. Unarunotai et al., Transfer of graphene layers grown on SiC wafers to other substrates and their integration into field effect transistors, *Appl. Phys. Lett.*, 2009, **95**, 202101.

227 A. J. Van Bommel et al., LEED and Auger Electron Observations of the SiC(0001) Surface, *Surf. Sci.*, 1975, **48**, 463–472.

228 M. Lotya et al., Liquid phase production of graphene by exfoliation of graphite in surfactant/water solutions, *J. Am. Chem. Soc.*, 2009, **131**, 3611–3620.

229 Y. Hernandez et al., High-yield production of graphene by liquid-phase exfoliation of graphite, *Nat. Nanotechnol.*, 2008, **3**, 563–568.

230 L. Jiao et al., Narrow graphene nanoribbons from carbon nanotubes, *Nature*, 2009, **458**, 877–880.

231 D. V. Kosynkin et al., Longitudinal unzipping of carbon nanotubes to form graphene nanoribbons, *Nature*, 2009, **458**, 872–876.

232 C. Mattevi et al., A review of chemical vapour deposition of graphene on copper, *J. Mater. Chem.*, 2011, **21**, 3324–3334.

233 R. S. Weatherup et al., In Situ Graphene Growth Dynamics on Polycrystalline Catalyst Foils, *Nano Lett.*, 2016, **16**, 6196–6206.

234 A. Dahal et al., Graphene-nickel interfaces: A review, *Nanoscale*, 2014, **6**, 2548–2562.

235 W. S. Leong et al., Paraffin-enabled graphene transfer, *Nat. Commun.*, 2019, **10**, 867.

236 J. W. Suk et al., Transfer of CVD-grown monolayer graphene onto arbitrary substrates, *ACS Nano*, 2011, **5**, 6916–6924.

237 L. Gao et al., Repeated growth and bubbling transfer of graphene with millimetre-size single-crystal grains using platinum, *Nat. Commun.*, 2012, **3**, 699.

238 J. Seo et al., Direct Graphene Transfer and Its Application to Transfer Printing Using Mechanically Controlled, Large Area Graphene/Copper Freestanding Layer, *Adv. Funct. Mater.*, 2018, **28**, 1707102.

239 O. J. Burton et al., Integrated Wafer Scale Growth of Single Crystal Metal Films and High Quality Graphene, *ACS Nano*, 2020, **14**, 13593–13601.

240 S. Y. Yang et al., Metal-etching-free direct delamination and transfer of single-layer graphene with a high degree of freedom, *Small*, 2015, **11**, 175–181.

241 S. Bae et al., Roll-to-roll production of 30-inch graphene films for transparent electrodes, *Nat. Nanotechnol.*, 2010, **5**, 574–578.

242 W. H. Lin et al., A direct and polymer-free method for transferring graphene grown by chemical vapor deposition to any substrate, *ACS Nano*, 2014, **8**, 1784–1791.

243 J. Liu et al., Controlled synthesis of Zirconium Oxide on graphene nanosheets by atomic layer deposition and its growth mechanism, *Carbon*, 2013, **52**, 74–82.

244 S. Cha et al., Low-temperature, dry transfer-printing of a patterned graphene monolayer, *Sci. Reports*, 2015, **5**, 17877.

245 G. P. Dai et al., Direct growth of graphene films on TEM nickel grids using benzene as precursor, *Chem. Phys. Lett.*, 2012, **531**, 193–196.

246 Y. Dong et al., Transfer-free, lithography-free and fast growth of patterned CVD

graphene directly on insulators by using sacrificial metal catalyst, *Nanotechnology*, 2018, **29**, 365301.

247 A. Ismach et al., Direct chemical vapor deposition of graphene on dielectric surfaces, *Nano Lett.*, 2010, **10**, 1542–1548.

248 H. Sojoudi et al., Transfer-Free Selective Area Synthesis of Graphene Using Solid-State Self-Segregation of Carbon In Cu/Ni Bilayers, *ECS J. Solid State Sci. Technol.*, 2013, **2**, M17.

249 S. Xu et al., Chemical vapor deposition of graphene on thin-metal films, *Cell Reports Phys. Sci.*, 2021, **2**, 100372.

250 Z. Shi et al., Direct-Chemical Vapor Deposition-Enabled Graphene for Emerging Energy Storage: Versatility, Essentiality, and Possibility, *ACS Nano*, 2022, **16**, 11646–11675.

251 Y. Li et al., Recent Advances in Transfer-Free Synthesis of High-Quality Graphene, *ChemSusChem*, 2023, **16**, 202300865.

252 F. Xiong et al., Transfer-free rapid growth of 2-inch wafer-scale patterned graphene as transparent conductive electrodes and heat spreaders for GaN LEDs, *npj 2D Mater. Appl.*, 2023, **7**, 72.

253 Y. Yang et al., Bottom-up Fabrication of Graphene on Silicon/Silica Substrate via a Facile Soft-hard Template Approach, *Sci. Reports*, 2015, **5**, 13480.

254 W. S. Tseng et al., Direct large-area growth of graphene on silicon for potential ultra-low-friction applications and silicon-based technologies, *Nanotechnology*, 2020, **31**, 335602.

255 A. Cortés et al., CVD synthesis of graphene from acetylene catalyzed by a reduced CuO thin film deposited on SiO2 substrates, *J. Chil. Chem. Soc.*, 2015, **60**, 2911–2913.

256 R. Liu et al., CO2-promoted transfer-free growth of conformal graphene, *Nano Res.*, 2023, **16**, 6334–6342.

257 J. Chen et al., Oxygen-aided synthesis of polycrystalline graphene on silicon dioxide substrates, *J. Am. Chem. Soc.*, 2011, **133**, 17548–17551.

258 J. Chen et al., Two-stage metal-catalyst-free growth of high-quality polycrystalline graphene films on silicon nitride substrates, *Adv. Mater.*, 2013, **25**, 992–997.

259 H. Tissot et al., Deciphering Radiolytic Oxidation in Halide Aqueous Solutions: A Pathway Toward Improved Synchrotron NAP-XPS Analysis, *J. Phys. Chem. C*, 2023, **127**, 15825–15838.

260 L. Zheng et al., Robust ultraclean atomically thin membranes for atomic-resolution electron microscopy, *Nat. Commun.*, 2020, **11**, 541.

261 J. Y. Lim et al., Pattern pick and place method for twisted Bi- and multi-layer graphene, *Materials*, 2019, **12**, 3740.

262 R. S. Weatherup et al., Long-Term Passivation of Strongly Interacting Metals with Single-Layer Graphene, *J. Am. Chem. Soc.*, 2015, **137**, 14358–14366.

263 D. I. Patel et al., Argon gas, by near-ambient pressure XPS, *Surf. Sci. Spectra*,

2019, **26**, 014024.

264 S. B. Desai et al., Gold-Mediated Exfoliation of Ultralarge Optoelectronically-Perfect Monolayers, *Adv. Mater.*, 2016, **28**, 4053–4058.

265 T. A. Green, Gold etching for microfabrication, *Gold Bull.*, 2014, **47**, 205–216.

266 P. Ahlberg et al., A two-in-one process for reliable graphene transistors processed with photo-lithography, *Appl. Phys. Lett.*, 2015, **107**, 203104.

267 W. R. Salaneck et al., Photoelectron spectroscopy of iodine - doped polyacetylene, *J. Chem. Phys.*, 1980, **3678**, 3674–3678.

268 M. S. Ahsan et al., Probing the molecular structure of aqueous triiodide via X-ray photoelectron spectroscopy and correlated electron phenomena, *Phys. Chem. Chem. Phys.*, 2022, **24**, 15540–15555.

269 D. Zheng et al., HAXPES reference spectra of KI with Cr Kα excitation, *Surf. Sci. Spectra*, 2023, **30**, 024026.

270 N. Ottosson et al., Photoelectron spectroscopy of liquid water and aqueous solution: Electron effective attenuation lengths and emission-angle anisotropy, *J. Electron Spectrosc. Relat. Phenom.*, 2010, **177**, 60–70.

271 B. Winter et al., Hydrogen bonds in liquid water studied by photoelectron spectroscopy, *J. Chem. Phys.*, 2007, **126**, 124504.

272 M. A. Brown et al., Spatial distribution of nitrate and nitrite anions at the liquid/vapor interface of aqueous solutions, *J. Am. Chem. Soc.*, 2009, **131**, 8354–8355.

273 J. Bin Wang et al., A review of graphene synthesis at low temperatures by CVD methods, *New Carbon Mater.*, 2020, **35**, 193–208.

274 R. S. Weatherup et al., On the mechanisms of Ni-catalysed graphene chemical vapour deposition, *ChemPhysChem*, 2012, **13**, 2544–2549.

275 Y. F. Shi et al., Methanol Synthesis from CO2/CO Mixture on Cu-Zn Catalysts from Microkinetics-Guided Machine Learning Pathway Search, *J. Am. Chem. Soc.*, 2022, **144**, 13401–13414.

276 X. Liu et al., In Situ Spectroscopic Characterization and Theoretical Calculations Identify Partially Reduced ZnO1−x/Cu Interfaces for Methanol Synthesis from CO2, *Angew. Chemie - Int. Ed.*, 2022, **61**, 202202330.

277 Z. Chen et al., The origin of the mediocre methanol selectivity of Cu/ZnO-based catalysts for methanol synthesis from CO2 hydrogenation, *Appl. Catal. B Environ.*, 2024, **340**, 123192.

278 R. Dalebout et al., Insight into the Nature of the ZnO x Promoter during Methanol Synthesis , *ACS Catal.*, 2022, **12**, 6628–6639.

279 D. Großmann et al., Surface Alloy or Metal–Cation Interaction-The State of Zn Promoting the Active Cu Sites in Methanol Synthesis Catalysts, *ChemCatChem*, 2017, **9**, 365–372.

280 X. K. Wu et al., Unraveling the catalytically active phase of carbon dioxide hydrogenation to methanol on Zn/Cu alloy: Single atom versus small cluster, *J. Energy Chem.*, 2021, **61**, 582–593.

281 S. Saedy et al., Copper-zinc oxide interface as a methanol-selective structure in Cu-ZnO catalyst during catalytic hydrogenation of carbon dioxide to methanol, *Catal. Sci. Technol.*, 2022, **12**, 2703–2716.

282 X. Ai et al., Highly dispersed mesoporous Cu/γ-Al2O3 catalyst for RWGS reaction, *Int. J. Hydrogen Energy*, 2022, **47**, 14884–14895.

283 I. Kasatkin et al., Role of lattice strain and defects in copper particles on the activity of Cu/ZnO/Al2O3 catalysts for methanol synthesis, *Angew. Chemie - Int. Ed.*, 2007, **46**, 7324–7327.

284 T. Lunkenbein et al., Formation of a ZnO Overlayer in Industrial Cu/ZnO/Al 2 O 3 Catalysts Induced by Strong Metal-Support Interactions , *Angew. Chem.*, 2015, **127**, 4627–4631.

285 S. Kuld et al., Quantification of Zinc Atoms in a Surface Alloy on Copper in an Industrial-Type Methanol Synthesis Catalyst, *Angew. Chem.*, 2014, **126**, 6051–6055.

286 S. Kuld et al., Quantifying the promotion of Cu catalysts by ZnO for methanol synthesis, *Science*, 2016, **352**, 969–974.

287 T. Koitaya et al., Operando Characterization of Copper-Zinc-Alumina Catalyst for Methanol Synthesis from Carbon Dioxide and Hydrogen by Ambient-Pressure Hard X-ray Photoelectron Spectroscopy, *J. Phys. Chem. C*, 2023, **127**, 13044–13054.

288 F. Liao et al., Morphology-Dependent Interactions of ZnO with Cu Nanoparticles at the Materials' Interface in Selective Hydrogenation of CO2 to CH3OH, *Angew. Chem.*, 2011, **123**, 2210–2213.

289 M. S. Spencer, The role of zinc oxide in Cu/ZnO catalysts for methanol synthesis and the water-gas shift reaction, *Top. Catal.*, 1999, **8**, 259–266.

290 R. Burch et al., The role of copper and zinc oxide in methanol synthesis catalysts, *J. Chem. Soc., Faraday Trans.*, 1990, **86**, 2683–2691.

291 A. O. Elnabawy et al., Why ZnO is the Support for Cu in Methanol Synthesis? A Systematic Study of the Strong Metal Support Interactions, *ACS Sustain. Chem. Eng.*, 2022, **10**, 1722–1730.

292 W. T. Figueiredo et al., Understanding the Strong Metal-Support Interaction (SMSI) Effect in CuxNi1- x/CeO2 (0 < x < 1) Nanoparticles for Enhanced Catalysis, *ACS Appl. Nano Mater.*, 2019, **2**, 2559–2573.

293 P. Amann et al., A high-pressure x-ray photoelectron spectroscopy instrument for studies of industrially relevant catalytic reactions at pressures of several bars, *Rev. Sci. Instrum.*, 2019, **90**, 103102.

294 W. Tu et al., Gas-Dependent Active Sites on Cu/ZnO Clusters for CH3OH Synthesis, *J. Am. Chem. Soc.*, 2023, **145**, 8751–8756.

295 S. Yue et al., Structural and chemical transformations of CuZn alloy nanoparticles under reactive redox atmospheres : an in situ TEM study, *Nano Res.*, 2024, **17**, 6265–6273.

296 W. Wang et al., CO2 hydrogenation to methanol over Cu/CeO2 and Cu/ZrO2 catalysts: Tuning methanol selectivity via metal-support interaction, *J. Energy*

Chem., 2020, **40**, 22–30.

297 M. Bowker et al., Mechanism and kinetics of methanol synthesis on zinc oxide, *J. Chem. Soc. Faraday Trans. 1 Phys. Chem. Condens. Phases*, 1981, **77**, 3023–3036.

298 T. Reichenbach et al., Ab initio study of CO2 hydrogenation mechanisms on inverse ZnO/Cu catalysts, *J. Catal.*, 2018, **360**, 168–174.

299 M. Zabilskiy et al., Copper-Zinc Alloy-Free Synthesis of Methanol from Carbon Dioxide over Cu/ZnO/Faujasite, *ACS Catal.*, 2020, **10**, 14240–14244.

300 T. Fujitani et al., The chemical modification seen in the Cu/ZnO methanol synthesis catalysts, *Appl. Catal. A Gen.*, 2000, **191**, 111–129.

301 H. S. Jeon et al., Operando insight into the correlation between the structure and composition of CuZn nanoparticles and their selectivity for the electrochemical CO2 reduction, *J. Am. Chem. Soc.*, 2019, **141**, 19879–19887.

302 S. Maroie et al., Surface oxidation of polycrystalline α(75%Cu/25%Zn) and β(53%Cu/47%Zn) brass as studied by XPS: influence of oxygen pressure, *Appl. Surf. Sci.*, 1984, **17**, 463–476.

303 R. Gleißner et al., Role of Oxidation-Reduction Dynamics in the Application of Cu/ZnO-Based Catalysts, *ACS Appl. Nano Mater.*, 2023, **6**, 8004–8016.

304 H. Chi et al., Dependence of H2 and CO2 selectivity on Cu oxidation state during partial oxidation of methanol on Cu/ZnO, *Appl. Catal. A Gen.*, 2018, **556**, 64–72.

305 F. Cocco et al., Nanosized surface films on brass alloys by XPS and XAES, *RSC Adv.*, 2016, **6**, 31277–31289.

306 D. H. Simonne et al., THORONDOR: A software for fast treatment and analysis of low-energy XAS data, *J. Synchrotron Radiat.*, 2020, **27**, 1741–1752.

307 G. E. Hammer et al., The oxidation of zinc in air studied by XPS and AES, *J. Vac. Sci. Technol. A Vacuum, Surfaces, Film.*, 1983, **1**, 1026–1028.

308 R. Wang et al., Exploring the phase transformation in ZnO/Cu(111) model catalysts in CO2 hydrogenation, *J. Energy Chem.*, 2021, **60**, 150–155.

309 B. H. Liu et al., Ultrathin Zn and ZnO films on Cu(111) as model catalysts, *Appl. Catal. A Gen.*, 2017, **548**, 16–23.

310 P. B. Rasmussen et al., The interaction of carbon dioxide with Cu(100), *Surf. Sci.*, 1992, **269**–**270**, 352–359.

311 P. Company et al., Interaction of O2 with Low Index Faces of α-CuZn, *Surf. Sci.*, 1983, **127**, 200–222.

312 M. P. L. Kang et al., The Role of Undercoordinated Sites on Zinc Electrodes for CO2 Reduction to CO, *Adv. Funct. Mater.*, 2022, **32**, 2111597.

313 R. M. Palomino et al., Hydrogenation of CO2 on ZnO/Cu(100) and ZnO/Cu(111) Catalysts: Role of Copper Structure and Metal-Oxide Interface in Methanol Synthesis, *J. Phys. Chem. B*, 2018, **122**, 794–800.

314 S. Ullah Awan et al., Ferromagnetism in Li doped ZnO nanoparticles: The role of interstitial Li, *J. Appl. Phys.*, 2012, **112**, 103924.

315 A. M. Pineda-Reyes et al., Recent advances in ZnO-based carbon monoxide sensors: Role of doping, *Sensors*, 2021, **21**, 4425.

316 R. Heinhold et al., Influence of polarity and hydroxyl termination on the band bending at ZnO surfaces, *Phys. Rev. B - Condens. Matter Mater. Phys.*, 2013, **88**, 235315.

317 R. Heinhold et al., Stability of the surface electron accumulation layers on the nonpolar (1010) and (1120) faces of ZnO, *J. Phys. Chem. C*, 2014, **118**, 24575–24582.

318 R. Heinhold et al., Polarity-dependent photoemission of in situ cleaved zinc oxide single crystals, *J. Mater. Res.*, 2012, **27**, 2214–2219.

319 V. Schott et al., Chemical activity of thin oxide layers: Strong interactions with the support yield a new thin-film phase of zno, *Angew. Chemie - Int. Ed.*, 2013, **52**, 11925–11929.

320 H. L. Hong et al., Understanding the Cu-Zn brass alloys using a short-range-order cluster model: Significance of specific compositions of industrial alloys, *Sci. Reports*, 2014, **4**, 7065.

321 A. A. Makarova et al., Insight into Bio-metal Interface Formation in vacuo: Interplay of S-layer Protein with Copper and Iron, *Sci. Reports*, 2015, **5**, 8710.

322 O. Dulub et al., Growth of copper on single crystalline ZnO: surface study of a model catalyst, *Top. Catal.*, 2005, **36**, 65–76.

323 Z. Zheng et al., Investigation of heat-of-fusion heat sinks for polymer-type metal oxide surge arresters, *Conf. Rec. IEEE Int. Symp. Electr. Insul.*, 2007, 253–256.

324 Y. Song et al., Tunable properties and composition of ZnO films supported on metal surfaces, *J. Mater. Chem. A*, 2023, **11**, 13665–13676.

325 H. V. Thang et al., H2 Adsorption on Wurtzite ZnO and on ZnO/M(111) (M=Cu, Ag and Au) Bilayer Films, *ChemNanoMat*, 2019, **5**, 932–939.

326 A. Gotti et al., Basic metal oxides as Co-catalysts in the conversion of synthesis gas to methanol on supported palladium catalysts, *J. Catal.*, 1998, **175**, 302–311.

327 R. S. Weatherup et al., In situ characterization of alloy catalysts for Low-temperature graphene growth, *Nano Lett.*, 2011, **11**, 4154–4160.

328 W. Zhou et al., in *Scanning Microscopy for Nanotechnology: Techniques and Applications*, 2007, pp. 1–40.

329 D. Stojakovic, Electron backscatter diffraction in materials characterization, *Process. Appl. Ceram.*, 2012, **6**, 1–13.

330 P. Blake et al., Making graphene visible, *Appl. Phys. Lett.*, 2007, **91**, 063124.

331 N. John et al., *Raman Spectroscopy*, Elsevier Inc., 2017, vol. 2.

332 J. H. Scofield, Theoretical Photoionization Cross Sections From 1 To 1500 keV, *Lawrence Livermore Lab.*, 1973, 5–6.

333 C. J. Powell et al., *NIST Electron Inelastic-Mean-Free-Path Database*, 2000.

334 P. Leidinger et al., Toward the perfect membrane material for environmental x-

ray photoelectron spectroscopy, *J. Phys. D: Appl. Phys.*, 2021, **54**, 234001.

335 J. Wan et al., Negative Poisson's ratio in graphene oxide, *Nanoscale*, 2017, **9**, 4007–4012.

336 J. W. Suk et al., Mechanical properties of monolayer graphene oxide, *ACS Nano*, 2010, **4**, 6557–6564.

337 J. Brenker et al., X-ray compatible microfluidics for in situ studies of chemical state, transport and reaction of light elements in an aqueous environment using synchrotron radiation, *Lab Chip*, 2022, **22**, 1214–1230.

338 L. J. Cote et al., Langmuir-blodgett assembly of graphite oxide single layers, *J. Am. Chem. Soc.*, 2009, **131**, 1043–1049.

339 Y. Unutulmazsoy et al., Reduction of thermally grown single-phase CuO and Cu2O thin films by in-situ time-resolved XRD, *Appl. Surf. Sci.*, 2022, **588**, 152896.

340 A. Cabrero-Vilatela et al., Towards a general growth model for graphene CVD on transition metal catalysts, *Nanoscale*, 2016, **8**, 2149–2158.

341 L. G. De Arco et al., Synthesis, Transfer, and Devices of Single- and Few-Layer Graphene by Chemical Vapor Deposition, *IEEE Trans. Nanotechnol.*, 2009, **2**, 135–138.

342 P. W. Sutter et al., Epitaxial graphene on ruthenium, *Nat. Mater.*, 2008, **7**, 406–411.

343 Z. Sun et al., Growth of graphene from solid carbon sources, *Nature*, 2010, **468**, 549–552.

344 Z. Li et al., Low-temperature growth of graphene by chemical vapor deposition using solid and liquid carbon sources, *ACS Nano*, 2011, **5**, 3385–3390.

345 M. Thakur et al., Wafer-Scale Fabrication of Nanopore Devices for Single-Molecule DNA Biosensing using MoS2, *Small Methods*, 2020, **4**, 200072.

346 N. S. Mueller et al., Growing graphene on polycrystalline copper foils by ultra-high vacuum chemical vapor deposition, *Carbon*, 2014, **78**, 347–355.

347 S. Kumar et al., Electronic structure, magnetic and structural properties of Ni doped ZnO nanoparticles, *Mater. Res. Bull.*, 2014, **59**, 377–381.

348 A. Shimamura et al., XANES characterizations of amorphous mixed metal oxides derived from Zn/Al layered double hydroxides through thermal treatment, *J. Solid State Chem.*, 2022, **316**, 123567.

349 R. Bhardwaj et al., Role of low energy transition metal ions in interface formation in ZnO thin films and their effect on magnetic properties for spintronic applications, *Appl. Surf. Sci.*, 2019, **479**, 1021–1028.

350 O. Trejo et al., XANES Studies of Zinc Tin Oxide Films Deposited by Atomic Layer Deposition: Revealing Process-Structure Relationships for Amorphous Oxide Semiconductors, *J. Phys. Chem. C*, 2023, **127**, 338–349.

351 D. J. Keavney et al., Where does the spin reside in ferromagnetic Cu-doped ZnO?, *Appl. Phys. Lett.*, 2007, **91**, 91–94.

352 S. B. Singh et al., Observation of the origin of d0 magnetism in ZnO nanostructures using X-ray-based microscopic and spectroscopic techniques, *Nanoscale*, 2014, **6**, 9166–9176.

353 A. Sharma et al., Effect of Cu insertion on structural, local electronic/atomic structure and photocatalyst properties of TiO2, ZnO and Ni(OH)2 nanostructures: XANES-EXAFS study, *Mater. Chem. Phys.*, 2017, **191**, 129–144.

354 J. W. Chiou et al., Diameter dependence of the electronic structure of ZnO nanorods determined by x-ray absorption spectroscopy and scanning photoelectron microscopy, *Appl. Phys. Lett.*, 2004, **85**, 3220–3222.

355 S. Hageraats et al., X-ray Nanospectroscopy Reveals Binary Defect Populations in Sub-micrometric ZnO Crystallites, *J. Phys. Chem. C*, 2020, **124**, 12596–12605.

356 D. Y. Cho et al., Spectroscopic evidence for limited carrier hopping interaction in amorphous ZnO thin film, *Appl. Phys. Lett.*, 2009, **95**, 261903.